Modelling of long High Voltage AC Cables in the Transmission System

Gudmundsdottir, Unnur Stella

Publication date:
2010

Document Version
Accepted author manuscript, peer reviewed version

Modelling of long High Voltage AC cables in Transmission Systems

Unnur Stella Guðmundsdóttir

ENERGINET.DK

Department of ENERGY TECHNOLOGY E.T.

Modelling of long High Voltage AC cables in Transmission Systems

by

Unnur Stella Guðmundsdóttir

Dissertation submitted to the Faculty of Engineering, Science and Medicine
at Aalborg University
in partial fulfilment of the requirements for the degree of
Doctor of Philosophy in Electrical Engineering

Department of Energy Technology
Aalborg University, Denmark
May 2010

PhD Thesis
Modelling of long High Voltage AC cables in Transmission Systems

Printed in Denmark by Energinet.dk, Fredericia
September 2010, 2nd ed.

ISBN 978-87-90707-73-6

Aalborg University
Department of Energy Technology
Pontoppidanstræde 101
DK-9220 Aalborg East, Denmark.
www.iet.aau.dk

To my family and friends.
Especially my two wonderful boys, Gunnar Máni and Guðmundur Magnús, for all their patience and understanding.

Preface

This thesis is submitted to the Faculty of Engineering, Science and Medicine at Aalborg University in partial fulfilment of the requirements for the PhD degree in Electrical Engineering. The research has been conducted at the Department of Energy Technology for Energinet.dk, of which I was hired as an employee for the entire project period.

The project has been followed by two supervisors: Associate Professor Claus Leth Bak (Department of Energy Technology) and Dr. Wojciech Wiechowski (Energinet.dk).

Energinet.dk has fully funded the research leading to this thesis "Modelling of long High Voltage AC cables in Transmission Systems". This funding has been vital for this research project. Renting of expensive laboratory equipment, performance of field measurements and participation in international working groups was made possible thanks to generous support from the company.

All of November 2008 was spent at SINTEF, Trondheim, Norway, where I visited Dr. Bjørn Gustavsen, working on analysing the first set of measurements and planning the other measurements performed. This work resulted in a co-authored paper, by myself, Dr. Gustavsen and my supervisors, for IEEE Transactions on Power Delivery.

In the summer of 2009 I spent three months at The Manitoba HVDC Research Centre in Winnipeg, Canada, where I worked in co-operation with Dr. Jeewantha Da Silva on analysing the deviation between field measurements and simulation results when explicitly exciting the modes. Furthermore during this stay I worked on the cable model improvements, which are one of the major contributions in my research work. The work resulted in two papers. One for the IEEE PES GM 2010, co-authored by myself, Dr. Da Silva and my supervisors. The other for IEEE Transactions on Power Delivery, authored by myself and my supervisors.

This thesis is constructed in 5 parts and appendices. An overall literature reference list is presented at the end of the main report. A list of the authored publications, written in relation to this research project is presented at the end of the thesis. Literature references are shown as [i], where i is the number of the literature in the reference list. References to figures and tables are shown as figure C.F or table C.F and references to equations are shown as equation C.F, where C is the chapter number and F indicates the figure, table or equation.

Acknowledgements

I owe gratitude to many people that helped me in various ways. In particular, I would like to thank:

- My supervisors, Claus Leth Bak and Wojciech Wiechowski for all their support, help and comments during the project period.
- Jens Christian Hygebjerg, project manager of HR2 connection, for allowing and organizing field measurements on HR2 cables while under laying.
- Carl-Erik Madsen, Dr. Wojciech Wiechowski and Filipe Faria da Silva all from Energinet.dk for their help with carrying out the field measurements.
- Claus Leth Bak, Wojciech Wiechowski, Filipe Faria da Silva, Per Holst, Thomas Kvarts, Jakob Kessel, Martin Randrup and Ole Graabæk for their contribution during status meetings throughout the entire project period. I would like to give special thanks to Per Holst for his help with preparing and reading all the text of the final thesis.
- Everyone at Planning Dept. and Transmission Dept. at Energinet.dk for their hospitality and contributions.
- All the people working at SINTEF for their hospitality and help with the research. The month I spent in Trondheim was very fruitful for my project. Especially I thank Dr. Bjørn Gustavsen for his invaluable advice and guidance.
- All the people at the Manitoba HVDC Research Centre for their hospitality and help with the research. The three months I spent in Winnipeg were tremendously fruitful for my research. Especially I thank Dr. Jeewantha Da Silva for his invaluable time, numerous professional discussions and tremendous help as well as for the great co-operation with preparing documents for CIGRE WG C4.502. Also I would like to thank John Nordström from the Manitoba HVDC Research Centre for his invaluable help and time.
- All the people of CIGRE WG C4.502 for numerous professional discussion during WG meetings.
- My parents and all my family on Iceland for all their support and help with my kids.
- Finally I owe special thanks to the father of my two children, Jóhann Gunnar Jónsson, for his support, patience with me and remarkable understanding throughout the entire project period, which demanded tremendous amount of time spent away from family and understanding during long nights at the office.

Unnur Stella Guðmundsdóttir May 2010, Aalborg

Abstract

The research documented in this thesis addresses Modelling of long High Voltage AC cables in Transmission Systems. Modelling techniques of HV AC cables has been a subject to researchers as early as in the 1920'ies and research in the field continues steadily as cables become more complicated in design and more popular at higher voltage levels and for longer transmission lengths.

In recent years, the interest towards using underground cables in power transmission has increased considerably. In Denmark, the entire 150 kV and 132 kV transmission network shall be undergrounded during the next 20 years. Even 400 kV transmission lines will be undergrounded gradually as more experience is gathered. Precise modelling of long and many (meshed) underground cable lines is therefore essential and it is important that differences between simulations and measurements are identified, studied and eliminated. A study of the cable model accuracy for transmission line modelling is the topic of the research documented in this thesis. The main part of the work is split in two. Firstly planning, performing and analysing high frequency field measurements for model validation. Secondly improvements to the existing cable models.

Before the two main parts are discussed, transmission cables are described; their physical layout and mathematical representation. Relevant literature study on modelling transmission cables by introducing existing models and explaining how to model in the software used in this thesis, EMTDC/PSCAD is provided.

A typical HV AC underground power cable is formed by 4 main layers, namely; Conductor-Insulation-Screen-Insulation. In addition to these main layers, the cable also has semiconductive screens, swelling tapes and metal foil. For high frequency modelling in EMT-based software, each of these layers must be correctly represented. Description of how to perform such simulations is therefore given in the thesis.

The first main part of the work is the field measurements. The usual practice for validating a cable model has been to compare the simulation results to frequency domain calculations transformed to the time domain by use of Inverse Fast Fourier Transform (IFFT). This however, does not ensure the accuracy of the entry parameters of the modelling procedure, the parameter conversion and the modelling assumptions. Therefore, in order to analyse how cables behave field tests are performed. The purpose of the field measurements is to analyse the cable model, investigate the accuracy of the model, identify origin of disagreement between measurement and simulation results and validate the improved simulations when identified origin of disagreement has been eliminated by more accurate modelling.

Before starting any field tests, the measurement preparation is of great importance. All field measurements are therefore planned with simulations based on manufacturer cable data. Such preparation is performed both in order to plan where and what to measure and more importantly, to have a base for comparison at the measuring site.

Measurements are performed on a 400 kV 7.6 km long cable, which is a part of a hybrid OHL/cable transmission line. The cables are laid in flat formation and have been in operation for several years. For performing the measurements, the cables are disconnected from the OHL, and a single cable is energised with a fast front impulse generator. The field measurements are compared to simulations using the Frequency dependent Phase Model in EMTDC/PSCAD (this is based on the Universal Line Model). From the comparison it is observed how a deviation between field measurements and simulations appears after some time and by modal analysis it is possible to identify the source of deviation. Based on this analysis it is suggested that the existing simulation model, is precise and accurate for short cables or cables with no crossbonding points. In order to verify this, field measurements on a 150 kV 1.78 km long cable are performed. This cable is laid in a tight trefoil configuration and field measurements are performed under construction of the cable line. The suggestion of the existing model being accurate for non-crossbonded cables is verified, by excitation of exclusively the coaxial mode, which will dominate when no crossbondings are present. The identified source of deviation is also validated and suggestions for improvements of the cable model are given.

In order to validate the suggested improvements, after implementation, field measurements on longer parts of the 150 kV cable line are performed. Field measurements on a single major section, containing 2 crossbonding points, are performed as well as on a 55 km long part of the cable, having 33 crossbonding points. Comparison of field measurement and simulation results show deviation appearing after some time. From analysing the modal currents, the source of deviation is identified.

The same phenomena and source for deviation between field measurements and simulation results is identified for a 400 kV flat formation crossbonded 7.6 km cable line, a 150 kV tight trefoil crossbonded 2.5 km cable line and 150 kV tight trefoil crossbonded 55 km cable line. The source of the deviation is validated by explicitly exciting the intersheath mode of a 150 kV tight trefoil formation non-crossbonded 1.78 km cable line.

The main conclusions in the first part of the thesis are:

- The existing cable model is precise and accurate for short cables or cables with no crossbonding points
- There is deviation between simulation and field measurement results on long cables. The existing cable model is not of acceptable accuracy for crossbonded cable lines
- Inaccurate modelling of the cable screen is the reason for deviation between simulation and field measurement results. This is because of intersheath mode reflecting from the crossbonding points.

The second main part of the work deals with improving the cable model based on the findings from analysis of the field measurements. The existing EMT-based models have the configuration for cables: conductor-insulation (with or without SC layers)-conductor-insulation(-conductor-insulation), whereas a transmission line single core XLPE cable will normally have the configuration: conductor-SC layer-insulation-SC layer-conductor-SC layer-conductor-insulation. Furthermore the existing cable models use analytical equations to calculate the series impedances and shunt admittances of the cable line. These analytical equations include skin effect, whereas they do not include proximity effect.

The cable model is firstly improved in such a way, that the correct physical layout of the screen (wired conductor-SC layer-solid hollow conductor) is implemented in the model. These improvements result in a more correct series impedance and hence a more correct damping of the simulations. Even though

the series impedance is more correct, it does still not include the proximity effect and high frequency oscillations are not correctly damped in the simulations. At higher frequencies the proximity effect will force the current to be more constrained to smaller regions, resulting in a change in the impedance of the conductor. Therefore the cable model is secondly improved in such a way, that the impedance matrix is no longer calculated from the analytical equations but from a finite element method including the proximity effect.

A MATLAB program is constructed in order to calculate the impedance matrix based on the finite element method. Furthermore, this MATLAB program also includes the correct physical layout of the cable screen. The modelling procedure is then changed so that the existing model will no longer use analytical equations, but call the series impedance matrix from the output of the MATLAB program. The shunt admittance matrix is still calculated inside the existing model with analytical equations and calculations of the cable's terminal conditions is performed as before, where the difference lies in the new series impedance matrix. By including the proximity effect, the impedance matrix will change at higher frequencies, resulting in more correct damping. By combining both the correct physical layout of the screen and the proximity effect, the damping of the simulation results becomes correct and the simulated signals become identical to field measurement results.

The main conclusions in the second part of the thesis are:

- By improving the cable model with respect to correct physical layout of the screen, a correct damping will appear in the simulation results.
- The correct physical layout of the cable screen does not eliminate high frequency oscillations that appear.
- By including the proximity effect in the model, the impedance will change at high frequencies resulting in accurate damping of the high frequency oscillations.
- By combining the proximity effect and the correct physical layout of the screen, the simulation results agree with field measurement results within the tolerance of the field measurements. This is the case for a non-crossbonded cable where the intersheath mode is explicitly excited, for a 2.5 km cable with two crossbonding points and for a 55 km long cable line with 33 crossbonding points.

Dansk Resumé

Denne afhandling er dokumentation for et forskningsprojekt omhandlende modellering af lange HV AC kabler i transmissionssystemer. Modellerings teknikker for HV AC kabler har været et emne til forskere siden i 1920'erne og forskning på området fortsætter i takt med at kabler bliver mere kompliceret i design og mere populære ved højere spændings niveauer og for lange transmissions længder.

I de seneste år er interessen for anvendelse af højspændingskabler i transmissionsnettet steget betydeligt. I Danmark skal hele 150 kV og 132 kV transmissionsnettet kabellægges i løbet af de næste 20 år. Selv 400 kV luftledninger vil blive kabellagt efterhånden som mere erfaring er samlet. Præcis modellering af lange og mange (mæskede) kabellinjer er derfor afgørende, og det er vigtigt, at forskel mellem simuleringer og målinger er identificeret, undersøgt og fjernet. Emnet for forskningen dokumenteret i denne afhandling er en undersøgelse af nøjagtigheden for transmission kabel modellering. Den væsentligste del af arbejdet er delt i to. For det første planlægning, gennemførelse og analyse af høj frekvens målinger for modelvalidering. For det andet forbedringer af det eksisterende kabel model.

Før selve forskningen er diskuteret, er transmissionskabler beskrevet; deres fysiske indretning og matematiske repræsentation. Relevant litteratur omkring modellering af transmissionskabler er givet og de eksisterende modeller er forklaret. Derudover er modellering i softwaren der anvendes i denne afhandling, EMTDC / PSCAD, forklaret.

En typisk HV AC strømkabel er dannet af 4 lag, nemlig; Leder-Isolering-Skærm-Isolering. Ud over disse primære lag, har kablet også halvledende skærme, kvælbånd og metalfolie. For høj frekvens modellering i EMT-baseret software, skal hver af disse lag være korrekt repræsenteret. Beskrivelse af, hvordan sådanne simuleringer udføres er derfor givet i rapporten.

Den første del af arbejdet fokuserer på målinger. Sædvanlige praksis for validering af et kabel model har været at sammenligne simuleringsresultaterne med frekvens domæne beregninger transformeret til tidsdomænet ved hjælp af Inverse Fast Fourier Transform (IFFT). Dette sikrer dog ikke nøjagtigheden af de elektriske parametre anvendt i modellering proceduren, parameter konvertering og modelleringens antagelser. Derfor, for at analysere, hvordan kablerne opfører sig er målinger udført. Formålet med målingerne er at analysere kabel modellen, undersøge nøjagtigheden af den model, identificere årsag til forskel mellem måle og simulerings resultater og validere de forbedrede simuleringer når den identificerede årsag til forskellen er blevet elimineret med mere præcise modelleringer.

Måle forberedelse før ethvert forsøg, er af stor betydning. Alle målinger er derfor planlagt med simuleringer baseret på producentens kabel data. De pågældende simuleringer er udført både for at planlægge, hvor og hvad der skal måles og endnu vigtigere, at have en base for sammenligning på målepladsen.

Målinger er udført på et 400 kV 7,6 km lang kabel, som er en del af en hybrid OHL/kabel transmis-

sion linje. Kablerne ligger i flad formation og har været i drift i flere år. For at udføre målingerne, er kablerne koblet fra luftledningen, og en hurtig front impuls er påført et enkelt kabel. Måle resultaterne er sammenlignet med simuleringer med "Frequency Dependent Phase Model" i EMTDC / PSCAD (dette er baseret på "the Universal Line Model"). Det er observeret hvordan afvigelse mellem målinger og simuleringer forekommer efter et stykke tid. Med hjælp af modal analyse er det muligt at identificere kilden til afvigelsen. Baseret på denne analyse foreslås det, at den eksisterende simuleringsmodel, er præcist og nøjagtig for korte kabler eller kabler uden nogen krydskoblinger. For at kontrollere dette, er målinger også udført på et 150 kV 1,78 km langt kabel uden krydskoblinger. Dette kabel er lagt i en tight trefoil konfiguration og målinger er udført under opførelse af kablet. Forslaget om at den nuværende model er nøjagtig for ikke-krydskoblede kabler er blevet bekræftet, ved udelukkende at spændingssætte en koaksial mode, som vil dominere, når krydskoblinger ikke er til stede. Den identificerede kilde til afvigelsen er også valideret og forslag til forbedringer af kabel modellen er givet.

For at validere de foreslåede forbedringer, efter implementation, udføres der målinger på længere dele af 150 kV kabel linjen. Målinger på en single major afsnit, der indeholder 2 krydskoblinger, udføres samt målinger på en 55 km lang del af kablet, med 33 krydskoblinger. Sammenligning af målinger og simulerings resultater viser en afvigelse efter et stykke tid. Fra analyse af modal strømme, er kilden til afvigelsen identificeret.

Det samme fænomen og kilde til afvigelsen mellem målinger og simulerings resultater er identificeret for en 400 kV flad formation krydskoblet 7,6 km kabel linje, en 150 kV tight trefoil krydskoblet 2,5 km kabel linje og en 150 kV tight trefoil krydskoblet 55 km kabel linje. Kilden til afvigelsen er valideret ved at spændingssætte en 150 kV tight trefoil, ikke-krydskoblet, 1,78 km kabel linje i en intersheath mode.

De vigtigste konklusioner i den første del af afhandlingen er:

- Det eksisterende kabel model er præcist og nøjagtigt for korte kabler eller kabler uden krydskoblinger.
- Der opstår afvigelse mellem simuleringer og måleresultater på lange kabler. Det eksisterende kabel model har en ikke acceptabel nøjagtighed for krydskoblede kabellinjer
- Upræcise modellering af kabel skærmen er årsagen til afvigelsen mellem simuleringer og måleresultaterne. Dette skyldes intersheath mode der reflekterer ved krydskoblinger.

Det andet del af arbejdet omhandler forbedring af kabel modellen, der bygger på resultaterne fra analyse af målingerne. De eksisterende EMT-baserede modeller har den konfiguration for kabler: leder-isolering (med eller uden SC lag)-leder-isolering (-leder-isolering), hvorimod en transmissions enleder XLPE kabel vil normalt have konfigurationen: leder-SC lag-isolering-SC lag-leder-SC lag-leder-isolering. Derudover anvender de eksisterende kabel modeller analytiske beregninger til at finde serie impedansen og shunt admittancen af kabel linjen. Disse analytiske ligninger omfatter skin effekt, hvorimod de ikke omfatter næreffekten.

Kabel modellen forbedres først således, at den korrekte fysiske layout af skærmen (wired leder-SC lag-solid hollow leder) er implementeret i modellen. Disse forbedringer resulterer i en mere korrekt serie impedans og dermed en mere korrekt dæmpning af simuleringer. Selvom serie impedans er mere korrekt, omfatter den stadigvæk ikke næreffekten og høje frekvens oscillationer er ikke korrekt dæmpet i simuleringerne. Ved højere frekvenser vil næreffekten tvinge strømmen til at være mere begrænset til mindre områder, hvilket resulterer i en ændring af impedansen. Derfor forberedes kablet også således, at impedans matricen beregnes ikke længere ud fra de analytiske ligninger, men fra en finite element metode, der inkluderer næreffekten.

Et MATLAB program er implementeret med henblik på at beregne impedans matricen baseret på finite element metoden. Desuden omfatter denne MATLAB program også den rigtige fysiske layout af kabel skærmen. Modelleringen ændres derefter, således at den nuværende model vil ikke længere bruge analytiske ligninger, men kalder serie impedans matricen fra outputtet af MATLAB programmet. Shunt matricen er fortsat beregnet i den eksisterende model med analytiske ligninger og beregninger af kablets terminal betingelser udføres som før, hvor forskellen ligger i den nye serie impedans matrice. Ved at inkludere næreffekten vil impedans matricen ændres ved højere frekvenser, hvilket resulterer i mere korrekt dæmpning. Ved at kombinere både det korrekte fysiske layout af skærmen og næreffekten, vil dæmpning af simuleringsresultaterne blive korrekte, og de simulerede signaler bliver identiske med måleresultaterne.

De vigtigste konklusioner i den anden del af afhandlingen er:

- Ved at forbedre kabel modellen med hensyn til at rette fysiske layout af skærmen, vises en korrekt dæmpning i simuleringsresultaterne.
- Den korrekte fysiske layout af kablet skærmen ikke fjerne højfrekvente oscillationer, der eksisterer.
- Ved at inkludere næreffekten i modellen, vil ændringen i impedansen ved høje frekvenser medføre præcis dæmpning af højfrekvente oscillationer.
- Ved at kombinere næreffekten og den korrekte fysiske layout af skærmen, bliver simuleringsresultaterne identiske med måleresultaterne inden for tolerance af målinger. Dette er tilfældet for en ikke-krydskoblet kabel, hvor udelukkende intersheath mode er magnetiseret, for en 2,5 km kabel med to krydskoblinger og for en 55 km lange kabel linje med 33 krydskoblinger.

Contents:

Part I

Preliminaries

CHAPTER 1

Introduction

The aim of the research presented in this thesis is to give an understanding of cable modelling as well as to design and describe a comprehensive model for high voltage (HV) AC cables. A model to be used as an instrument in planning and problem solving for long distance HV AC underground power transmission. HV transmission cables are normally modelled using EMT-based computer simulation software. These models are meant to correctly simulate low-frequency switching behaviour (up to 10 kHz) in underground cable system, caused by for instance disconnection of transformers, shunt reactors, lines and cables as well as high-frequency transients from for instance fault on the cable or lightning surges on a hybrid overhead line-cable system. In this thesis, the high frequency (above 10 kHz) transient behaviour of the underground cable system is not only simulated correctly but also explained thoroughly. A model, proven to be accurate at power frequency and for low frequency transients is improved in order to also simulate accurately high frequency transients.

In this project there are two major contributions. First of all designed, performed and analysed field tests on HV AC cables for high frequency cable model validation. Second of all implementation of methods for cable impedance calculations giving accurate high frequency cable simulations.

1.1 Background

The state of power transmission becomes increasingly more complicated as power usage escalates and people's knowledge of the environment grows. The problems concerning distribution of power, from where it is produced to where it is to be used, increases as rules regarding transmission become more complicated due to the expansion of cities and further additions of land reserves, all the while as demand for power increases. This is one of the main reasons why interest towards underground HV cables, in preference to the customary OHL, has increased considerably.

In Denmark, as a leading country, the entire 150 kV and 132 kV transmission network shall be undergrounded during the next 20 years. Even 400 kV transmission lines will be undergrounded gradually as more experience is gathered.

In order to research the possibility of using HV AC cables for entire transmission systems, it is necessary to have precise simulation models. Small errors for short cables can become a larger problem when length of the cables and number of crossbonding points are increased. It is therefore important that differences between simulations and measurements are identified, studied and eliminated. Because of this, modelling cables for various transient studies has become a popular topic in the past few years.

A review of work from recognised pioneers in cable impedance calculations and in cable modelling, as well as others, is outlined and commented in chapter 2 of this thesis. All publications in the field, used

by the author, are listed on page 169-173. From this list it can be seen how even though as early as the 1920'ies the first major contributions were published, research in the field has continued steadily to our days.

The usual practice for validating a cable model has been to compare the simulation results with frequency domain calculations transformed to the time domain by use of Inverse Fast Fourier Transform (IFFT). This however, does not ensure the accuracy of the entry parameters of the modelling procedure (e.g. geometry), the parameter conversion and the modelling assumptions. Some authors have used measurement results from [1] for transient voltage comparison [2, 3]. Other authors obtain the cable model validation by simulations only [4, 5] or by comparison with field tests for cables with only few or no crossbondings and grounding of the screen only at the cable ends [6, 7].

This project has therefore been formulated due to the lack of knowledge of actual accuracy and reliability of available cable models, when compared to high frequency transient field measurements for long HV cables with several crossbondings and screen groundings.

1.2 Problem formulation

When forming a hybrid transmission system by combining OHL's and underground cables, whose electrical properties differ considerably, the result is a significantly different steady-state and transient behaviour from currently almost pure OHL transmission system. Therefore, in order to extend the current transmission grid to include some long distance and many underground cables, there is a demanding need for analysis of hybrid systems as well as fully cabled systems. This analysis should help in planning, designing and operating a fully undergrounded transmission system, by giving an overview of the systems behaviour and reliability.

In order to understand the models used for such system studies, this thesis provides an into depth analysis of the physical layout of relevant cable structures as well as a description of mathematical representation of the cables and software modelling.

As shown in [8], the cable modelling at power frequency and low frequency switching is quite good for long cables. It is therefore the scope of this thesis to investigate the model at high frequency. Because of modal representation and cable parameter calculations, it is also relevant to validate cable impedances at high frequencies, where the number of modes for decoupled propagation analysis are limited with an almost frequency independent velocity. It will be shown in chapter 7.3.2 of this thesis, how the modes have frequency independent velocity at frequencies of 10 kHz and higher. Therefore, onward in this thesis, the meaning of high frequency is 10 kHz and higher.

In order to fulfil the requirements of describing cable modelling, validating and verifying their accuracy and improving if necessary, the following goals for the project have been set:

- To theoretically analyse and investigate accuracy of existing cable models
- To perform field test measurements for model validation
- To investigate and identify the cause of inaccurate simulation results
- To improve the cable model and obtain acceptable simulation results
- To validate and verify the model accuracy against long cable measurements

The aim is to deliver a reliable model, which can be used as an instrument in planning and problem solving for long distance cables and a transmission system that is mostly or fully underground.

1.3 Thesis outline

The research documented in this thesis is organised into V main parts.

I - Preliminaries

Starting with an introduction to the thesis and giving a description of relevant HV cables by going through their physical and mathematical representation, this part forms the technical literature study on transmission cables, relevant for the thesis.

II - Modelling Transmission Cables

With an understanding of the physical and mathematical theory on transmission cables, this part provides relevant literature study on modelling tranmission cables. It starts by introducing existing models and finishes by explaining how to model in the software used in this thesis, EMTDC/PSCAD.

III - Field measurements

One of the major contributions from the research presented in this thesis is the field measurements used for model validation.

The chapter describes measurements, on installed cable systems, used for model validations. From these measurements parameters sensitivity is observed. Furthermore preliminary ideas for simulation inaccuracy can be found. As a result, measurements on a cable line under installation are performed. A non-crossbonded cable, a minor section, is tested as well as a cable segment with few crossbonding points, a major section, and a whole cable line with several crossbondings and screen groundings, several major sections. The purpose of these measurements is single model validation with parameter and source of inaccuracy identification, crossbonding model validation and long cable model validation respectively.

IV - Cable Model Improvements

Based on the single minor section measurements and results from investigations of the model accuracy, model improvements are suggested and implemented. The cable model improvements are the second major contributions described in this thesis.

Furthermore, the improved model is verified for long cables with crossbonding points, by use of field measurements on several major sections.

V - Conclusions

The thesis is finalised by a conclusion of the main summaries drawn in individual chapters. The contributions and final conclusions are highlighted and future work is identified.

CHAPTER 2

Transmission cables

Cables have been used in power transmission since the late 19^{th} century, and for transmission of high and extra high voltage (HV/EHV) since the beginning of the 20^{th} century [9].

There are three main types of land and sea cables; fluid filled cables (FF), gas filled cables (GF) and extruded cables. Figure 2.1 subcategorises these cables depending on the insulation type.

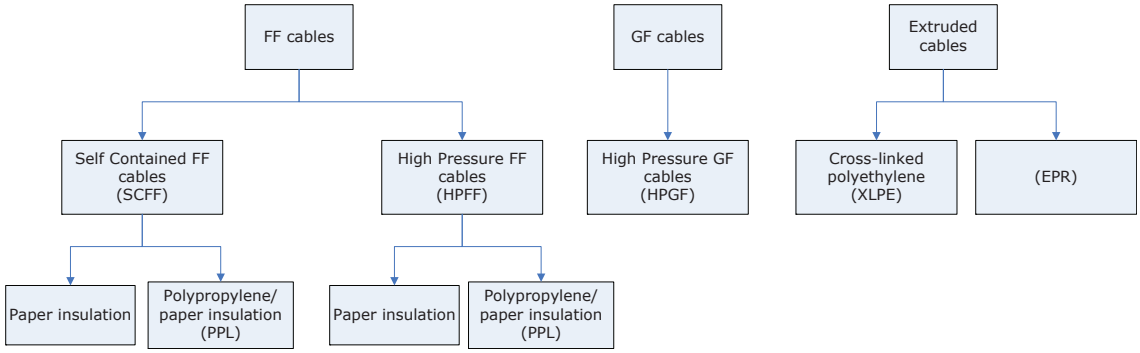

Figure 2.1: *Types of land and sea cables categorised depending on insulation type.*

The use of extruded cables at transmission level began in the 1960's. Since then, XLPE cables on higher voltage levels has become more popular than FF cables and GF cables. This is due to less environmental hazards, as gas or oil leak is no longer an issue, and less costs because of no external accessories such as pumping and pressurizing systems. In the new undergrounded AC transmission system, Denmark exclusively plans to install extruded cables.

A typical HV AC underground power cable is formed by 4 main layers, namely; Conductor-Insulation-Screen-Insulation. In addition to these main layers, the cable also has semiconductive screens, swelling tapes and metal foil. A cross section of a 400 kV 1200 mm^2 XLPE single core cable is shown in figure 2.2.

Core conductor

The purpose of the conductor is to transmit the required current with low losses. The transmission capacity of cable systems with natural cooling is significantly lower than the transmission capacity of OHL of the same nominal voltage, because of thermal resistance in the surrounding earth. It is therefore often necessary to use several parallel cable systems, even though such can increase the risk for resonance circuits, such as near resonance. Different types of conductor design can be seen in figure 2.3. Hollow

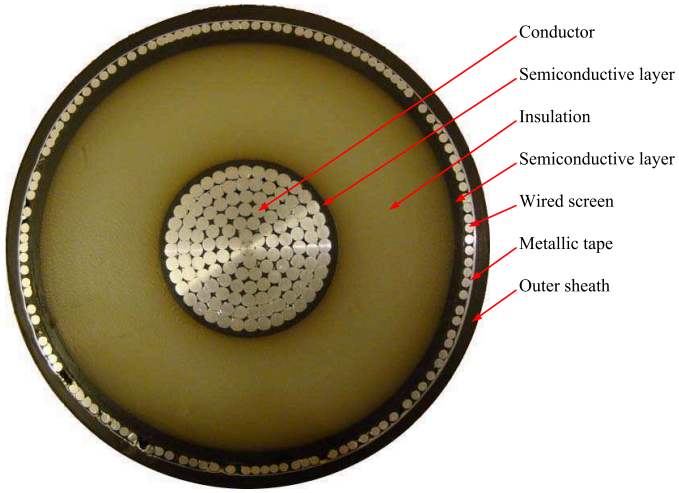

Figure 2.2: *Cross section of a 400 kV cable in northern Denmark.*

conductors are usually used for oil or water to cool down the conductor. Stranded and segmental conductors provide more flexibility and have reduced current displacement because of skin effect.

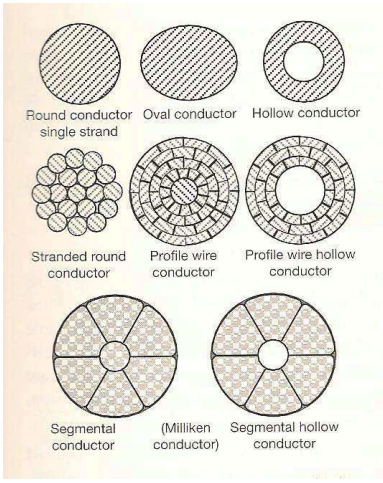

Figure 2.3: *Conductor design for HV cables, [9].*

The conductor in HV and EHV cables is either made of copper (Cu) or aluminium (Al) where Cu has a lower specific resistance which leads to smaller conductor cross sectional area in order to obtain the same current capacity as for Al conductor. The advantage of Al over Cu, is that Al has lower density which leads to much less weight for the same cable capacity. The cable in figure 2.2 has a stranded Al conductor.

Insulation and Semiconductive layers

There are two main types of dielectrics for extruded HV and EHV cables, cross-linked polyethylene (XLPE) and Ethylene-propylene rubber (EPR). The difference in the two is that EPR is less sensitive to insulation impurities than XLPE, while XLPE has less dielectric losses than EPR. The purpose of the insulation is to ensure no electrical connection between the two current carrying components of the cable, the conductor and the metallic screen.

The insulation between the two conducting layers resembles a very long cylindrical capacitor. AC loads will therefore draw a capacitive charging current I_C which is superimposed on the desired current transmitted by the conductor. as shown in equation 2.1, [9].

$$I_C = U_0 \omega C^{'} L \propto U_0 \omega \epsilon_r L \tag{2.1}$$

where U_0 is the phase voltage
ω is the angular frequency $\omega = 2\pi f$
C' is the capacitance of the insulation
ϵ_r is the relative permittivity of the cable
L is the length of the cable.

The semiconductive (SC) layers are placed between the insulation and the conductor and again between insulation and the metallic screen. The purpose of the SC screens is to reduce the electrical stress in the inner insulation and prevent formation of voids between either core conductor or metallic screen and insulation, due to bending of the cable or other mechanical stress.

Cable models do normally not include SC layers. The models have available several conductive layers, such as conductor and screen, and insulation materials in-between, but no SC layers. Instead the SC layers are considered a part of the insulation, where the thickness and the permittivity of the insulation are changed accordingly.

Wired screen and Metallic tape

The purpose of the cable's metallic screen is to have a metallic covering used as an electrostatic screening as well as a return path for the cable's charging current and a conduction path for earth fault current in the case of a fault on the cable.

To avoid screen over-voltages at cable terminals, the metallic screen is grounded [10]. Under normal operation, the metallic screen will carry the charging current, which would result in large steady state losses, due to that the metallic screen grounded in both ends. Grounding the metallic screen only at one terminal will not eliminate possible overvoltages at the ungrounded end. Instead, long cables have crossbonded screen as shown in figure 2.4.

By using such cross bonding method, the induced screen currents can be cancelled and by grounding in between, the screen overvoltages can be reduced. The crossbonding points demarcate part of the cable, called a minor section, and the grounding points demarcate a so called major section.

The cable's metallic screen is formed by wired screen and metallic tape (laminate layer), separated with a thin SC swelling tape. The wired screen and metallic tape are directly connected together both at each

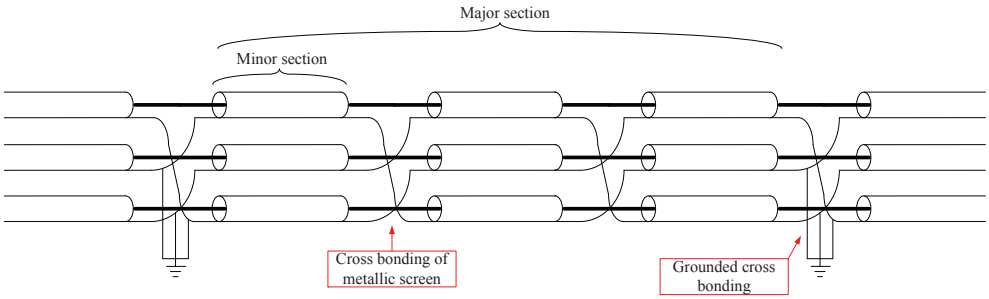

Figure 2.4: *Cross bonding of a metallic screen. A minor section is marked off by two crossbonding points. Every third crossbonding point is grounded and those groundings demarcate a major section.*

junction and cable ends and are therefore normally considered as a single conducting layer in cable modelling.

The laminate layer is included for water resistance. The swelling tape between the wired screen layer and the laminate layer is SC in order to ensure no potential difference between the two conducting screen layers in the occurrence of a failure on the cable. The two conducting layers are not touching each other in order to protect the laminate from mechanical stress because of bending and for thermal protection as the laminate can not tolerate more than 180°C while the wired screen layer can be up to 250°C. It is a common practise when modelling the screen in EMT-based software, to model it as a single solid hollow conductor with the resistivity equal to the wired screen resistivity doubled [11].

In the literature, these layers are either named screen or sheath. In this thesis, the wired part will henceforward be named wired screen, or simply screen, while the laminate part will be named sheath or simply laminate foil. A combination of the two will be named screen.

Outer sheath

The purpose of the cable's outer coverings is mechanical protection against the surroundings. The outer insulation is normally made of high density polyethylene with a relative permittivity of 2.5.

When considering the electrical properties and simulating HV cables, it is necessary to consider each of these layers and include them in the modelling process.

2.1 Electrical properties of High Voltage cables

For a long HV/EHV transmission cable, the electrical properties of the cable can not be correctly explained by using simple lumped parameters. The cable should instead be explained as a series connection of many line elements of a differential length dx as is shown in figure 2.5, or by using wave characteristics.

By applying Kirchhoff's voltage law on the equivalent circuit in figure 2.5 the voltage $v(x,t)$ can be found and by using Kirchhoff's current law the current $i(x,t)$ can be found, as shown in equation 2.2.

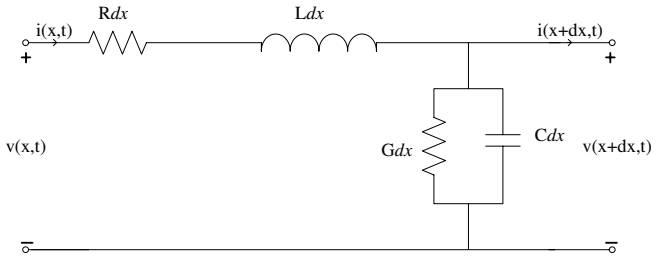

Figure 2.5: *Equivalent circuit of a differential length dx cable elements for one cable, without mutual coupling to other cables.*

$$\begin{aligned} v(x,t) \quad &- \quad Rdx \cdot i(x,t) - Ldx\frac{di(x,t)}{dt} - v(x+dx,t) = 0 \\ &\Rightarrow \quad -\frac{v(x+dx,t) - v(x,t)}{dx} = Ri(x,t) + L\frac{di(x,t)}{dt} \end{aligned}$$

and (2.2)

$$\begin{aligned} i(x,t) \quad &- \quad Gdx \cdot v(x+dx,t) - Cdx\frac{dv(x+dx,t)}{dt} - i(x+dx,t) = 0 \\ &\Rightarrow \quad -\frac{i(x+dx,t) - i(x,t)}{dx} = Gv(x+dx,t) + C\frac{dv(x+dx,t)}{dt} \end{aligned}$$

If the differential length dx is considered infinitely small, $-\frac{v(x+dx,t)-v(x,t)}{dx} = \frac{\delta v(x,t)}{\delta x}$ equation 2.2 can be simplified to the time-harmonic transmission-line equation 2.3.

$$\frac{\delta V(x,\omega)}{\delta x} = (R + j\omega L) \cdot I(x) = [Z(\omega)] \cdot I(x) \tag{2.3a}$$

$$\frac{\delta I(x,\omega)}{\delta x} = (G + j\omega C) \cdot V(x) = [Y(\omega)] \cdot V(x) \tag{2.3b}$$

This gives the cable parameters, which is then used to explain the electrical behaviour of the cable by using wave characteristics.

The wave characteristic method is based on equations 2.3 where series connection of many line elements of length dx represent the transmission cable. This method is used to solve for $V(x,\omega)$ and $I(x,\omega)$ by combining the current and voltage derivatives in equations 2.3 and introducing the propagation constant γ.

$$\frac{\delta^2}{\delta x}V(x,\omega) = \gamma^2 V(x,\omega) \tag{2.4a}$$

$$\frac{\delta^2}{\delta x}I(x,\omega) = \gamma^2 I(x,\omega) \tag{2.4b}$$

where the complex propagation constant is defined as:

$$\gamma = \sqrt{(R + j\omega L)(G + j\omega C)} = \alpha + j\beta \tag{2.5}$$

where α is the attenuation constant
and β is the phase constant.

The solution for the voltage and current by using the wave characteristic is obtained by solving the differential equations and is given by equations 2.6.

$$V(x,\omega) = V_0^+ e^{-\gamma x} + V_0^- e^{\gamma x} \tag{2.6a}$$
$$I(x,\omega) = I_0^+ e^{-\gamma x} + I_0^- e^{\gamma x} \tag{2.6b}$$

Where V_0^+/I_0^+ and V_0^-/I_0^- are constants of the solution to the differential equation. By solving for equation 2.6, as shown in appendix A, the electrical properties of the cable can be described by the cable's terminal conditions, equation 2.7.

$$I_{\text{send}} = Y_c \cdot V_{\text{send}} - H \cdot (Y_c \cdot V_{\text{rec}} - I_{\text{rec}}) \tag{2.7a}$$
$$I_{\text{rec}} = Y_c \cdot V_{\text{rec}} - H \cdot (Y_c \cdot V_{\text{send}} - I_{\text{send}}) \tag{2.7b}$$

where all parameters are a function of ω
$I_{\text{send}}/V_{\text{send}}$ is the sending end current/voltage
$I_{\text{rec}}/V_{\text{rec}}$ is the receiving end current/voltage
$Y_c(\omega) = \frac{Y(\omega)}{\sqrt{Y(\omega)\cdot Z(\omega)}}$ is the cable's characteristic admittance
$H(\omega) = e^{-\gamma l} = e^{-\sqrt{Y(\omega)Z(\omega)}l}$ is the cable's propagation matrix

By means of wave characteristics, it is now possible to calculate the terminal conditions of the cable from the cable parameters Y_C and H. Calculation of the cable parameters is shown in appendix B.

From appendix B.2 and B.3, the full impedance and admittance matrices for calculations of equation 2.7 have been derived. These matrices are shown in equations 2.8-2.9.

$$Z(\omega) = \begin{bmatrix} z_{11}^1 & -z_{12}^1 & z_{gm_{12}} & z_{gm_{12}} & z_{gm_{13}} & z_{gm_{13}} \\ -z_{12}^1 & z_{22}^1 & z_{gm_{12}} & z_{gm_{12}} & z_{gm_{13}} & z_{gm_{13}} \\ z_{gm_{12}} & z_{gm_{12}} & z_{11}^2 & -z_{12}^2 & z_{gm_{23}} & z_{gm_{23}} \\ z_{gm_{12}} & z_{gm_{12}} & -z_{12}^2 & z_{22}^2 & z_{gm_{23}} & z_{gm_{23}} \\ z_{gm_{13}} & z_{gm_{13}} & z_{gm_{23}} & z_{gm_{23}} & z_{11}^3 & -z_{12}^3 \\ z_{gm_{13}} & z_{gm_{13}} & z_{gm_{23}} & z_{gm_{23}} & -z_{12}^3 & z_{22}^3 \end{bmatrix} \tag{2.8}$$

where z_{11}^i is the impedance in the loop core-ground
z_{12}^i is the mutual impedance between the loops core-ground and screen-ground
z_{22}^i is the impedance in the current loop screen-ground
$z_{gm_{ij}}$ is the ground mutual impedance between cables i and j.

$$Y_{shunt} = \begin{bmatrix} y_1^1 & -y_1^1 & 0 & 0 & 0 & 0 \\ -y_1^1 & y_1^1 + y_2^1 & 0 & 0 & 0 & 0 \\ 0 & 0 & y_1^2 & -y_1^2 & 0 & 0 \\ 0 & 0 & -y_1^1 & y_1^2 + y_2^2 & 0 & 0 \\ 0 & 0 & 0 & 0 & y_1^3 & -y_1^3 \\ 0 & 0 & 0 & 0 & -y_1^1 & y_1^1 + y_2^1 \end{bmatrix} \tag{2.9}$$

where y_1^i and y_2^i for each cable i is given in equation B.25.

2.2 Wave propagation

Wave propagation characteristic analysis refers to studying voltage and current waves in a cable system, by looking at the wave's velocity and attenuation. By such an analysis, it is possible to evaluate the form of the cable's terminal conditions, both amplitude and time delay of I_{send}, V_{send}, I_{rec} and V_{rec}.

The wave propagation characteristic analysis for transient studies on cable systems is based on the line equations 2.3.

These equations can be rewritten in order to decouple I and V:

$$\frac{\delta^2 V(x,\omega)}{\delta x^2} = [Z(\omega)][Y(\omega)]V(x) \tag{2.10a}$$

$$\frac{\delta^2 I(x,\omega)}{\delta x^2} = [Y(\omega)][Z(\omega)]I(x) \tag{2.10b}$$

Both $[Z(\omega)][Y(\omega)]$ and $[Y(\omega)][Z(\omega)]$ are square matrices. The propagation constant, $[\gamma]$, for the phase equations is given by $\gamma = \sqrt{[Z][Y]} = \alpha + j\beta$. This propagation constant can not be solved directly in order to find the propagation velocity and attenuation. Instead a diagonalization is used, which results in the modal propagation constant $[\Lambda(\omega)]$. As $[\Lambda(\omega)]^2$ is a diagonal matrix, it is possible to solve the modal propagation constant directly. The calculation of modal propagation characteristics is therefore done via eigendecomposition where for each eigenvalue, the propagation attenuation $\alpha_i(\omega)$ and velocity $v_i(\omega)$ is defined by equation 2.11.

$$\begin{aligned} [\Gamma_V(\omega)]^2 &= [T(\omega)][\Lambda(\omega)]^2[T(\omega)]^{-1} \\ \Lambda_{(i,i)}(\omega) &= \alpha_i(\omega) + j\frac{\omega}{v_i(\omega)} = \alpha_i(\omega) + j\beta_i(\omega) \end{aligned} \tag{2.11}$$

This makes the modal domain much more feasible than phase domain, because there is no mutual coupling in the modal domain and analysis of wave propagation is much simpler, [11, 12, 13]

2.3 Modal domain representation

For single core cables, it is practical to introduce coaxial current loops in order to calculate $[Z(\omega)]$ without coupling between all conductors [14]. In this case, the cable parameters are derived in the

form of equations for coaxial loops [15]. The individual impedances of the series impedance matrix are calculated as shown in appendix B.

At lower frequencies, $f < f_s$ where f_s is the characteristic frequency of the cable line, the screen does not give shielding and there is a mutual coupling between cores and screen of different phases. When $f_s < f < f_c$, where f_c is the critical frequency at which the waves fully reflect, there is induced voltage on the screen and there is a mutual coupling between screen of different phases. Only for higher frequencies, $f > f_c$, there is no mutual coupling between conductors (core or screen) and there is a speaking of six mutually decoupled modes of propagation [16].

These six modes of three single core cables are formed by decoupled current loops:

3 coaxial modes: there are three different core-screen loops where for each of the three coaxial modes, the current in core conductor fully returns in the screen of the same cable and no net current flows in the ground. These three different coaxial modes are shown in figure 2.6.

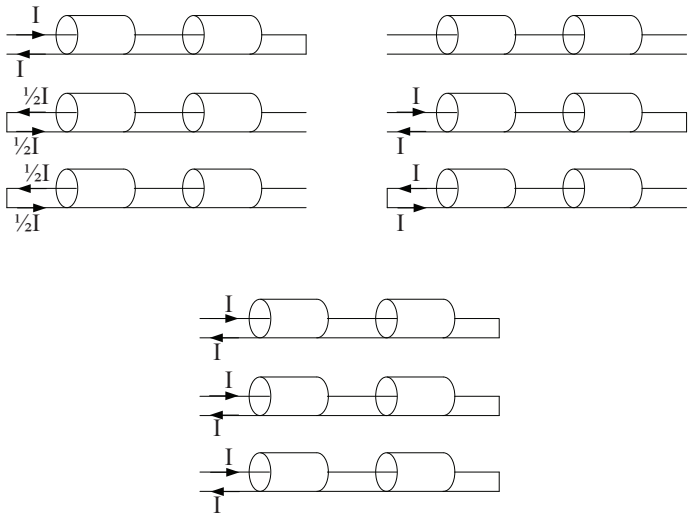

Figure 2.6: *Representation of the three coaxial modes.*

2 intersheath modes: there are two different screen-screen loops where for each of the two intersheath modes, the current in screen conductor fully returns in one or both of the other screens and no net current flows in any of the core conductors. These two different intersheath modes are shown in figure 2.7. In this thesis, even though the name screen is used rather than sheath, it is chosen to keep the name intersheath mode, because of historical reasons and connection to other litterature.

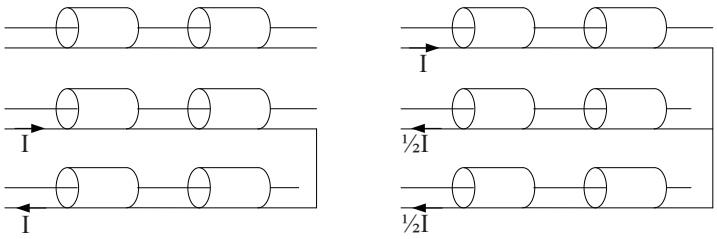

Figure 2.7: *Representation of the two intersheath modes.*

1 ground mode: screen-ground loop, current in the three screens fully returns through the ground and no net current flows in any of the cores, se figure 2.8.

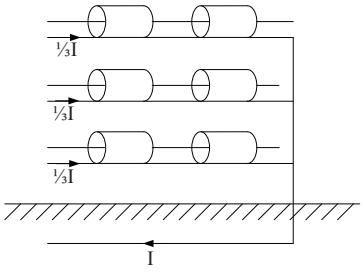

Figure 2.8: *Representation of the ground mode.*

Transformation between modes and phases can be achieved by analysing the above description of the modes.
If the modal voltages are named V_a (ground mode), V_b and V_c (intersheath modes) and V_d, V_e and V_f (coaxial modes) then the transformation based on the above description, is given by equation 2.12.

$$\begin{bmatrix} V_a \\ V_b \\ V_c \\ V_d \\ V_e \\ V_f \end{bmatrix} = \begin{bmatrix} 0 & 0 & 0 & 1/3 & 1/3 & 1/3 \\ 0 & 0 & 0 & 1/2 & 0 & -1/2 \\ 0 & 0 & 0 & -1/3 & 2/3 & -1/3 \\ 0 & 0 & 1 & 0 & 0 & -1 \\ 1 & 0 & 0 & -1 & 0 & 0 \\ 0 & 1 & 0 & 0 & -1 & 0 \end{bmatrix} \cdot \begin{bmatrix} V_{c1} \\ V_{c2} \\ V_{c3} \\ V_{s1} \\ V_{s2} \\ V_{s3} \end{bmatrix} \tag{2.12}$$

where V_{c1}, V_{c2} and V_{c3} are the three core voltages
V_{s1}, V_{s2} and V_{s3} are the three screen voltages.

The transformation matrix for the phase/mode currents can be found similarly; the ground mode I_a is the loop of current in all three screens returning in the ground. I_a will therefore relate to $\frac{1}{3}I_{s1}$, $\frac{1}{3}I_{s2}$ and $\frac{1}{3}I_{s3}$. Similarly, one intersheath mode will relate to I_{s2} and $-I_{s3}$ while the other intersheath mode will relate to I_{s1}, $-\frac{1}{2}I_{s2}$ and $-\frac{1}{2}I_{s3}$. Same can be used on the three coaxial modes and the transformation matrix will be as shown in equation 2.13.

$$\begin{bmatrix} I_{c1} \\ I_{c2} \\ I_{c3} \\ I_{s1} \\ I_{s2} \\ I_{s3} \end{bmatrix} = \begin{bmatrix} 0 & 0 & 0 & 1 & 0 & 1 \\ 0 & 0 & 0 & -1/2 & 1 & 1 \\ 0 & 0 & 0 & -1/2 & -1 & 1 \\ 1/3 & 0 & 1 & -1 & 0 & -1 \\ 1/3 & 1 & -1/2 & 1/2 & -1 & -1 \\ 1/3 & -1 & -1/2 & 1/2 & 1 & -1 \end{bmatrix} \cdot \begin{bmatrix} I_a \\ I_b \\ I_c \\ I_d \\ I_e \\ I_f \end{bmatrix} \tag{2.13}$$

where I_{c1}, I_{c2} and I_{c3} are the three core currents
I_{s1}, I_{s2} and I_{s3} are the three screen currents.

As shown in appendix B.2 the full phase domain impedance matrix from equation 2.8 can be simplified because of the no mutual coupling between phases in modal domain. The modal domain impedance matrix is given in equation 2.14.

$$Z(\omega)_{modal} = \begin{bmatrix} z_1^1 & -Z_{Sm}^1 & 0 & 0 & 0 & 0 \\ -Z_{Sm}^1 & z_2^1 & 0 & z_{gm_{12}} & 0 & z_{gm_{13}} \\ 0 & 0 & z_1^2 & -Z_{Sm}^2 & 0 & 0 \\ 0 & z_{gm_{13}} & -S_{Sm}^2 & z_2^2 & 0 & z_{gm_{23}} \\ 0 & 0 & 0 & 0 & z_1^3 & -Z_{Sm}^3 \\ 0 & z_{gm_{13}} & 0 & z_{gm_{23}} & -Z_{Sm}^3 & z_2^3 \end{bmatrix} \quad (2.14)$$

where $z_1^i = Z_{C_{outer}}^i + Z_{C-Sh_{insulation}}^i + Z_{Sh_{inner}}^i$ given in appendix B.1.1-B.1.3
Z_{Sm}^i is the sheath mutual
$z_2^i = z_{Sh_{outer}}^i + z_{Sh-G_{insulation}}^i + z_{ground}^i$ given in appendix B.1.4-B.1.7.
$z_{gm_{ij}}$ is the ground mutual impedance between cables i and j.

CHAPTER 3

Summary for Preliminaries

This first part of the thesis starts by introducing the problem faced and formulating it as well as giving an outline for the format of the report.

For gaining an understanding of the nature of transmission cables before starting to simulate them, a physical and mathematical description of the cables, their parameters and terminal conditions is given. For propagation analysis the modal domain and transformation is discussed. This is done because modal analysis will be used later in the thesis for analysing comparison of field measurements and simulation results. With the theory of cables and cable calculations defined, it is possible to move on to modelling the nature of transmission cables.

Part II

Modelling Transmission Cables

Modelling transmission cables has been an ongoing task for several years. As the electrical properties of underground cables differ considerably from those of OHL, the modelling and studies of cables are considered very challenging. Not too much is known about long or many underground cables in a transmission system, as until today transmission systems have mainly been constructed of OHL's. Nevertheless, the modelling of cables has been an issue for several decades. This part provides the reader with relevant state of the art for modelling underground cables and introduces how transmission cables are normally modelled in the software used in the thesis, the emt-based software EMTDC/PSCAD.

CHAPTER 4

Existing models

Cable models can be mainly divided into two categories: Models based on lumped parameters and models that use distributed parameters and are normally called travelling wave models.

In the literature, there are various cable model descriptions to be found and in order to develop a precise cable model, to be used in large high voltage transmission cable system studies, it is necessary to perform state of the art study on existing cable models.

4.1 π-section model

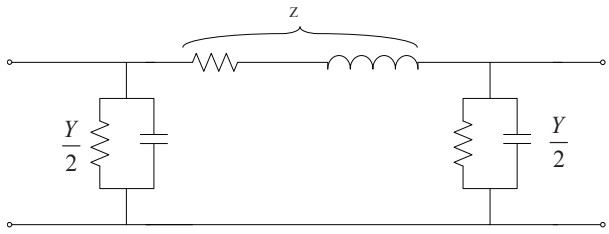

Figure 4.1: *Representation of a π section cable model.*

4.1.1 Nominal π

Cable models, using multiple nominal π-sections, are often used for short distances, or where the travel time does not exceed the solution time step for the simulation [17]. The model is based on lumped R, C and L parameters for the transmission line/cable where coupling to ground is considered. The lumped parameters are simply multiplied by the cable length, thus not taking distribution of the parameters into account. If one three phase cable is used instead of three single core cables, the mutual coupling between phases is also considered in the model.

As this cable model contains lumped parameters for both the inductance and capacitance of the cable, there is a possibility for resonance at high frequencies that only exist in the model and do not represent real life resonances. The main goal of this PhD project is to give a cable model that gives a correct and accurate solution for cables of large distances, therefore this type of cable modelling will not be useful, and the simple π-section cable modelling will not be considered further.

4.1.2 Exact π

The exact π-section model is often used for frequency scan mathematical validation of other cable models. The exact π model is the most accurate model known, as long as it is in the frequency domain, used for only a single exactly known frequency and when numerical calculations of the impedances are used.

Normally one aims for time domain solutions, and therefore this model is only preferred for frequency scan validation of the other models and not for system analysis studies.

In order to include the distributed nature of the parameters, Z and Y for the entire cable length are calculated by equation 4.1 [18], where l is the cable length and Z' and Y' are calculated as shown in appendix B.

$$\begin{aligned} Z &= Z'l\left(\frac{sinh(Z'Y')^{1/2}l}{(Z'Y')^{1/2}l}\right) \\ \frac{Y}{2} &= \frac{Y'l}{2}\left(\frac{tanh(Z'Y')^{1/2}l}{\frac{(Z'Y')^{1/2}l}{2}}\right) \end{aligned} \tag{4.1}$$

For long cables, one must be careful that the nature of crossbonding points and screen groundings is not included in the model.

4.2 Bergeron's model

Bergerons's model is a Norton equivalent model based on travelling wave theory [17]. This model is often used when modelling longer power transmission networks and represents the cables inductance and capacitance by its Norton equivalent with lumped resistance representing the cables distributed series resistance, where the Norton equivalent is lossless and the resistance represents losses in the transmission line.

The model is usually set up so that the lumped resistance is represented by dividing the line length into only two sections, where each end has $\frac{1}{4}$-part of the resistance and the center contains $\frac{1}{2}$-part, [19]. This is shown in figure 4.2.

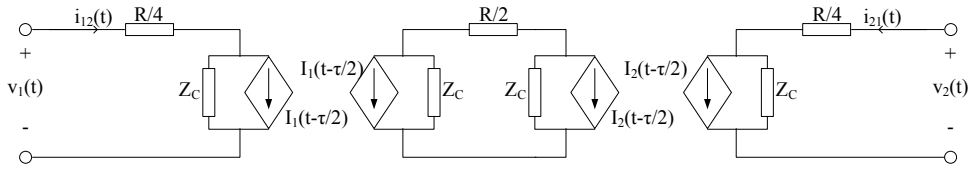

Figure 4.2: *Bergeron model for a transmission cable, [17].*

For the model in figure 4.2, it is possible to set up equations to calculate the current in the cable. When looking at only half a section of the line model, where the middle resistance has been divided into two

$\frac{1}{4}$-parts, the cable flowing currents can be calculated using voltage division as it is shown in equation 4.2 and 4.3, [17].

$$i_{12}(t) = \frac{v_1(t)}{Z_C + R/4} + I_1(t - \tau/2) \tag{4.2}$$

$$I_1(t - \tau/2) = \frac{-v_2(t - \tau/2)}{Z_C + R/4} - \left(\frac{Z_C - R/4}{Z_C + R/4}\right) I_2(t - \tau/2) \tag{4.3}$$

where $\tau/2$ is the half the travel time of the line. The half is used, as only half a section of the line model is used.

When examining such a cable model, only the terminals of the models are of interest. Therefore the two half-time sections are cascaded and the midpoint variables are eliminated. This gives the cable model currents shown in equations 4.4 and 4.5, [20].

$$I_1(t - \tau) = \frac{v_2(t - \tau)}{Z_C + R/4} + \left(\frac{Z_C - R/4}{Z_C + R/4}\right) I_2(t - \tau) \tag{4.4}$$

$$I_2(t - \tau) = \frac{v_1(t - \tau)}{Z_C + R/4} + \left(\frac{Z_C - R/4}{Z_C + R/4}\right) I_1(t - \tau) \tag{4.5}$$

where definition of current direction defines the signs in the equation.

This type of cable modelling is recommended for use, when only one specific frequency is under consideration [21]. This is because the model represents the fundamental frequency only, and not other higher harmonics, due to the surge impedance and the travel time of the wave is given as a steady state value. It is therefore not suited for fast front transient studies.

4.3 Frequency dependent models

The frequency dependent model is a model with all parameters distributed (RLC), based on travelling wave theory and without any lumped parameters. These models are frequency dependent in all parameters, [22].

From all available cable models, there has been much more publication in the area of frequency dependent cable modelling than any other available cable modelling techniques. This is due to the importance of accuracy in underground cable system simulations and the fact that frequency dependent models give much more realistic overview over current and voltage behaviour than models using lumped parameters.

In his article, L. Martí divides cable models into time domain models and frequency domain models, [3], where previously described π-section and Bergeron models are classified as time domain models.

The advantage of using frequency domain lies in accuracy, as parameters depend on the frequency as was shown with the line equations in chapter 2.1.

In order to review the solution in the time domain, the frequency dependent modification of the model must be transformed from the frequency domain to the time domain, using transformations such as Fourier or z-transformations, [6, 23].

When using the time domain, it is easier to see the true behaviour of the model during transient simulations, [10]. This is because it becomes easier to follow the progress of current and voltage as time passes. This is also used in the principle of EMTDC/PSCAD, where you can graphically follow the behaviour of the signal. Therefore all frequency dependent models, using EMTDC/PSCAD must give results in the time domain, even though the models use frequency domain for calculations.

In order to get an idea of the function of frequency dependent models it is useful to follow their major development through the years. Some of the development history has been introduced in [4] and [10].

- Already in 1970 Budner presented one of the first frequency dependent cable models for transient simulations in time domain, [24]. This model has also been called the exact π-model and uses weighting functions in the admittance line model. This is an analytically possible method which can give good results, but when the line becomes very long, the order of the π-model can become very high which makes this model very time consuming. This model is therefore not a good candidate for large underground cable systems.
- In 1972 Snelson tried to improve Budner's exact π-model by using Bergeron's method of travelling wave theory for ideal lines, [25]. Snelson used the travelling functions to calculate the currents and voltages of the cable. Then he transposed this to the frequency domain and compared to the line equations in frequency domain.
- Snelson's frequency dependent model method was further improved by Meyer and Dommel in 1974. Meyer and Dommel used Snelsons model and simplified the representation for the backward travelling function, which caused some calculation difficulties in the frequency domain. They obtained the backward travelling function from the weighted past history of currents and voltages at both ends of the line, instead of only one end as Snelson did, [26]. This formulation is a convolution integral which is evaluated at each time step of the solution. So even though this method gives considerably accurate results, the long time consumed in performing the integral is a big disadvantage. Another disadvantage is low accuracy for low frequencies caused by the weighted function of the past history of currents and voltages, [27]. Therefore Snelsons and the improved Meyer and Dommel models are not considered as good candidates for large underground cable systems.
- It is possible to say that a new chapter was written in cable model history when J. R. Martí introduced his frequency dependent line model in 1982. This model is based on the travelling wave approach with frequency dependent modes and a constant transformation matrix, [27]. The transformation matrix is a constant modal transformation matrix relating phase voltages and currents to modal voltages and currents, where multiphase lines are decoupled so that each mode can be studied separately as a single-phase circuit.
- In 1988 L. Martí, then a PhD student at The University of British Columbia where both Dommel and J. R. Martí worked in close cooperation, represented some improvements on J. R. Martí's frequency dependent modal line model. This new model uses the same principles as J. R. Martí represented in 1982, but includes frequency dependence in the modal transformation matrix as well as in cable parameters, [3].

- Because of difficulties in J. R. and L. Martí's frequency dependent mode model caused by modal transformation matrix, it became of interest to develop a method in time-domain that did not use the modal domain. Such a model was represented in 1996 by Noda, Nagaoka and Ametani. They represented a cable model in the phase domain, and not in the time domain as Budner, Snelson, Meyer and Dommel, J.R Martí and L. Martí had done before them, which did not depend on convolution due to modal transformation matrix. Instead there was used an ARMA model, where ARMA stands for Auto-Regressive Moving Average, which minimizes the computation time, [6]. The problem with this model is, that it uses the z-domain, so whenever there is a need for a change in the time step of particular simulations, the propagation function of the system needs to be refitted.
- After the representation of frequency dependent model in the phase domain there was some development in such cable modelling, and in 1999 an important discovery in this field was represented by Gustavsen and his colleagues. They presented a new frequency dependent model in the phase domain using s-domain instead of z-domain, [4]. This model, universal line model, is still used today in EMTDC/PSCAD for both cable and overhead line modelling, and Manitoba HVDC research centre goes as far as saying: *this type of cable model should always be the model of choice, unless another model is chosen for a specific reason. This model is the most advanced and accurate time domain line model in the world* , [22]. In the software EMTDC/PSCAD, the model named Frequency Dependent Phase Model is based on the universal line model theory.
- Since 1999 development of frequency dependent models has been mainly performed as modifications of the frequency dependent mode and phase models. For instance in 2000 Dufour and Le-Huy presented modifications of the already used J. R. Martí model where they tried to improve the line responses, [28]. The quality of this model did though not exceed the ones already achieved in the frequency dependent phase model. Also in 2001 a new zcable model was represented by T.C. Yu and J.R. Martí. This model splits the representation of the travelling wave model into two parts. Namely the ideal line section with constant parameters (as is done in the Bergeron model) and the loss section with frequency dependent parameters (here the Bergeron model uses lumped resistance), [5]. An EMTP implementation procedure was presented for this method in 2003 [29], though the model has not been adopted in commercial EMTDC/PSCAD algorithms.

From the above history reference of frequency dependent models, the strongest candidate models for this project, are the frequency dependent mode and phase models represented by J. R. Martí and Gustavsen and colleagues respectively. Furthermore the zcable model is of interest as a new candidate in cable modelling technique. When comparing the two frequency dependent models from the above description, previous researchers have stated the phase model to be more favourable for cable models and the mode model for overhead lines. Because of this, the frequency dependent phase model is chosen for further work in this PhD project, and not the frequency dependent mode model.

In order to investigate the accuracy and shortcomings of the most favourable cable models, the theory for the frequency dependent phase model will be further described in the following. Also the more recent idea of the semi frequency dependent zcable model will be presented.

4.3.1 Universal Line Model (Frequency dependent phase model)

The description of this model is based on the literature from Morched, Gustavsen and Tartibi which is presented in [4].

When a transmission line, either an overhead line or an underground cable, is represented it can be characterized by the propagation matrix H and the admittance matrix $Y_C = \frac{1}{Z_C}$ as shown in equation 2.7. As these matrices are frequency dependent, because of frequency dependent parameters of the cable line, only the frequency domain is used to calculate the discrete functions of the matrices and in order to obtain the time-domain values, a convolution of the matrices time-domain equivalents, obtained with inverse Fourier or other similar transformation, is used. In order to reduce computing time and simplify the calculations, it is much more efficient to use frequency domain H and Y_C where no convolution is necessary (convolution in time-domain is equalized with multiplication in the s-domain).

The main principle of the universal line model is to fit all of the cable parameters directly in the phase domain and calculate the terminal conditions presented by equation 4.6, based on equations 2.7.

$$\begin{aligned} v_{send}(\omega) &= v_{rec}(\omega)\cosh(\gamma(\omega)l) - i_{rec}(\omega)Z_C(\omega)\sinh(\gamma(\omega)l) \\ i_{send}(\omega) &= \frac{v_{rec}(\omega)}{Z_C(\omega)}\sinh(\gamma(\omega)l) - i_{rec}(\omega)\cosh(\gamma(\omega)l) \end{aligned} \tag{4.6}$$

where the sign of the current is dependent on the defined direction. Here both sending end and receiving end currents flow from the terminal and into the circuit.

Fitting of cable parameters

When all cable parameters are fitted directly in the phase domain, this means that the matrix elements of the propagation matrix $H(\omega)$ and the admittance matrix $Y_C(\omega)$ are fitted in the phase domain.

In order to fit $H(\omega)$ and $Y_C(\omega)$ in the phase domain, a least squares fitting routine, Vector Fitting (VF), is used [4].

The VF technique estimates all coefficients of a function $f(s)$ so that a least squares approximation of $f(s)$ is obtained over a given frequency interval, [30]. The function approximation used is given in equation 4.7 where a_n represents the poles and c_n the residues for the function.

$$f(s) = \sum_{n=1}^{N} \frac{c_n}{s - a_n} \tag{4.7}$$

where N is the number of poles.

When fitting propagation matrix $H(\omega)$ in the phase domain, each mode i must be related back in time, relative to its time delay τ_i. This is because different permittivity of inner and outer insulators in underground cables lead to different propagation velocities for each mode and $H(\omega) = e^{-(\alpha+j\beta)l}$ where α is the modal attenuation constant and β is the phase constant containing the modal velocity. This results in different travelling times and time delays for each mode. Therefore each mode i is fitted as shown in equation 4.8.

$$e^{s\tau_i} H_m^i(s) = \sum_{m=1}^{N} \frac{c_m}{s - a_m} \tag{4.8}$$

By using equation 4.8, each element of the propagation matrix is calculated by 4.9.

$$h(s) = \sum_{i=1}^{N_g} \left[\sum_{m=1}^{N} \frac{c_{mi}}{s - a_{mi}} \right] e^{-s\tau_i} \tag{4.9}$$

where N_g is the number of modes
N is the number of poles for each mode
τ_i is the precalculated time constant for mode i.

When $H(\omega)$ has been estimated using VF, only the admittance matrix $Y_C(\omega)$ needs to be fitted so that the terminal conditions can be obtained from equation 4.6.

The admittance matrix has no time delays like the different modal components in the propagation matrix have. Therefore the proper poles can be found by fitting the sum of all modes. This can though be simplified even further, because the sum of all modes of a square matrix is the same as the sum of all eigenvalues for that matrix, [31]. Therefore the poles for $Y_C(\omega)$ can be found by using VF to fit the sum of all the diagonal elements of $Y_C(\omega)$.

With both $H(\omega)$ and $Y_C(\omega)$ known, $v_{send}(\omega)$ and $i_{send}(\omega)$ can be calculated. Then the purpose of the frequency dependent phase model has been accomplished, where the terminal conditions of the cable have been calculated using cable parameters in the phase domain. After all this is done, the solution is transformed to time domain for user purposes.

4.3.2 zCable model

As described before, the zcable model splits up the cable model into two parts; the ideal line section with constant parameters and the loss section with frequency dependent parameters. Both the frequency dependent phase model and the zcable model try to calculate the cable terminal voltage and current, without transforming frequency dependent parameters between mode and phase-domain. The frequency dependent phase model fits all parameters of the cable directly in the phase domain, using VF-technique, while the zcable model fits the frequency independent ideal line section in the modal domain and the loss section directly in the phase domain. The zcable method can be considerably faster, as not all of the cable parameters need to be fitted in the frequency domain.

The principle of the zcable model was proposed for overhead lines by [32, 33]. This principle was then improved for adoption as a cable model, [5, 29]. In this chapter, the description of the zcable model is based on [5] and [29].

The wave propagation equations in the frequency domain have been described by equations 2.4 and 2.5. Instead of using the propagation constant γ, the equations can be expressed as:

$$
\begin{aligned}
-\frac{d^2V(x)}{dx^2} &= [ZY] \cdot V(x) \\
-\frac{d^2I(x)}{dx^2} &= [YZ] \cdot I(x)
\end{aligned} \tag{4.10}
$$

where $[ZY]$ and $[YZ]$ are full matrices that couple the wave propagation of voltage and current in every phase, [5].

In order to split the model of the cable into an ideal section and a loss section, the inductance in the impedance matrix is split up into an internal inductance, L^{int}, and an external inductance, L^{ext}, as is shown in equation 4.11.

$$
Z_{ij}(\omega) = R_{ij}(\omega) + j\omega(L_{ij}^{int}(\omega) + L_{ij}^{ext}) \tag{4.11}
$$

where Z_{ij} are the elements of the $[Z]$-matrix
$R_{ij}(\omega)$ is the resistance of the conductor and the ground return
$L_{ij}^{int}(\omega)$ is the internal inductance of the flux inside the conductor and ground return
L_{ij}^{ext} is the external inductance of the flux outside the conductor, which is not frequency dependent.

By splitting the inductance up like this, it is possible to split the whole impedance matrix for the cable in two parts:

$$
\begin{aligned}
[Z(\omega)] &= ([R(\omega)] + j\omega[L^{int}(\omega)]) + j\omega[L^{ext}] \\
&= [Z_{loss}(\omega)] + j\omega[L^{ext}]
\end{aligned} \tag{4.12}
$$

The shunt admittance is expressed as before, $[Y] = [G] + j\omega[C]$, where $[C]$ is the shunt capacitance matrix and $[G]$ is the shunt conductance matrix, which represents the dielectric losses. In the presented zcable model method of [5, 29] the dielectric losses, represented by the shunt conductance matrix, are assumed to be constant as well as the shunt capacitance matrix, which's elements depend on the permittivity of the insulation and the diameter of the conductor and insulation.

In order to distribute the nature of the losses in longer cables, the total length of the cable is subdivided into many shorter segments which are then split up into an ideal section and a loss section, as described above. The losses of the cables are given as the losses of the conductor and other metallic layers associated with skin effect, as well as the dielectric losses. Therefore the loss section of the cable model is split even further into these two loss subsections. A graphical representation of the cable parameters in the zcable model is shown in figure 4.3.

Ideal line section

As shown in figure 4.3, the ideal line section consists of the external inductance and the shunt capacitance. The elements of $[C]$ are dependent on the permittivity of the insulator, but as the permittivity of inner and outer insulation layers of a cable are different, because different materials are used, the travelling times and time delays for each mode of the ideal line section are different from each other. The modal domain is therefore chosen to solve for the ideal line section.

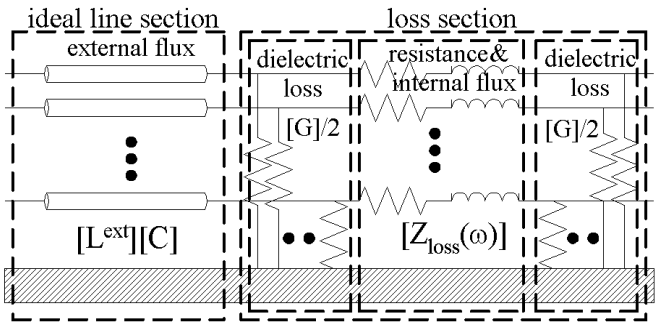

Figure 4.3: *A graphical representation of the cable parameters in the zcable model showing the separation of the cable sections, [5].*

The modal domain end voltages of each ideal line section are dependent of the characteristic admittance given in equation 2.7, the currents into the terminals and the history voltage depending on the travelling wave, as is shown in figure 4.4 where 1 is the sending end and 2 is the receiving end, as before.

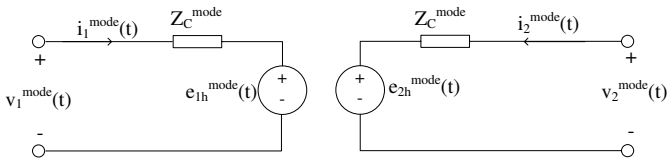

Figure 4.4: *Ideal line section model in modal domain.*

The history voltages are updated at each time step as shown in equation 4.13.

$$\begin{aligned} e_{1h}^{mode}(t) &= Z_C^{mode} i_2^{mode}(t-\tau) + v_2^{mode}(t-\tau) \\ e_{2h}^{mode}(t) &= Z_C^{mode} i_1^{mode}(t-\tau) + v_1^{mode}(t-\tau) \end{aligned} \tag{4.13}$$

where τ is the travelling time of the wave. The time step has to be much smaller than the travelling time.

This is then used to calculate the terminal conditions of the ideal section, at each time step.

Loss section

The loss section consists of the dielectric loss subsection and the resistance and internal flux loss subsection. As stated before, the dielectric loss subsection in considered as constant, whereas the resistance and internal flux loss subsection is frequency dependent.

The impedance matrix of the frequency dependent loss section of the cable model, is therefore fitted in the frequency domain. The elements of $[Z_{loss}(\omega)]$ are approximated using the same set of stable poles for all elements, in order to ensure the stability of the $[Z_{loss}(\omega)]$-matrix in the zcable model, [5]. Therefore each element, ij, of the matrix must be fitted in coordination with each other, where each element is expressed as a sum of the same number of parallel RL blocks.

$$
\begin{aligned}
Z_{fii}^{loss}(\omega) &= R_{iiDC} + \sum_{l=1}^{m} \frac{sK_{ii(l)}}{s + p_{ii(l)}} \\
Z_{fij}^{loss}(\omega) &= \sum_{l=1}^{m} \frac{sK_{ij(l)}}{s + p_{ij(l)}}
\end{aligned}
\tag{4.14}
$$

where f stands for fitted.
ii are the diagonal elements and ij are the off-diagonal elements.
The function $\frac{sK}{s+p}$ is the basic fitting block that corresponds to a parallel RL-block.
m is the number of parallel RL-blocks.
R_{iiDC} is the DC resistance of the cable.

By using this, each constant K and pole p is calculated for each element of the matrix $Z^{loss}(\omega)$ to exactly match the line data at a particular frequency and the impedance function for the loss section is fitted, where possible optimization procedures can also be necessary in order to ensure correct fitting.

In order to better represent the distributed nature of the losses, the loss section is divided into two halves, one at each end of the ideal line section.

When the loss section has been fitted correctly and the ideal line terminal conditions have been calculated, the whole model is put together in the frequency domain. This means that the ideal line parameters need to be transformed from the modal domain to the frequency domain, which is not a problem as the ideal line parameters are frequency independent. Now the cable has been modelled using the zcable model, where cable terminal conditions are calculated using equation 4.10 with the zcable model of $[ZY]$ and $[YZ]$.

4.3.3 Choise of cable model

From existing modelling methods, two are evaluated to be most adequate for high frequency transient studies for validating cable parameters and modelling procedures against field measurements. Those methods are the universal line model (frequency dependent phase model) and the zcable model. The aim in this PhD project is to validate and deliver a accurate cable model to be used by a utility when designing and problem solving for mostly or fully undergrounded transmission systems. As the zcable model, as of today, is not available in commercial simulations software, it is decided to focus on the universal line model which is available in EMTDC/PSCAD (Frequency Dependent Phase Model). Furthermore, it has been shown by recent studies how this model in EMTDC/PSCAD is extremely accurate at power frequency and for low frequency transients [8].

CHAPTER 5

Simulations using EMTDC/PSCAD

The aim of this project is to validate and improve if necessary a known frequency dependent model. As explained in chapter 4 the frequency dependent phase model [4] in EMTDC/PSCAD is used, tested and improved.

This chapter describes how to use the model and what to be aware of when implementing the cables electrical parameters.

5.1 Simulation setup

A layout of what the cable model looks like in EMTDC/PSCAD is shown in figure 5.1.

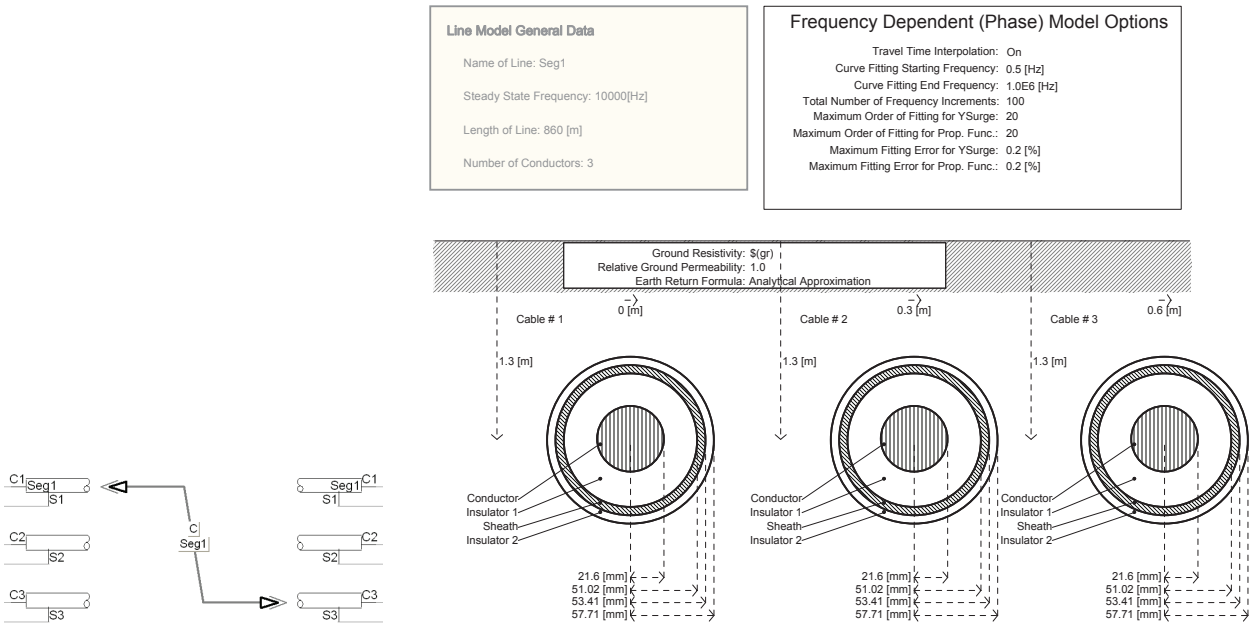

(a) The cable model.

(b) The model segment cross section.

Figure 5.1: *The simulation setup in EMTDC/PSCAD for cable modelling.*

When modelling a cable, there is more to be modelled than only the cable parameters. For instance the resistivity of the ground return path must be modelled. As the resistivity of the ground depends on the type of soil and the temperature, this resistivity must be roughly evaluated. Soil resistivity of a very moist soil is 30 Ωm, for clay soil it is 100 Ωm and for a sandy clay soil it is 150 Ωm, [34]. In Denmark the soil has a large contain of sand and clay. Therefore for the simulations to best present the soil it is normal to

use either a resistivity of 100 or 150 Ωm.

When using the frequency dependent phase model (FDPM), some important boundaries and parameters for the calculations must be selected, see figure 5.2.

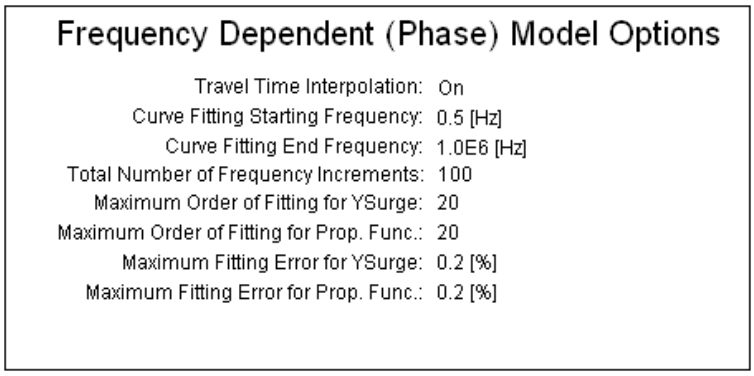

Figure 5.2: *Options when using the frequency dependent phase model in EMTDC/PSCAD.*

Travel time Interpolation

The model uses travelling wave theory to calculate the terminal conditions of the cable. Therefore, the travelling time must be larger than the time step. When using this travelling wave theory in the FDPM the calculated travelling time will not be an exact integer multiple of the time step. Therefore it is possible to interpolate the travel time for short cables or cable segments. This means that there will be a more correct calculation of the travelling time from the length of the cable, as the cable end can be reached in between time steps.

Curve fitting starting and end frequency

The model uses curve fitting with an Nth order approximation to approximate the impedance and admittance of the cable. These calculations are performed over a frequency range. The selection of this frequency range will affect the calculated characteristic impedance of the cable, $Z = \sqrt{\frac{R+j\omega L}{G+j\omega C}}$.

The selection of the curve fitting starting frequency will affect the shunt conductance (G) of the line because this limits the DC surge impedance. This is because the solution at the minimum frequency is used for all frequencies from DC to the minimum. At low frequencies or DC, the surge impedance is $Z = \sqrt{\frac{R}{G}}$. This means that at frequencies below the starting frequency, the shunt conductance has an effective value. If the lower limit of the frequency range is too high, this could result in a very large shunt conductance and shunt losses. Care must be taken not to choose a too small starting frequency as that can affect the accuracy of the curve fitting. This is because the specified maximum error is a percentage of the maximum, and the maximum surge impedance is larger for lower minimum frequency. PSCAD recommends a good starting frequency at approximately 0.5 Hz.

The curve fitting end frequency does not have as much effect on the calculations as the starting frequency. PSCAD states that this end frequency can usually be left at 1 MHz. This is because the time step used

in the simulation uses the Nyquist criteria and places an upper limit on the frequencies. The cable model will therefore truncate any elements of the curve fitted approximations, which are more then 1 decade above the Nyquist Criteria.

Total number of frequency increments

It is possible to select between 100, 200, 500 or 1000. This is the total number of calculation steps used in the frequency range for the curve fitting. An increased number of steps will result in a longer simulation time.

Maximum order of fitting for Y_{surge} and the propagation function

The frequency dependent phase model calculates the terminal conditions of the cable by use of the propagation function and the surge admittance, see equation 5.1.

$$\begin{aligned} Y_{surge} &= \frac{\gamma}{R + j\omega L} \\ H &= exp(-\gamma \cdot l) \end{aligned} \tag{5.1}$$

where $\gamma = \sqrt{(R + j\omega L)(G + j\omega C)}$
Y_{surge} is the characteristic admittance, Y_C
H is the propagation function

In order to find the surge admittance and the propagation function, the FDPM uses curve fitting.

Usually the cable constants program will iterate and continuously increase the order of curve fitted waveforms until the error is below a specified error for the fitting. On the other hand, for some real-time applications there is not enough time to continuously increase the curve fitted waveforms until an acceptable accuracy is reached. Therefore it is possible to set the maximum order of fitting for both the surge admittance and the propagation function.

Maximum fitting error for Y_{surge} and the propagation function

Choosing a large number here will result in a poorly fitted surge admittance and propagation function. This will then lead to an inaccurate calculation of the terminal conditions for the cable model. On the other hand choosing a very small fitting error can lead to unstable simulations. It is recommended by PSCAD to use 0.2% for these values. This can be approximated by using the smallest value that does not lead to unstable simulation.

The curve fitting algorithm is based on a weighted least squares fitting. It is possible to specify different weighting factors for

- the frequency range from DC to the curve fitting starting frequency
- the given frequency at the curve fitting starting frequency
- from the lower limit to the curve fitting end frequency

Specifying a higher weighting factor results in the curve fitting at that frequency being more important. This will lead to placing poles and zeros so that the error at the given frequency is reduced.
When the model boundaries and parameters have been implemented, the cable parameters need to be set for impedance calculations.

5.2 Parameters for cable constant calculations

The outcome of the simulations can only be as accurate as the input parameters to the program, therefore care must be taken when implementing a model for the cable. In this chapter, an overview over how model parameters should be chosen is given, as well as an overview over the model layout.

Conductor

In most modelling software, it is only possible to model the conductor either as a solid conductor or as a hollow conductor. For stranded or segmental conductors the cross section is not solid and this is compensated by increasing the resistivity of the conductor. If the measured DC resistance per km and the actual radius of the cable is known, then it is possible to correct the resistivity of the core by equation 5.2. $\rho^{'}$ is the corrected resistivity, R_{DC} is the given DC resistance per km of the conductor, r_1 is the core conductor radius and l is the length.

$$\rho^{'} = R_{DC}\frac{r_1^2\pi}{l} \tag{5.2}$$

When the DC resistance is not exactly known, it is possible to correct the core resistivity from the cross sectional area and the given radius of the conductor. As shown in equation 5.2, the resistivity is given by the resistance of a uniform specimen of the material, the nominal cross sectional area and the length of the material.

$$\rho = R_{DC}\frac{A}{l} \tag{5.3}$$

The new increased resistivity can be expressed as $\rho\,' = R_{DC}\frac{r^2\pi}{l}$, where the resistance of a uniform specimen of the conductor is unchanged as well as the conductor length. Equation 5.4 can therefore be used to calculate the increased resistivity for modelling the stranded conductor of the cable.

$$\begin{aligned} R_{DC} &= \rho\cdot\frac{l}{A} = \rho\,'\cdot\frac{l}{r^2\pi} \\ &\Rightarrow \rho\,' = \rho\frac{l}{A}\cdot\frac{r^2\pi}{l} \\ &\Rightarrow \rho\,' = \rho\cdot\frac{r^2\pi}{A} \end{aligned} \tag{5.4}$$

Insulation and semiconductive layers-permittivity

It is normally not possible to model directly the semiconductive layers. The inner and outer semiconductive layers have permittivity around 1000, [35], compared to insulation permittivity of app. 2.3, and a conductivity much lower than for both the core and screen conductors. Therefore, from the point of conduction, the semiconductive layers can be neglected while from the point of insulation, they can not. The effects of the semiconductive layers are included by expanding the thickness of the insulation and increasing the relative permittivity, by assuming constant capacitance between the conductor and the metallic screen [36]. The capacitance between the conductor and the screen can be calculated using equation 5.5.

$$C = \epsilon \cdot \frac{2\pi l}{ln(b/a)} \tag{5.5}$$

When the corrected permittivity, $\epsilon^{'}$, is calculated, the capacitance and the length of the cable are kept constant.

$$\begin{aligned} C &= \epsilon \cdot \frac{2\pi l}{ln(b/a)} = \epsilon^{'} \cdot \frac{2\pi l}{ln(r_2/r_1)} \\ &\Rightarrow \epsilon^{'} = \epsilon \cdot \frac{2\pi l}{ln(b/a)} \cdot \frac{ln(r_2/r_1)}{2\pi l} \\ &\Rightarrow \epsilon^{'} = \epsilon \cdot \frac{ln(r_2/r_1)}{ln(b/a)} \end{aligned} \tag{5.6}$$

where ϵ is the known relative permittivity for the insulation.
b is the outer radius of the insulation and a is the inner radius of the insulation.
r_2 is the inner radius of the screen and r_1 is the outer radius of the conductor.

Insulation and semiconductive layers-permeability

The permeability is related to the inductance, caused by the magnetic field from both the conductor and the metallic screen. Normally it is only possible to model coaxial conductors (both for the conductor and the screen). In reality, the conductor is often stranded and the metallic screen is made of a thin foil and wires that are helically wounded around the outer SC layer. The associated axial magnetic field will cause a solenoid effect and increase the total inductance, [11]. By use of Ampéres circuital law, $\oint_C \mathbf{B} \cdot \mathbf{dl} = \mu_\mathbf{0}\mathbf{I}$, the inductance of the conductors can be calculated from the stored inductive energy and the stored energy of the magnetic field, $\frac{1}{2}LI^2 = \int_V \frac{\mathbf{B}}{2\mu} dV$. The magnetic field for the coaxial cable is calculated using equation 5.7.

$$\begin{aligned} 0 \leq r \leq r_1 : \quad B(r) &= \frac{\mu_c I r}{2\pi r_1^2} \\ r_1 \leq r \leq r_2 : \quad B(r) &= \frac{\mu_d I}{2\pi r} \end{aligned} \tag{5.7}$$

where r_1 is the radius of the conductor.
r_2 is the radius of the outer semiconductive layer.
μ_c is the permeability of the conductor.
$\mu_d = 4\pi \cdot 10^{-7}$ is the given permeability of the insulation.

This magnetic field is used to calculate the inductance. The inductance is shown in equation 5.8.

$$\begin{aligned} 0 \leq r \leq r_1: \quad L &= \frac{\mu_c}{8\pi} \\ r_1 \leq r \leq r_2: \quad L &= \frac{\mu_d}{2\pi} ln\left(\frac{r_2}{r_1}\right) \end{aligned} \tag{5.8}$$

The flux density B_{sol} caused by the solenoid effect is given by the expression in equation 5.9 together with the associated inductance L.

$$\begin{aligned} B_{sol}(r) &= \mu_d N I \\ L &= \mu_d N^2 \pi (r_2^2 - r_1^2) \end{aligned} \tag{5.9}$$

where N is the number of turns per meter of the cable.

In order to include the solenoid effect in the coaxial modes of propagation, the relative permeability of the main insulation is set larger than unity by the expression in equation 5.10.

$$\begin{aligned} \frac{\mu_c}{8\pi} + \frac{\mu_{d_{sol}}}{2\pi} ln\left(\frac{r_2}{r_1}\right) &= \frac{\mu_c}{8\pi} + \frac{\mu_d}{2\pi} ln\left(\frac{r_2}{r_1}\right) + \mu_d N^2 \pi (r_2^2 - r_1^2) \\ \Rightarrow \quad \mu_{d_{sol}} &= \mu_d + \frac{\mu_d}{ln\left(\frac{r_2}{r_1}\right)} 2\pi^2 N^2 (r_2^2 - r_1^2) \end{aligned} \tag{5.10}$$

where $\mu_{d_{sol}}$ is the corrected insulation permeability.

It should be noted that in EMTDC/PSCAD the relative permeability is used, so the corrected $\mu_{d_{sol}}$ should be divided by $\mu_0 = 4\pi \cdot 10^{-7}$.

Metallic screen

As explained in chapter 2 the screen is constructed of two layers, a wired screen and metallic tape (laminate layer), separated with a thin SC swelling tape. The wired screen and metallic tape are directly connected together both at each junction and cable ends and are therefore normally considered as a single conducting layer in cable modelling. It is a common practise when modelling the screen in EMT-based software, to set the resistivity equal to the wired screen resistivity doubled [11]. This approximation has been implemented, because most of the current will be flowing in the wired screen. As it can be seen in figure 2.2 the wired screen does not fill the whole area around the outer semiconductive layer, i.e. there are some spaces in between some of the wires of the screen. Therefore the resistivity of the screen is increased. This is an assumption and must be considered when comparing simulations and field test results.

Outer insulation

There is no SC layer that needs to be taken into account when modelling the outer insulation, neither any solenoid effect. Therefore, when modelling the outer sheath, the permittivity is chosen as stated by the manufacturer and the permeability is chosen as unity. Normally the outer insulation is made of polyethylene with a permittivity of 2.3.

With an understanding of the frequency dependent phase model in EMTDC/PSCAD and how to set modal boundaries and parameters, the model can be used for simulation studies and validation against field measurements.

CHAPTER 6

Summary for Modelling Cables

Before starting to simulate long cables, validate the accuracy and perform improvements, the existing modelling techniques are analysed and described. The major literature in this field is evaluated.

The Nominal and exact π-section models, the Bergeron's model and various frequency dependent models are discussed. As the research documented in this thesis aims for validating cable models at high frequncies, the frequency dependent models are of more interest than π-models and the Bergeron model. Therefore a short analysis of the history of frequency dependent models is given. From existing frequency dependent modelling methods, two are evaluated to be most adequate for high frequency transient studies for validating cable parameters and modelling procedures against measurements. Those methods are the universal line model (frequency dependent phase model) and the zcable model. The aim in this PhD project is to validate and deliver a accurate cable model to be used by a utility when designing and problem solving for mostly or fully undergrounded transmission systems. As the zcable model, as of today, is not available in commercial simulations software, it is decided to focus on the universal line model which is available in EMTDC/PSCAD. Furthermore, it has been shown by recent studies how this model is extremely accurate at power frequency and for low frequent transients [8]. Hence, this model will be used for simulations and model validations in the following chapters. In chapter 5, the modelling procedure in EMTDC/PSCAD is described and documented. Simulation setups in the remaining parts of the report are based on this description.

Part III

Field Measurements

The electrical properties of a cable's surrounding soil can affect the transmission properties of the cables, as well as cross bonding used in longer cables. Such an affect can be a source of possible errors when simulating a physical cable system. Therefore, in order to analyse how cables behave in their normal surroundings, field tests become important.

The aim for the measurements is to

- investigate accuracy of up to date models
- analyse what exactly causes inaccuracy of cable models
- verify model accuracy after improvements are implemented

In the project, measurements were performed on two different cable systems. First of all measurements were performed on a crossbonded 400 kV 7.6 km long cable system and second of all on a three phase 150 kV 55 km long underground cable line. Measurements on the 150 kV underground cable system were performed during cable installation allowing for measurements both on parts of the cable and the

whole cable line.

Before starting any field tests, the measurement preparation is of great importance. Field measurements on long underground transmission cables can not be repeated after need, as they usually are restricted in time by the utility company. All field measurements are therefore planned with simulations based on the technique descriped in chapter 5, using manufacturer cable data.

Such preparation was performed both in order to plan where and what to measure and more importantly, to have a base for comparison at the measuring site. The comparison base is vital in order to make sure that all connections and instruments are working properly.

CHAPTER 7

Field measurement set #1, 400 kV crossbonded cable

The crossbonded 400 kV cable system is a part of a transmission line, which is a combination of OHL and cables. The cable line is placed between Gistrup and Skudshale in Northern Jutland of Denmark, see figure 7.1.

Figure 7.1: *Geographical placement of the Gistrup-Skudshale 400 kV cable system.*

The purpose of the field measurements on the 400 kV cable system was to analyse the cable model, investigate the accuracy of the model and use wave propagation to identify origin of disagreement between measurements and simulations.

The cable line consists of 2 identical parallel three phase cable systems with 400 kV single core 1200 mm^2 XLPE cables. The cross section of the single core cable is shown in figure 2.2 on page 8. The cables are laid in flat formation with 0.3 m lateral distance between the phases, 6 m between the two systems and 1.3 m below the surface, see figure 7.2.

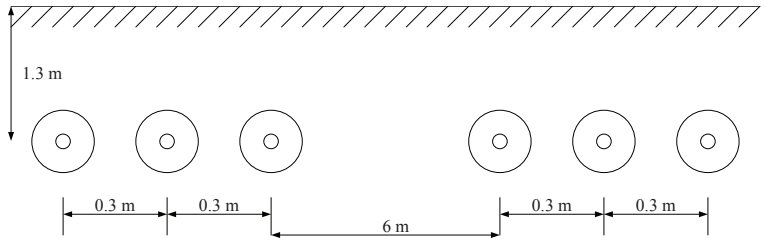

Figure 7.2: *Cross sectional layout for the cable line used in this chapter. The line consists of two 2 parallel three phase systems placed in flat formation 1.3 m below the surface.*

The cables are formed by 2 major sections made of 9 cable segments. The total length of each cable is 7625 m. Each cable segment is approximately 11 % of the total cable length, see figure 7.3. Cross-bondings are used between segments 2 and 3, 4 and 5, 7 and 8, and between 8 and 9. There is a single grounding point of screen between segments 6 and 7. There are joints without cross bonding between segments 1 and 2, 3 and 4, and between 5 and 6.

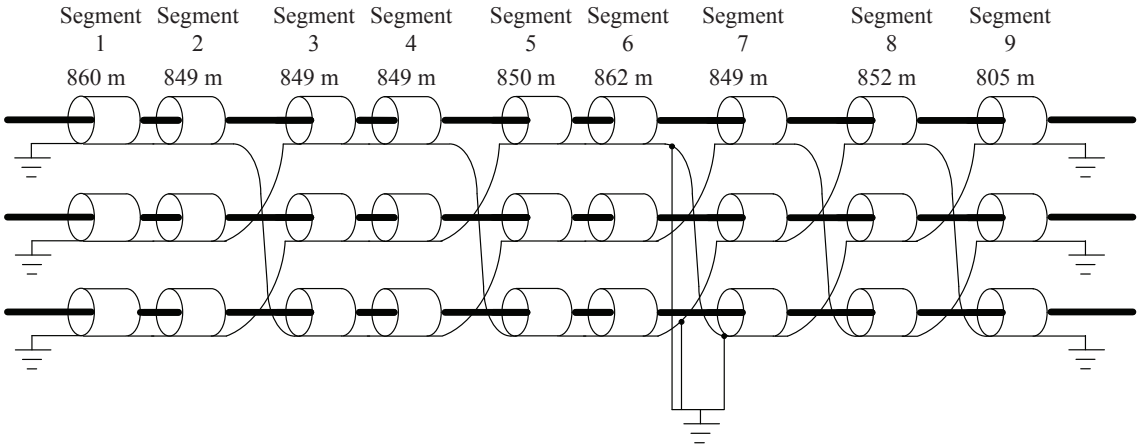

Figure 7.3: *Cross bonding schematic for each of the two 3 phase cable systems of the measured 400 kV cable line in Northern Jutland.*

All cable data are given in appendix C.1

7.1 Planning field measurement set #1

A simulation setup for the cables of the 400 kV system is shown in figure 7.4.

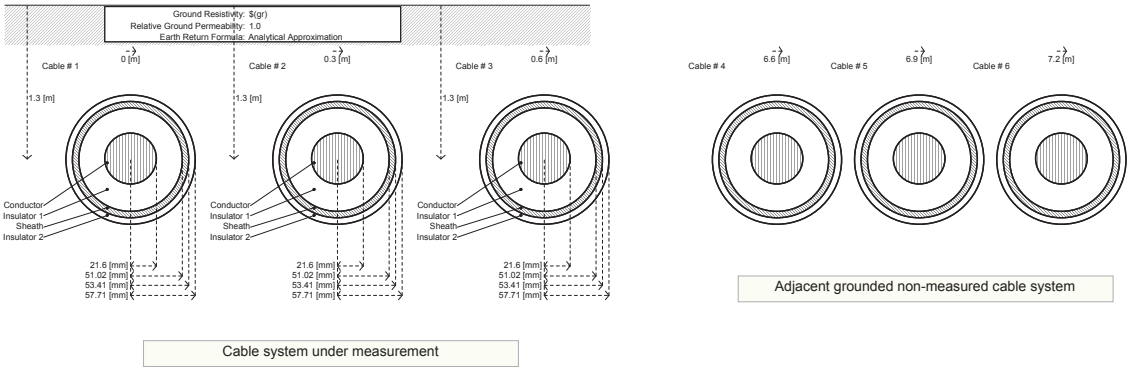

Figure 7.4: *The model segment cross section for the simulation setup of the 400 kV system.*

The purpose of the measurements is to obtain a base for validation of simulation models. The measurements should validate the models for fast transient behaviour. According to IEC 60071-2 an impulse of 1.2x50 μs can be used to simulate lightning overvoltages. The field measurements therefore use an impulse test to validate the cable performance and model calculations for the cable terminal conditions given in equation 2.7.

The impulse used, will be of the form shown in figure 7.5, [37].

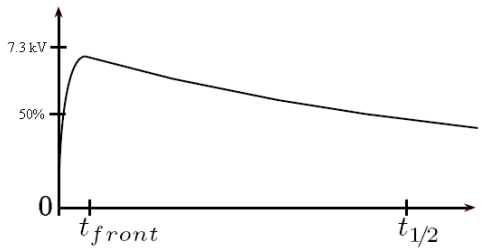

Figure 7.5: *A plot of the impulse similar to the one used in an impulse response test. For the shown example, t_{front}, will be smaller, or close to 0 μs.*

This impulse is applied to the sending end of the cable and the impulse itself, relevant sending end currents and voltages as well as relevant receiving end voltages will be used as a validation template for the cable model.

As a lightning surge generator is not available in EMTDC/PSCAD, the impulse of figure 7.5 is formed by use of two exponential functions [38]. This is implemented in EMTDC/PSCAD as shown in figure 7.6, where the front time is 1,2 μs, the half time is 50 μs and the output is the voltage impulse surge in kV.

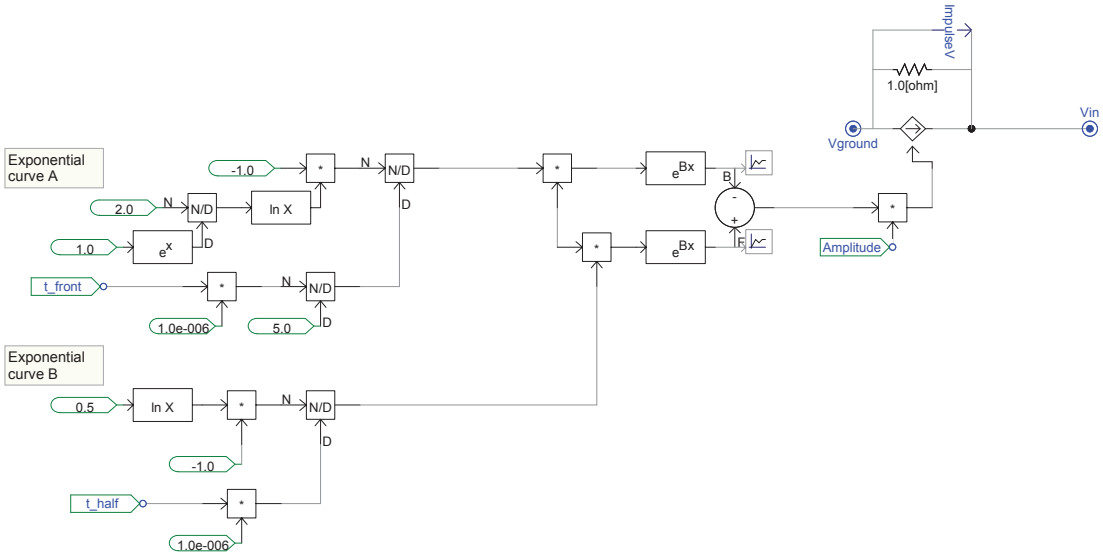

Figure 7.6: *Implementation of the double exponential surge wave in EMTDC/PSCAD. [38]*

The 400 kV cable between Gistrup and Skudshale consists of 9 segments each of ca. 800 m. Each of these segments uses its own cable model. The travelling time, assuming the speed of light, for 800 m is approximately 2,67 μs. The front time of the impulse used to energise phase 1 of the cable system is 1.2 μs. Therefore the time step should be no larger than 1.2/10 = 0.12 μs. Using this time step, the travelling time will be app. 22 times larger than the time step which suggests that the use of the travelling wave theory is correct for each modelled cable segment.

It is chosen to energise one of the outer phases of the measured cable system in the layout from figure 7.4.

The principal test layout based on [2] is shown in figure 7.7.

In cable modelling, the terminal conditions, for both voltage and current, are the conditions of interest. The simulation results for those conditions are calculated from fitting of cable parameters. As the measuring strategies in this report are to be used for cable model validation, both currents and voltages at both ends of the cable are of interest. In order to ensure measurable currents at the terminals, the conductors of all phases are connected to ground through a 500 Ω resistance instead of keeping the end open. The screen is directly grounded. A small resistance of 1 Ω is used to represent the grounding resistance at the substation. The amplitude of the simulated impulse voltage is 5 kV.

7.1.1 Crossbondings and screen grounding

The measured cable system consists of 2 major sections. The simulation layout, when including every cable segment is shown in figure 7.8 on page 48.

When modelling the cable line, each cable segment and crossbonding is modelled separately. The crossbonding is placed underground, approximately 1 m from the centre of the junction. 300 mm^2 Cu wires are used to perform both the crossbonding and the grounding of screen; the inductance in such a wire is estimated to be 1 μH per meter.

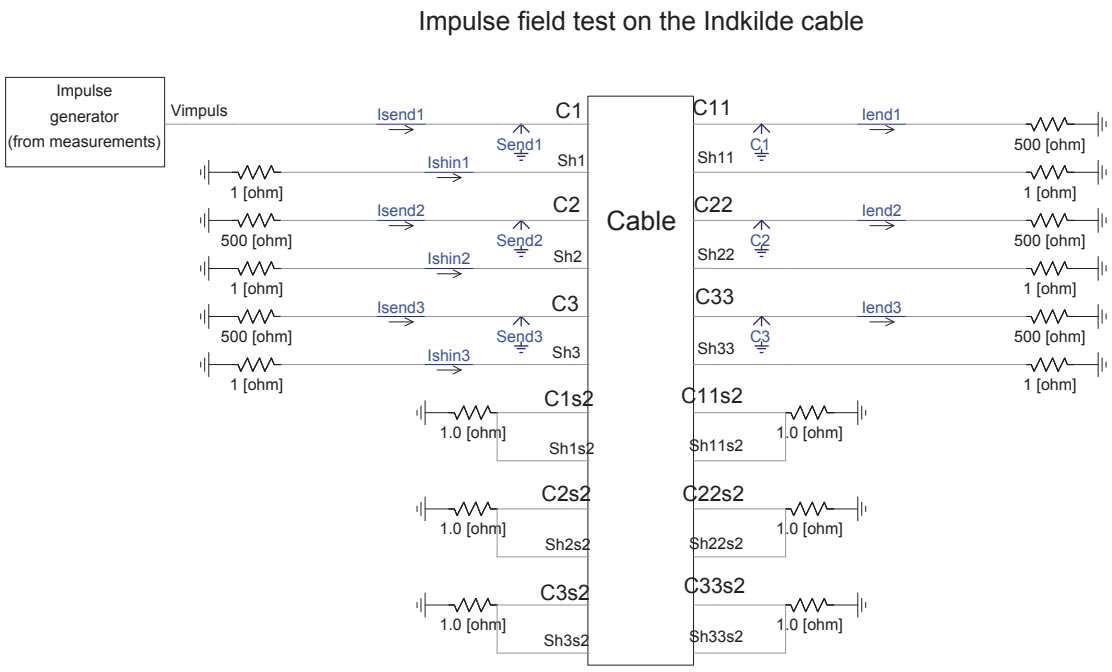

Figure 7.7: *Simulation layout for the impulse response test on the 400 kV cable system.*

The grounding point for the screen is placed in a box, standing on top of the ground. The distance between the box and the HV cables is approximately 10 m. The simulation layout of the crossbonding is shown in figure 7.9(a) on page 49 and the simulation layout of the grounding is shown in figure 7.9(b).

7.1.2 Simulation results

The sending end core voltages and currents and the receiving end voltages and currents are of interest to be used as a validation template for the cable model. The simulation results for the sending end voltage and currents are shown in figure 7.10 on page 49.

The results in figure 7.10(a) show the applied impulse at one of the outer phases and the transients of the other two cables. The other two cables are open circuited by connecting them together and grounding them through a large 500 Ω resistance.

The results in figure 7.10(b) show the currents at the sending end of the three cables. The energised phase has somewhat larger amplitude as expected and the other two phases have the same current result, with $180°$ phase difference.

The simulation results for the receiving end voltage and current is shown in figure 7.11 on page 50.

Figure 7.11(a) show how the transients in the energised phase are much larger than for the other phases. What is interesting is, that because of the cross bonding used there will be induced voltage in the two non-energised phases

From figure 7.11 there is one issue to be addressed in particular. Some receiving end currents shown in figure 7.11(b) are of very low amplitude. The current in the energised phase is approximately 10 A, while the current in the other two phases is only around 1 A and 0.3 A. The problem with such low currents lies

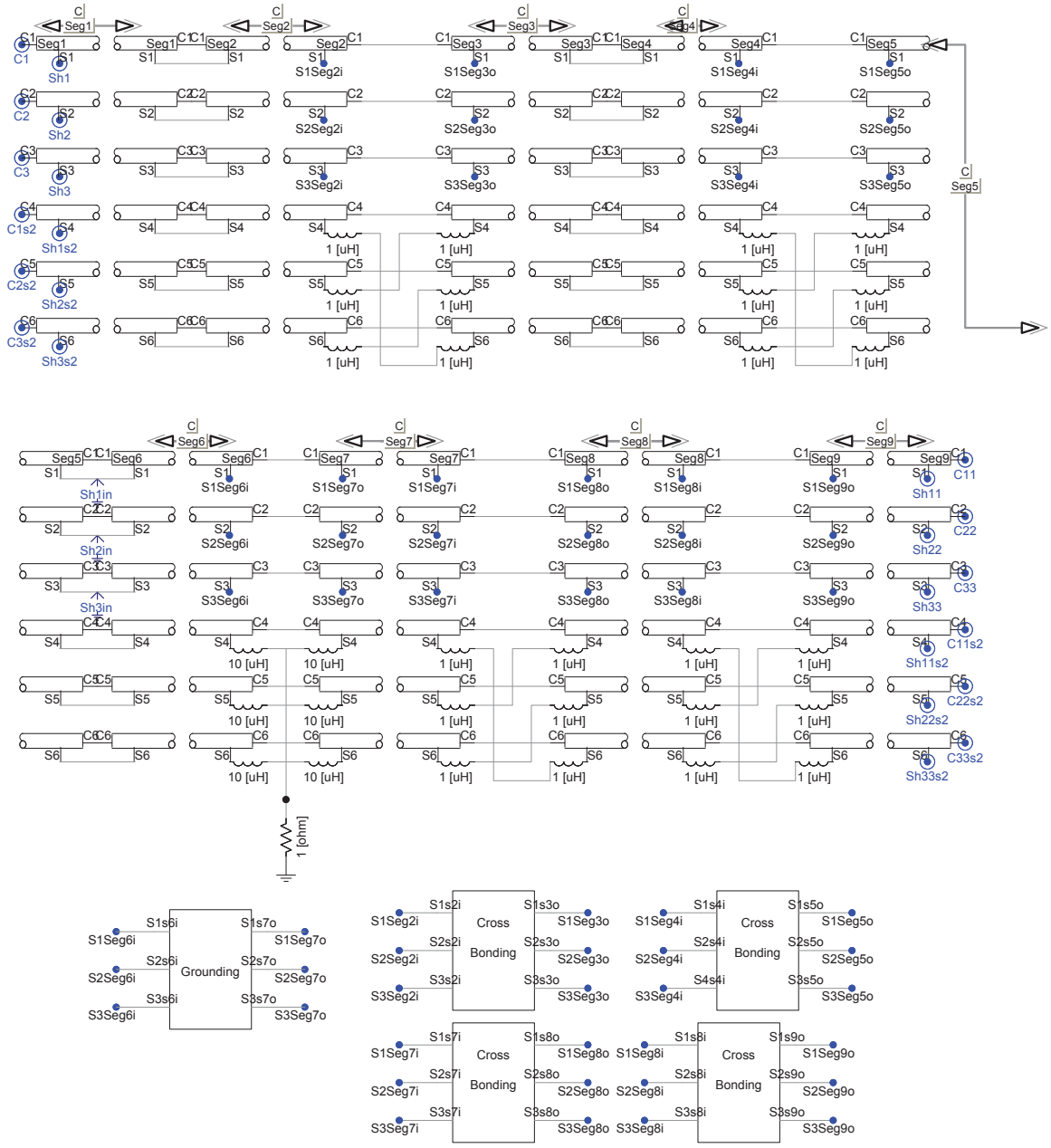

Figure 7.8: *Simulation layout showing modelling of every cable segment.*

in the practical issues of measuring. When trying to measure such a low value where the measurement instruments are surrounded by energised systems, such as the alongside cable system, there is a risk of measuring mainly noise and not the correct measurement value.

One solution would be to boost the input signal, in order to get a higher output current. Because of the surge generators low amplitude, this could lead to the risk of the generator not being able to drive the signal boosting transformer connected to the roughly 7 km long high voltage cable.

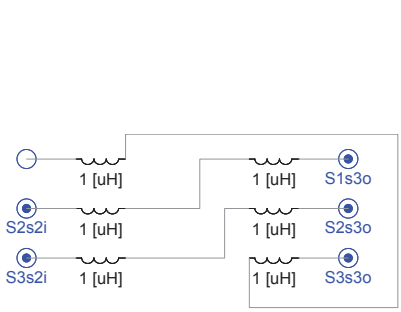

(a) Model representation of crossbonding. The crossbonding is placed approximately 1 m from the centre of the junction.

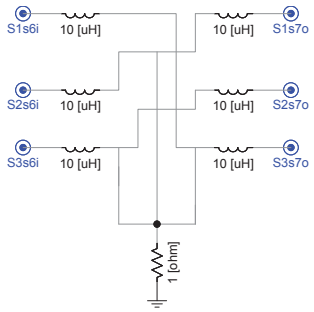

(b) Model representation of the grounding point. The grounding is placed approximately 10m from the centre of the junction.

Figure 7.9: *Modelling of crossbonding and grounding points. 300 mm^2 Cu wires are used to perform the crossbonding and grounding of the screen. The inductance in such a wire is estimated as 1 μH per meter.*

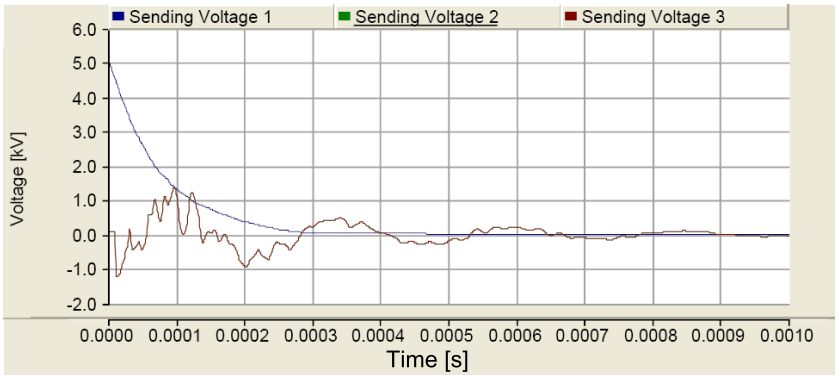

(a) Voltage at the sending end of the cables.

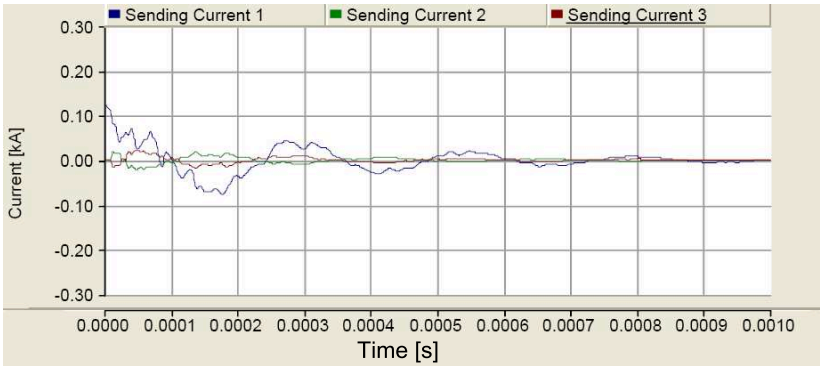

(b) Current at the sending end of the cables.

Figure 7.10: *Simulation results from EMTDC/PSCAD for the impulse response test given in figure 7.7.*

Another solution could be lowering the resistance in those two phases. By simulations, the resistance in the receiving end would have to be lowered down to 10 Ω in order to reach 10 A in the phase which is nearer to the energised phase, while the third phase has only roughly 5 A. When the resistance has been

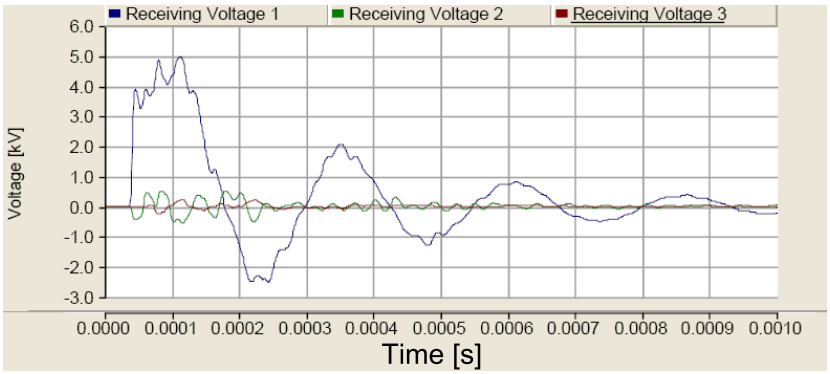

(a) Voltage at the receiving end of the cables.

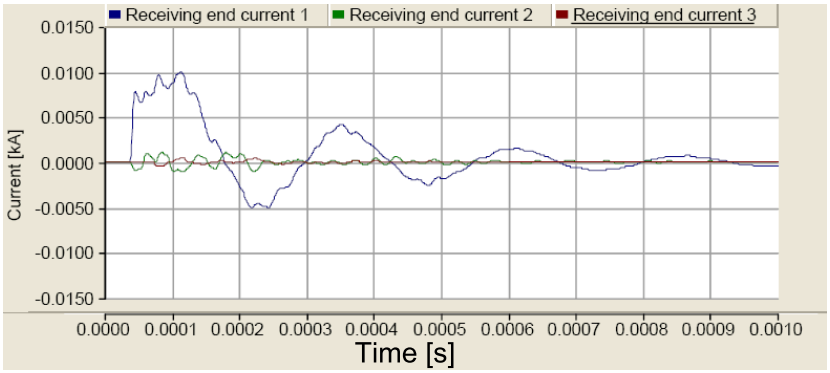

(b) Current at the receiving end of the cables.

Figure 7.11: *Simulation results from EMTDC/PSCAD for the impulse response test given in figure 7.7.*

lowered to only 10 Ω, it has reached the same value as for the direct connection resistance in the screen of all phases.

The third solution could lie in the setup strategy. If the two non-energised phases in the measurement setup in figure 7.7 is studied further, it is possible to see how the current in the two phases is divided into two different current circuits. This is because of two different receiving end 500 Ω resistance. By connecting the two phases together and grounding through a single 500 Ω resistance, the output currents will increase because of the combination of two current circuits into one with only one 500 Ω resistance.

The results in figures 7.10 and 7.11 show that for the simulation setup, with the given surge generator, the energy in the impulse should be enough to give measurable results. One important aspect for the practical measurements is the noise during measurements. In order to ensure that the results represent the actual behaviour of the cable, it is important that possible surrounding noise can be filtered out. Therefore it is important that noise measurements are performed in advance. This could be done to analyse what kind of noise is present.

From the above description, the field measurements on the 400 kV cable are planned and the results compared.

7.2 Performing field measurement set #1

The field measurements are planned and prepared with simulations. The field test setup is based on the simulation layout in figure 7.7.

7.2.1 Field test setup

The field test setup is shown in figure 7.12.

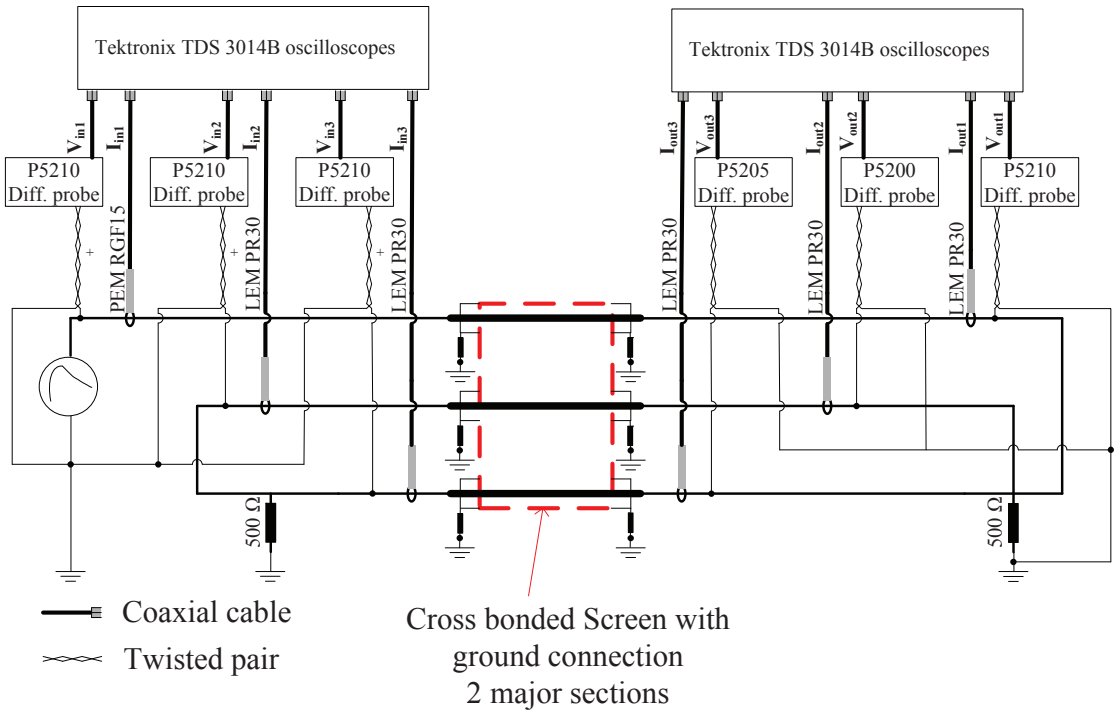

Figure 7.12: *Measurement setup for the field tests. A fast front impulse generator is used to energise a coaxial wave in one of the outer phases.*

Measurements are performed on both sending and receiving end of the cables. The performance of synchronised measurements at both cable ends requires minimum of two persons for performing the measurements, where one person controls the instruments at the sending end (in Gistrup) and the other person controls instruments at the receiving end (in Skudshale). Figure 7.13 shows the test setups at both ends of the cable.

One of the outer phases in the flat formation is energised, while the other two phases are connected to ground via a 500 Ω resistor. A 500 Ω load is also connected to the receiving end of all phases. This is done in order to ensure a measurable current flowing for the otherwise open ended receiving end. All screen connections, in both cable ends, are directly grounded as shown in figure 7.14.

The type of the resistors used is shown in figure 7.15. This type of resistance has an internal 5 mH inductance as well, which must be taken into account during accurate simulations for model validation.

The measurements are only performed on one of the two three phase cable systems shown in figure 7.2. The cable system which is subjected to measurements is physically disconnected from the OHL, while

(a) The test setup in Gistrup.

(b) The test setup in Skudshale.

Figure 7.13: *The test setups for field tests on the 400 kV cable between Gistrup and Skudshale.*

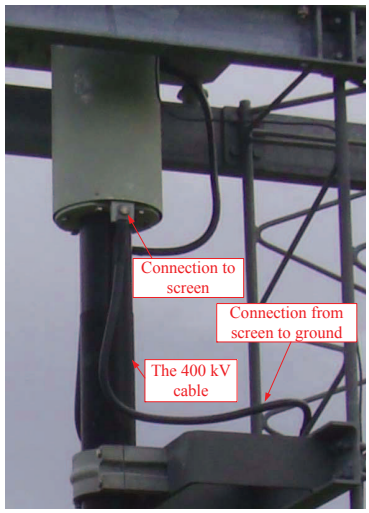

Figure 7.14: *Grounding of screen in the cable ends.*

the other system is physically connected to the OHL. The OHL is grounded at both ends forming a closed grounded loop for the conductors of the non-measured cable system. This can be seen in figure 7.16.

As can be seen in figure 7.16(a), the cable ends are place 8 m above the ground with 4 m between the phases in air. The connection to cable ends were performed by using grounding cables (for connection of generator), measuring cables and earthing clamps for connection to cable ends, as shown in figure 7.17.

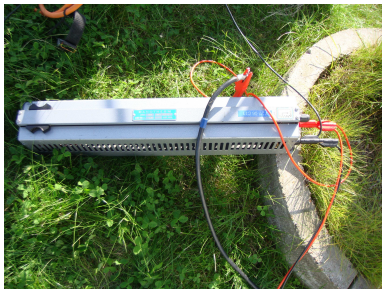

Figure 7.15: *500 Ω resistances.*

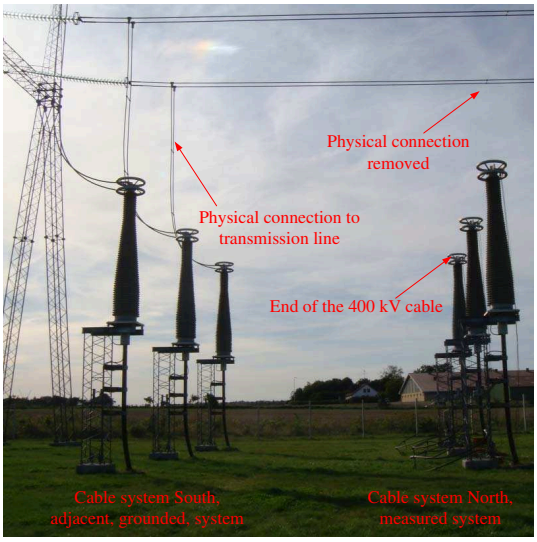

(a) The measured 400 kV cable and the adjacent cable.

(b) Ground connection of the transmission line.

Figure 7.16: *The measured 400 kV cables are physically disconnected from the transmission line, which was grounded. Adjacent cable system is grounded through the transmission line.*

7.2.2 Instruments

The power source used for the impulse test is a HAEFELY PC6-288.1 surge tester, shown in figure 7.18. It is used to generate a 4.28 kV 1.2/50 μs impulse propagating into the core conductor on one of the phases.

Due to the front time of 1.2 μs there should at least be 10 samples during the front time, in order to have an acceptable resolution. The sample time should therefore be no less than 120 ns. This demands measuring equipment of at least 8 MHz. In order to obtain graphical display of the signals 6 identical Tektronix TDS 3014B oscilloscopes are used.

The oscilloscopes have 100 MHz bandwidth and can sample 10000 samples per record, [39]. Each scope has 4 input channels with maximum input voltage of 150 V_{RMS} (212 V_{pk}) and sensitivity of 1 mV/div to 10 V/div. In order to measure only the first 1 ms, it is possible to use an external trigger signal and freeze the first 1 ms on the oscilloscope. This acquired data can then be saved to a computer.

(a) The measuring cable.

(b) Connection of measuring cable to the end of the cable.

Figure 7.17: *The impulse generator is connected to one of the outer phases through a measuring cable.*

Figure 7.18: *The impulse generator.*

Simulation results from the planning procedure, performed before execution of field measurements revealed that some of the expected measuring voltages should be above 212 V_{pk}. Therefore a differential probe was used. There are three types of differential probes used. These are Tektronix P5200 shown in figure 7.19(a), P5205 and P5210 shown in figure 7.19(b). The reason for this is that the P5200 and P5205 have an input voltage limit of 1.3 kV, while the P5210 has a limit of 5.6 kV [40].

In order to obtain the current measurements for the setup shown in figure 7.12, current probes are used. According to planning simulations, the current measurements vary from 7 mA to 141 A. Therefore two types of current probes were chosen. For measuring sending current, on energised core conductor, a

(a) Tektronix P5200. (b) Tektronix P5210.

Figure 7.19: *The differential probes to be used for the cable measurements.*

probe of the type PEM RGF15, shown in figure 7.20(a), is used. The measuring range for this probe is from 20 A to 60 kA, [41]. For other current measurements a probe of the type LEM PR30, shown in figure 7.20(b), are used. The measuring range for the LEM probe is 5 mA to 30 A, [42]. The output signal from the used current probe is a voltage signal which can be fed into the oscilloscope.

(a) PEM RGF15. (b) LEM PR30.

Figure 7.20: *The current probes to be used for the cable measurements.*

Setup of the voltage and current probes can be seen in figure 7.21 on the next page.

Six identical oscilloscopes are used to obtain the measurements, three at each end of the cable, see figure 7.22. The first scope on both ends of the cable uses channel 1 to measure core voltage on energised core conductor, channel 2 to measure core current on energised core conductor. On these two scopes, the trigger signal is fed to an external trigger on the back of the scope and channel 4 is used to synchronize the time of the cable ends.

In order to be able to compare measurement results for both ends of the cable for travelling time analysis, a signal at each end of the cable is generated. These two identical signals are generated using the OMICRON CMC-256 and synchronized by GPS signals, see figure 7.23. The signals are measured at both ends of the cable.

The remaining two oscilloscopes at each end of the cable, are used to measure core voltage and core current on the non-energised phases. Channel 4 is used to trigger the scopes and the trigger signal is the measured core current on the energised phase.

(a) Current measurement.

(b) Voltage probes for voltage measurements.

Figure 7.21: *Current and voltage measurements.*

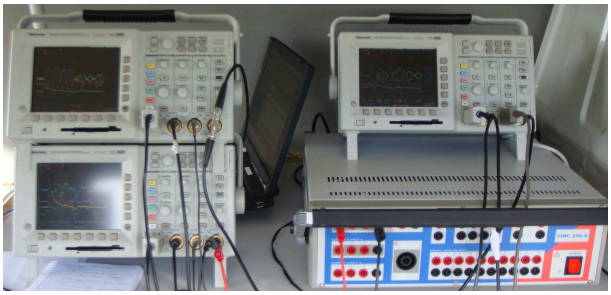

(a) Three connected oscilloscopes placed in Gistrup.

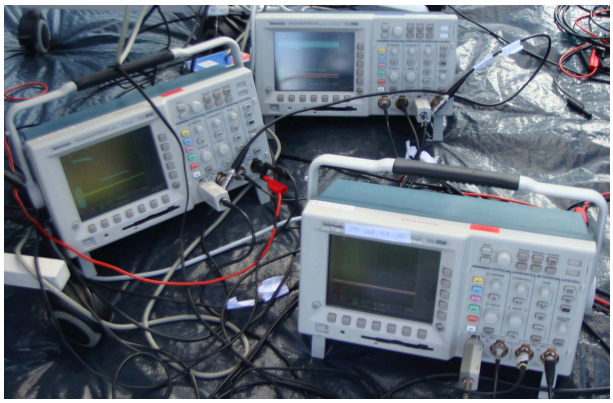

(b) Three connected oscilloscopes placed in Skudshale.

Figure 7.22: *Six identical oscilloscopes are used. Three placed in Gistrup and three placed in Skudshale.*

The oscilloscopes are set to measure over 1 ms and the record length is 10K points. The time for each sample is therefore 100 ns and the sampling frequency is $F_s = \frac{1}{100\text{ns}} = 10$ MHz, which meets the minimum requirement of 8 MHz.

7.2.3 Measuring accuracy

The purpose of the measurements is to obtain a basis that can be used for validating a simulation model for underground cables. The accuracy of the measurements is therefore highly important. When the measurement results are used to validate simulation results, the simulation results should fit with measurement results within the accuracy of the measurements.

(a) The OMICRON CMC-256.

(b) A GPS unit for the CMC-256.

Figure 7.23: *A signal is generated using the OMICRON CMC-256. Two such signals are synchronized by GPS.*

Surrounding noise

In order to estimate the noise because of surrounding transmission systems, measurements of induced voltage/current are performed with no voltage on the measured 400 kV cables. Core voltage and current for all phases is measured. This is done both for the sending end at Gistrup and the receiving end at Skudshale. To record these measurements an OMICRON CMC-256 with enerlyzer was used.

The results for induced voltage and current at sending end are shown in figure 7.24

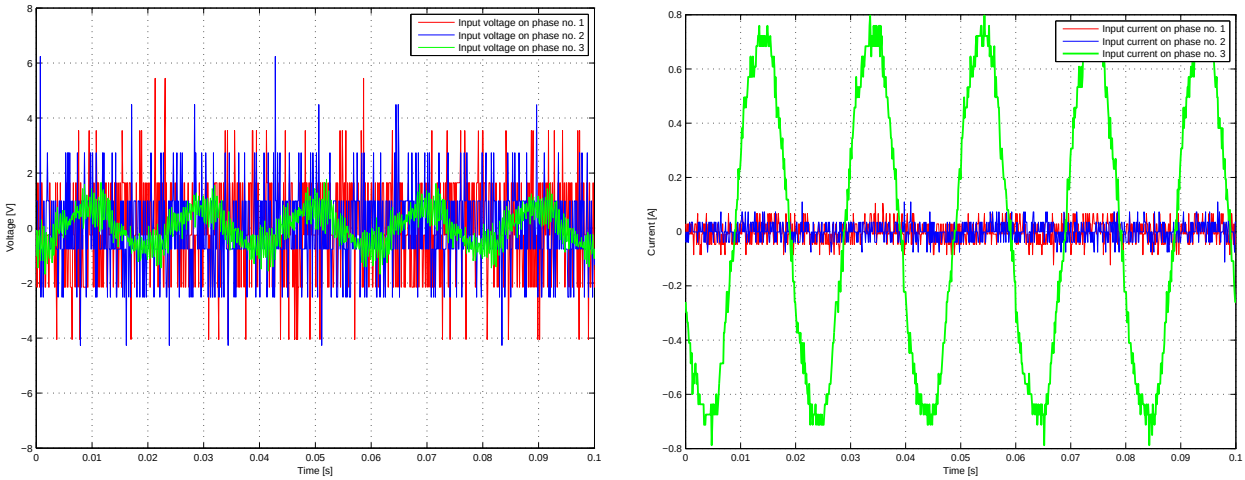

(a) Core voltages.

(b) Core currents.

Figure 7.24: *Core voltages/currents for all three phases in sending end at Gistrup. This is a measurement of induced noise, performed with no voltage on the measured 400 kV cables. Phase 1 is the energised phase, phase 2 is the middle cable in the flat formation and phase 3 is the other outer phase.*

The measurement results for voltages on two out of three phases are almost non-measurable, as shown in figure 7.24(a). The largest and most clear signal is for phase 3, a non-energised outer phase. This induced signal has a peak of approximately 1.8 V. A 150 kV transmission line transmitting power to a near by city, Aalborg Øst, is placed few hundred meters away from the cables. This explains the induced voltage.

All measured voltages are in the level of 1.5-4.3 kV, which is approximately 1000-2500 times the measured noise signal. Furthermore the noise signal only appears at power frequency, 50 Hz, while the impulse response test is measuring for many and much higher frequencies.

The induced noise current is measured largest as approximately 0.7 A for phase 1 and 0.1 A for the other phases. As for the induced voltage, the induced current only appears at power frequency. The measured currents during the impulse test are approximately 100 A for energised phase and 2 A on the adjacent phases. The induced noise current is therefore 20-100 times smaller than the measured currents during the field test. Furthermore, the field test currents propagate at many and much higher frequencies than 50 Hz.

The results for induced voltage and current at receiving end are shown in figure 7.25

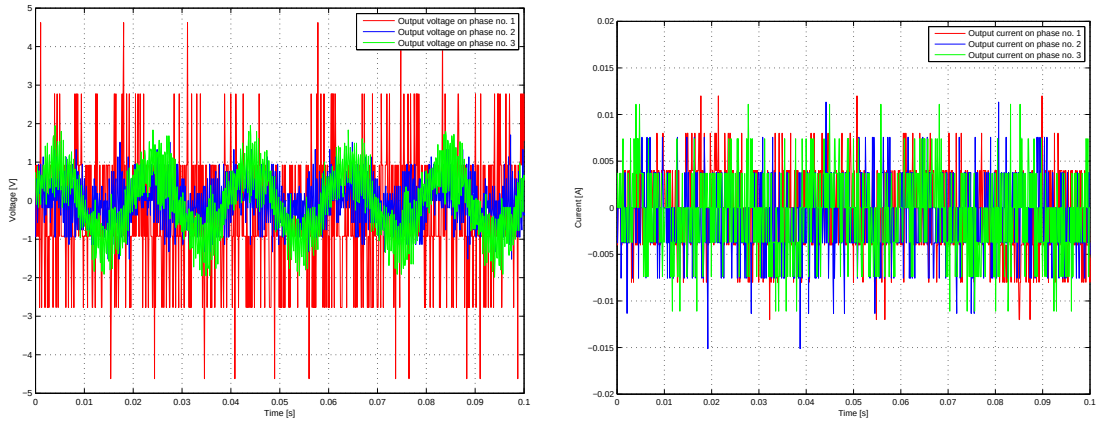

(a) Induced core voltage

(b) Induced core current

Figure 7.25: *Core voltages/currents for all three phases in receiving end at Skudshale. This is a measurement of induced noise, performed with no voltage on the measured 400 kV cables. Phase 1 is the energised phase, phase 2 is the middle cable in the flat formation and phase 3 is the other outer phase.*

The results for induced noise voltages and currents at the receiving are even smaller than at the sending end because of less surrounding high voltage transmission lines. During the impulse field test, measured voltages are similar in size as for the sending end. The receiving end current for the energised phase is smaller, but the ratio between induced noise and field test measurements are still similar to the sending end.

It can therefore be concluded that the induced noise voltage and currents at both sending and receiving end do not affect the measured values during the field test. Filtering of noise is therefore not necessary.

Equipment accuracy

There are two types of accuracy to be considered, time accuracy and amplitude accuracy. The time accuracy is dependent on the horizontal accuracy of the used oscilloscopes. The sampling rate accuracy for the TDS3014B oscilloscope is ± 20 ppm, or 0.002 $\%$, for any interval ≥ 1 ms, [43, p. A-6]. The time interval for the described measurements is 1 ms in total for all measurements. This results in time inaccuracy of:

$$\Delta t = \pm 1ms \cdot 0.002\% = \pm 20ns$$

This means that the resulting signals can be shifted in time for maximum of 20 ns. For front time and half time of the applied impulse, this inaccuracy of 20 ns must be considered. The front time is 1.2 μs and the half time is 50 μs. The inaccuracy is therefore only 0.04$\%$ for the half time and 1.6$\%$ for the front time.

The amplitude accuracy is calculated from warranted characteristics of all used instruments. First the accuracy of the used probe is calculated. The signal out of the used probe has a value of $A \pm \Delta A$, which is the signal with maximum inaccuracy values. This value is an input for the oscilloscope, which also has some boundaries for accuracy.

Calculating the maximum accuracy

A high voltage differential probe Tektronix P5210 the Tektronix TDS3014B oscilloscope are used to measure the core voltage for the energised phase at the sending end in Gistrup. The accuracy for the differential probe is given as $\pm 3\%$, [44, p. 8]. The accuracy given for the oscilloscope is somewhat more complicated and depends on the setting for the channel of the oscilloscope, [43, p. A4-A5].The accuracy for the oscilloscope is:

$$\pm\,[0.02 \cdot |\text{reading} - (\text{offset position})| + (\text{offset accuracy}) + 0.15\text{div} \cdot \text{V/div setting} + 0.6mV]$$

Where the offset position for all measurements is equal to 0 and the offset accuracy is dependent on the setting for each channel as following:

Scale range for each setting of channel	Accuracy
1 mV/div to 100 mV/div	$\pm[0.002 \cdot \lvert\text{net offset}\rvert + 1.5mV + 0.1\text{div} \cdot \text{V/div setting}]$
101 mV/div to 1 V/div	$\pm[0.0025 \cdot \lvert\text{net offset}\rvert + 15mV + 0.1\text{div} \cdot \text{V/div setting}]$
1.01 V/div to 10 V/div	$\pm[0.0025 \cdot \lvert\text{net offset}\rvert + 150mV + 0.1\text{div} \cdot \text{V/div setting}]$

To demonstrate how the maximum accuracy for a measurement is obtained, the accuracy of the core voltage of the energised phase in Gistrup can be calculated.

First of all, the "‘reading"’ for the oscilloscope accuracy is the outcome of the probe. Therefore the "‘reading"’ is actually "‘reading $\pm 3\%$ of reading"’.

The scope setting is 1 kV/div, where the probe has the setting of x1000. Therefore, the V/div setting is 1kV/1000=1 V/div and the offset accuracy is

$$\pm\left[0.0025 \cdot |0| + 15mV + 0.1\text{div} \cdot 1\text{V/div}\right] = \pm[15mV + 0.1V] = \pm 0.115V$$

The maximum accuracy of the core voltage of phase 1 in Gistrup is shown in equation 7.1.

$$\begin{aligned} \Delta V_{in1} &= \pm[0.02 \cdot |\text{reading } \pm 3\% \text{ of reading}| + 0.115V + 0.15\text{div} \cdot 1\text{V/div} + 0.6mV] \\ &= \pm[0.02 \cdot |\text{reading } \pm 3\% \text{ of reading}| + 0.2656V] \end{aligned} \tag{7.1}$$

The accuracy for all the measurements can be found in a similar way and the results for all of the warranted characteristics are given in table 7.1 on the facing page, where voltage/current 1 refer to the energised phase, voltage/current 2 refer to the middle phase and voltage/current 3 refer to the non-energised outer phase.

7.2.4 Measurement results

With the certainty that the induced voltages and currents at both ends of the cables will barely have any disturbance on the measurement results, the field test results for the impulse response test can be analysed.

There were performed 4 identical impulse response tests. This was done for comparison, in order to assure reliability of obtained data. All 4 tests give fairly the same results.

Core voltage at Gistrup

The field test results for core voltages at the sending end of the cable, in Gistrup, are shown in figure 7.26 on page 62.

Figure 7.26(a) shows the impulse voltage applied to phase 1 (the energised phase). The actual magnitude of the applied impulse is 4280 V. The front time is calculated as the time between 30 % and 90 % of the total amplitude, [37]. 30% is 1284 V and 90 % is 3852 V. The time in between is 2.66 μs. This means that the actual front time of the measured impulse is not 1.2 μs but 2.7 μs. The impulse has lowered to half its amplitude after 54.1 μs. This means that the actual half time of the measured impulse is not 50 μs but 54.1 μs. Actual amplitude, front time and half time of the impulse must be taken into consideration when performing simulations for this impulse test.

Figure 7.26(b) shows the measured core voltage on phase 2 (the middle cable in the flat formation). This voltage appears when a large impulse is applied to phase 1, which is an adjacent identical cable in 0.3 m distance. Phase 2 is grounded through a 500 Ω resistance in both ends, which creates a closed current circuit. As it can be seen in figure 7.26(b), the first pulse of the core voltage on phase 2 is negative. This is because of Faradays law of induced voltage, see equation 7.2, [45].

$$V_{induced} = -\frac{d\Phi}{dt} \tag{7.2}$$

Faradays law states that the voltage induced in a closed circuit is equal to the negative rate of increase of the magnetic flux linking the circuit. The increase of the magnetic flux linking the circuit, $\frac{d\Phi}{dt}$, is

Measurement	**Probe setting**	**Probe accuracy**	**Oscilloscope setting**	**Oscilloscope accuracy**
Sending voltage 1	1000x	$\pm 3\%$	1 kV/div	$\pm[0.02 \cdot \lvert\text{reading } \pm 3\% \text{ of reading}\rvert + 0.2656 \text{ V}]$
Sending voltage 2	1000x	$\pm 3\%$	500 V/div	$\pm[0.02 \cdot \lvert\text{reading } \pm 3\% \text{ of reading}\rvert + 0.1406 \text{ V}]$
Sending voltage 3	1000x	$\pm 3\%$	500 V/div	$\pm[0.02 \cdot \lvert\text{reading } \pm 3\% \text{ of reading}\rvert + 0.1406 \text{ V}]$
Sending current 1	2mV/A	$\pm 1\%$	50 mV/div	$\pm[0.02 \cdot \lvert\text{reading } \pm 1\% \text{ of reading}\rvert + 0.0146 \text{ V}]$
Sending current 2	100mV/A	$\pm 1\%$ of reading ± 2 mA	100 mV/div	$\pm[0.02 \cdot \lvert\text{reading } \pm 1\% \text{ of reading} \pm 0.2\text{mV}\rvert + 0.0271 \text{ V}]$
Sending current 3	100mV/A	$\pm 1\%$ of reading ± 2 mA	100 mV/div	$\pm[0.02 \cdot \lvert\text{reading } \pm 1\% \text{ of reading} \pm 0.2\text{mV}\rvert + 0.0271 \text{ V}]$
Receiving end voltage 1	1000x	$\pm 3\%$	1 kV/div	$\pm[0.02 \cdot \lvert\text{reading } \pm 3\% \text{ of reading}\rvert + 0.2656 \text{ V}]$
Receiving end voltage 2	1/500	$\pm 3\%$	1 V/div	$\pm[0.02 \cdot \lvert\text{reading } \pm 3\% \text{ of reading}\rvert + 0.2656 \text{ V}]$
Receiving end voltage 3	500x	$\pm 3\%$	500 V/div	$\pm[0.02 \cdot \lvert\text{reading } \pm 3\% \text{ of reading}\rvert + 0.2656 \text{ V}]$
Receiving end current 1	100mV/A	$\pm 1\%$ of reading ± 2 mA	200 mV/div	$\pm[0.02 \cdot \lvert\text{reading } \pm 1\% \text{ of reading}\rvert + 0.0656 \text{ V}]$
Receiving end current 2	100mV/A	$\pm 1\%$ of reading ± 2 mA	100 mV/div	$\pm[0.02 \cdot \lvert\text{reading } \pm 1\% \text{ of reading}\rvert + 0.0271 \text{ V}]$
Receiving end current 3	100mV/A	$\pm 1\%$ of reading ± 2 mA	100 mV/div	$\pm[0.02 \cdot \lvert\text{reading } \pm 1\% \text{ of reading}\rvert + 0.0271 \text{ V}]$

Table 7.1: *Table showing warranted characteristics for all measuring instruments for the field measurements of setup #1.*

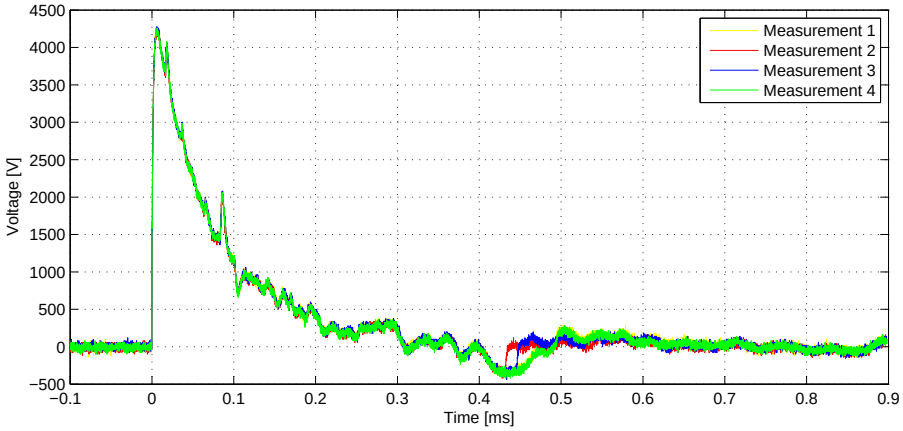

(a) Sending end voltage on phase 1

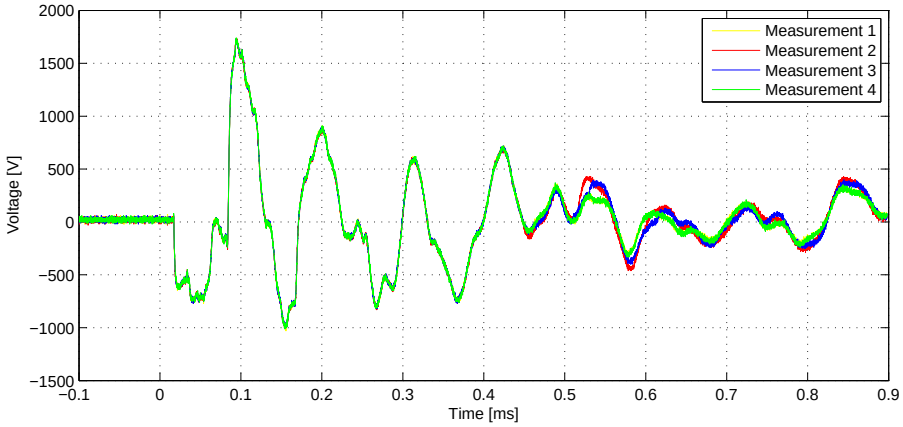

(b) Sending end voltage on phase 2

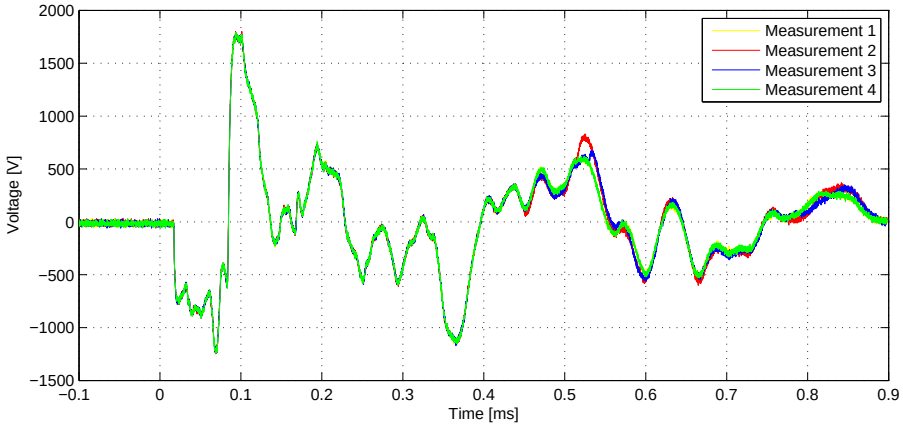

(c) Sending end voltage on phase 3

Figure 7.26: *Test results for impulse test. Core voltages at the sending end of the cable, in Gistrup. Phase 1 is the energised phase, phase 2 is the middle cable in the flat formation and phase 3 is the other outer phase.*

caused by the energised closed circuit nearby. This is illustrated in figure 7.27, where $\Phi = \int_S Bds$ for the magnetic flux crossing surface S.

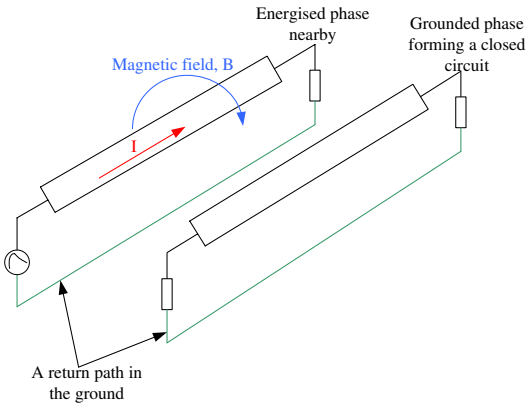

Figure 7.27: *The voltage induced in a closed circuit is equal to the negative rate of increase of the magnetic flux linking the circuit.*

Furthermore, the first peak of the induced voltage happens some time after the impulse is applied to phase 1. This can be explained by the theory for impulse response. The induced voltage in phase 2 is phase shifted from the original voltage of phase 1. This is because of the impedance in the cable and the ground. The induced voltage can be calculated by means of convolution, where convolution is a mathematical operator which takes two functions, f and g, and produces a third function that in a sense represents the amount of overlap between f and a reversed and translated version of g.

Figure 7.26(c) shows the measured core voltage on phase 3 (the flat formation other outer phase). This voltage appears when a large impulse is applied to phase 1, which is an adjacent identical cable in 0.6 m distance. As for phase 2, phase 3 is grounded through a 500 Ω resistance in both ends, which creates a closed current circuit. As for phase 2, the first pulse is negative and occurs some time after the impulse is applied to phase 1.

Core current at Gistrup

The field test results for core currents at the sending end of the cable, in Gistrup, are shown in figure 7.28 on the next page.

Figure 7.28(a) shows the current applied to phase 1. As it can be seen the current peak is approximately 130 A. This is approximately the same as expected, and shown in chapter 7.1.2, for this phase, as the simulated peak was 141 A with a 5 kV peak impulse. For the measurements, the peak impulse is 4.28 kV.

Figure 7.28(b) shows the measured core current on phase 2. As it can be seen, the first peak of the current is in the same direction as for phase 1. This is because of the negative sign for Faraday's law, called Lenz's law. Lenz's law states that a variation in the magnetic field around a closed energised circuit induces a current in a nearby closed circuit with a direction trying to oppose the change in the original magnetic field. This can be seen in figure 7.29.

For this case, the magnetic field around phase one is increased, and according to Lenz's law the current in phase two should produce a magnetic field opposing the change in the original magnetic field caused

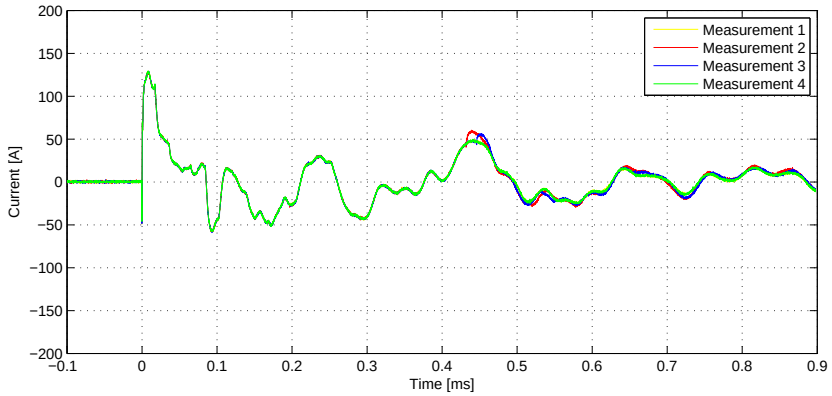

(a) Sending end current on phase 1

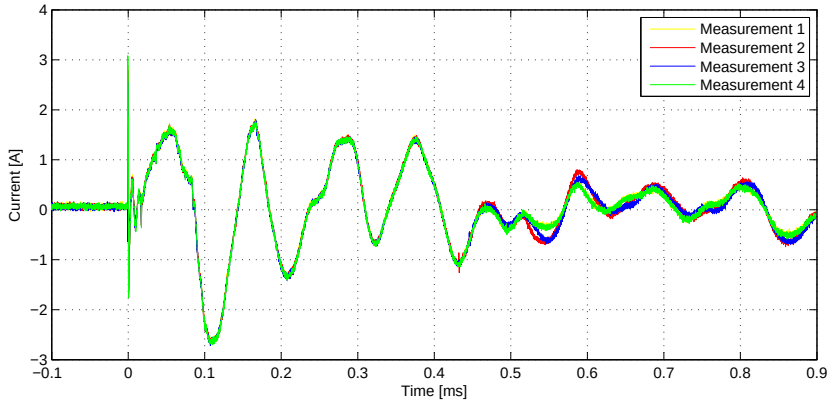

(b) Sending end current on phase 2

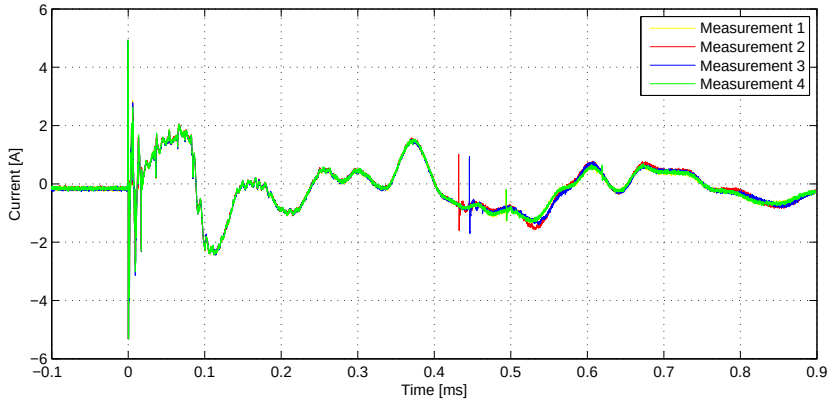

(c) Sending end current on phase 3

Figure 7.28: *Test results for impulse test. Core currents at the sending end of the cable, in Gistrup.*

by the change in current of phase 1. Figure 7.29(a) shows an opposing magnetic field caused by enlarging the original current and figure 7.29(b) shows an upholding magnetic field caused by diminishing the original current. The case for applying an impulse voltage to phase one and having an induced current in phase two, is in accordance to figure 7.29(a).

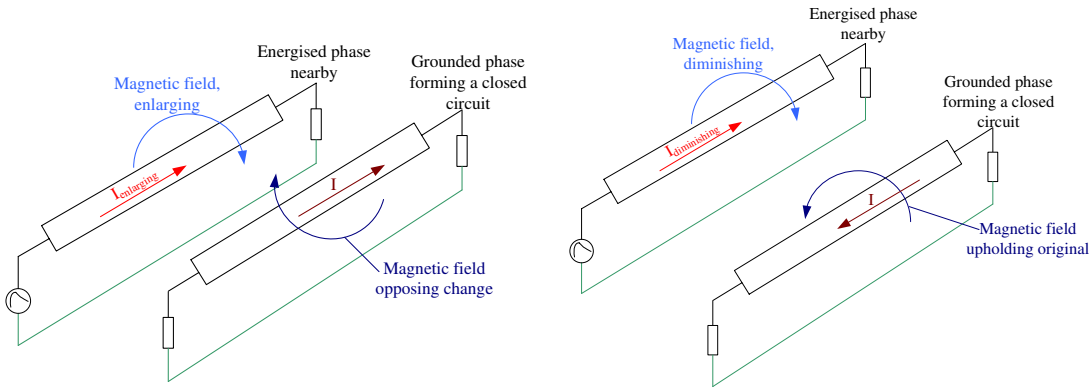

(a) Enlarging original current.

(b) Diminishing original current.

Figure 7.29: *The current induced in a closed circuit will produce a magnetic field that opposes the change in the original magnetic field.*

Figure 7.28(c) shows the measured core current on phase 3. The same principle applies for the direction of the current in phase 3, as for the current in phase 2. Therefore the direction of the current in all three phases is the same.

For the induced current in phases 2 and 3, there should be a delay before the current starts flowing. As it can be seen, the current measurements always show results different from zero. This is because during the delay, the measurements are picking up noise from the impulse generator. The noise in figure 7.28(b) and 7.28(c) have a duration of 20 μs. This is also in accordance with the delay of core voltages for phases 2 and 3. From figure 7.26(b) and 7.26(c) the delay is equal to 20 μs. In order to have a correct overview over the actual current in the conductor of phase 2 and phase 3, the disturbances are therefore filtered out. The filtered results can be seen in figure 7.30 on the following page.

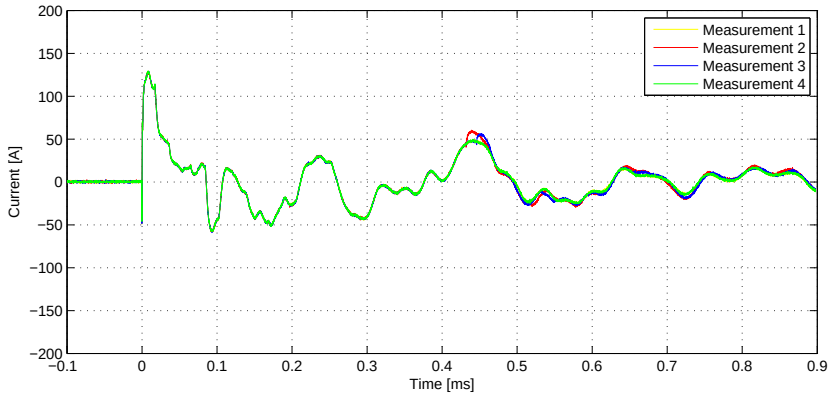

(a) Sending end current on phase 1

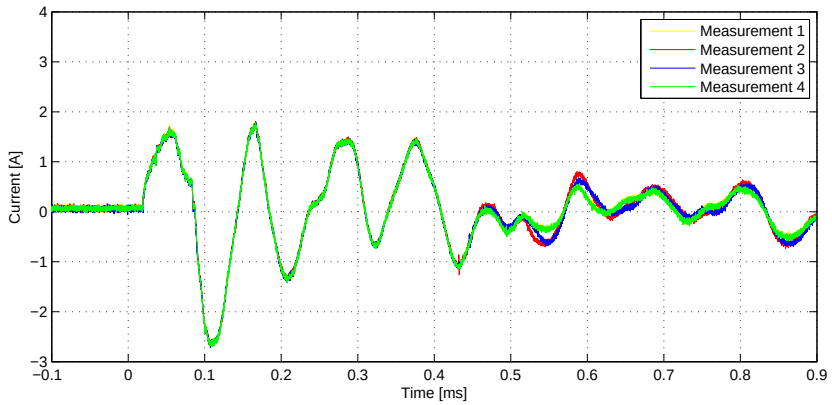

(b) Sending end current on phase 2

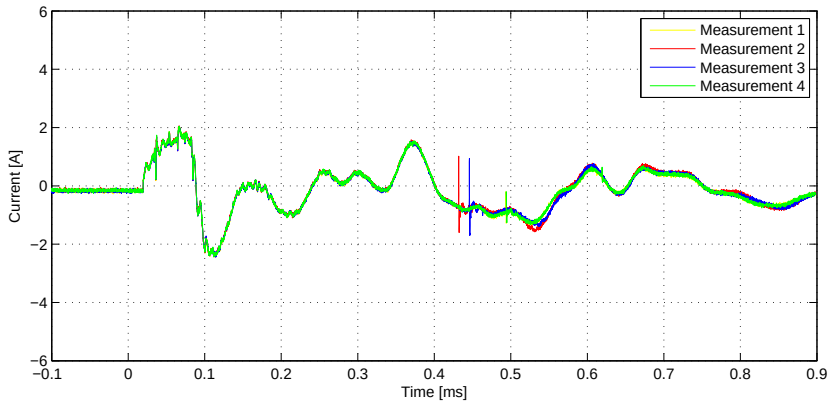

(c) Sending end current on phase 3

Figure 7.30: *Test results for impulse test. Core currents at the sending end of the cable, in Gistrup.*

Core voltage at Skudshale

The field test results for core voltages at the receiving end of the cable, in Skudshale, are shown in figure 7.31 on the next page.

Figure 7.31(a) shows the measured core voltage on phase 1. The first peak of this measured core voltage

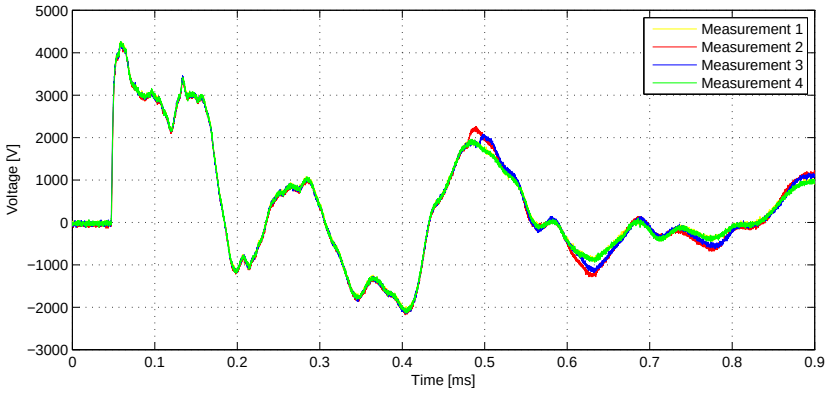

(a) Receiving end voltage on phase 1

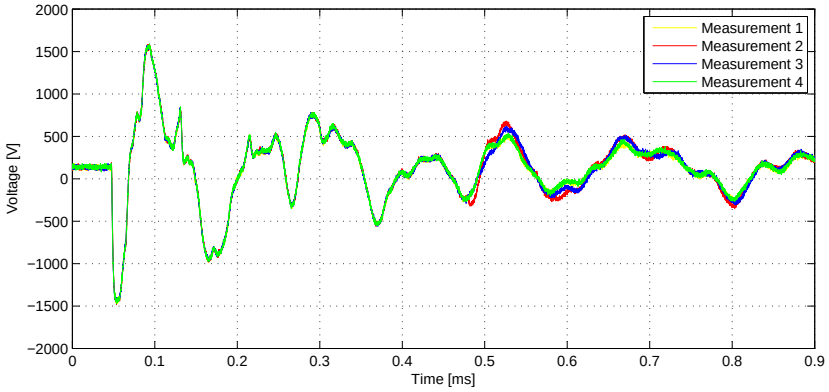

(b) Receiving end voltage on phase 2

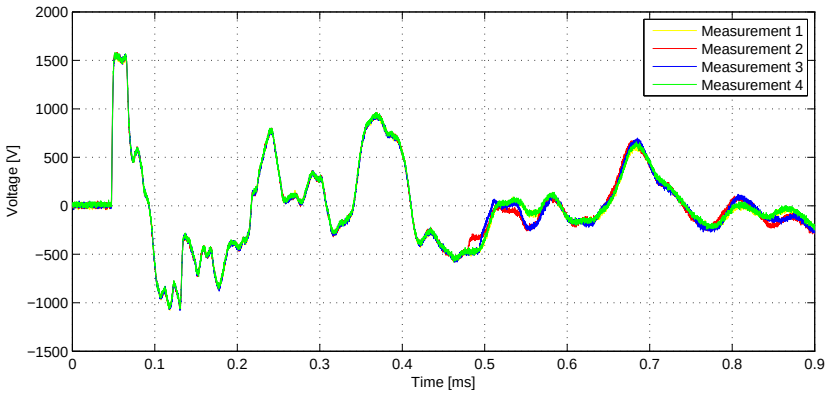

(c) Receiving end voltage on phase 3

Figure 7.31: *Test results for impulse test. Core voltages at the receiving end of the cable, in Skudshale.*

on phase 1 happens after 39 μs of delay and is 4260 V. As it can be seen in figure 7.31(a) the form of the core voltage has changed from the sending end, see figure 7.26(a).

Because of distributed parameters of the cable and the wave characteristics, the voltage and current at the receiving end of the cable can be calculated using equation 7.3.

$$V_{receiving}(x) = k_{v1}e^{-\gamma x} + k_{v2}e^{\gamma x}$$
$$I_{receiving}(x) = k_{i1}e^{-\gamma x} + k_{i2}e^{\gamma x} \tag{7.3}$$

where k_{x1} and k_{x2} are constants to the solution of the terminal condition differential equation.

> γ is the complex propagation constant, defined as: $\gamma = \sqrt{(R + j\omega L)(G + j\omega C)} = \alpha + j\beta$ where α is the attenuation constant and γ is the phase constant.

From equation 7.3 it can be seen how the voltage at the receiving end of the cable depends both on the wave travelling from the sending end, $k_{v1}e^{-\gamma x}$, and on the wave reflected at the receiving end and then travelling to the sending end, $k_{v2}e^{\gamma x}$. Because of this characteristic, the voltage at the receiving end of the cable has a different form than the voltage at the sending end. For an infinite lossless line, the voltages at the two ends of the cable should be identical.

Figures 7.31(b) and 7.31(c) show the measured core voltage on phase 2 and phase 3 respectively. The first peak in both cases is of approximately 1.5 kV and the signals contain some higher frequencies.

Core current at Skudshale

The field test results for core currents at the receiving end of the cable, in Skudshale, are shown in figure 7.32 on the facing page.

The delay of 39 μs appears for the current measurements, as it does for the voltage measurements.

By comparing the measuring results of figure 7.32 and figure 7.31 it can bee seen how the voltage and current forms are similar for each phase. This is also according to the theory, as the current measured is the current right before the connected 500 Ω load resistance and the voltage is measured over the load resistance. This is according to the theory, as the load resistance is pure resistive.

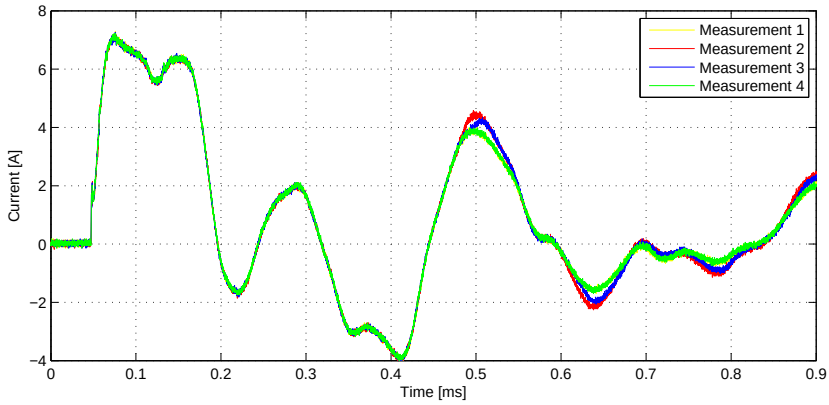

(a) Receiving end current on phase 1

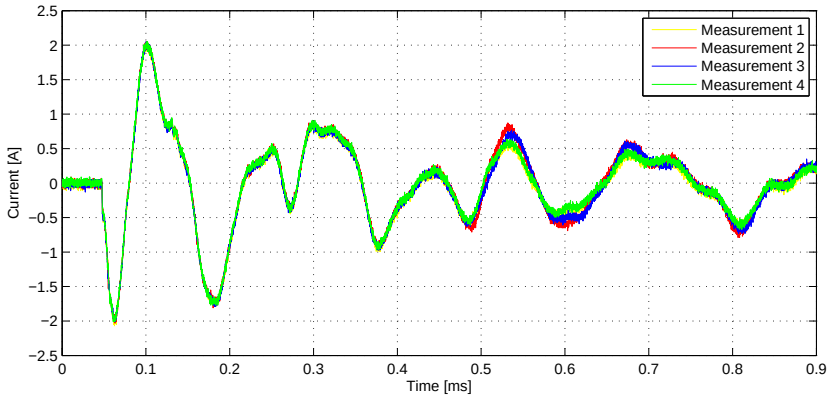

(b) Receiving end current on phase 2

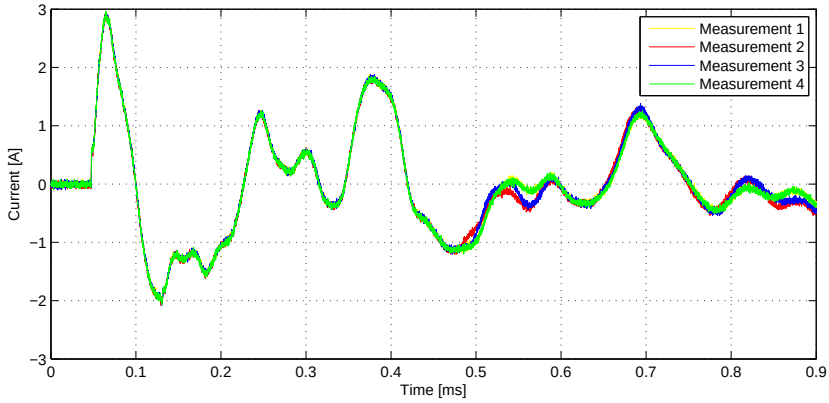

(c) Receiving end current on phase 3

Figure 7.32: *Test results for impulse test. Core currents at the receiving end of the cable, in Skudshale.*

7.3 Analysing field measurement set #1

The purpose of the field measurements on the 400 kV cable system was to analyse the cable model, investigate the accuracy of the model and use wave propagation to identify origin of disagreement between measurements and simulations.

For the validation, a simulation model in ETDC/PSCAD, as described in chapter 7.1 is used. In order to simulate the behaviour of the cable as close to results from field tests as possible, the excitation voltage of the energised phase used as an input to the simulation model must be identical for measurements and simulations. It is impossible to model an impulse, by the theory from chapter 7.1, that is identical to generated pulse during the field tests. Therefore, measurements of the generated impulse from the field test are used to create a voltage source, instead of using a double exponential surge. This is done by constructing a component that retrieves data from the measured impulse and feeds that into a source. This source is then used to energise in the simulation model. When using the measured impulse for energising the cable, one must be careful regarding reflections. The input impulse contains reflections from crossbonding points and receiving end of the cable and if the travelling time is not identical for field measurements and simulations, it can cause deviations between simulations and field measurements of sending end currents and receiving end voltages. In this project, this has been taken into account and the travelling time validated to be identical.

As explained on page 51, the resistances used include a 5 mH inductance which in the simulations is added in series to the 500 Ω resistance. The simulation setup for the impulse is shown in figure 7.33(a) and the comparison of measured and simulated impulse voltage can be seen in figure 7.33(b).

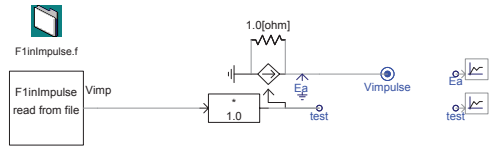

(a) Model representation of the impulse generator.

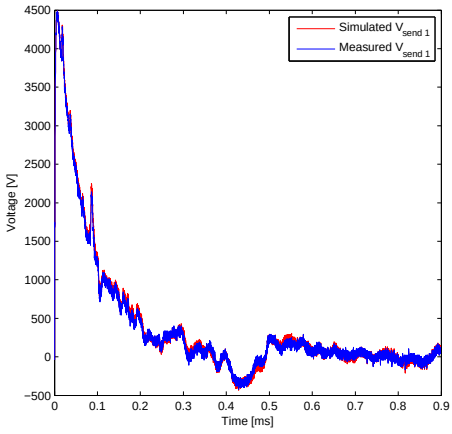

(b) Measured and simulated impulse generator voltage.

Figure 7.33: *Model of the measured impulse and measured results.*

By using identical sending end voltage, the simulated and measured response of the cable can be compared. The simulation model calculates the terminal conditions for each cable by use of the surge admittance and the propagation function. The model uses wave theory with reflections at cable ends and crossbonding points. In order to verify the accuracy of the cable model, the model must first be tuned by use of the sending end current on the energised phase.

7.3.1 Comparison of sending end current for energised phase

As the screens in the setup given in figure 7.12 are grounded at the sending end, the application of the impulse voltage to a cable core conductor will cause a coaxial wave to propagate into the energised phase. The sending end current vector **i** is only dependent on the sending end voltage vector **v** and the

cables characteristic admittance Y_C as shown in equation 7.4, where **Z** and **Y** are the per-unit-length series impedance and shunt admittance of the cable system.

$$\begin{aligned} \mathbf{i} &= Y_C \mathbf{v} \\ Y_C &= Z^{-1}(\mathbf{ZY})^{1/2} \end{aligned} \tag{7.4}$$

Response of first cable section

Until the reflection from the first crossbonding point reaches the sending end, the height of the current wave is only dependent on the high-frequency characteristic admittance and the input voltage. As the input voltage is the same for simulations and field tests, a difference between the curves can be explained by inaccuracies in the characteristic admittance. The sending end current therefore only depends on the cable parameters. This is why the response of the first minor cable section is used for comparison when analysing the accuracy of the series impedances and shunt admittances of the different cable layers.

The total length of the cable is 7625 m. The measured travelling time for the coaxial wave of the energised phase from the sending to the receiving end is 39 μs. The wave velocity is therefore 196 m/μs. The first crossbonding point is at 1709 m. The coaxial wave travelling from the sending end will therefore reach the first crossbonding point after 8.7 μs. The reflected coaxial wave from this first crossbonding point arrives at the measuring point at the sending end after 17.4 μs.

The cable model is very sensitive to cable parameters. The parameters explained in chapter 5.2 use thickness of various layers of the cable. The physical thickness of the cable must therefore be correctly implemented in the model. This thickness can be acquired by various means. In this project, three different approaches have been used in order to show how sensitive the model is to different layer thickness.

- Information from the datasheet given by the cable manufacturer has been used
- The cable supplier, Sagem, has given a test report with measured diameter of the layers for various test samples. Thicknesses of the cable have been obtained by using the average of each layer for the several test samples.
- A 5 cm thick sample of the cable has been used for simulation purposes, where the thickness of each layer is measured directly. As this sample is very small, it does not necessarily represent the whole cable line.

The sending end current of the energised phase for the first 18 μs is shown in figure 7.34, which demonstrates the sensitivity of the cable model to the thickness of different layers. The different thicknesses used are shown in table 7.2.

Layers	Datasheet	Measured diameter	Test report
Conductor diameter	42.9 mm	43 mm	43.2 mm
Inner semiconductor thickness	1.6 mm	1.5 mm	1.3 mm
Isolation thickness	28 mm	31 mm	27 mm
Outer semiconductor thickness	1.5 mm	3 mm	1.12 mm
Wired screen diameter	1.89 mm	2 mm	1.89 mm
Aluminium foils thickness	0.5 mm	0.1 mm	0.5 mm
Outer sheath thickness	5 mm	4 mm	4.3 mm

Table 7.2: *Thickness of cable layers for three different situation. 1-Parameters from the cable datasheet, 2-Parameters measured from a small cable piece and 3-Parameters given in a test report by the manufacturer of the cable.*

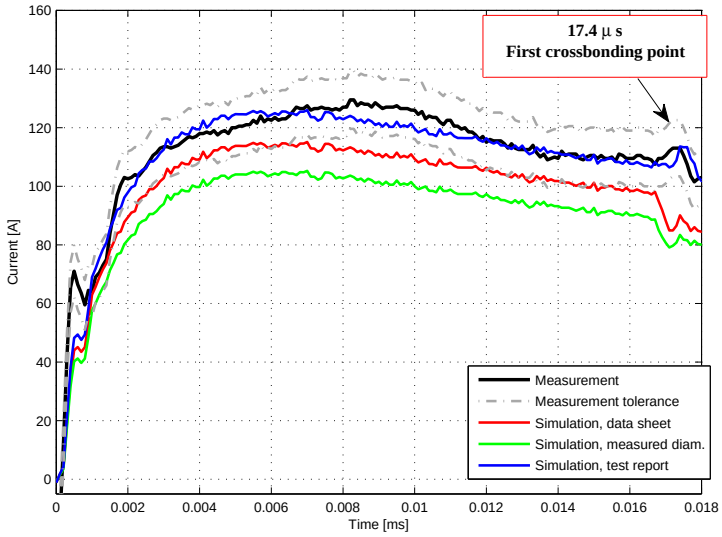

Figure 7.34: *Comparison of the sending end current at the energised phase for the first 18 μs.*

From figure 7.34 it can be seen how simulation using parameters from test report best fit the measurement results from the field test. This was to be expected, as the parameters from the test report are taken for several examples of the cable, while the datasheet contains nominal values for the cable and the measured values are only for one 5 cm example, which does not necessarily represent the whole cable line. This cable line will therefore henceforward be modelled using the physical parameters given in test report by the cable manufacturer.

The second crossbonding point is placed 3407 m from the sending end of the cable. The reflection of the coaxial wave from the second cross bonding point therefore arrives at the sending end after approximately 35 μs. Grounding point is 5119 m from the sending end and the reflected coaxial wave from the grounding point therefore arrives at the sending end after approximately 52 μs. The response of the first major section, formed by two crossbonding points, up to the screen grounding, is shown in figure 7.35.

From simulations it has been observed that the screen current of adjacent cables starts flowing after

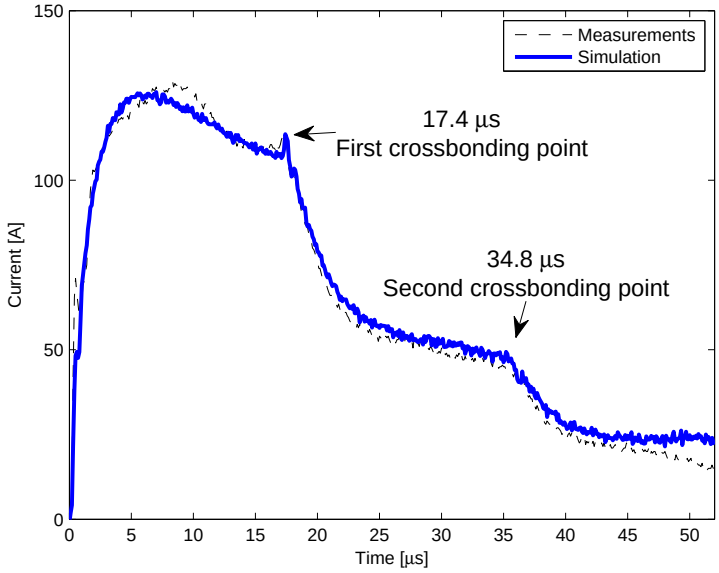

Figure 7.35: *Comparison for the measured and simulated core current at the sending end of the energised phase. Comparison of the first 52 μs, or time including reflections for the first major section.*

48 μs. Before that time it is certain that only the coaxial wave is in the system, as this wave consists of current in conductor returning the screen of the same cable. Therefore before this time, there is no mutual impedance between the conductors and the screen of different phases, between two different screens or from screen to ground and there is only current flowing in the loop core-screen of the energised cable and therefore only the first column of the modal impedance matrix is of importance. The modal impedance matrix, **Z** in equation 7.4 based on equation B.22 is therefore as shown in equation 7.5

$$\begin{bmatrix} Z_{C1} \\ Z_{S1} \\ Z_{C2} \\ Z_{S2} \\ Z_{C3} \\ Z_{S3} \end{bmatrix} = \begin{bmatrix} z_1^1 & -Z_{Sm}^1 & 0 & 0 & 0 & 0 \\ -Z_{Sm}^1 & z_2^1 & 0 & z_{gm12} & 0 & z_{gm13} \\ 0 & 0 & z_1^2 & -Z_{Sm}^2 & 0 & 0 \\ 0 & z_{gm12} & -Z_{Sm}^2 & z_2^2 & 0 & z_{gm23} \\ 0 & 0 & 0 & 0 & z_1^3 & ->_{Sm}^3 \\ 0 & z_{gm13} & 0 & z_{gm23} & -Z_{Sm}^3 & z_2^3 \end{bmatrix} \tag{7.5}$$

$$= \begin{bmatrix} z_1^1 & \dots & \dots & \dots & \dots & \dots \\ -Z_{Sm}^1 & \dots & \dots & \dots & \dots & \dots \\ 0 & \dots & \dots & \dots & \dots & \dots \\ 0 & \dots & \dots & \dots & \dots & \dots \\ 0 & \dots & \dots & \dots & \dots & \dots \\ 0 & \dots & \dots & \dots & \dots & \dots \end{bmatrix}$$

where $z_1^1 = Z_{C_{outer}} + Z_{CS_{insulation}} + Z_{S_{inner}}$ as explained in appendix B.
Z_{Sm}^1 is the mutual impedance between current loops core-screen and screen-ground.

Each element of the total series impedance is calculated from cable parameters. The relation between the cable parameters and the layer impedances is shown in appendix B.1.

When not only the coaxial wave is present the impedance matrix in equation 7.5 becomes more and more complicated, including mutual impedances.

The good agreement observed in figure 7.35 implies that the cable model is quite accurate for coaxial waves and for short cables with no or few crossbondings. It is therefore also accepted that the cable parameters used for the simulations are correct and that the calculated series impedance z_1^i and z_{Sm}^i for only the coaxial mode is correct.

Response of the complete cable length

After the grounding point, there are two more crossbonding points and then the cable end. The reflected coaxial wave from the cable end reaches the sending end after 78 μs. A comparison for the first 90 μs is shown in figure 7.36.

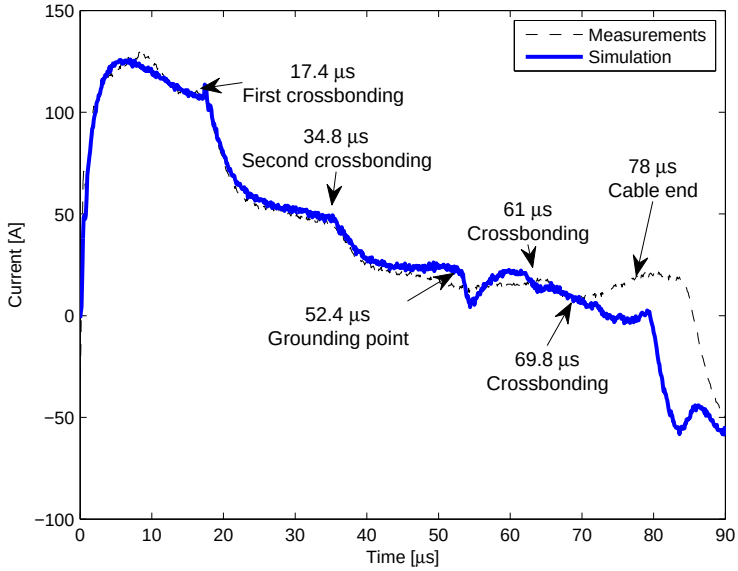

Figure 7.36: *Comparison for the measured and simulated core current at the sending end of the energised phase. Comparison of the first 90 μs, or time including coaxial reflections for the whole cable line.*

It is observed from figure 7.36 that no significant deviation appears before about 48 μs. As this is the time when simulated current in the screen of the adjacent cables start flowing, it is assumed that screen current influences the cable model accuracy. For analysing this suggestion, a modal analysis on the wave propagation is performed.

7.3.2 Wave propagation for disagreement analysis

The sending end current was measured for 900 μs. The comparison of simulations and field test results for the entire measured time of 900 μs is shown in figure 7.37.

It can be seen from figure 7.37 that the simulated current follows the measured current very closely until about 48 μs. After this time, the current waves become more and more out of phase as the current

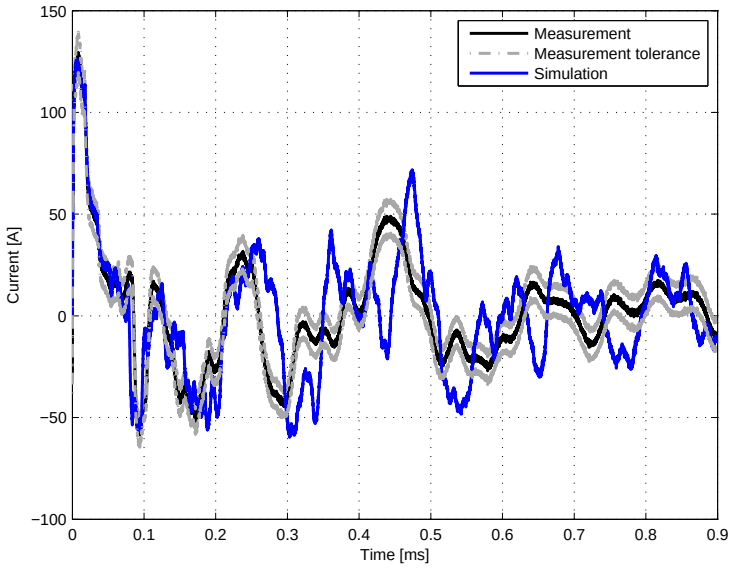

Figure 7.37: *Comparison of the sending end current on the energised phase for the entire measured 900* μs.

becomes affected by more crossbondings, grounding points and reflected waves. It can also be observed how, despite deviation, some similarities between simulations and measurements, where the simulated wave appears to be less damped and delayed. this can be caused by inaccuracies in the real and imaginary parts of the characteristic admittance.

Modal propagation characteristics

In order to evaluate the difference between simulated and measured sending end current, it is practical to have a look at the modal currents and estimate which modes cause the differences. As explained in chapter 2.3, then at high frequencies, the six modes of propagation can be described as three coaxial modes, two intersheath modes and one ground mode. The modal currents can be calculated from the phase currents by use of equation 7.6, where a is the ground mode, b and c are the intersheath modes and d-f are the coaxial modes. The modal current transformation matrix [T] is given by [11].

$$[I_{mode}] = [T]^{-1}[I_{phase}]$$

$$\begin{bmatrix} I_a \\ I_b \\ I_c \\ I_d \\ I_e \\ I_f \end{bmatrix} = \begin{bmatrix} 1 & 1 & 1 & 1 & 1 & 1 \\ 0 & 1/2 & -1/2 & 0 & 1/2 & -1/2 \\ 2/3 & -1/3 & -1/3 & 2/3 & -1/3 & -1/3 \\ 2/3 & -1/3 & -1/3 & 0 & 0 & 0 \\ 0 & 1/2 & -1/2 & 0 & 0 & 0 \\ 1/3 & 1/3 & 1/3 & 0 & 0 & 0 \end{bmatrix} \cdot \begin{bmatrix} I_{C1} \\ I_{C2} \\ I_{C3} \\ I_{Sh1} \\ I_{Sh2} \\ I_{Sh3} \end{bmatrix} \tag{7.6}$$

where $C1 - C3$ represents the core currents of the three cables and
$Sh1 - Sh3$ represents the screen current of the three cables.

In order to calculate the modal currents, the screen currents must be known. The screen currents have not been measured. It is therefore not possible to calculate the modal currents from measurement results. Instead the modal currents are calculated from the simulated phase domain currents. The calculation of modal propagation characteristics is done via the eigendecomposition explained in chapter 2.2, where for each eigenvalue the propagation attenuation $\alpha_i(\omega)$ and phase constant $\beta_i(\omega) = \frac{\omega}{v_i(\omega)}$ for the propagation velocity $v_i(\omega)$, give the propagation characteristics of the wave.

Figure 7.38(a) shows the modal velocities when the modal currents are calculated from simulated phase currents. The increase in the modal velocities is relatively small. Above approximately 10 kHz, all modal velocities become frequency independent. The modal attenuation is shown in figure 7.38(b). At high frequencies the damping is largest for the ground mode, which means that the losses are largest in the ground mode.

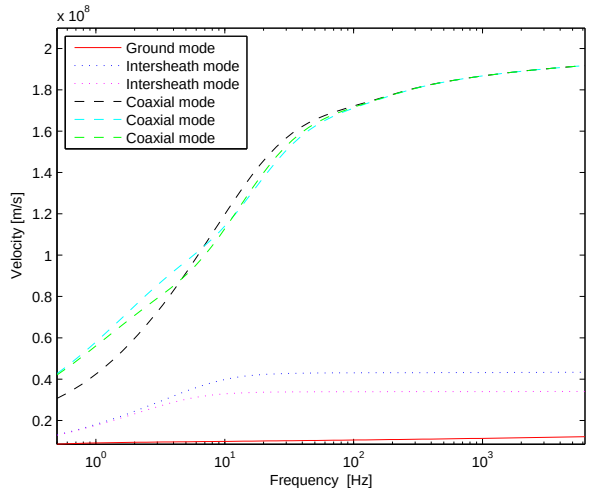

(a) Modal velocities

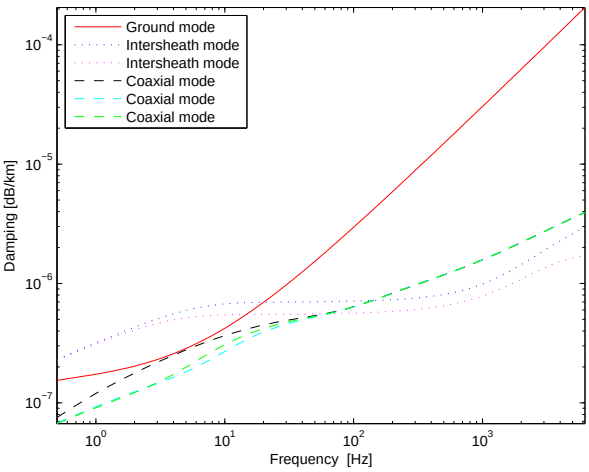

(b) Modal damping

Figure 7.38: *Simulated modal velocity and damping for one cable segment (cable parameters for each segments are identical).*

Modal analysis

The modal velocity is used for the modal analysis in order to estimate which modes cause deviation between simulated current and field measurements. A comparison of the sending end current including coaxial reflections for the whole cable line, or the first 90 μs is used, see figure 7.36. For evaluating the affects of the modes, simulated phase and modal currents, calculated from the phase currents by use of equation 7.6, are plotted in the same time view. The simulated phase currents for each conductor and screen at the cable sending end together with the measured core 1 current are shown in figure 7.39(a). The calculated modal currents are shown in figure 7.39(b).

It was pointed out from figure 7.36 that no significant deviation between simulated and measured sending end current on energised phase appears before about 48 μs. This is when simulated current in the screen of the adjacent cables start flowing. This is supported in figure 7.39 where it can be observed that the sending end current only contains coaxial components until at time $t = 48\ \mu s$. At that point, an intersheath wave arrives at the sending end.

As shown before, the coaxial wave reaches the first crossbonding point at $t = 8.7\ \mu s$. The crossbonding of screens results in a discontinuity in the characteristic admittance matrix and therefore both coaxial waves and intersheath waves are reflected back towards the sending end as well as being transmitted towards the receiving end. According to the measured coaxial velocity of $1.96 \cdot 10^8\ m/s$, then the reflected coaxial wave reaches the sending end after 17.4 μs where it gives the reduction in the sending end current shown starting at point (i) in figure 7.39.

The transmitted part of the coaxial wave, from the first crossbonding point, reaches the second crossbonding at $t = 17.38\ \mu s$, where it becomes again decomposed into reflected and transmitted coaxial and intersheath waves. The reflected coaxial wave meets the first crossbonding point, becomes decomposed into transmitted and reflected coaxial and intersheath waves. This coaxial wave is at the measurement point of the sending end at $t = 34.8\ \mu s$ reducing the sending end current even further, as shown at point (ii) in figure 7.39.

As mentioned before, when the original coaxial wave reaches the first crossbonding point at $t = 8.7\ \mu s$, it becomes decomposed into transmitted and reflected coaxial and intersheath waves. From the intersheath wave velocity in figure 7.38(a), it can be calculated that the reflected intersheath wave reaches the sending end at $t = 48.4\ \mu s$, see equation 7.7. This time fits exactly with point (iii) in figure 7.39, where the intersheath mode is first observed and the screen currents of the adjacent cables.

$$t = t_{coax} + t_{intersheath} = 8.7\mu s + \frac{1709\ \ m}{43\ \ m/\mu s} = 48.4\mu s \tag{7.7}$$

where the time is calculated from the time it takes the coaxial wave to reach the first crossbonding point, and become decomposed, plus the time it takes the intersheath wave to travel from the first crossbonding point to the cable's sending end.

From this time and onwards, deviations develop between the measured and simulated current at the sending end. Before this time, the comparison is close to perfect, which indicates a fundamentally correct model of the cable and crossbonding points, as the reflected coaxial wave does not cause deviation between measurements and simulations. The reason for increased deviation as time passes, is because of increasing number of complicated reflected and transmitted intersheath waves caused by each crossbonding point, the screen grounding and cable ends.

Because deviation first appears when current first is observed in the adjacent screens, it is concluded

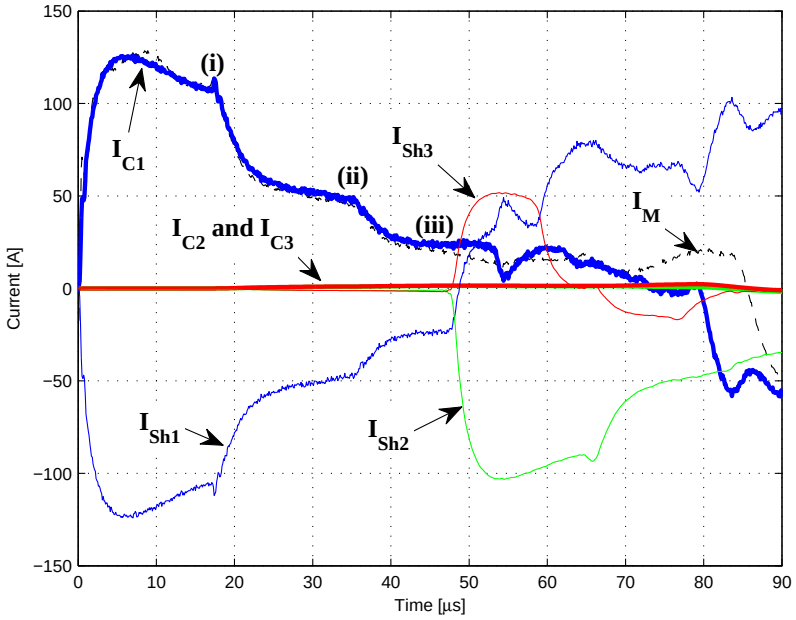

(a) Phase currents

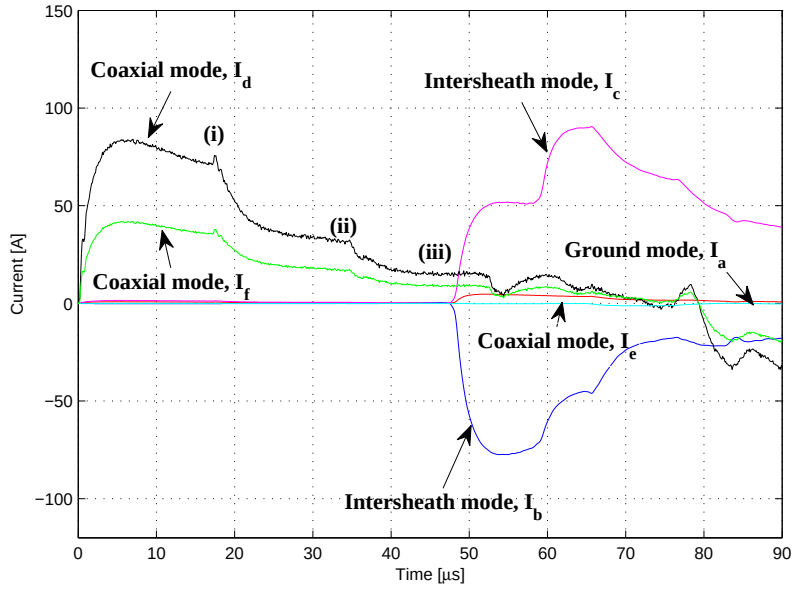

(b) Modal currents

Figure 7.39: *Simulated phase and modal currents plotted in the same time view.* $I_{C1} - I_{C3}$ *are core conductor currents,* $I_{Sh1} - I_{Sh3}$ *are screen currents and* I_M *is the measured core conductor 1 current.*

that the model does not represent the propagation characteristics of the intersheath modes correctly. The propagation characteristics of the intersheath modes are strongly dependent on proximity effects [7]. The

proximity effect is ignored in the simulation software, which could be the cause for the deviation between simulations and field measurements.

The ground mode can also be difficult to simulate accurately and can easily cause deviation between simulations and field measurements. According to modal velocities in figure 7.38(a), the ground mode current will not reach the sending end until after $t = 475\ \mu s$, see equation 7.8. This time is outside the scope of comparison.

$$t = t_{coax} + t_{ground} = 26.2\mu s + \frac{5119\ \ m}{11.4\ \ m/\mu s} = 475\mu s \tag{7.8}$$

where the time is calculated from the time it takes the coaxial wave to reach the grounding point, and become decomposed, plus the time it takes the ground wave to travel from the grounding point to the cable's sending end.

As the cable line is crossbonded, it is not possible to further analyse the measured waves, because of disturbances of decomposed reflections from crossbonding points. Therefore, in order to further validate the intersheath mode as the origin of deviation and in order to improve the cable model, energisation of coaxial and intersheath modes is performed. Because of the findings from analysis of the sending end current and because further measurements are performed for the exact identification of disagreement origin, there is no need for comparison of other measured waveforms of the tested 400 kV cable system.

CHAPTER 8

Field measurement set #2, 150 kV single minor section

The 150 kV cable system is a combination of a 58 km long underground cable and a 42 km long submarine cable, connected with one junction and with a compensating shunt reactor between them, creating a 100 km long HV AC cable line that is operated as a single element. This cable system is for the new offshore wind farm Horns Rev 2 (HR2) commissioned in 2009, which is placed in Western Denmark, see figure 8.1.

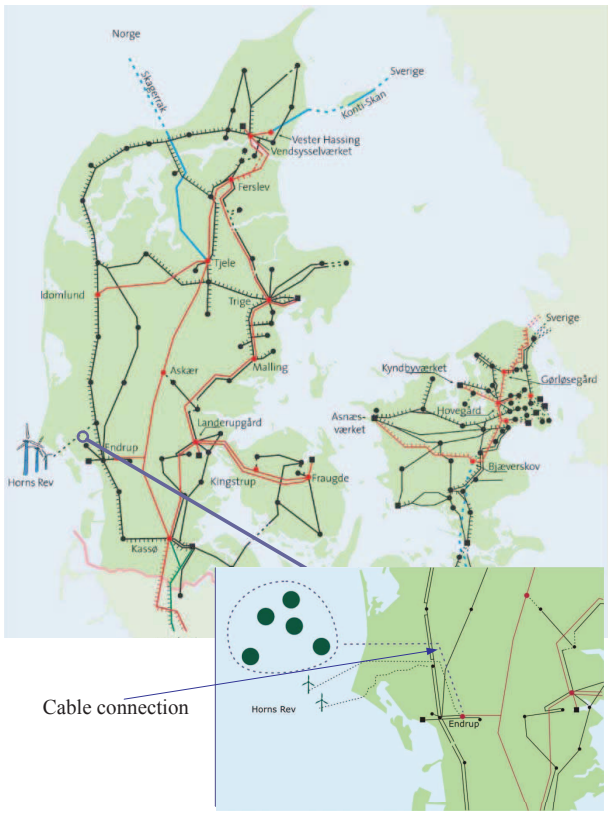

Figure 8.1: *Geographical placement of the HR2 150 kV cable system.*

Analysis of field measurement set #1, chapter 7.3, suggested that the cable model and crossbonding points are accurately modelled, as long as only the coaxial mode propagates in the cable. Inadequate modelling of the intersheath mode is suggested to be the source of deviation between simulations and field test results.

The purpose of the single minor section measurements on the 150 kV cable system, is to verify if the

intersheath mode is a origin of disagreement between measurements and simulations and to find how the cable model should be improved in order to eliminate deviation. Because the single minor section has no crossbonding points, it is possible to directly energise the different propagation modes and gain a better insight in exact origin of disagreement and methods of improving the cable model.

The cable line consists of three cables, one for each phase, with 150 kV single core 1200 mm^2 XLPE cables. The cables are laid in a tight trefoil with the bottom cables at 1.3 m depth, see figure 8.2.

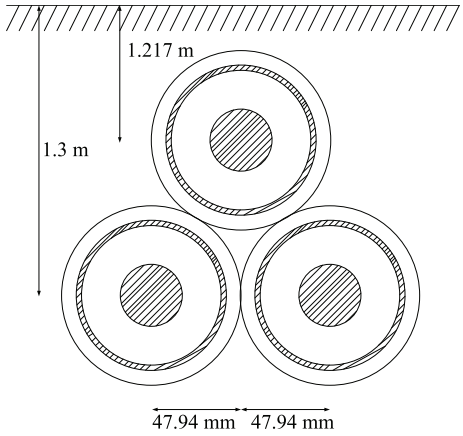

Figure 8.2: *Cross sectional layout for the 150 kV cable system.*

The cable section is 1.78 km long with a cross section shown in figure 8.3. The similarities of this 150 kV cable and the 400 kV cable shown in figure 2.2 on page 8 should be noticed. The number of layers is the same, whereas the wired screen for the 150 kV cable is made of Cu instead of Al. The metallic screen is still made of two conducting materials, the wired screen and an Al laminate. All cable data are given in appendix C.2.

Figure 8.3: *Cross section of the 150 kV underground cable of the HR2 cable system in Western Denmark.*

8.1 Planning field measurement set #2

A simulation setup for the non-crossbonded 150 kV minor cable section is shown in figure 8.4. This simulation cross sectional layout is the same for all measurements on the 150 kV cable; single minor section, single major section and multiple major sections.

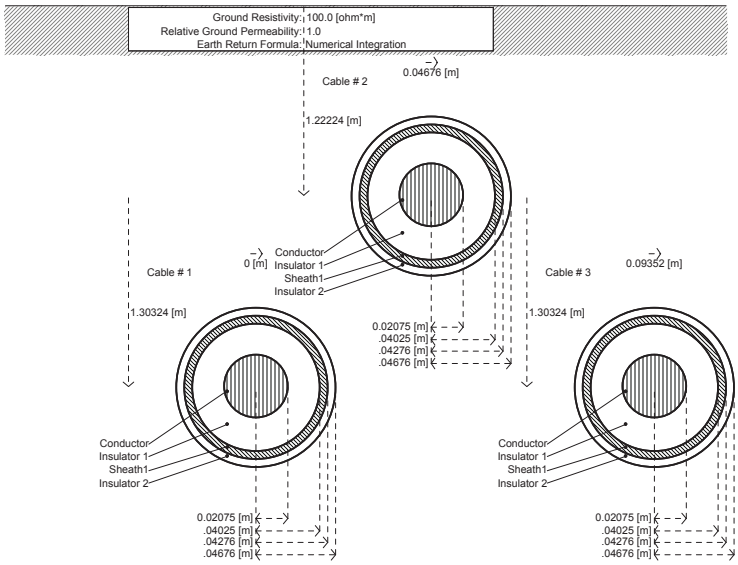

Figure 8.4: *The model segment cross section for the simulation setup of the 150 kV system.*

The single section of the underground 150 kV cable for the offshore HR2 wind farm is 1780 m long. The travelling time, assuming the speed of light, for 1780 m is approximately 5.94 μs. The front time of the impulse is still the dominating shortest time, and therefore the time step should be no larger than 0.12 μs as for the simulated 400 kV cable system.

In order to evaluate the velocity and attenuation of the waves propagating in the cable, it is practical to have a look at the modal currents. At high frequencies, there are six modes of propagation which can be described as three coaxial modes (conductor-screen loop), two intersheath modes (screen-screen loop) and one ground mode (screen-ground loop).

As shown in chapter 7.3.2, at high frequency the velocity of the ground mode for the 400 kV measurements is more than 3 times less than the intersheath mode and more than 17 times less than the coaxial mode. To make sure that there is similar difference in velocities for the 150 kV cable system, figure 8.5 shows the modal velocities of the 150 kV system calculated from the simulated sending end phase currents.

From figure 8.5 it can be seen how at high frequency the ground mode has a velocity more than 4 times less than the intersheath mode and more than 11 times less than the coaxial mode. Because of how slow the ground mode travels, only the coaxial and intersheath modes are tested in the field, as the ground mode return will not reach the sending end before after several hundreds of μs which is outside the scope of the high frequency comparison in this thesis.

The aim for the single minor section measurements on the 150 kV cable system, is to directly energise

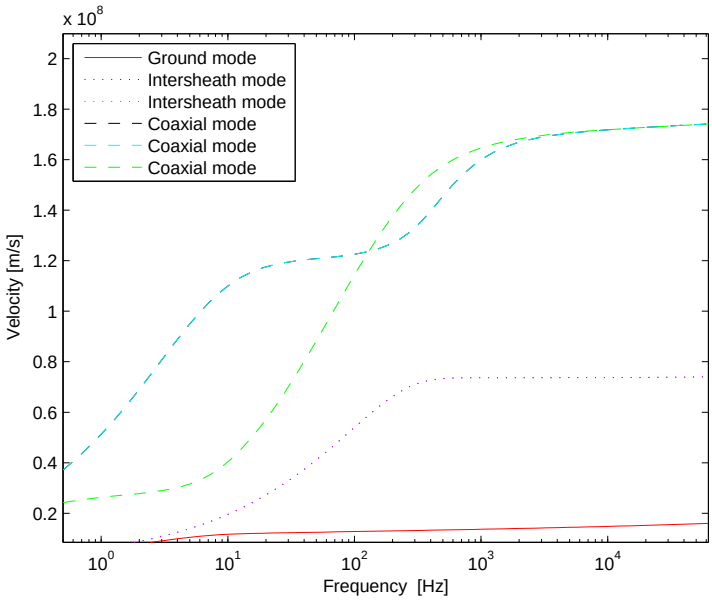

Figure 8.5: *Simulated modal velocity for the single minor section of the measured 150 kV cable system.*

the different propagation modes and gain a better insight in exact origin of disagreement and methods of improving the cable model. The principal test layout for the coaxial mode and intersheath mode setups are shown in figure 8.6.

As explained in chapter 2.3, for the coaxial mode, the current flows in the core conductor and fully returns in the screen of the same phase and for one of the intersheath modes, the current flows in one screen and fully returns in the screen of an adjacent cable. This is verified, for the simulation setups shown in figure 8.6. Figure 8.7(a) shows the simulation results for the coaxial mode excitation. Here the current in the core conductor and the reciprocal of the current in the screen at the sending end of the excited cable are compared. As the two currents are identical, when all other sending end currents are zero, all the current flowing in the core conductor is returning in the screen of the same phase and the measurements setup can be used to purely excite a coaxial mode. Furthermore, it is interesting to observe, because there is no current in adjacent cables, no flux exists outside of the excited cable. For this case, proximity effect because of the tight trefoil layout can therefore be neglected when comparing simulated and measured values.

As the only current path is through the conductor with return in the screen of the same cable, for high frequencies, as for an impulse, there is no current flowing in other conductors or the ground. The modal impedance matrix, from equation 2.14, can be simplified as shown in equation 8.1, when only one cable is excited.

$$\begin{bmatrix} V_{CS1} \\ V_{SG1} \\ V_{CS2} \\ V_{SG2} \\ V_{CS2} \\ V_{SG2} \end{bmatrix} = \begin{bmatrix} Z_1^1 & \dots & \dots & \dots & \dots & \dots \\ -Z_{Sm}^1 & \dots & \dots & \dots & \dots & \dots \\ 0 & \dots & \dots & \dots & \dots & \dots \\ 0 & \dots & \dots & \dots & \dots & \dots \\ 0 & \dots & \dots & \dots & \dots & \dots \\ 0 & \dots & \dots & \dots & \dots & \dots \end{bmatrix} \cdot \begin{bmatrix} I_{CS1} \\ 0 \\ 0 \\ 0 \\ 0 \\ 0 \end{bmatrix} \tag{8.1}$$

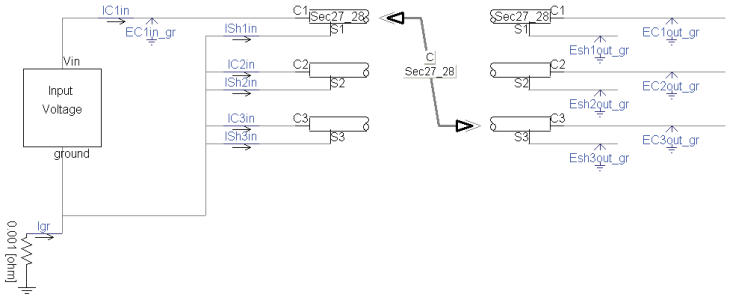

(a) Excitation of the coaxial mode.

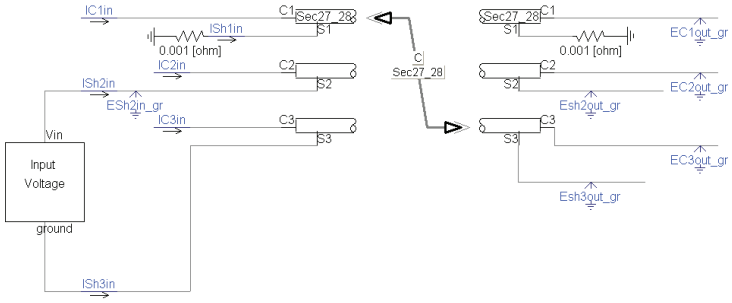

(b) Excitation of the intersheath mode.

Figure 8.6: *Simulation layout for excitation of the coaxial and intersheath modes when measuring on a single minor section of the 150 kV cable system.*

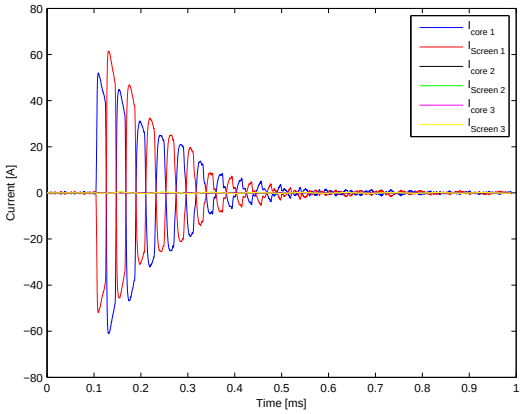

(a) Comparison of simulated currents at the sending end of the cable, for excitation of a coaxial mode.

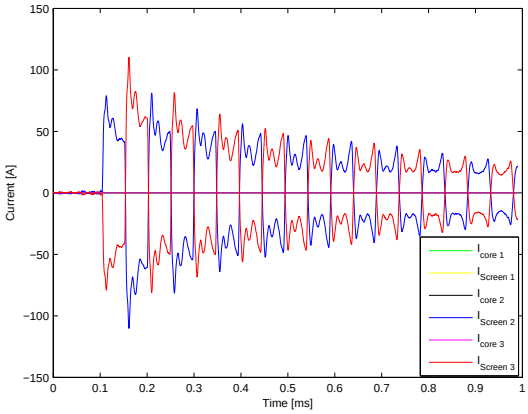

(b) Comparison of simulated currents at the sending end of the cable, for excitation of an intersheath mode.

Figure 8.7: *Current for the sending end when exciting the coaxial and the intersheath modes respectively. This validates the described current loops for the two modes.*

where Z_x^1 denotes an impedance of cable 1.
V_{CSi} and V_{SGi} are cable i conductor-screen and screen-ground loop voltages respectively.
I_{CS1} is the conductor-screen loop current of cable 1.

Therefore by exciting a coaxial mode with an impulse, the only cable impedances of interest are the screen mutual impedance, Z_{Sm}, given in appendix B.1.6 and Z_1 which has been defined in the literature [14, 46, 47] and is shown here in equation 8.2.

$$Z_1 = z_{c_{outer}} + z_{cs_{insul}} + z_{s_{inner}} \tag{8.2}$$

where $z_{c_{outer}}$ is given in appendix B.1.1.
$z_{cs_{insul}}$ is given in appendix B.1.2.
$z_{s_{inner}}$ is given in appendix B.1.3.

Figure 8.7(b) shows the simulation results for the intersheath mode excitation. Here the currents in screen 2 and the reciprocal of the current in screen 3 at the sending end of the excited cables are identical. Therefore all the current flowing in screen 2 is returning in screen 3, with all other sending end currents equal to zero, and the setup of figure 8.6(b) can be used to purely excite an intersheath mode. This is the case at high frequencies, as for fast front impulse excitation. At lower frequencies, the current might penetrate into the ground around the three cables and this would therefore not be a pure excitation of only the intersheath mode.

When the current path is exclusively through screen of one cable, with return in the screen of an adjacent cable, the modal voltage-current relationship can be simplified as shown in equation 8.3.

$$\begin{bmatrix} V_{CS1} \\ V_{SG1} \\ V_{CS2} \\ V_{SG2} \\ V_{CS2} \\ V_{SG2} \end{bmatrix} = \begin{bmatrix} \dots & \dots & \dots & 0 & \dots & 0 \\ \dots & \dots & \dots & Z_{gm12} & \dots & Z_{gm13} \\ \dots & \dots & \dots & -Z_{Sm}^2 & \dots & 0 \\ \dots & \dots & \dots & Z_2^2 & \dots & Z_{gm23} \\ \dots & \dots & \dots & 0 & \dots & -Z_{Sm}^3 \\ \dots & \dots & \dots & Z_{gm23} & \dots & Z_2^3 \end{bmatrix} \cdot \begin{bmatrix} 0 \\ 0 \\ 0 \\ I_{SG2} \\ 0 \\ I_{SG3} \end{bmatrix} \tag{8.3}$$

where Z_{gmij} denotes the mutual earth impedance between cables i and j.
I_{SG2} and I_{SG3} are the screen-ground loop currents of cables 2 and 3 respectively.

By exciting an intersheath mode, with an impulse, the only cable impedances of interest are the screen mutual impedance Z_{Sm}, the mutual earth impedance, Z_{gmij}, given in equation B.21 from appendix B.2 and Z_2 which has been defined in the literature [14, 46, 47] and is shown here in equation 8.4.

$$Z_2 = z_{s_{outer}} + z_{sg_{insul}} + z_{ground} \tag{8.4}$$

where $z_{s_{outer}}$ is given in appendix B.1.4.
$z_{sg_{insul}}$ is given in appendix B.1.5.
z_{ground} is given in appendix B.1.7.

Furthermore, as the current of screen 2 is fully returned in screen 3, then $I_{SG3} = -I_{SG2}$, and if $Z_{gm12} = Z_{gm13} = Z_{gm23}$, then equation 8.3 reduces to equation 8.5.

$$\begin{bmatrix} V_{CS1} \\ V_{SG1} \\ V_{CS2} \\ V_{SG2} \\ V_{CS2} \\ V_{SG2} \end{bmatrix} = \begin{bmatrix} 0 \\ 0 \\ -Z_{Sm}^2 I_{SG2} \\ Z_2^2 I_{SG2} - Z_{gm23} I_{SG2} \\ Z_{Sm}^3 I_{SG2} \\ Z_{gm23} I_{SG2} - Z_2^3 I_{SG2} \end{bmatrix} \tag{8.5}$$

For the intersheath mode, the earth return impedance therefore has an impact on the results. This is as expected, as the current path is from screen of one cable with return in screen of another cable, when the two screens have no direct electrical connection.

The three cables are identical, and Z_1 is therefore identical for all three cables. Same applies for Z_2 and Z_{Sm}. Equation 8.6 therefore applies for the intersheath mode.

$$\begin{aligned} V_{CS2} &= -V_{CS3} = -Z_{Sm} I_{SG2} \\ V_{SG2} &= -V_{SG3} = Z_2 I_{SG2} - Z_{Sm} I_{SG2} \end{aligned} \tag{8.6}$$

By exciting only the coaxial and intersheath modes of propagation, it is possible to evaluate the accuracy for separate impedance parts of the full cable impedance matrix in equation 2.8. As the cables are identical and in a thight trefoil, the different cable impedances for each phase are assumed identical.

8.1.1 Simulation results, excitation of coaxial mode

The sending end core voltage and core current for the excited phase, as well as receiving end voltages on all core and screen conductors are of interest to be used as a validation template for the cable model. The simulation results for the sending end voltage and current is shown in figure 8.8 on the following page.

The results in figure 8.8(a) show the applied impulse. The front and half time of this impulse is identical to simulations for the 400 kV measurements, as the same impulse generator for the field measurements will be used. Here the amplitude is 1.6 kV. The reflections from the receiving end can be clearly seen in the form of the sending end impulse voltage.

The results in figure 8.8(b) show the sending end current of the excited core. The reflections from the receiving end can also be clearly seen in the simulated current, as for the voltage. Comparing the time of the reflections, it can be observed that, as expected, reflections appear at exact same time for both sending end voltage and current.

The simulation results for the receiving end voltages are shown in figure 8.9 on the next page.

Figure 8.9 shows the simulated core voltage transients for the energised phase. The amplitude of this voltage is double the sending end voltage. This agrees with the theory of an open ended cable, where the reflected wave will have the double amplitude, the incident wave plus the reflected one [48].

The first peak is measured approximately 10 μs after the simulated impulse is applied. For the cable length of 1780 m, this simulates the travelling time of the voltage wave as close to the speed of light, or

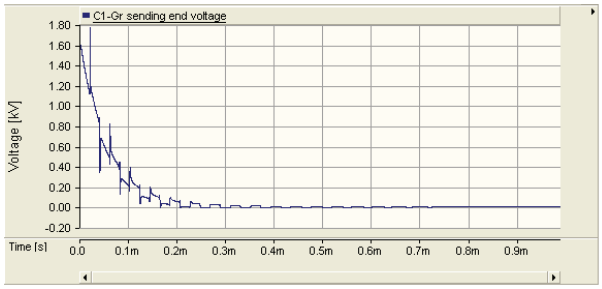

(a) Core voltage at the sending end of the excited cable.

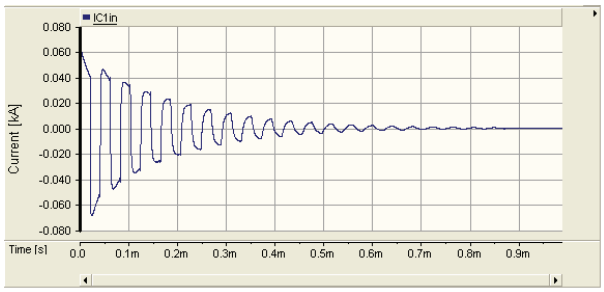

(b) Core current at the sending end of the excited cable.

Figure 8.8: *Simulation results from EMTDC/PSCAD when exciting a coaxial mode of the 150 kV minor section cable. The simulation setup is shown in figure 8.6(a).*

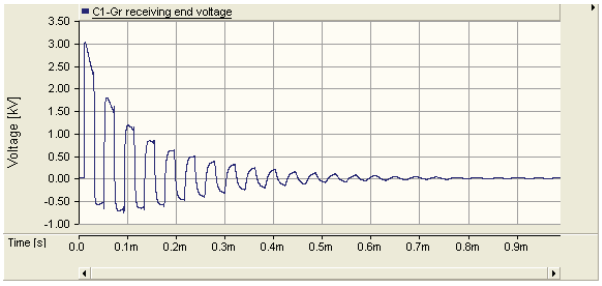

(a) Core voltage at the receiving end of the excited cable.

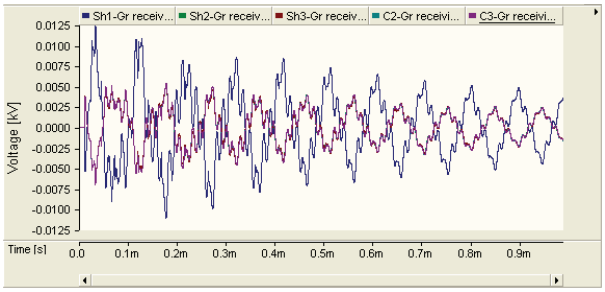

(b) Other voltages at the receiving end of the cable line.

Figure 8.9: *Receiving end simulation results from EMTDC/PSCAD when exciting a coaxial mode.*

$1.78 \cdot 10^8$ m/s. Furthermore, the reflections from the sending end, can be observed in the receiving end

voltage.

Figure 8.9(b) shows the simulated transients in the core voltages of the non-energised phases and all screen voltages. These voltages are induced transients, because of the impulse in the energised phase. The amplitude of the induced screen voltage of the energised phase is somewhat larger than voltages of other phases. This is also to be expected, as the current returns through this screen, which is separated from the energised core with much less insulation than all other conductors. The induced voltages on all other conductors are identical. This is to be expected, as the cables are laid in a tight trefoil. The amplitude of all induced voltages are small compared to the energised phase and for the cable model validation procedure in this thesis, the adjacent, non-energised phases are not further considered.

As for the simulation results of the 400 kV cable, the given impulse for excitation has enough energy in order to give measurable results. This is as to be expected, as the 400 kV cable system is much longer and more complicated than the single minor section setup.

8.1.2 Simulation results, excitation of intersheath mode

The sending end screen voltage and current for the excited screen, as well as receiving end core voltages on all cores and the screen voltages on the excited screens are of interest to be used as a validation template for the cable model. The simulation results for the sending end voltage and current on the excited screen (screen 2) are shown in figure 8.10.

As for the excitation of the coaxial wave, the reflections from the sending end can clearly be seen in the applied impulse. The applied impulse is 2 kV, between screen 2 and screen 3, the screen 2-ground impulse is therefore 1 kV as shown in figure 8.10(a).

The simulation results for the receiving end voltages are shown in figure 8.11.

As the screens at the receiving end are open ended, the simulated receiving end voltage are identical for both core and screen (which are separated by the cables capacitance) and double the sending end voltage. The screen of the adjacent cable (phase 1) is grounded in both ends and the simulated voltage of the conductor of phase 1 is close to zero or only approximately 10 mV.

The simulated impulse voltage has enough energy in order to give measurable results for a field test in the same manner as these simulations.

From the above description, the field measurements on the single minor section of the 150 kV cable system are planned and the results compared.

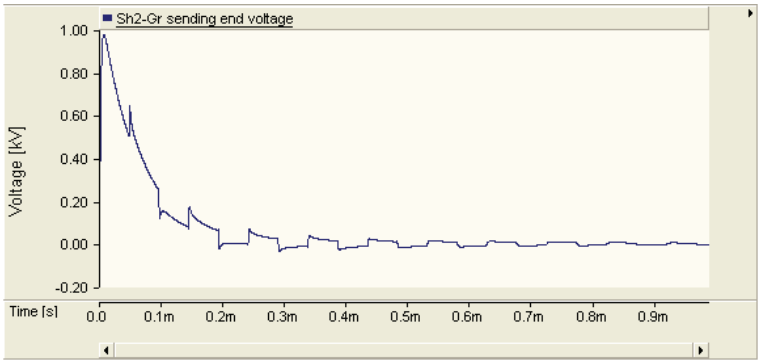

(a) Screen voltage at the sending end of the excited cable.

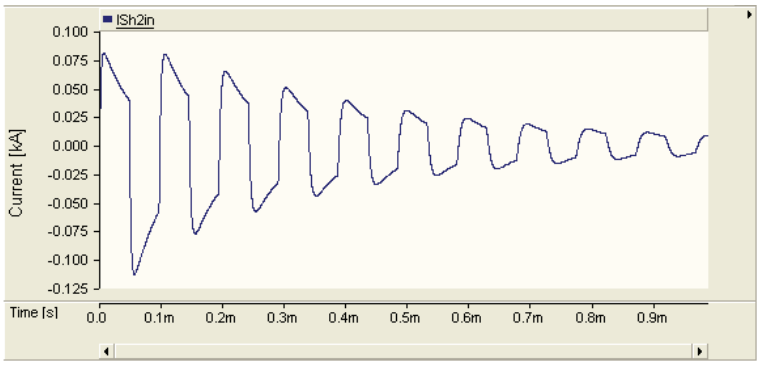

(b) Screen current at the sending end of the excited cable.

Figure 8.10: *Simulation results from EMTDC/PSCAD when exciting an intersheath mode of the 150 kV minor section cable. The simulation setup is shown in figure 8.6(b).*

8.2 Performing field measurement set #2

The field measurements are planned and prepared with simulations. As explained in chapter 8.1, the coaxial and intersheath modes of propagation are excited, based on figure 8.6.

8.2.1 Field test setup

During the installation of the land and sea cables of the HR2 cable system, there was a unique opportunity of performing various tests on different segments of the land cable before they were connected with a junction. This made it possible to test the cable parameters for a short cable segment with no cross-bonding points and directly excite the coaxial and intersheath modes. Measurements on such a single minor section were performed on an open cable end out in the field.

As the cable had not been installed in a substation and the end finished, with accessible terminals, it was neccesary to prepare the open ends by stripping them and ensuring possibility for proper electrical access to core and screen conductors. Such preparation of open cable ends is shown in figure 8.12 on page 92.

The core conductor is stripped and at least 5 cm are kept bare, for easy access. An electrical connection to the core conductor is achieved via a hose around the conductor.

For ensuring a proper electrical connection to the aluminium foil, small cuts are made in order to turn

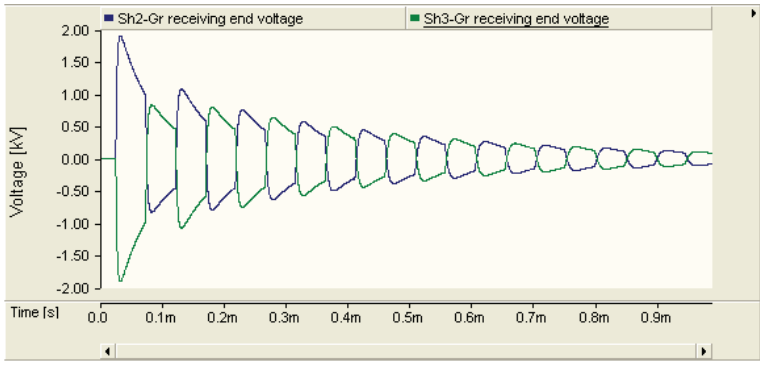

(a) Screen voltages at the receiving end of the excited cables.

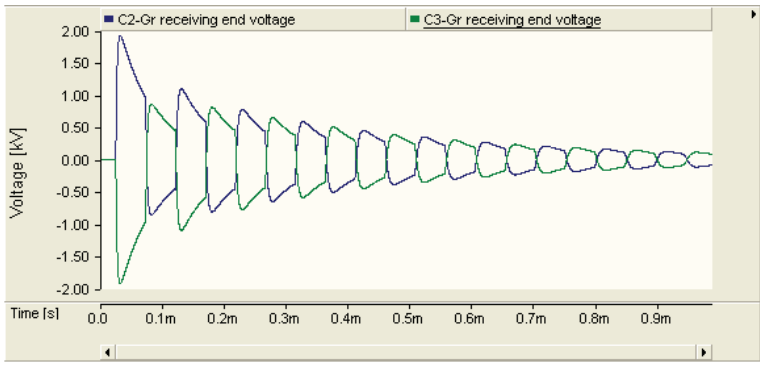

(b) Core voltages at the receiving end of the excited cables.

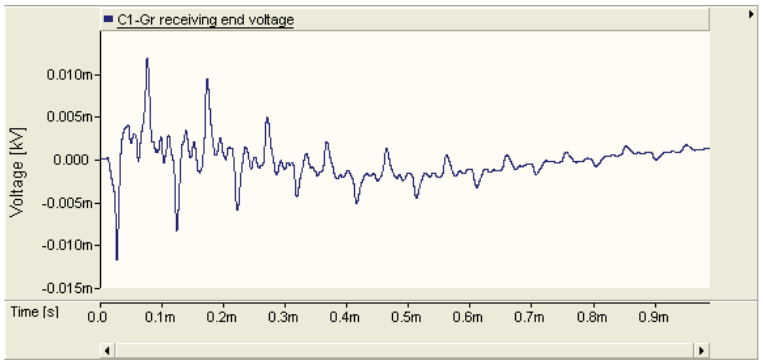

(c) Core voltage at the receiving end of the non-excited cable.

Figure 8.11: *Simulation results from EMTDC/PSCAD when exciting an intersheath mode of the 150 kV minor section cable. The simulation setup is shown in figure 8.6(b).*

it upside down. Before this is done, a thin semiconductive substance is scraped of the outer insulation, to ensure no connection between screen and ground. A hose is put around the aluminium foil and wired screen. The two parts of the screen are then connected together and to the measuring point.

Coaxial mode test

The field test setup for excitation of the coaxial mode is shown in figure 8.13 on the next page.

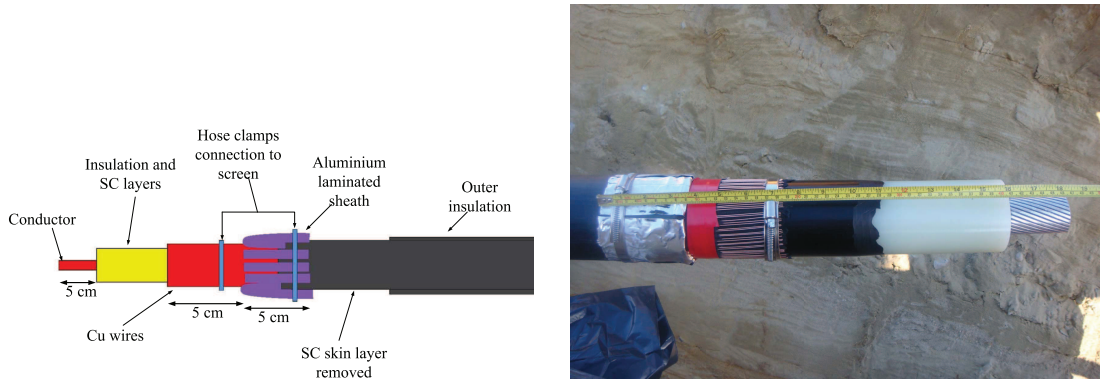

(a) A schematic for cable end stripping instructions.

(b) The prepared cable open end.

Figure 8.12: *Open cable end during installation, before connection of junction.*

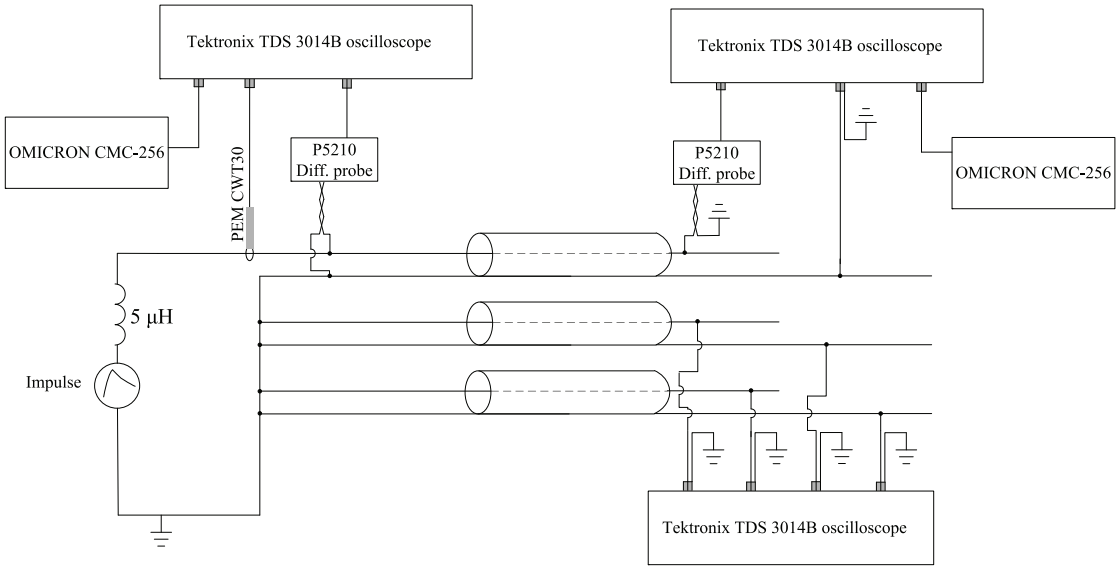

Figure 8.13: *Measurement setup for the field tests of the coaxial mode. A fast front impulse generator is used for excitation.*

All receiving end core and screen conductor voltages were measured, as well as the sending end voltage and excited core conductor current.

The impulse generator was connected to the HV cable by use of a 5m long 300 mm^2 Cu wire. The inductance in such a wire is estemated as 1 μH per meter. The wire is therefore represented by a 5 μH inductance connected in series to the surge generator.

Measurements at sending and receiving ends are synchronised in the same way as was done for field measurement set #1, described in chapters 7.2.1 and 7.2.2.

Intersheath mode test

The field test setup for excitation of the intersheath mode is shown in figure 8.14.

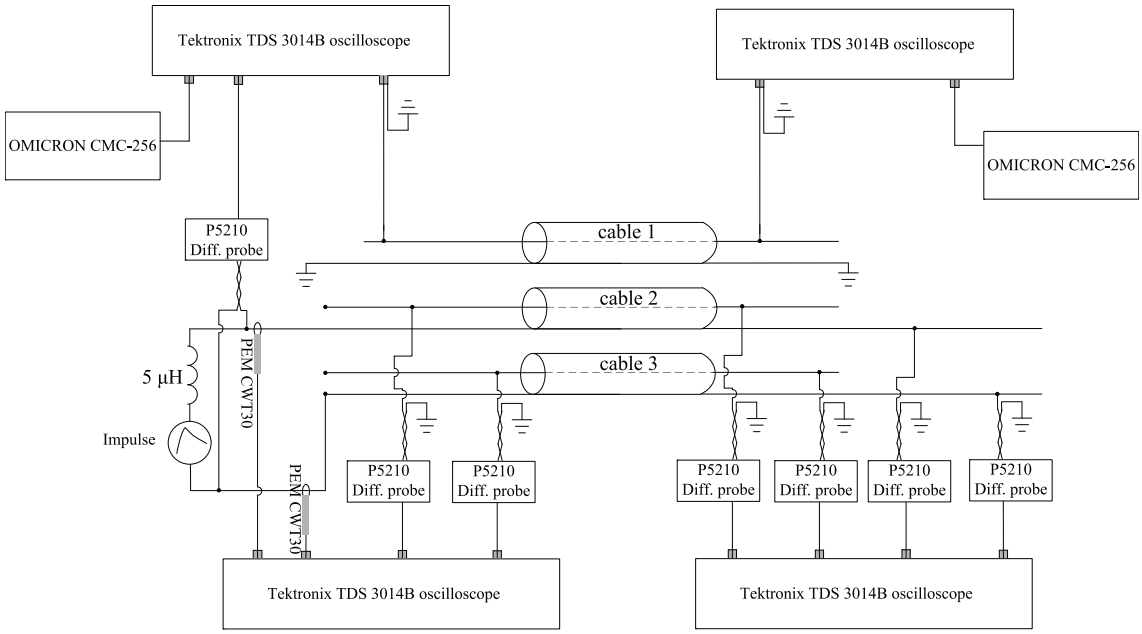

Figure 8.14: *Measurement setup for the field tests of the intersheath mode. A fast front impulse generator is used for excitation.*

Core conductor voltages at both sending and receiving end, screen voltages of cables 2 and 3 at both sending and receiving end and screen currents of cables 2 and 3 at sending end were measured.

Measurements at sending and receiving ends are synchronised in the same way as was done for field measurement set #1, described in chapters 7.2.1 and 7.2.2.

8.2.2 Instruments

The generator used is the same HAEFELY PC6-288.1 surge tester as described in chapter 7.2.2 for field measurement set #1. For excitation of the coaxial mode, a 1.4 kV impulse is used and for excitation of the intersheath mode a 2 kV impulse is used. These impulses correspond to a sampling frequency range of app. 8 MHz.

As the excitation of both coaxial and intersheath modes use the same input impulse as for field test measurement set #1, all the same instruments are used; identical Tektronix TDS 3014B oscilloscopes with sampling frequency of 10 MHz and Tektronix P5210 voltage probes with an input limit of 5.6 kV. The two field measurement sets, #1 and #2, use different current probes. Here PEM CWT30 R, shown in figure 8.15, is used.

The measuring range of the CWT is 30 mA to 6 kA with a 16 MHz bandwidth. The output signal from the current probe is a voltage signal which is fed into the oscilloscobes.

Figure 8.15: *CWT current probe, to be used for the cable measurements.*

8.2.3 Measuring accuracy

The field measurements were performed on a new cable line out in the open field. There were no surrounding OHL nearby the transmission cables or other electrical disturbances of any kind. Therefore, there was no surrounding noise and filtering of results unneccesary.

The accuracy for the current probe is $\pm 1\%$ [49]. The overall equipment accuracy is calculated as explained on page 59-60 in chapter 7.2.3. The results for all of the warranted characteristics are given in table 8.1 on the facing page.

8.2.4 Measurement results

Coaxial mode results

Field test results for excitation of the coaxial mode are shown in figure 8.16 on page 96.

As for the simulation results in chapter 8.1.1, the sending end impulse voltage is distorted because of reflections from the receiving end. These reflections also dominate in the waveform of the sending end current in figure 8.16(b).

The receiving end voltage of the excited core, is twice as large as the sending end voltage. This is caused by the open ended terminal at the receiving end, where the wave will double at the point of reflection.

When comparing voltages at sending and receiving end, the travelling time of the coaxial wave is observed as being 10 μs for the 1780 m long cable section. This results in measured coaxial wave traveling velocity of $1.78 \cdot 10^8$ m/s, which is identical to the simulated travelling time given on page 8.1.1.

Excitation of coaxial mode				
Measurement	**Probe setting**	**Probe accuracy**	**Oscilloscope setting**	**Oscilloscope accuracy**
Sending voltage	1000x	$\pm 3\%$	200 V/div	$\pm[0.02 \cdot \lvert\text{reading } \pm 3\% \text{ of reading}\rvert + 0.0656 \text{ V}]$
Sending current	2mV/A	$\pm 1\%$	40 mV/div	$\pm[0.02 \cdot \lvert\text{reading } \pm 1\% \text{ of reading}\rvert + 0.0245 \text{ V}]$
Receiving end voltage V_{C1}	1000x	$\pm 3\%$	1 kV/div	$\pm[0.02 \cdot \lvert\text{reading} \pm 3\% \text{ of reading}\rvert + 0.2656 \text{ V}]$
Receiving end voltage V_{C2}	–	–	2 V/div	$\pm[0.02 \cdot \lvert\text{reading }\rvert + 0.7 \text{ V}]$
Receiving end voltage V_{C3}	–	–	1 V/div	$\pm[0.02 \cdot \lvert\text{reading}\rvert + 0.2656 \text{ V}]$
Receiving end voltage V_{Sh1}	–	–	1 V/div	$\pm[0.02 \cdot \lvert\text{reading }\rvert + 0.2656 \text{ V}]$
Receiving end voltage V_{Sh2}	–	–	1 V/div	$\pm[0.02 \cdot \lvert\text{reading }\rvert + 0.2656 \text{ V}]$
Receiving end voltage V_{Sh3}	–	–	1 V/div	$\pm[0.02 \cdot \lvert\text{reading }\rvert + 0.2656 \text{ V}]$

Excitation of intersheath mode				
Measurement	**Probe setting**	**Probe accuracy**	**Oscilloscope setting**	**Oscilloscope accuracy**
Sending end voltage V_{C1}	–	–	10 mV/div	$\pm[0.02 \cdot \lvert\text{reading}\rvert + 0.0046 \text{ V}]$
Sending end voltage V_{C2}, V_{Sh2}, V_{C3} and V_{Sh3}	1000x	$\pm 3\%$	200 V/div	$\pm[0.02 \cdot \lvert\text{reading} \pm 3\% \text{ of reading}\rvert + 0.0656 \text{ V}]$
Sending current I_{Sh2} and I_{Sh3}	2mV/A	$\pm 1\%$	40 mV/div	$\pm[0.02 \cdot \lvert\text{reading } \pm 1\% \text{ of reading}\rvert + 0.0245 \text{ V}]$
Receiving end voltage V_{C1}	–	–	20 mV/div	$\pm[0.02 \cdot \lvert\text{reading}\rvert + 0.0071 \text{ V}]$
Receiving end voltage V_{C2}, V_{Sh2}, V_{C3} and V_{Sh3}	1000x	$\pm 3\%$	200 V/div	$\pm[0.02 \cdot \lvert\text{reading} \pm 3\% \text{ of reading}\rvert + 0.0656 \text{ V}]$

Table 8.1: *Table showing warranted characteristics for all measuring instruments for the field measurements of setup #2.*

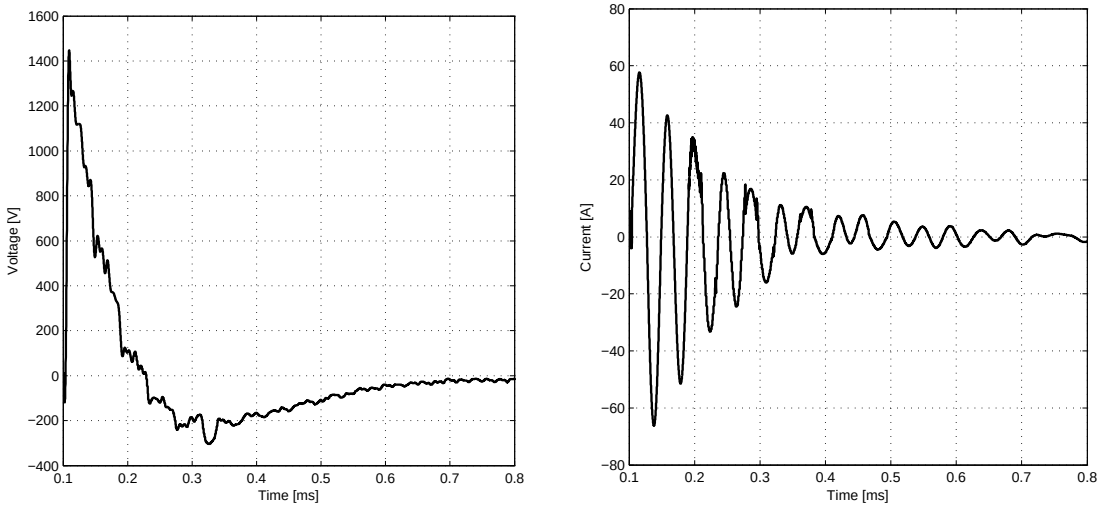

(a) Sending end voltage, energised core conductor

(b) Sending end current, energised core conductor

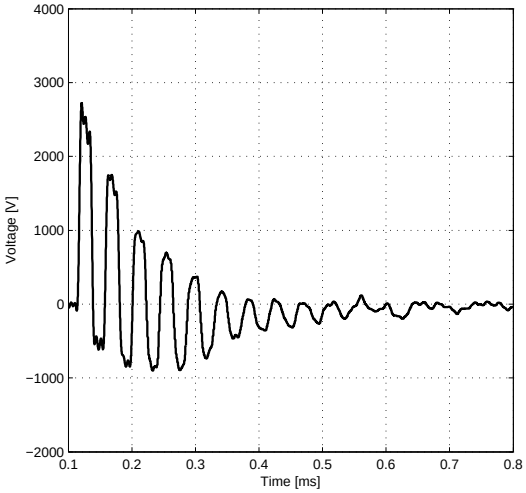

(c) Receiving end voltage, energised core conductor

Figure 8.16: *Field test results for excitation of the coaxial mode, field measurement setup #2.*

Intersheath mode results

Field test results for the sending end, when exciting the intersheath mode, are shown in figures 8.17 and 8.18. The measured voltages of the receiving end are shown in figure 8.19.

The applied impulse is 2 kV, between screen 2 and screen 3, the screen 2-ground impulse is therefore 1 kV and the screen 3-ground impulse is -1 kV, as shown in figures 8.17(a) and 8.17(b) respectively. It is also clear from figures 8.17 and 8.19 how for energised cables terminated in an open end, with core open in both ends, the core conductor voltage becomes identical to the screen conductor voltage. This is due to the fact that there is no closed current path and only a capacitor seperates each core conductor from the energised screen conductor.

As expected for an open terminated cable, the receiving end voltage amplitude is twice as large as the sending end voltage amplitude. Furthermore as shown by simulations in chapter 8.1.2, the induced

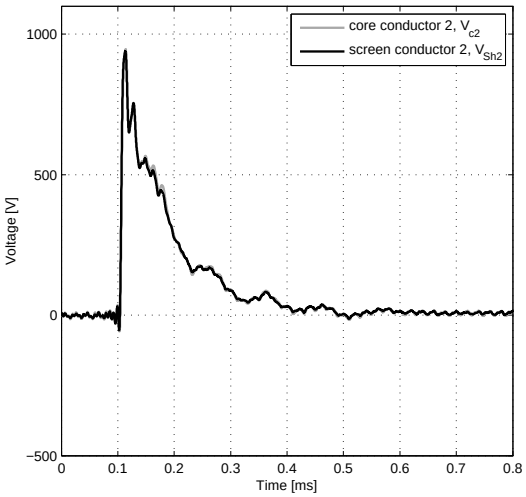

(a) Sending end voltage, screen and core conductors cable 2, V_{sh2} and V_{c2} respectively

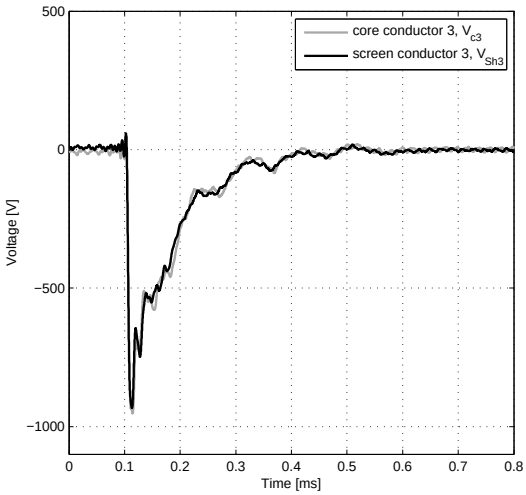

(b) Sending end voltage, screen and core conductors cable 3, V_{sh3} and V_{c3} respectively

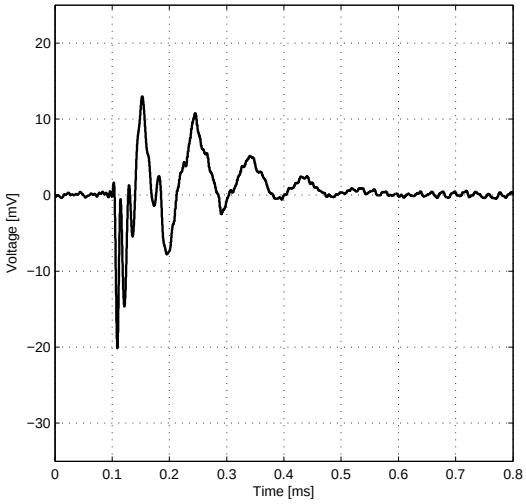

(c) Sending end voltage, induced voltage on core conductor cable 1

Figure 8.17: *Field test results for measured voltages on the sending end, when exciting the intersheath mode, field measurement setup #2.*

voltage on cable 1 is close to zero. This induced voltage has such a small value, that it is not used for model validation, as validation of the cable model focuses on the energised cables.

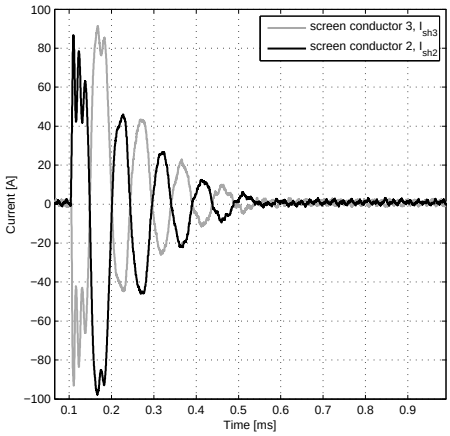

Figure 8.18: *Field test measured currents on the sending end, when exciting the intersheath mode.*

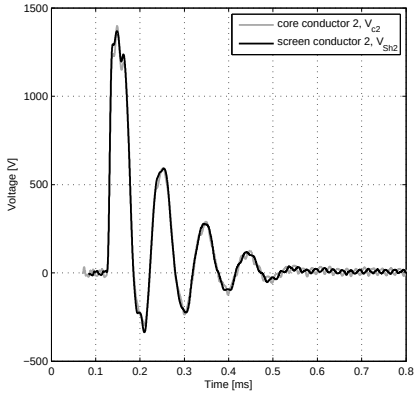

(a) Receiving end voltage, screen and core conductors cable 2, V_{sh2} and V_{c2} respectively

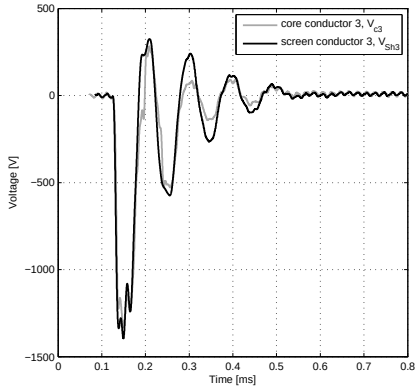

(b) Receiving end voltage, screen and core conductors cable 3, V_{sh3} and V_{c3} respectively

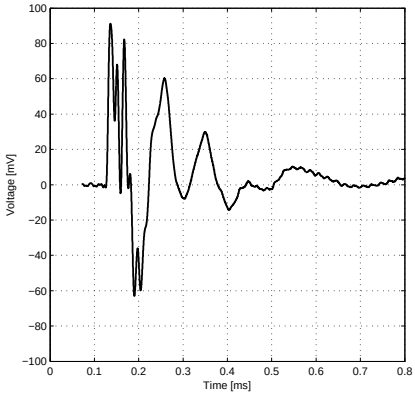

(c) Receiving end voltage, induced voltage on core conductor cable 1

Figure 8.19: *Field test measured voltages on the receiving end, when exciting the intersheath mode.*

When comparing voltages at sending and receiving end, the travelling time of the intersheath wave is observed as being 23.8 μs for the 1780 m long cable section. This results in intersheath wave traveling velocity of $7.48 \cdot 10^7$ m/s, which is 2 times less than the measured coaxial mode velocity. Further analysis of this is given in chapter 8.3.

8.3 Analysing field measurement set #2

The purpose of field measurements set #2, is to verify if the intersheath mode is a origin of disagreement between measurements and simulations, as suggested from analysing the results of field measurements set #1. Furthermore the purpose is to find how the cable model should be improved in order to eliminate deviation.

For the validation the simulation model described in chapter 8.1 is used. In order to simulate the behaviour of the cable as close to results from field tests as possible, the excitation voltage of the energised phase used as an input to the simulation model must be identical for measurements and simulations. As for field measurement set #1 this is obtained by creating a voltage source from field measurements. The impulse used is measured in the test and the results used for the simulation model. This is done by constructing a component that retrieves data from the measured impulse and feeds that into a source. This source is then used to energise in the simulation model. As for fieald measurement set #1, then it is validated that the traveling time of measured and simulated signals is the same.

8.3.1 Excitation of coaxial mode

The excitation causes a coaxial wave to propagate into the energised cable. As there are no crossbonding points, there are only coaxial modes being reflected back and forth between the cable ends while decaying to zero. This is validated in figure 8.20, where the simulated modal currents for the cable are plotted as a function of time.

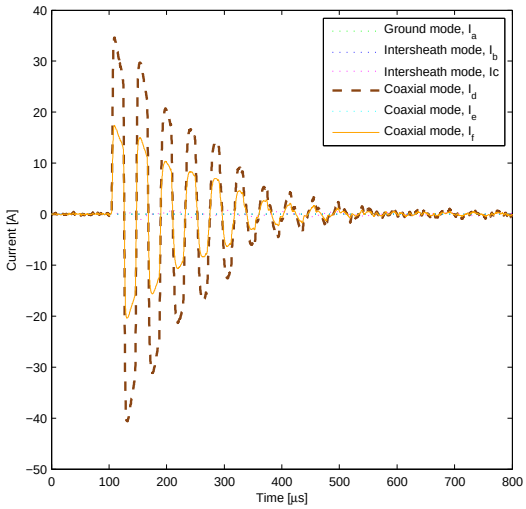

Figure 8.20: *Simulated modal currents for the coaxial mode field test setup.*

The propagation velocity and attenuation for the two non-zero coaxial modes in figure 8.20 are given in

figure 8.21, where at 1 MHz the damping is $1.05 \cdot 10^{-4}$ dB/km and the velocity is $1.78 \cdot 10^{8}$ m/s. This velocity is the same as calculated for field measurement results, given on page 94.

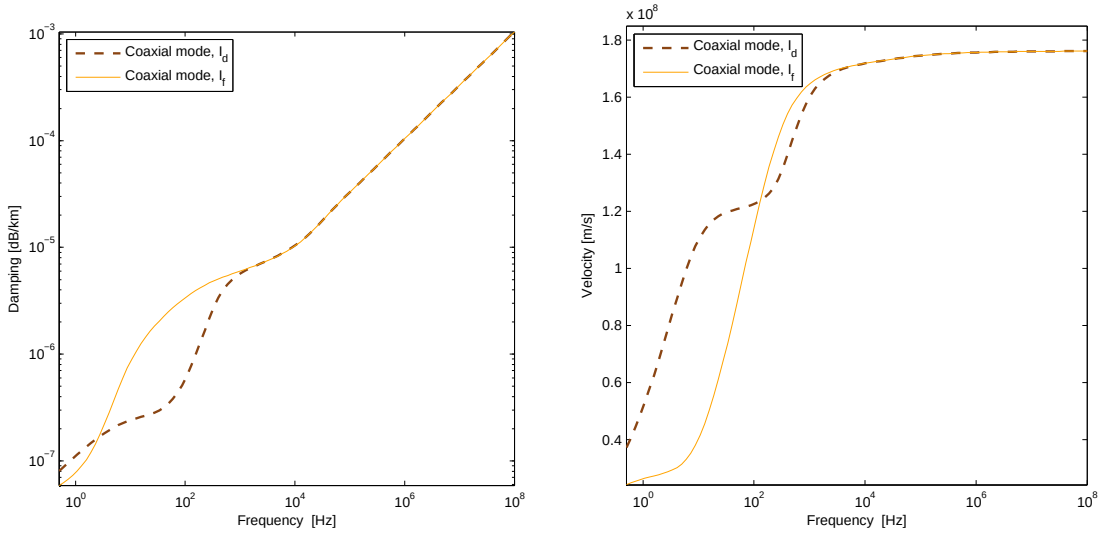

(a) Damping (b) Velocity

Figure 8.21: *Propagation damping and velocity for the two non-zero coaxial modes of figure 8.20.*

As shown for simulations and measurement, relevant waves for model validation are the receiving end core voltage and the sending end core conductor current of the excited phase. The measured sending end excited core conductor voltage is used as an input to the simulation model, and is therefore already identical for measurements and simulations.

The sending end current and receiving end voltage, as a function of frequency, is calculated by use of equation 8.7 (also given in chapter 2.1).

$$\begin{aligned} I_{\text{sending}} &= Y_c \cdot V_{\text{sending}} - H \cdot \left(Y_c \cdot V_{\text{receiving}} - I_{\text{receiving}}\right) \\ V_{\text{receiving}} &= \tfrac{1}{Y_c} \cdot I_{\text{receiving}} + H \cdot \left(V_{\text{sending}} + \tfrac{1}{Y_c} \cdot I_{\text{sending}}\right) \end{aligned} \tag{8.7}$$

where $Y_c(\omega) = \left(\frac{Y(\omega)}{Z(\omega)}\right)^{1/2}$

$H = e^{-(Y(\omega)Z(\omega))^{1/2}l}$

$I_{receiving} = 0$ for this measurement setup.

For identical comparison, the only cable impedances of interest are the screen mutual impedance, Z_{Sm}, given in appendix B.1.6 and Z_1 explained in equation 8.2.

Comparison of field measurements and simulations of coaxial mode values for the energised phase are given in figures 8.22(a) and 8.22(b). All relevant cable data for the simulations are given in appendix C.2.

From figure 8.22 it can be seen how the amplitude and phase of both the simulated current and voltage agree with the field test measurements for the entire measured time interval. This suggests that the

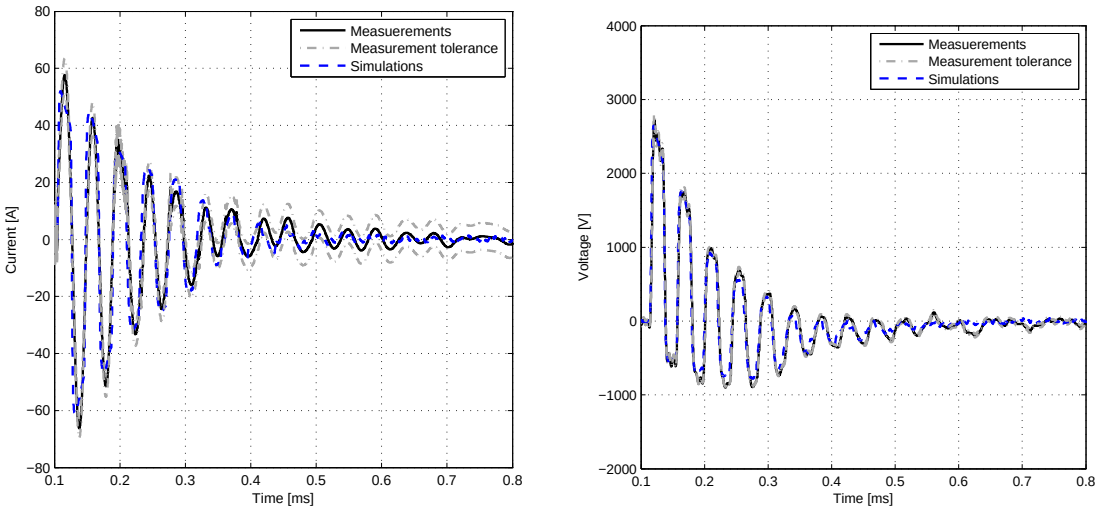

(a) Sending end current

(b) Receiving end voltage

Figure 8.22: *Comparison of the sending end current and receiving end voltage on energised core conductor for the coaxial mode.*

calculation of sending end current and the receiving end voltage in the simulation software is correct when only the inner loop of the cable is excited.

As shown in equation 8.2 the only series impedances influencing the resutls for the coaxial mode are $z_{C_{outer}}$, $z_{CS_{insul}}$, $z_{S_{inner}}$ and Z_{Sm}. From the very good agreement in figure 8.22, it can be concluded that the model calculations of these 4 impedances are accurate and correct. This is not very surprising, as the model is frequency dependent, there is no flux outside of the excited cable. For this case, proximity effect because of the tight trefoil layout can therefore be neglected. Furthermore, the model has already been validated for coaxial waves in chapter 7.3, for a different type of HV AC cable.

8.3.2 Excitation of intersheath mode

The excitation causes a pure intersheath wave to propagate into screen 2 and back in screen 3. As there are no crossbonding points, there are only coaxial modes being reflected back and forth between the cable ends while decaying to zero. This is validated in figure 8.20, where the simulated modal currents for the cable are plotted as a function of time. In the figure, all modes are equal to zero except for the excited intersheath mode.

The propagation velocity and attenuation for the non-zero intersheath mode is given in figure 8.24, where at 1 MHz the damping is $1.18 \cdot 10^{-4}$ dB/km and the velocity is $7.43 \cdot 10^{7}$ m/s.

As shown for simulations and measurement, relevant waves for model validation are the core conductor voltages for cable 2 and 3 at both sending and receiving end, screen voltages of cables 2 and 3 at both sending and receiving end and screen currents of cables 2 and 3 at sending end. Both simulations and field measurement results give identical voltages for core and screen. Furthermore the sending end currents are identical in opposite directions. Therefore, only currents and voltages of cable 2 are used for model validation. As for the coaxial mode, the measured sending end excited screen conductor voltage is used as an input to the simulation model, and is therefore already identical for measurements and sim-

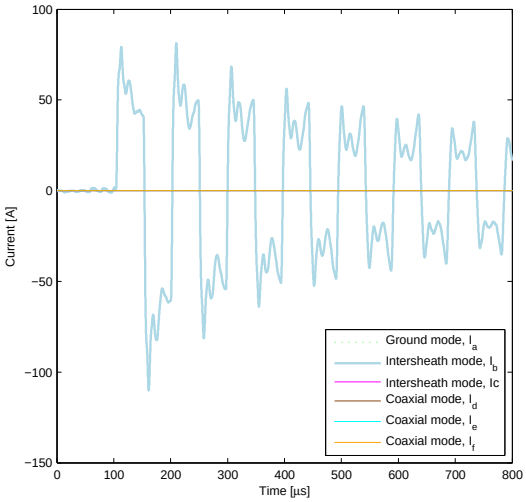

Figure 8.23: *Simulated modal currents for the intersheath mode field test setup.*

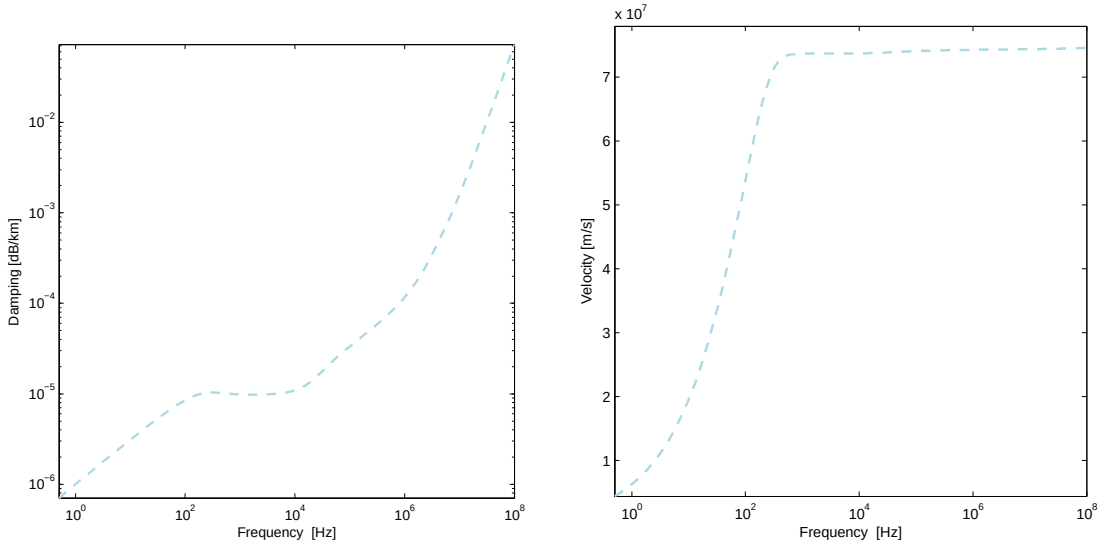

(a) Damping (b) Velocity

Figure 8.24: *Propagation damping and velocity for the non-zero intersheath mode of figure 8.23.*

ulations.

For identical comparison of the intersheath mode results, the only cable impedances of interest are the screen mutual impedance, Z_{Sm}, given in appendix B.1.6 and x_2 explained in equation 8.4. Z_{Sm} has already been validated as correctly calculated by the coaxial mode setup.

Comparison of field measurements and simulations of intersheath mode values are given in figures 8.25(a) and 8.25(b). All relevant cable data for the simulations are given in appendix C.2.

As shown in figure 8.25 there is a considerable difference between simulations and field test results when

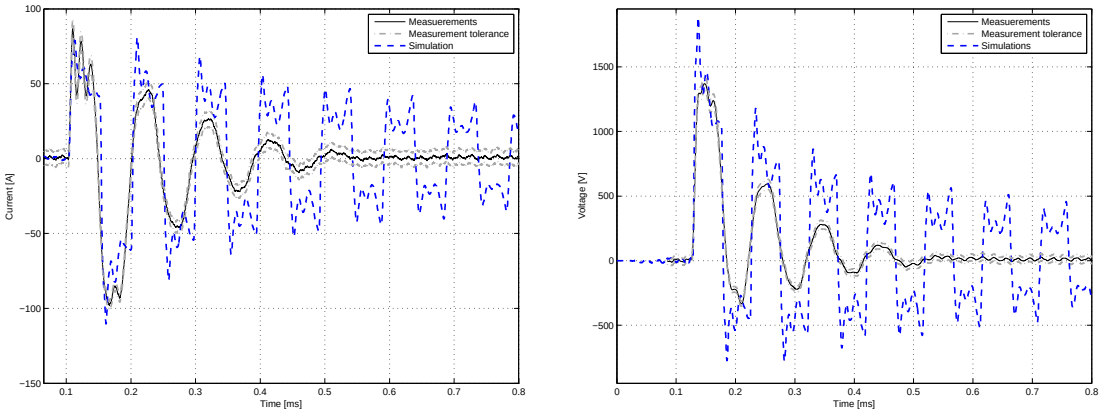

(a) Sending end current

(b) Receiving end voltage

Figure 8.25: *Comparison of the sending end current and receiving end voltage on energised screen conductor for the intersheath mode.*

the intersheath mode of the HV cable is excited. The velocity of the measured intersheath wave is given as $7.48 \cdot 10^7$ m/s on page 99. From figure 8.24(b), the simulated velocity is $7.43 \cdot 10^7$ m/s. The simmulated velocity therefore differs from the measured velocity by only 0.67%. This is also validated in figure 8.25, as the simulations agree quite well with measurements regarding the time delay.

The period for the measured reflections in figure 8.25 is 95 μs. The frequency of the reflections is therefore approximately 10.5 kHz. The damping for this frequency of the measured waves is app. times 0.59 while the simulated damping of figure 8.24(a) is $1.1 \cdot 10^{-5}$ dB/km or $3.9 \cdot 10^{-5}$ dB for twice the cable length (to include the reflected wave measured at the sending end). This equals a damping of times 0.99996 instead of times 0.59. Furthermore when comparing measurements and simulation results in figure 8.25, it is obvious that the propagation damping is incorrectly simulated. In addition, higher frequency damping is incorrect in the simulations, as can be seen by the non-damped high frequency oscillations. As the velocity of the simulated currents agree with the field test measurements for the entire measured time interval, while the amplitude does not agree, the real part of the propagation constant is correct while the imaginary part is not. This suggests that the shunt admittance calculations in the simulation software are correct, while the resistivity is incorrect. For the intersheath setup the resistivity is purely from the screen layers.

The propagation characteristics of an intersheath mode is strongly affected by the physical layout of the cable screen and the actual current distribution thereof. Wrong propagation characterstics affect the correctness of the calculations of z_{souter}, $z_{sginsul}$ and z_{ground}.

Incorrect current distribution is strongly affected by proximity affect [7]. There are two reasons for this. First of all, for the intersheath mode, the current flows in two adjacent screens as shown in figure 8.26. For higher frequencies, 10 kHz and above, the proximty effect causes the current distribution in the screens to be more concentrated where the two cables are close to each other, rather than where they are further apart. This again increases the series impedance of the cable.

Second of all, the actual screen is a stranded conductor, which results in proximity affect within the wires of each cable screen, which also changes the series impedance of the cable, especially at very high frequencies.

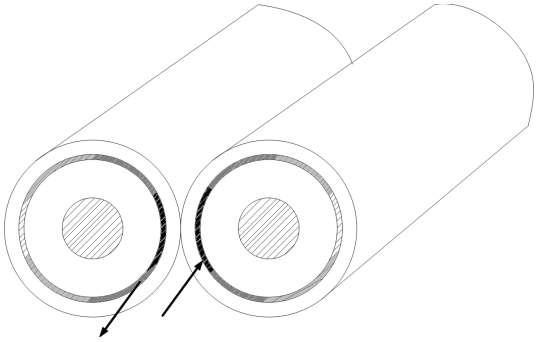

Figure 8.26: *Intersheath mode current distribution in two adjacent screens, because of proximity affect at higher frequencies. Darker colour of the screen indicates more concentrated current distribution.*

The physical layout of the cable also can affect the simulation results. A photo of the cable, is shown in figure 8.27.

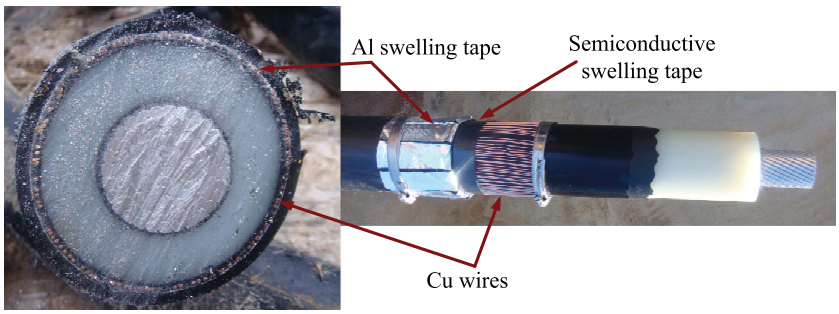

Figure 8.27: *The 150 kV single core 1200 mm^2 XLPE cable. The screen is constructed from Cu wires and Al foil with a semiconductive swelling tape in between.*

From figure 8.27 it can be seen how the cable's screen is not only formed by stranded Cu conductors but also an Al foil with a thin semiconductive swelling tape in between. This layout property is common in more recent underground XLPE cables, where the two conducting screen layers are either of same material or different as for the cable in this chapter. It should be noted, that because of the lower resistivity of Cu than Al, most of the current will flow in the wired layer and not in the Al foil.

The aim for field measurement set # 2 is to gain a better insight in exact origin of disagreement and methods of improving the cable model. The origin of disagreement has been proven to be incorrect simulation of propagation of intersheath waves. As showed in chapter 7, then for longer cables, the presence of crossbonding points causes excitation of intersheath waves. The large deviations shown in figure 8.25 will therefore affect the high frequency accuracy and the simulation model is insufficient for crossbonded cable systems.

CHAPTER 9

Field measurement set #3, 150 kV single major section

The purpose of the single major section measurements on the 150 kV cable system, is for validation. These measurements are performed on the same cable line as field measurement set #2 in chapter 8, where no crossbondings are included. Here there are two crossbonding points but no grounding of the screen. From the analysis in chapter 8.3, two improvements are suggested, simulating the correct physical layout of the cable's screen more accurately and including proximity effect in the calculations. These improvements will be discussed in chapters 12-13. In this part of field measurements, the setup and results of measurements for validating the implemented model improvements are described. These measurements will be used in chapter 14.

The cable setup and layout is the same as in chapter 8. For this field measurement set #3, there are 2 crossbonding points and the length of the cable is divided as shown in figure 9.1.

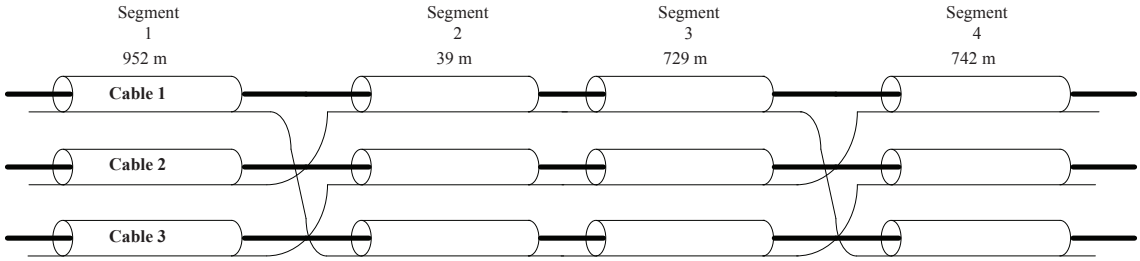

Figure 9.1: *Cross bonding schematic for the cable part of the 150 kV cable line in Western Jutland, used for field test setup #3.*

9.1 Planning field measurement set #3

The cable parameters are the same as used in chapter 8 and the simulation setup for the non-crossbonded 150 kV minor cable section is shown in figure 8.4. The principal test layout in EMTDC/PSCAD is shown in figure 9.2. The fast front impulse is used to excite one phase of the cable, where all screens are grounded at both ends. This should minimize the current flowing in the ground, making it possible to focus on the cable model without external disturbances. The sending end impulse voltage is simulated as showed in figure 7.6.

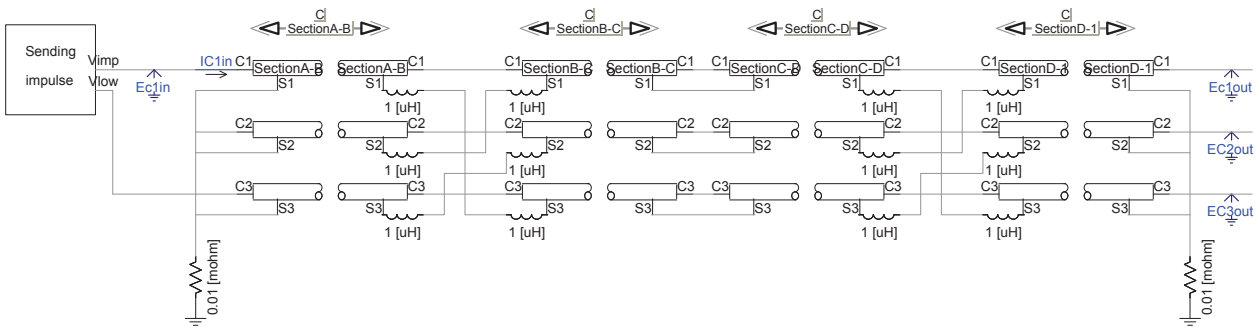

Figure 9.2: *A simulation model for planning the field test measurement setup for one major segment of the cable.*

9.1.1 Simulation results

The sending end core voltage and core current for the excited phase, as well as receiving end voltages on all core conductors are of interest to be used as a validation template for the improved cable model. The simulation results for the sending end voltage and current is shown in figure 9.3.

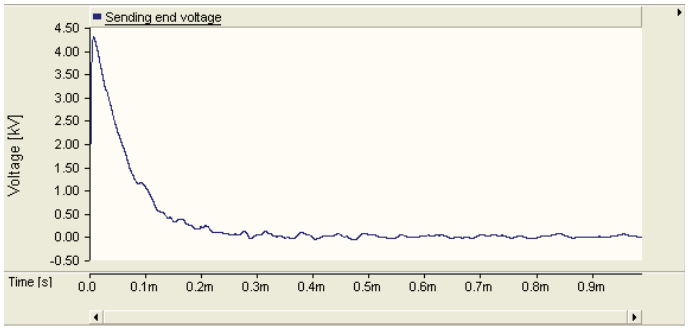

(a) Core voltage at the sending end of the excited cable.

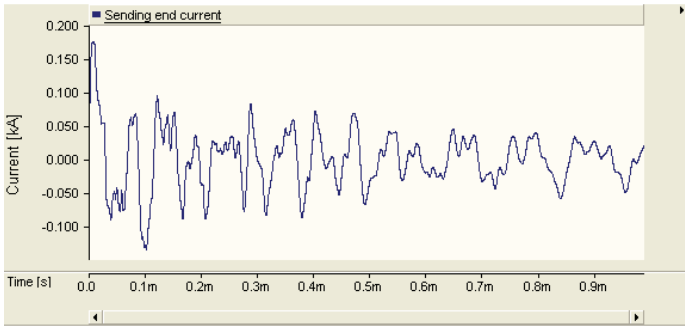

(b) Core current at the sending end of the excited cable.

Figure 9.3: *Simulation results from EMTDC/PSCAD for the simulation setup is shown in figure 9.2. Sending end excited phase.*

The results in figure 9.3(a) show the applied impulse. The front and half time of this simulated impulse is based on the impulse generator to be used for the field measurements. Here the amplitude is 4.25 kV. The

results in figure 9.3(b) show the sending end current of the excited core. The form of the current wave is similar to field measurement set # 1 in chapter 7, i.e. distorted by many reflections from crossbonding points and cable end.

The simulation results for the receiving end voltages are shown in figure 9.4.

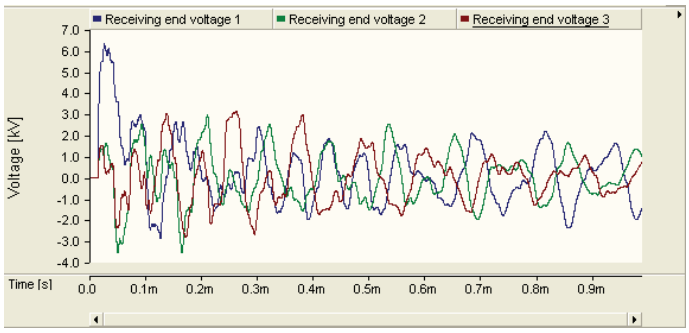

Figure 9.4: *Simulation results from EMTDC/PSCAD for the simulation setup is shown in figure 9.2. Receiving end voltages.*

The amplitude of the receiving end voltage of phase 1 is only 1.5 times larger than the sending end voltage and not 2 times larger as would be expected by an open ended cable. This is caused by the crossbonding points. At every crossbonding, the wave is divided into reflected and transmitted, resulting in a small deduction of the transmitted wave amplitude.

9.2 Performing field measurement set #3

Based on the simulations, the field measurements on the single major section of the 150 kV cable system are planned and the results used for improved model validation.

9.2.1 Field test setup

As for field test setup #2, the measurements on the single major section were performed during cable installation. The sending end was open, as described in chapter 8.2.1, while the receiving end was terminated in a GIS breaker unit, connecting the cable to the centre placed shunt reactor of the whole cable line. The GIS breaker is shown in figure 9.5.

The earthing switch and the principal in the connection is shown in figure 9.6.

For electrical connection to the cable cores, an earthing switch of the breaker was disasembled. Each of the cable's core conductors are, inside the GIS unit, connected to a rod and each rod is connected with a switch to a grounding bar. By removing the connection of the rods to the grounding bar, it was possible to have a direct (non-earthed) connection to the cable's core conductors.

The field test setup for single major section measurements is shown in figure 9.7. This setup is based on the simulation layout in figure 9.2.

All receiving end core conductor voltages were measured, as well as the sending end voltage and excited core conductor current.

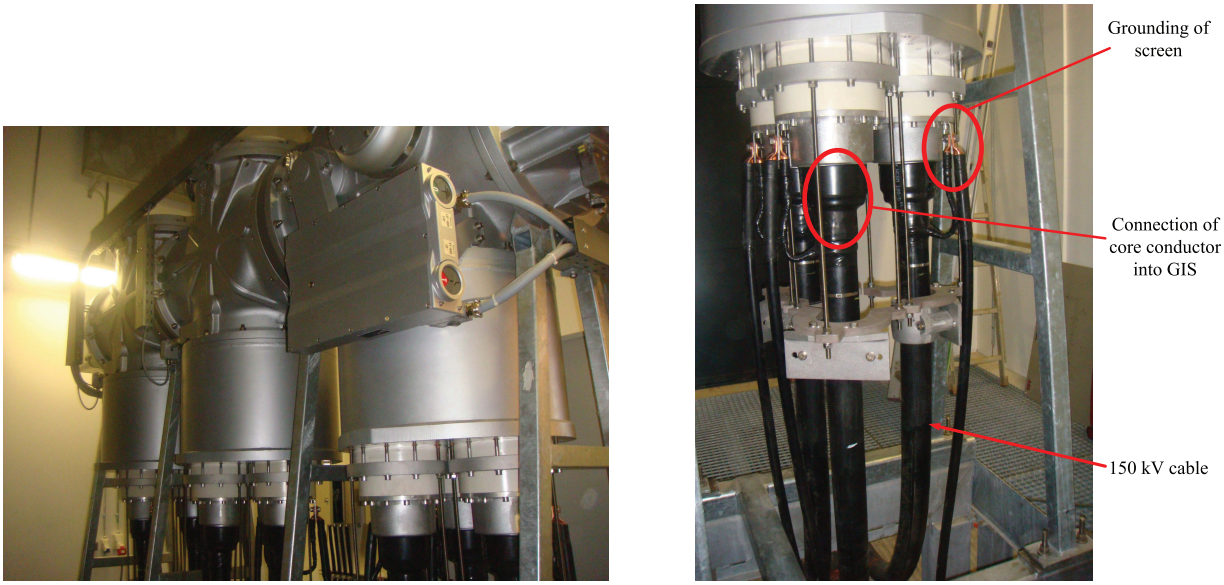

Figure 9.5: *A GIS breaker connecting the cable line to its centre placed shunt reactor.*

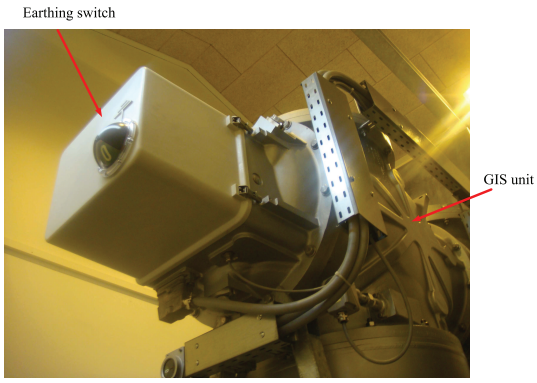

(a) Placement of earthing switch on GIS unit.

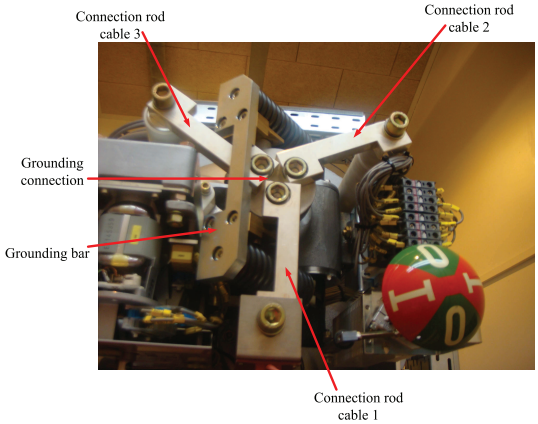

(b) Open earthing swtich.

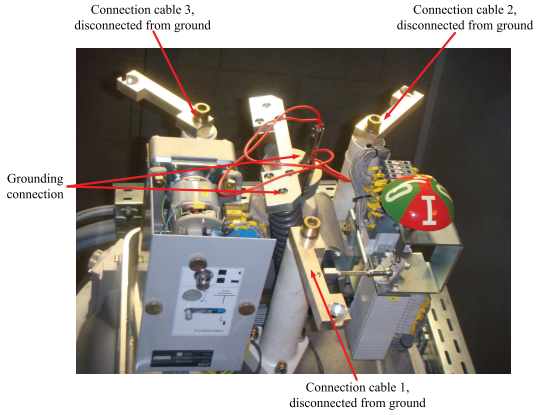

(c) Disasembled earthing switch.

Figure 9.6: *The earthing switch and the principal in the disasembling and core connection.*

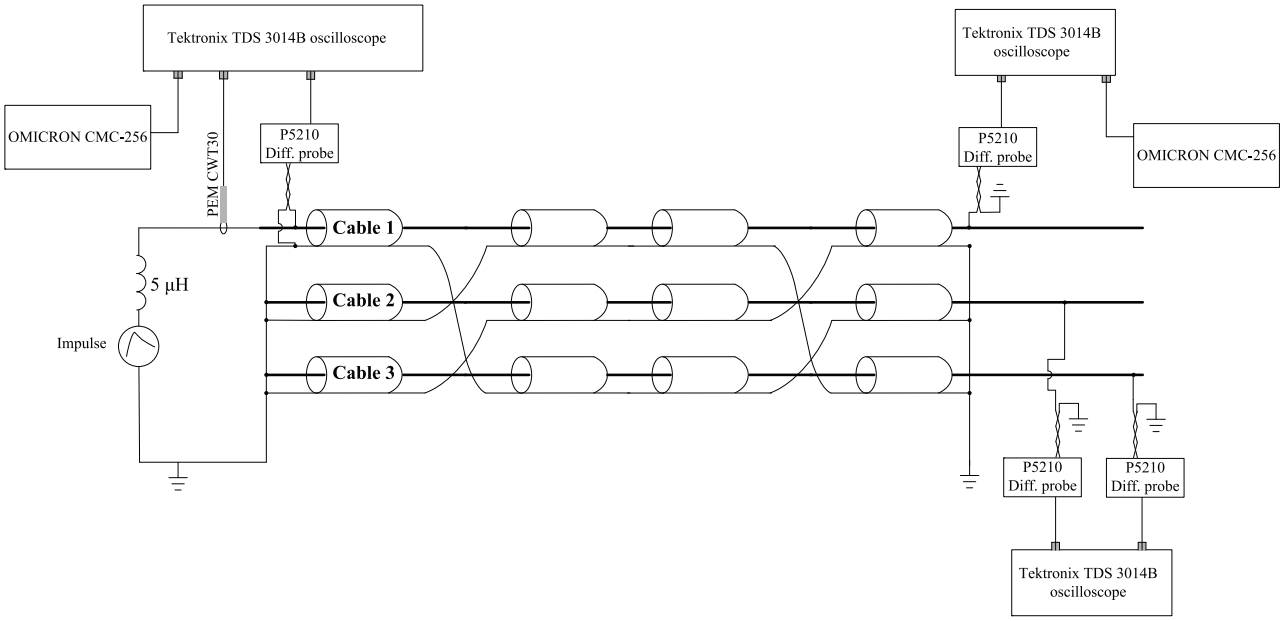

Figure 9.7: *The field test setup for single major section measurements.*

The impulse generator was connected to the HV cable by use of a 5m long 300 mm2 Cu wire. The inductance in such a wire is estemated as 1 μH per meter. The wire is therefore represented by a 5 μH inductance connected in series with the surge generator.

Measurements at sending and receiving ends are synchronised in the same way as was done for field measurement set #1 and #2, described in chapters 7.2.1 and 7.2.2.

9.2.2 Instruments

The generator used is the same HAEFELY PC6-288.1 surge tester as described in chapter 7.2.2 for field measurement set #1 and also used for field measurement set #2. A 4.3 kV impulse is used for excitation. The impulses correspond to a sampling frequency range of app. 8 MHz. As this field test setup utilizes the same input impulse as for field test measurement sets #2, all the same instruments are used; identical Tektronix TDS 3014B oscilloscopes with sampling frequency of 10 MHz, Tektronix P5210 voltage probes with an input limit of 5.6 kV and PEM CWT30 R current probe with measuring range of 30 mA-6 kA with a 16 MHz bandwidth. The equipment accuracy is given in table 9.1. Furthermore, the noise level is identical to field test setup #2, described in chapter 8.2.3. This is because the measurements are performed on the same cable line, at a close location, where there are no OHL's or other cables in near vicinity.

9.2.3 Measurement results

The field test results are shown in figure 9.8 on page 111.

Measurement	**Probe setting**	**Probe accuracy**	**Oscilloscope setting**	**Oscilloscope accuracy**
Sending voltage	1000x	$\pm 3\%$	500 V/div	$\pm[0.02 \cdot \lvert\text{reading } \pm 3\% \text{ of reading}\rvert + 0.1406 \text{ V}]$
Sending current	2mV/A	$\pm 1\%$	0.1 V/div	$\pm[0.02 \cdot \lvert\text{reading } \pm 1\% \text{ of reading}\rvert + 0.0271 \text{ V}]$
Receiving end voltage V_{C1}	1000x	$\pm 3\%$	1 kV/div	$\pm[0.02 \cdot \lvert\text{reading} \pm 3\% \text{ of reading}\rvert + 0.2656 \text{ V}]$
Receiving end voltage V_{C2}	1000x	$\pm 3\%$	1 kV/div	$\pm[0.02 \cdot \lvert\text{reading} \pm 3\% \text{ of reading}\rvert + 0.2656 \text{ V}]$
Receiving end voltage V_{C3}	1000x	$\pm 3\%$	1 kV/div	$\pm[0.02 \cdot \lvert\text{reading} \pm 3\% \text{ of reading}\rvert + 0.2656 \text{ V}]$

Table 9.1: *Table showing warranted characteristics for all measuring instruments for the field measurements of setup #3.*

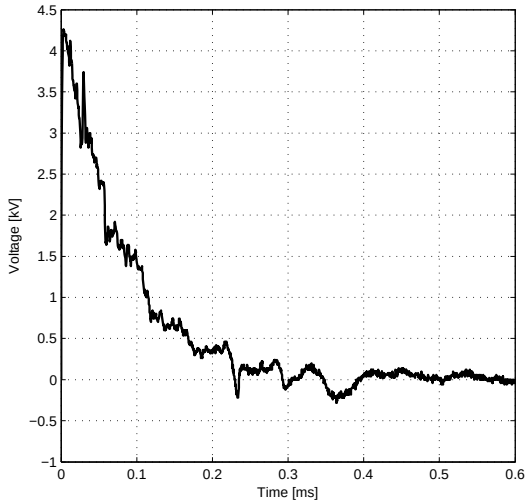

(a) Excitation voltage, sending end cable 1.

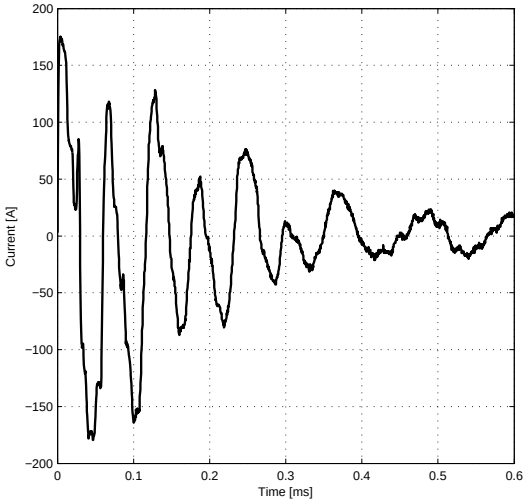

(b) Sending end current, energised phase.

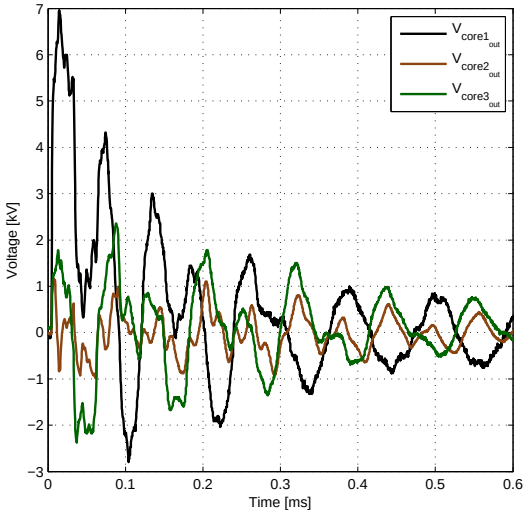

(c) Receiving end voltages.

Figure 9.8: *Field test results for measurements on a single major section, given in figure 9.7.*

9.3 Analysing field measurement set #3

The purpose of the single major section measurements is for validating the cable model after improvements have been implemented. The measurement results from chapter 9.2.3 will therefore not be thoroughly compared to the simulation results in chapter 9.1.1, but only in chapter 14, when improvements have been implemented.

The total length of the cable is 2510 m and the simulated traveling time of the voltage wave on the energised phase is 13.8 μs. The wave velocity is therefore 178.4 m/μs. The first crossbonding point is 952 m from the sending end. Therefore, during the first 10.6 μs only a coaxial wave is measured at the sending end of phase 1. According to analysis of both field test setup #1 and #2 in chapters 7.3 and 8.3 respectively, the comparison of field measurements and simulations during at least the first 10.6 μs

should give close agreement. Figure 9.9 shows a comparison of simulation and field test results for the sending end current.

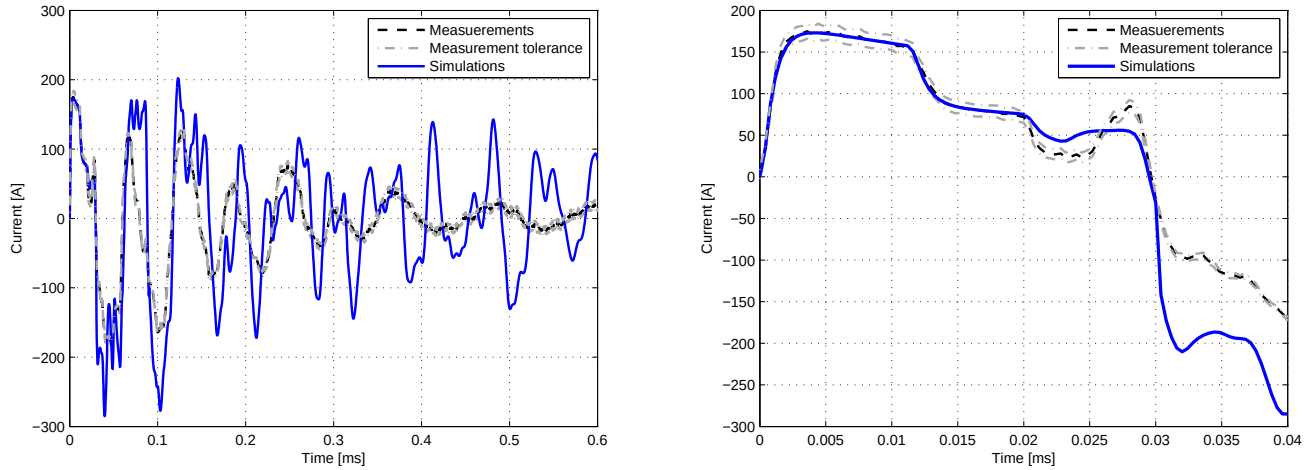

Figure 9.9: *Comparison for the measured and simulated core current at the sending end of the energised phase.*

As seen from figure 9.9, deviation between simulation and field test results for the sending end current does not happen until at time 20 μs. In order to analyse why the deviation starts at this point, figure 9.10 shows simulated phase and modal currents for the first minor section of the cable.

In figure 9.10(a) it can be seen how current starts flowing in the screens of the non-energised phases already when reflected current from first crossbonding point arrives at the sending end, point (i) in the figure. For the case in field test setup #1, this only happened at the time when intersheath mode started flowing. Here this is not the case. The reason for the current starting flowing so early in the screens of the two non-energinsed phases is because for the setup in figure 9.7, not only all screens are connected together at the sending end, but also the cores of the two non-energised phases. Because of this connection, current starts flowing in cores and screens of the non-energised phases as soon as the reflection in the energised phase reaches the sending end (the sending end screen of the energised phase is connected to all conductors of the other cables).

As it can be seen in figure 9.10(b), intersheath modes do not start flowing until at 20μs, point (ii) in figure 9.10(a), which is the same time as when the deviation starts appearing. This further supports the theory from chapter 8.3, that the intersheath mode causes differences mainly because of incorrect simulation of the cables screen. Improvements of the cable model, based on this, will be described in chapters 12-13. The field measurements shown in this chapter will then be used in chapter 14 to validate the improved model.

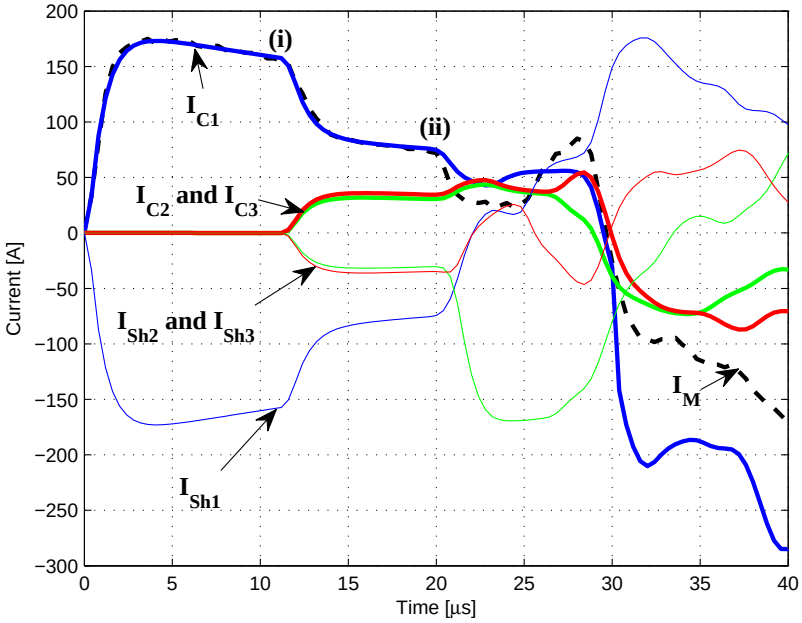

(a) Phase currents

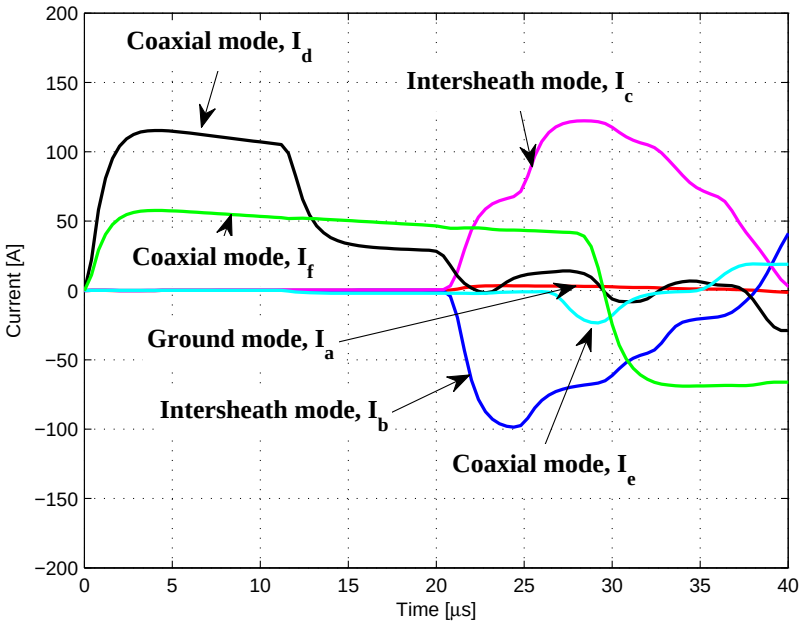

(b) Modal currents

Figure 9.10: *Simulated phase and modal currents plotted in the same time view.* $I_{C1} - I_{C3}$ *are core conductor currents,* $I_{Sh1} - I_{Sh3}$ *are screen currents and* I_M *is the measured core conductor 1 current.*

CHAPTER **10**

Field measurement set #4, 150 kV multiple major sections

The purpose of the multiple major section measurements on the 150 kV cable system is, as for the single major section, for validation. These measurements are performed on the same cable line as field measurement set #2 in chapter 8, where no crossbondings are included. Here there are 11 major sections with total of 22 crossbonding points and 10 grounding of the screens, apart from at cable ends. From the analysis in chapter 8.3, two improvements are suggested, simulating the correct physical layout of the cable's sheath more accurately and including proximity effect in the calculations. These improvements will be discussed in chapters 12-13. In this part of field measurements, the setup and results of measurements for validating the implemented model improvements are described. These measurements will be used in chapter 14.

The cable setup and layout is the same as in chapter 8. The lengths of each minor section, for this field measurement set #4, are given in table 10.1. Minor section 1-2 is the first section counting from the sending end towards the receiving end and is placed between junction 1 and 2.

Minor section #	**Length [km]**	**Minor section #**	**Length [km]**
Section 1-2	0.587	Section 2-3	0.930
Section 3-4	0.928	Section 4-5	1.743
Section 5-6	1.514	Section 6-7	1.78
Section 7-8	1.516	Section 8-9	1.512
Section 9-10	1.760	Section 10-11	1.827
Section 11-12	1.828	Section 12-13	1.830
Section 13-14	1.764	Section 14-15	1.744
Section 15-16	1.738	Section 16-17	1.769
Section 17-18	1.770	Section 18-19	1.770
Section 19-20	1.835	Section 20-21	1.761
Section 21-22	1.846	Section 22-23	1.824
Section 23-24	1.847	Section 24-25	1.832
Section 25-26	1.771	Section 26-27	1.770
Section 27-28	1.775	Section 28-29	1.861
Section 29-30	1.820	Section 30-31	1.816
Section 31-32	1.786	Section 32-33	1.783
Section 33-34	1.750		

Table 10.1: *The lengths of each minor section for this field measurement set #4.*

10.1 Planning field measurement set #4

The cable parameters are the same as used in chapters 8 and 9. The principal test layout in EMTDC/PSCAD is also the same as for field measurements set #3, shown in figure 9.2. The fast front impulse is used to excite one phase of the cable, where all screens are grounded at both ends. This should minimize the current flowing in the ground, making it possible to focus on the cable model without external disturbances. The sending end impulse voltage is simulated as showed in figure 7.6.

10.1.1 Simulation results

The sending end core voltage and core current for the excited phase, as well as receiving end voltages on all core conductors are of interest to be used as a validation template for the improved cable model. The simulation results for the sending end voltage and current is shown in figure 10.1.

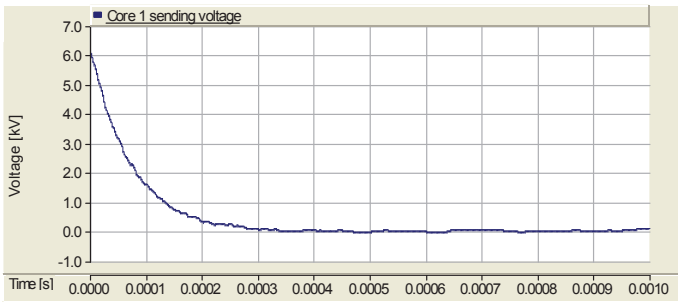

(a) Core voltage at the sending end of the excited cable.

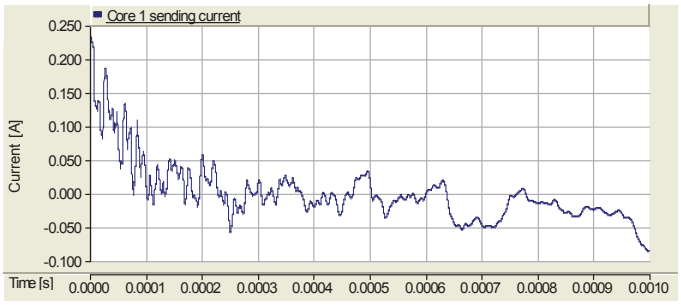

(b) Core current at the sending end of the excited cable.

Figure 10.1: *Simulation results from EMTDC/PSCAD for the simulation setup is shown in figure 9.2 for the whole line of 55 km. Sending end excited phase.*

The results in figure 10.1(a) show the applied impulse. The front and half time of this simulated impulse is based on the impulse generator to be used for the field measurements. Here the amplitude is 6 kV. The results in figure 10.1(b) show the sending end current of the excited core. The form of the current wave is even more distortet than for field measurement set # 1 in chapter 7, i.e. distorted by many reflections from crossbonding points and cable end.

The simulation results for the receiving end voltages are shown in figure 10.2.

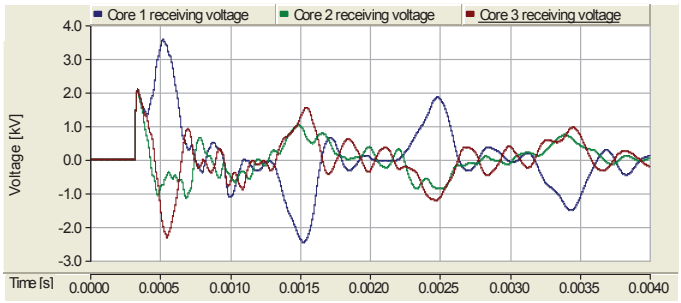

Figure 10.2: *Simulation results from EMTDC/PSCAD for the simulation setup is shown in figure 9.2 for the whole line of 55 km. Receiving end voltages.*

10.2 Performing field measurement set #4

Based on the simulations, the field measurements on the multiple major sections of the 150 kV cable system are planned and the results used for improoved model validation.

10.2.1 Field test setup

The measurements on the multiple major section were performed just after cable installation, before it was put into service. The sending end was in an outside substation, similar to field test setup #1 in chapter 7.2.1, while the receiving end was terminated in a GIS breaker unit, as described in chapter 9.2.1.

The field test setup is shown in figure 10.3. This setup is based on the simulation layout in figure 9.2.

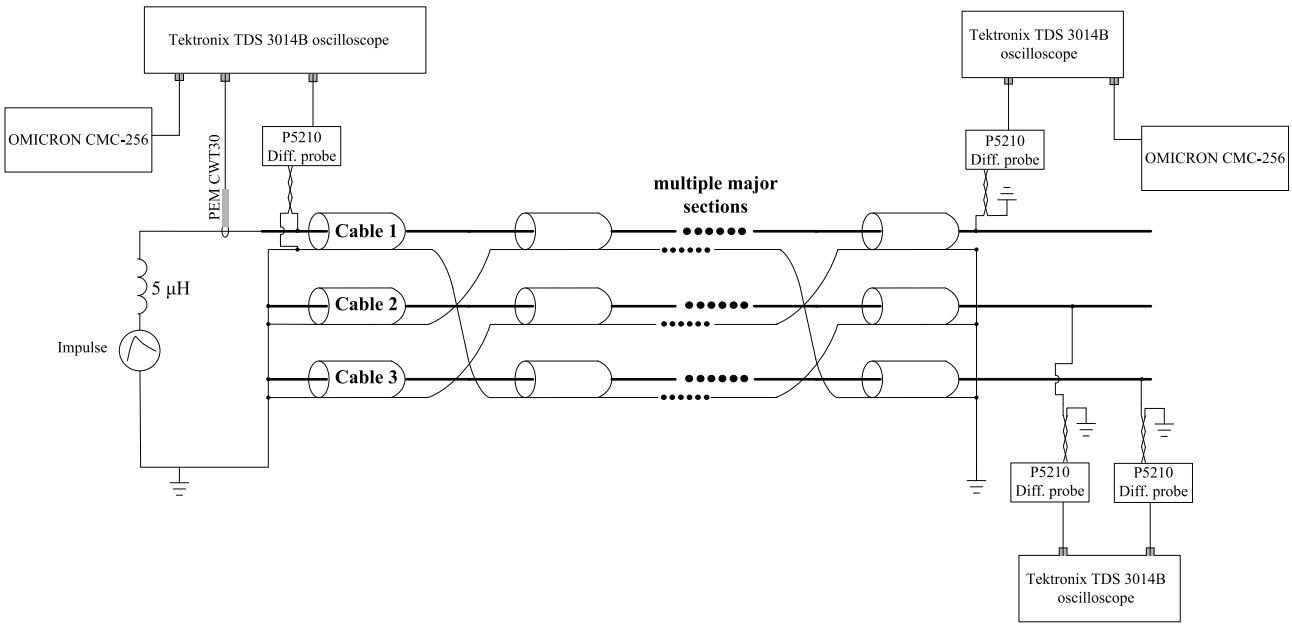

Figure 10.3: *The field test setup for single major section measurements.*

All receiving end core conductor voltages were measured, as well as the sending end voltage and excited

core conductor current.

The impulse generator was connected to the HV cable by use of a 5m long 300 mm^2 Cu wire. The inductance in such a wire is estemated as 1 μH per meter. The wire is therefore represented by a 5 μH inductance connected in series with the surge generator.

Measurements at sending and receiving ends are synchronised in the same way as was done for field measurement set $\#1$ and $\#2$, described in chapters 7.2.1 and 7.2.2.

10.2.2 Instruments

The generator used is the same HAEFELY PC6-288.1 surge tester as described in chapter 7.2.2 for field measurement set $\#1$ and also used for field measurement set $\#2$ and $\#3$. A 6 kV impulse is used for excitation. The impulses correspond to a sampling frequency range of app. 8 MHz. As this field test setup utilizes the same input impulse as for field test measurement sets $\#2$ and $\#3$, all the same instruments are used; identical Tektronix TDS 3014B oscilloscopes with sampling frequency of 10 MHz, Tektronix P5210 voltage probes with an input limit of 5.6 kV and PEM CWT30 R current probe with measuring range of 30 mA-6 kA with a 16 MHz bandwidth. The equipment accuracy is given in table 10.2. Furthermore, the noise level is identical to field test setup $\#2$, described in chapter 8.2.3. This is because the measurements are performed on the same cable line, at a very near location, where there are no OHL's or other cables in near vicinity.

Measurement	**Probe setting**	**Probe accuracy**	**Oscilloscope setting**	**Oscilloscope accuracy**
Sending voltage	1000x	$\pm 3\%$	500 V/div	$\pm[0.02 \cdot \lvert\text{reading } \pm 3\% \text{ of reading}\rvert + 0.1406 \text{ V}]$
Sending current	2mV/A	$\pm 1\%$	0.1 V/div	$\pm[0.02 \cdot \lvert\text{reading } \pm 1\% \text{ of reading}\rvert + 0.0271 \text{ V}]$
Receiving end voltage V_{C1}	1000x	$\pm 3\%$	500 V/div	$\pm[0.02 \cdot \lvert\text{reading} \pm 3\% \text{ of reading}\rvert + 0.1406 \text{ V}]$
Receiving end voltage V_{C2}	1000x	$\pm 3\%$	500 V/div	$\pm[0.02 \cdot \lvert\text{reading} \pm 3\% \text{ of reading}\rvert + 0.2656 \text{ V}]$
Receiving end voltage V_{C3}	1000x	$\pm 3\%$	500 V/div	$\pm[0.02 \cdot \lvert\text{reading} \pm 3\% \text{ of reading}\rvert + 0.2656 \text{ V}]$

Table 10.2: *Table showing warranted characteristics for all measuring instruments for the field measurements of setup #4.*

10.2.3 Measurement results

The field test results are shown in figure 10.4.

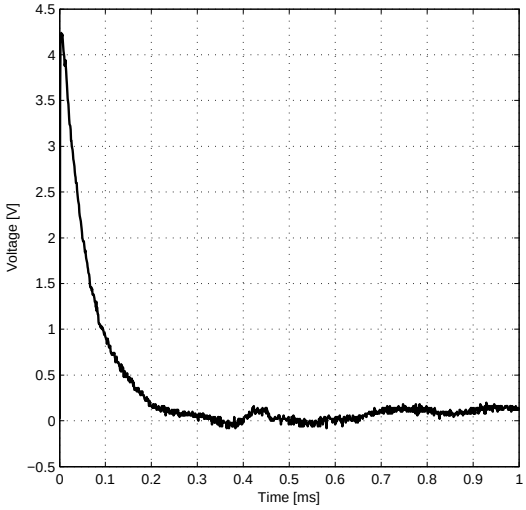

(a) Excitation voltage, sending end cable 1.

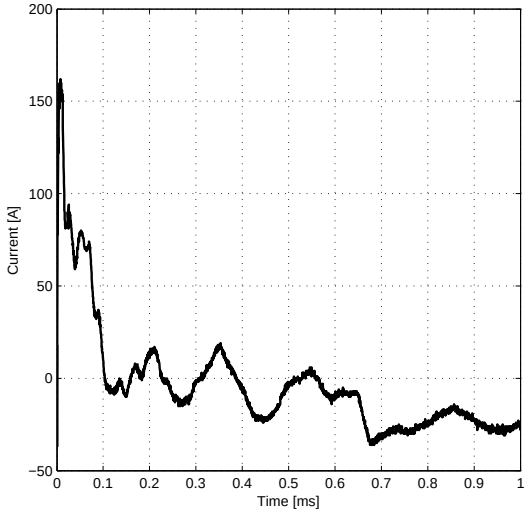

(b) Sending end current, energised phase.

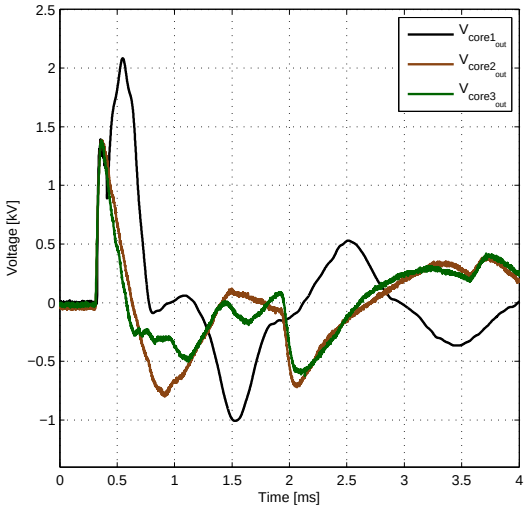

(c) Receiving end voltages.

Figure 10.4: *Field test results for measurements on multiple major section, given in figure 10.3.*

10.3 Analysing field measurement set #4

The purpose of the multiple major section measurements is for validating the cable model after improvements have been implemented. The measurement results from chapter 10.2.3 will therefore not be thoroughly compared to the simulation results in chapter 10.1.1, but only in chapter 14, when improvements have been implemented.

The total length of the cable is 55.441 km and the simulated traveling time of the voltage wave on the

energised phase is 311 μs. The wave velocity is therefore 178 $m/\mu s$. The first crossbonding point is 587 m from the sending end. Therefore, during the first 6.6 μs only a coaxial wave is measured at the sending end of phase 1. According to analysis of both field test setup $\#1$ and $\#2$ in chapters 7.3 and 8.3 respectively, the comparison of field measurements and simulations during the first 6.6 μs should give close agreement.

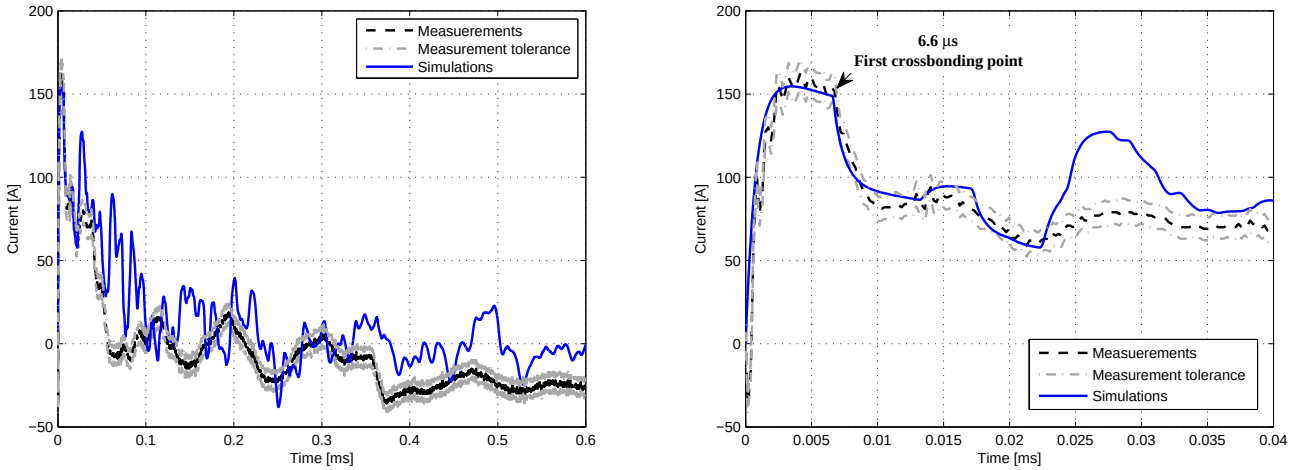

Figure 10.5: *Comparison for the measured and simulated core current at the sending end of the energised phase.*

As seen from figure 10.5, deviation between simulation and field test results for the sending end current does not happen until at approximately 11 μs. In order to analyse why the deviation starts at this point, figure 10.6 on the next page shows simulated phase and modal currents.

In figure 10.6(a) it can be seen how current starts flowing in the screens of the non-energised phases already when reflected current from first crossbonding point arrives at the sending end. This is the same as for field test setup $\#3$ in chapter 9.3.

As it can be seen in figure 10.6(b), intersheath modes do not start flowing until at 11 μs, which is the same time as when the deviation starts appearing. This further supports the theory from chapter 8.3, that the intersheath mode causes differences mainly because of incorrect simulation of the cables screen. Furthermore, as shown in figure 10.6(b), the ground mode is equal to zero and will therefore not affect the simulation results. It is therefore assumed that improving only the simulations of intersheath mode will result in accurate simulation results. Improvements of the cable model, based on this, will be described in chapters 12-13. The field measurements shown in this chapter will then be used in chapter 14 to validate the improved model.

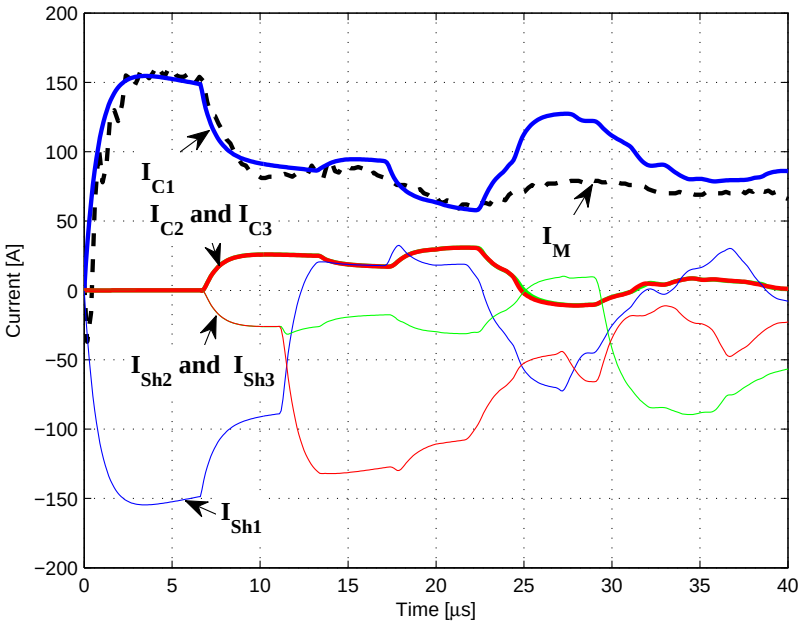

(a) Phase currents

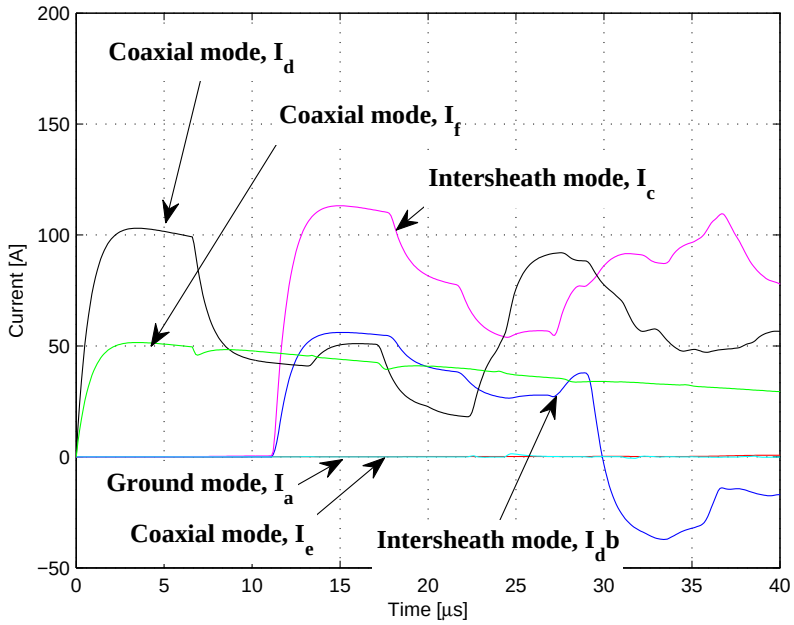

(b) Modal currents

Figure 10.6: *Simulated phase and modal currents plotted in the same time view.* $I_{C1} - I_{C3}$ *are core conductor currents,* $I_{Sh1} - I_{Sh3}$ *are screen currents and* I_M *is the measured core conductor 1 current.*

CHAPTER 11

Summary for Field Measurements

One of the major contributions from the research presented in this thesis is field measurements for model validation. By planning, performing and analysing field measurements, a much better understanding of the physical nature of cables can be gained.

The field measurements are started in chapter 7, "Field measurement set #1, 400 kV crossbonded cable". The purpose of the field measurements on the 400 kV cable system was to analyse the cable model, investigate the accuracy of the model and use wave propagation to identify origin of disagreement between measurements and simulations. From this analysis, it has been observed that disagreement between cable simulations and field test results start appearing because of crossbonding points. In order to validate this and identify the source of the deviation, measurements on a non-crossbonded cable are performed.

In chapter 8, "Field measurement set #2, 150 kV single minor section", excitation of exclusively the coaxial mode and exclusively the intersheath mode were performed on a non-crossbonded cable. From analysis of these field measurements, it is shown how the existing cable model is precise and accurate for non-crossbonded cables. This is because in non-crossbonded cables, the coaxial modal waves will dominate and when exclusively exciting the coaxial mode, the simulation results, by using existing cable model, fall within the tolerance of the field measurements. It is also showed in chapter 8 how deviation between simulation and field measurement results appear with intersheath mode. This phenomena has actually been shown also to appear for a 400 kV flat formation 7.6 km cable line, a 150 kV tight trefoil formation 2.5 km cable line and 150 kV tight trefoil 55 km cable line. The results of chapter 8 is therefore that modelling of the screen, because of the intersheath mode, needs to be improved. These improvements will be discussed in chapters 12-13.

From chapter 7 it has been suggested that the intersheath mode is the reason for deviation between simulation and field measurement results on crossbonded cables. In chapter 8 it has been verified that the intersheath mode does indeed cause deviation between simulation and field measurment results, when explicitly exciting the intersheath mode, on a non-crossbonded cable. From this, improvements are suggested. The presence of crossbonding points in long cables causes excitation of intersheath waves when the screens are shifted between cables. After the intersheath waves reach the measurement point, large deviations develop and the simulation model is therefore suggested to be insufficient for (long) crossbonded cable systems. In order to validate this suggestion, the improved model should be validated not only against non-crossbonded field measurements with explicit excitation of the intersheath mode, but also against long crossbonded cables. More field measurements on the 150 kV cable system are therefore performed, where larger sections, with crossbonding points, are used.

In chapter 9, "Field measurement set #3, 150 kV single major section", field measurements on a single major section show deviation between simulation and field measurement results because of intersheath mode. This is also the case for the field measurements described in chapter 10, "Field measurement set #4, 150 kV multiple major sections". The purpose of the field measurements described in chapters 9-10 is to allow for validation of the simulation results, for long crossbonded cables, when the modelling of the intersheath mode has been improved. The validation results will be described in chapter 14.

Part IV

Cable Model Improvements

It has been shown in chapter 8.3 how insufficient representation of the cables metallic screen in the modelling software, plays a role in inaccurate simulation results for high frequency model validation. This is particularly a problem for long cables where crossbonding points will cause an intersheath wave to flow in the cable system. An analysis of a deviation between field measurements and simulation results revealed how the screen conductor should be more accurately represented in the simulation software. The analysis revealed how the characteristics of the screens physical layout in the HV cable and the proximity effect should be included in the series impedance calculations.

This part of the report addresses how the cable model is improved in order to model in detail the physical layout of the HV underground XLPE cable and how to include the proximity effect in order to have more precise simulation results. Furthermore the improved modelling procedures are verified against field measurements, where the intersheath mode is explicitly excited. Finally the improved modelling method is validated against field measurements on long underground HV XLPE cables, described in chapters 9 and 10.

CHAPTER 12

Screen physical layout

The layout properties of an XLPE HV cable are described in chapter 2. The layout of the 150 kV HV cable used for field measurements in chapters 8 - 10 is shown in figure 12.1.

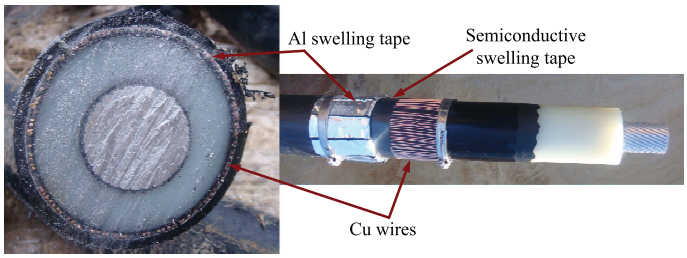

Figure 12.1: *The layout of the 150 kV HV cable used for field measurements in chapters 8 - 10.*

As shown in figure 12.1 and explained in chapter 8.3.2, the screen consists of several layers. There are two conducting screen layers, the wired Cu screen and the Al foil. Those two layers are seperated by a SC swelling tape and connected to each other at cable ends and each cable junction.

12.1 Modelling the cable screen

It is a common practise when modelling the screen in EMT-based software, to model it as a single solid hollow conductor with the resistivity increased [11], even though it physically consists of two conducting layers with a SC tape in between.

As shown in appendix B,the impedance equivalent circuit for three single core cables is as in figure 12.2.

In this equivalent, the screen is represented as a single conductor. The loop series impedance matrix from chapter 2.3 is given in equation 12.1, where the superior indices 1, 2 and 3 denote the respective cable number (phases).

$$\begin{bmatrix} Z_1^1 & -Z_{Sm}^1 & 0 & 0 & 0 & 0 \\ -Z_{Sm}^1 & Z_2^1 & 0 & Z_{gm12} & 0 & Z_{gm13} \\ 0 & 0 & Z_1^2 & -Z_{Sm}^2 & 0 & 0 \\ 0 & Z_{gm12} & -Z_{Sm}^2 & Z_2^2 & 0 & Z_{gm23} \\ 0 & 0 & 0 & 0 & Z_1^3 & -Z_{Sm}^3 \\ 0 & Z_{gm13} & 0 & Z_{gm23} & -Z_{Sm}^3 & Z_2^3 \end{bmatrix} \tag{12.1}$$

In order to correct for this screen representation, the screen mutual impedance should be divided into three;

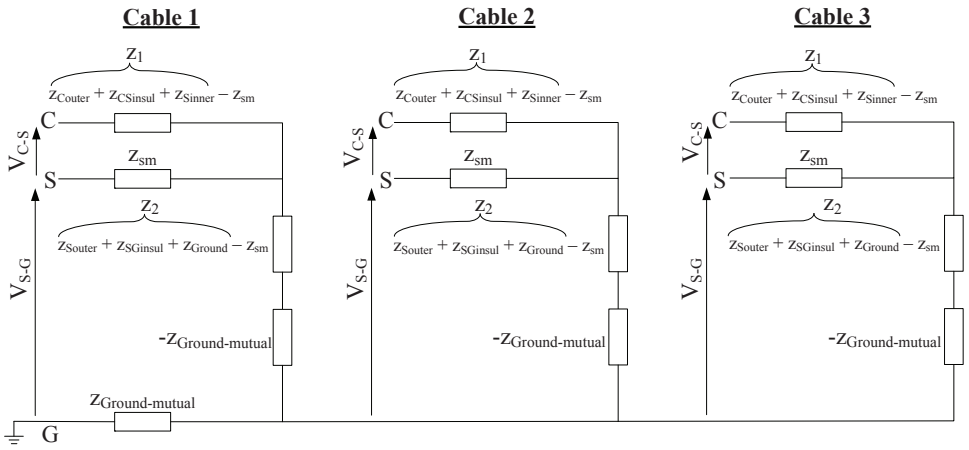

Figure 12.2: *Impedance equivalent circuit for the loop formation of three single core cables.*

a) impedance because of the wired screen layer

b) impedance because of the SC layer

c) impedance because of the laminate layer

The two conducting layers are connected at each cable junction and cable end. An impedance equivalent including this layered screen will therefore be a delta connection of impedances as shown in figure 12.3.

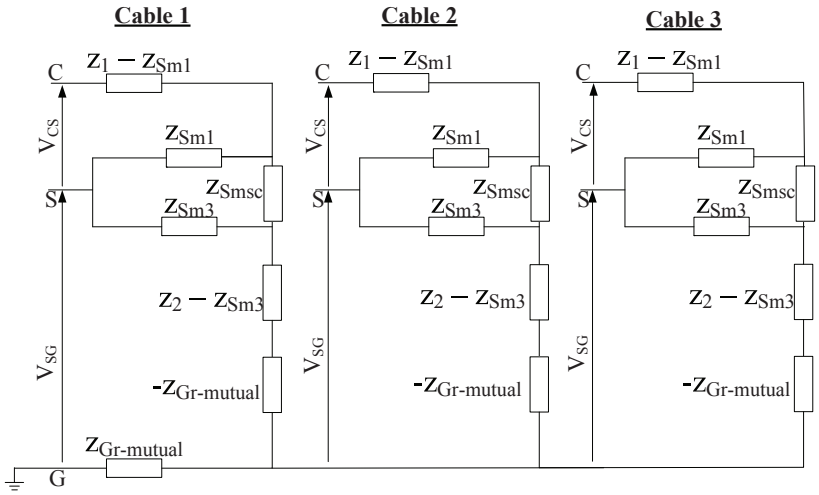

Figure 12.3: *Impedance equivalent circuit for the loop formation, where the layered screen is included.*

Every i-th series impedance of the impedance equivalent circuit is defined as $z_i - z_{mi-1} - z_{mi}$ [50] as can be seen in figure 12.2 where for $i = 1$ the series impedance is $Z_1 - z_{sm}$ as there is no shunt impedance z_{m0} and $z_{mi} = z_{sm}$. Similarly for $i = 2$ the series impedance is $Z_2 - z_{sm} - Z_{Ground-mutual}$ where

$z_{mi-1} = z_{sm}$ and $z_{mi} = Z_{Ground-mutual}$. The series impedance of the split mutual screen in figure 12.3 is therefore:

$$Z_{Smsc} = Z_3 - Z_{Sm1} - Z_{Sm3} \tag{12.2}$$

Where Z_{Sm1} and Z_{Sm3} are the mutual impedances of wired screen layer ($Sm1$) and laminate screen layer ($Sm3$) respectively and Z_3 is given by equation 12.3. Calculations of the mutual impedances Z_{Sm1} and Z_{Sm3} are given by [47] and shown in appendix B.1.6.

$$Z_3 = Z_{S1-outer} + Z_{SC-insul} + Z_{S3-inner} \tag{12.3}$$

Where $Z_{S1-outer}$, $Z_{SC-insul}$ and $Z_{S3-inner}$ are the $Sm1$-layer outer series impedance, the SC layer series impedance and the $Sm3$-layer inner series impedance respectively. These impedances are calculated based on the theory in appendix B.1.4, B.1.2 and B.1.3 respectively, where the corresponding radius of each layer must be taken into account. Note that $Z_{SC-insul}$ can often be neglected, as the thickness of the SC layer normally is less than 1 mm and therefore $ln\left(\frac{r_2}{r_1}\right) \approx 0$.

For representation of the cables impedance equivalent, the delta connection of figure 12.3 should be transformed to a star connection, as shown in figure 12.4.

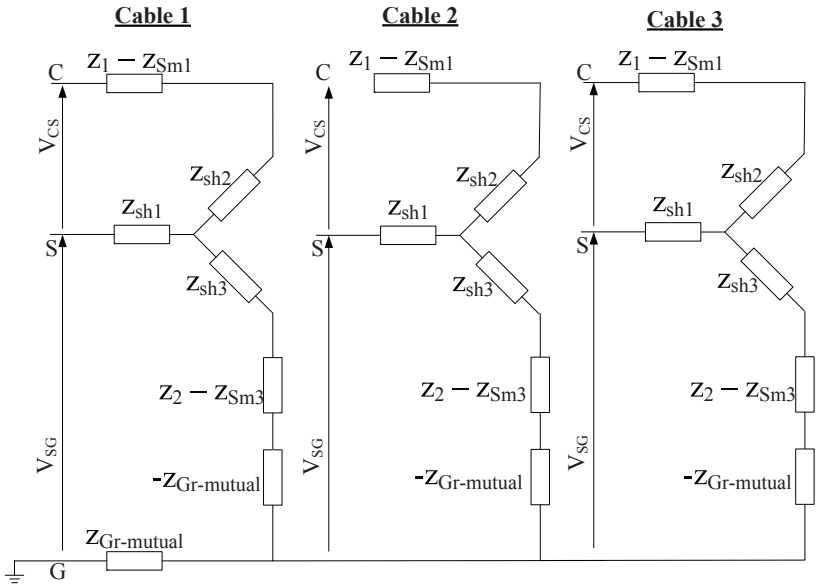

Figure 12.4: *Impedance equivalent circuit for the loop formation, where the layered screen is included as a star connection.*

The star connection impedances are calculated by the delta-star transformation based on [51] and given in equation 12.4.

$$Z_{sh1} = \frac{Z_{Sm1} \cdot Z_{Sm3}}{Z_{Smsc} + Z_{Sm1} + Z_{Sm3}} = \frac{Z_{Sm1} \cdot Z_{Sm3}}{Z_3} \tag{12.4a}$$

$$Z_{sh2} = \frac{Z_{Sm1} \cdot Z_{Smsc}}{Z_{Smsc} + Z_{Sm1} + Z_{Sm3}} = \frac{Z_{Sm1}(Z_3 - Z_{Sm1} - Z_{Sm3})}{Z_3} \tag{12.4b}$$

$$Z_{sh3} = \frac{Z_{Sm3} \cdot Z_{Smsc}}{Z_{Smsc} + Z_{Sm1} + Z_{Sm3}} = \frac{Z_{Sm3}(Z_3 - Z_{Sm1} - Z_{Sm3})}{Z_3} \tag{12.4c}$$

By using such a new modelling procedure for the screen, a new series impedance matrix is calculated. This is shown in equation 12.5 and based on equation 12.1.

$$\begin{bmatrix} Z^1_{11} & -Z^1_{sh1} & 0 & 0 & 0 & 0 \\ -Z^1_{sh1} & Z^1_{22} & 0 & Z_{gm12} & 0 & Z_{gm13} \\ 0 & 0 & Z^2_{11} & -Z^2_{sh1} & 0 & 0 \\ 0 & Z_{gm12} & -Z^2_{sh1} & Z^2_{22} & 0 & Z_{gm23} \\ 0 & 0 & 0 & 0 & Z^3_{11} & -Z^3_{sh1} \\ 0 & Z_{gm13} & 0 & Z_{gm23} & -Z^3_{sh1} & Z^3_{22} \end{bmatrix} \tag{12.5a}$$

$$Z_{11} = Z_1 - Z_{Sm1} + Z_{sh2} + Z_{sh1} \tag{12.5b}$$

$$Z_{22} = Z_{sh1} + Z_{sh3} + Z_2 - Z_{Sm3} \tag{12.5c}$$

This new series impedance matrix is used to calculate the cables terminal conditions, as given in chapter 2.1.

12.2 Comparison of field measurements and simulations

The new modelling procedure is verified against the intersheath field measurement results for setup #2 in chapter 8.2.4. The simulation results when including the new layered screen principle from chapter 12.1 are compared to both the field measurement results and normal EMTDC/PSCAD simulations from figure 8.25. The comparison of field measurements and simulation results, for both modelling the screen as a single conductor and for the new improved method of including the layered screen are given in figure 12.5.

As explained in chapter 8.3.2, only the propagation damping and not velocity is incorrectly simulated. This is also validated in figure 12.5, as the simulations agree quite well with measurements regarding the time delay. The simulating error lies in the amplitude and damping of the signals. Figure 12.5 shows how the new layered screen modelling method results in a smaller deviation, in amplitude, between simulations and field measurements. The reason for the better lower frequency damping of simulations when modelling the screen layer more precisely, is a more accurate impedance matrix, compared to the normal method of simplifying the screen to only a single coaxial conducting layer. By including the layered screen, the difference in the impedance matrix will lead to a correct damping, because of a larger series impedance. As the shunt admittance is not changed, the time delay is unchanged.

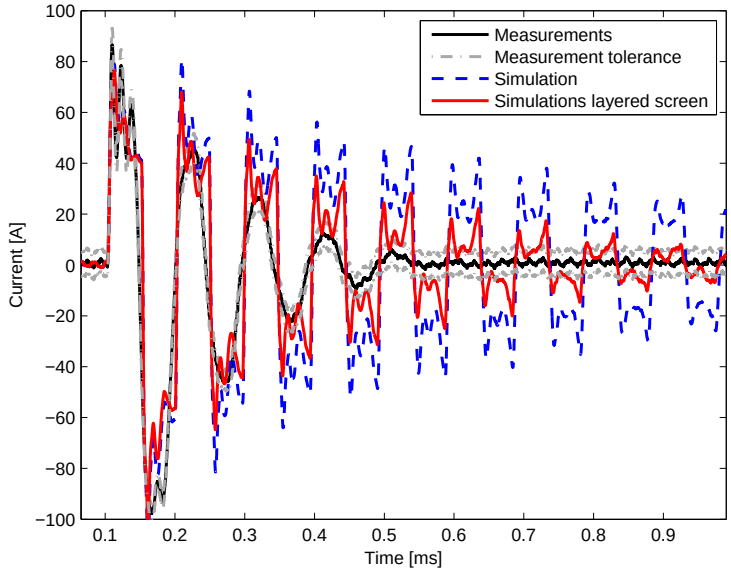

(a) Sending end current

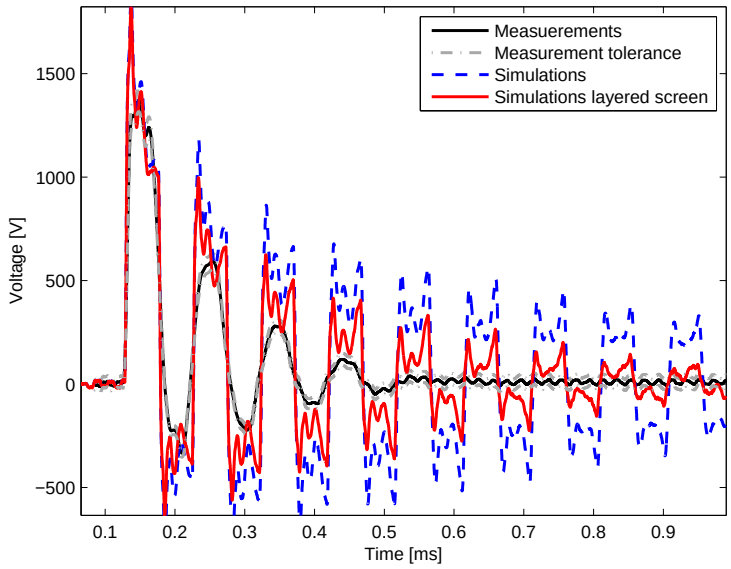

(b) Receiving end voltage

Figure 12.5: *Comparison of the sending end current and receiving end voltage on energised screen conductor for the intersheath mode.*

Even though the simulations of the new modelling procedure and field test results agree quite well regarding the damping in the waveforms of the lower frequency (below 10 kHz) component, all simulation results still have inadequate damping of higher frequency oscillations. Because of this, it is not sufficient to increase the damping at lower frequencies by introducing the layered screen. As the intersheath current propagates between the screens of adjacent cables, their propagation characteristics are also affected

by proximity effects which are not taken into account by the simulation software. The next chapter will therefore introduce how to include the proximity effect in impedance calculations.

CHAPTER 13

Proximity effect

When adjacent conductors carry current, the closeness of the conductors will cause the current distribution to be constrained to smaller regions. This phenomena is called proximity effect.

It was stated by Michael Faraday in 1831, that when a magnetic flux from a current carrying conductor starts changing, it will induce an electromotive force (emf) in an adjacent conductor. This emf will produce local currents in the adjacent conductor, that are perpendicular to the magnetic flux. These currents are called eddy currents. Because of the eddy currents, the overall distribution of current in the conductor will become non-homogen, or constrained to smaller regions.

When AC currents flow in a conductor, the resulting magnetic flux will be time varying. When the frequency increases, the magnetic flux $\frac{d\phi}{dt}$ will vary more, resulting in larger eddy currents of adjacent conductors. Therefore, the higher the frequency, the stronger the proximity effect. An example of proximity effect is shown in figure 13.1.

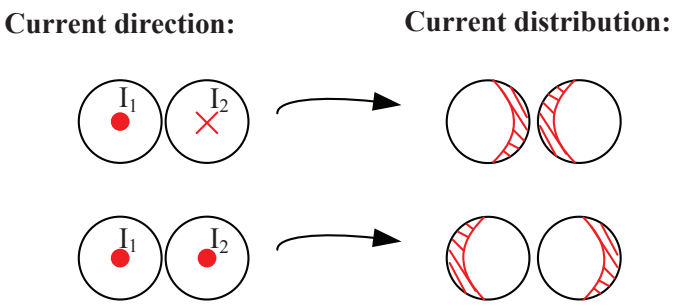

Figure 13.1: *Current distribution because of proximity effect for two adjacent conductors carrying current in teh same direction and in opposite direction. The red marked area is where the current distribution is constrained to a smaller region.*

As explained in chapter 8.3.2, for higher frequencies (10 kHz and above) the proximity effect causes the current distribution in the screens to be more non-homogen. This again changes the series impedance of the cable at the higher frequencies. Furthermore, the actual screen is a stranded conductor, which results in proximity effect within the wires of each cable screen, which also changes the series impedance of the cable, especially at very high frequencies.

The proximity effect is not included in the analytical series impedance calculations described in appendix B and used in EMT-based simulation software. Therefore another method, not based on the analytical equations, for series impedance calculations is chosen.

This new method is based on subdivision of conductors from [52] with some changes by including techniques from [53, 54] and with new improvements.

In the method, every conducting layer in the cable is divided into a number of subconductors, to be specified by the user. This is a finite element approach that assumes a constant current distribution over each subconductor. By forming a conductor of a suitably large amount of subconductors, the non-uniformity in the current distribution because of skin and proximity effects is included.

As well as uniform current distribution within each subconductor, also the resistivity of each subconductor is constant. It can though vary between subconductors as is the case for core conductors vs. screen layers and often for one screen layers vs. the other. It is also assumed, that the current flows longitudinally in each subconductor.

In [52, 53, 54] it is assumed that each intervening space (insulation) have the same and constant permeability. In this thesis, it is shown how to include different permeability for different intervening spaces, such as insulation and semiconductive layers for the case of layered screen. Furthermore in this thesis, some other improvements to the subdivision method are made:

- Not only an ideal fictitious return path is chosen, but the impedance of earth return is also included in the impedance calculations, by first eliminating the effect of the fictitious return path and then including separate earth return calculations.
- It is explained how it is possible to include the earth as a subdivided conductor by utilizing analytical equations for core conductor.
- The method used in this report introduces how to handle two screen layers with different impedances, because of different material, in order not to have a too large impedance matrix for the terminal condition calculations.
- When discussing single core cable [52, 53, 54] explain the theory for a single cable. In this thesis a real three phase cable system is used.

A flow diagram for the modelling procedure, when including proximity effect, is shown in figure 13.2 and the flow chart parts, between model input and simulation output are explained in chapters 13.1-13.4.

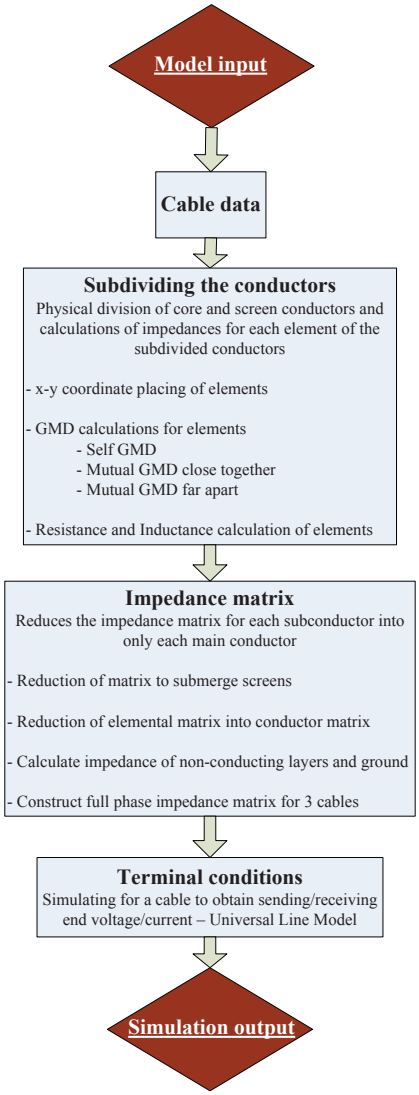

Figure 13.2: *Flow diagram for the modelling procedure, when including proximity effect. The flow chart parts, between model input and simulation output, are explained in chapters 13.1-13.4.*

13.1 Cable data

Inputs for the model are basically the same as for the previously used frequency dependent phase model in EMTDC/PSCAD. The cable physical data and electrical parameters must be given:

Conductors:	Inner/outer radius, resistivity and permeability
Insulations:	Inner/outer radius, permittivity and permeability
Earth:	The earth resistivity and permeability
Placement:	Physical placement of the cables, i.e. the (x, y) coordinates of each cables center, depth of each cable and distance between them
Frequency:	Minimum and maximum frequency for the frequency range to be used. This can be chosen by the user.

Furthermore, the number of subconductors for each conductor must be chosen as well as the radius of the fictitious return path.

The number of subconductors can be difficult to choose. This is a trade-off between simulation time and accuracy. The larger the number, the better the accuracy at the cost of large simulation time. This is because for every subconductor the current distribution is assumed uniform, which is more correct the smaller the size of each subconductor. But larger number of subconductors also means larger number of calculations.

The proximity effect changes the effective impedance because of the magnetic field of two conductors in close proximity to each other, which causes uneven current distribution in the conductors. The higher the frequency the faster the alternation of the magnetic flux from the conductor and hence the larger the change of the conductors impedance because of circulating currents. Therefore the higher the frequency study, the more accurate should the proximity simulations be. It is advised as a rule of thumb, for accurate high frequency studies (above 10 kHz), that when choosing the number of subconductors it should be done such that adding more subconductors will not lead to more than a 5% change in the impedance, compared to not adding more subconductors. This rule of thumb is validated on page 150.

For choosing the radius of the return path, it must be sufficiently large to enclose all conductors. The current in this fictitious no-loss return path will be zero at all times.

With all cable data and model input set, it is possible to proceed with subdivision of conductors.

13.2 Subdividing the conductors

The finite element method for subdivision of conductors has in the past been studied for numerical impedance calculations of arbitrary shaped conductors. This method has been proposed for modelling of sector shaped cables [54], rectangular shaped conductors [55], stranded conductor (circular subconductors) [52], pipe-type cables [52] and other arbitrarily shaped conductors [53]. For all these methods, the impedance calculations have only been compared to analytical calculations. The method used in this thesis is however aimed for accurate modelling of fast frequency cable studies and validated with field measurements.

13.2.1 x-y coordinate placing of elements

The most common methods for subdividing the conductors is by using circular, squared or elemental shaped filaments for the subconductors. Both square and circular filaments are fairly easy to construct whereas they do not correctly represent the form or shape of conductors with correct current distribution, unless the filaments are constructed very small which results in a large amount of computations. The elemental subconductors proposed in [53], give better calculations of the total impedances because of the non-uniformity of the current distribution. This is because of how the filaments are formed. They closely fill the entire volume of the real conductor and by distributing them exponentially, there is even a larger amount of elements where the current distribution is denser. Such a distribution indicates that the closer to the conductor surface, the larger amount and thinner the subconductors are, calculating more correctly for the non-uniformity of the current distribution. This distribution of filaments is shown in figure 13.3(a). The elemental subdivision of conductors is used in this thesis.

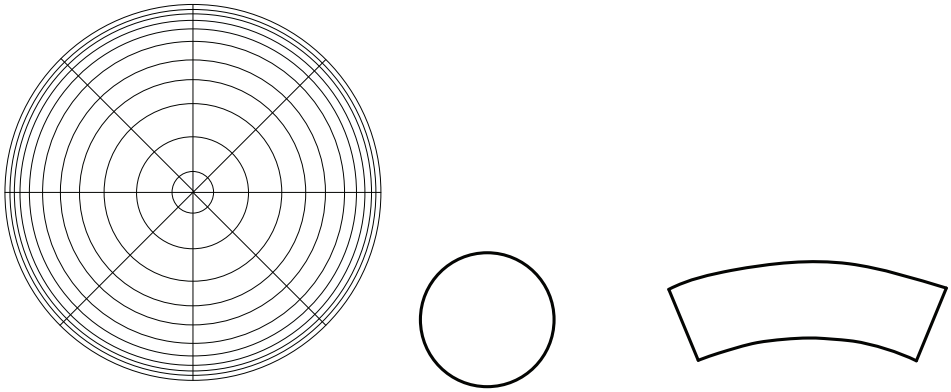

(a) Exponential distribution of elemental subconductors.

(b) Element types used for the subconductors.

Figure 13.3: *Distribution of elements and element types for subdivision of conductors.*

There are two types of elements used for such subdivision; the circle for core conductor centre and the circular arc shaped filament. These elements are shown in figure 13.3(b). Each element must be sized such that constant current density can be assumed. The non-uniform current distribution is obtained because of mutual coupling between elements and the fact that current density in one element can vary from the next.

The elements are placed by use of x-y coordinates, where the (0,0) coordinates is in the centre of one of the three cables. An example of how a single element is placed in a trefoil cable layout is given in appendix D.1. The same method is used for placing all elements and each output value will be given for each and every subconductor layer of all three cables.

13.2.2 GMD calculations for elements

For calculating the self and mutual inductances of the elements, the geometric mean distance (GMD) for each and every element must be known. For the subconductor division shown in figure 13.3 there are 3 different types of GMD's.

1 -Self GMD of the circular shaped element
-Self GMD of the arc shaped element

2 -Mutual GMD of a circular and arc shaped elements when far apart
-Mutual GMD of two arc shaped elements when far apart

3 -Mutual GMD of two arc shaped elements when close together

A logarithmic mean distance between two current paths is defined as the logarithmic of the GMD and is given by equation 13.1 [56].

$$ln(GMD_{ij}) = \frac{1}{S_i S_j} \int_{Aj} \int_{Ai} ln(x) dS_j dS_i \tag{13.1}$$

where S_i and S_j are surfaces of current path i and j respectively.
Ai and Aj are areas of current paths i and j respectively.

1- Self GMD

For circular areas, the self GMD, often called the geometric mean radius (GMR), is given as $re^{-\mu_r/4}$ where r is the radius of the circle and μ_r is the relative permeability of the material in the circle [52, 53, 57].

The GMD of an area is defined as the geometric mean distance of all points within the area with respect to each other. The GMD of the example in appendix D.1, with 6 positioned points inside a single element, there will be 15 distances and the GMD is calculated as $\sqrt[15]{d_{12} \cdot d_{13} \cdot \ldots \cdot d_{23} \cdot \ldots d_{56}}$, where d_{ij} is the distance between points i and j. In the literature, an approximation for the GMD of a rectangular surface of length l and width w has been introduced as being close to $0.2235(l + w)$ [53, 58]. By changing the constant to 0.2215 instead, the self GMD for a thin arc-shaped element is approximated as $0.2215(l + w)$ [53]. This has in the past been validated as giving very accurate results, and it lowers the amount of calculations by $[(n1 - 1) + n2 + n3] \cdot 14$, where n1 is the number of subconductors in core (1 is subtracted because of circular self GMD), n2 and n3 are numbers of subconductors for the two screen layers and multiplication of 14 is the number of distances to calculate for each subconductor. It is therefore chosen in this thesis to use the approximation of $0.2215(l + w)$, and take that into account when simulation results are validated

2- Mutual GMD, far apart elements

For calculating the GMD between elements with suitable accuracy, each element is divided into sectors and the GMD between points in each sector of two elements is calculated. See the division of an element in figure 13.4.

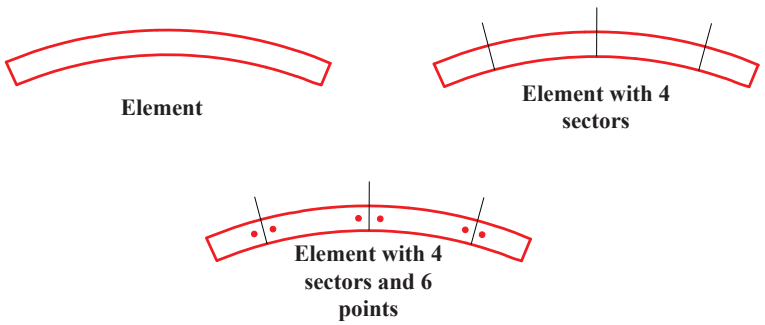

Figure 13.4: *Division of an element into sectors and with points for mutual GMD calculations.*

Such sector division is explained in appendix D.1 and shown in figure D.2(b). When calculating the GMD between every point in two sectors, the mean distance of each pair of points is calculated. The GMD between elements i and j, each containing 6 points, will therefore be $\sqrt[36]{d_{i_1j_1} \cdot d_{i_1j_2} \cdot \ldots \cdot d_{i_2j_1} \cdot \ldots d_{i_6j_6}}$. If one of the elements is a circular element (i.e. core conductor centre), all 6 points of that element will fall into one single point in the centre of the circle, resulting in only 6 distances between one element and the circle.

An example of how to obtain the GMD for two elements placed far apart is given in appendix D.2. The GMD's for three cables, each having three conductors (core and two screens), are calculated between every element (subconductor) in every conductor of every cable.

3- Mutual GMD, close elements

When two thin elements are close to each other, as shown in figure 13.5, the mutual GMD cannot be calculated as explained above. For two close elements the mutual coupling is much stronger and must therefore be calculate with more accuracy than by use of only 6 points. Instead of using a very large number of points and calculate the distances, which would explode the number of needed calculations, analytical calculations are used.

Figure 13.5: *Two different types of two thin elements that are placed close to each other.*

The analytical solution of the logarithmic mean distance from equation 13.1 is given in equation 13.2. This solution is based on the litterature of [53].

$$\begin{aligned} ln(GMD_{close_{ij}}) = & \frac{x_j^2+d^2}{2nl} ln(x_j^2+d^2) + \frac{x_i^2-x_j^2}{2nl} - \frac{x_i^2+d^2}{2nl} ln(x_i^2+d^2) + \\ & \frac{2dx_j}{nl} tan^{-1}\left(\frac{x_j}{d}\right) - \left(\frac{2dx_i}{nl}\right) tan^{-1}\left(\frac{x_i}{d}\right) + \left(\frac{d^2}{nl}\right) ln\left(\frac{d^2+x_i^2}{d^2+x_j^2}\right) - 1 \end{aligned} \tag{13.2}$$

where i and j are two elements.
$x_i = \frac{l-n}{2}$ and $x_j = \frac{l+n}{2}$.
l and n are the arc lengths along the centres of elements i and j respectively.
$d = \sqrt{(x_i - x_j)^2 + (y_i - y_j)^2}$ is the distance between two elements.

When all GMD's of the subconductors have been calculated it is possible to calculate the mutual and self inductances for each subconductor and form the impedance matrix.

13.2.3 Elemental impedances

For the current in each element, there is formed a loop through a fictitious lossless return path. Then it is possible to calculate the impedance of each element, where there is no total current flowing in the fictitious return. A lumped equivalent scheme of the constant impedances for each element is shown in figure 13.6. This figure demonstrates three conductors, core and two screens, for a single cable. Each conductor is subdivided into n_1, n_2 and n_3 subconductors respectively and there are three cables.

For the conductors of figure 13.6 the voltage/current relationship for a single cable is described by equation 13.3.

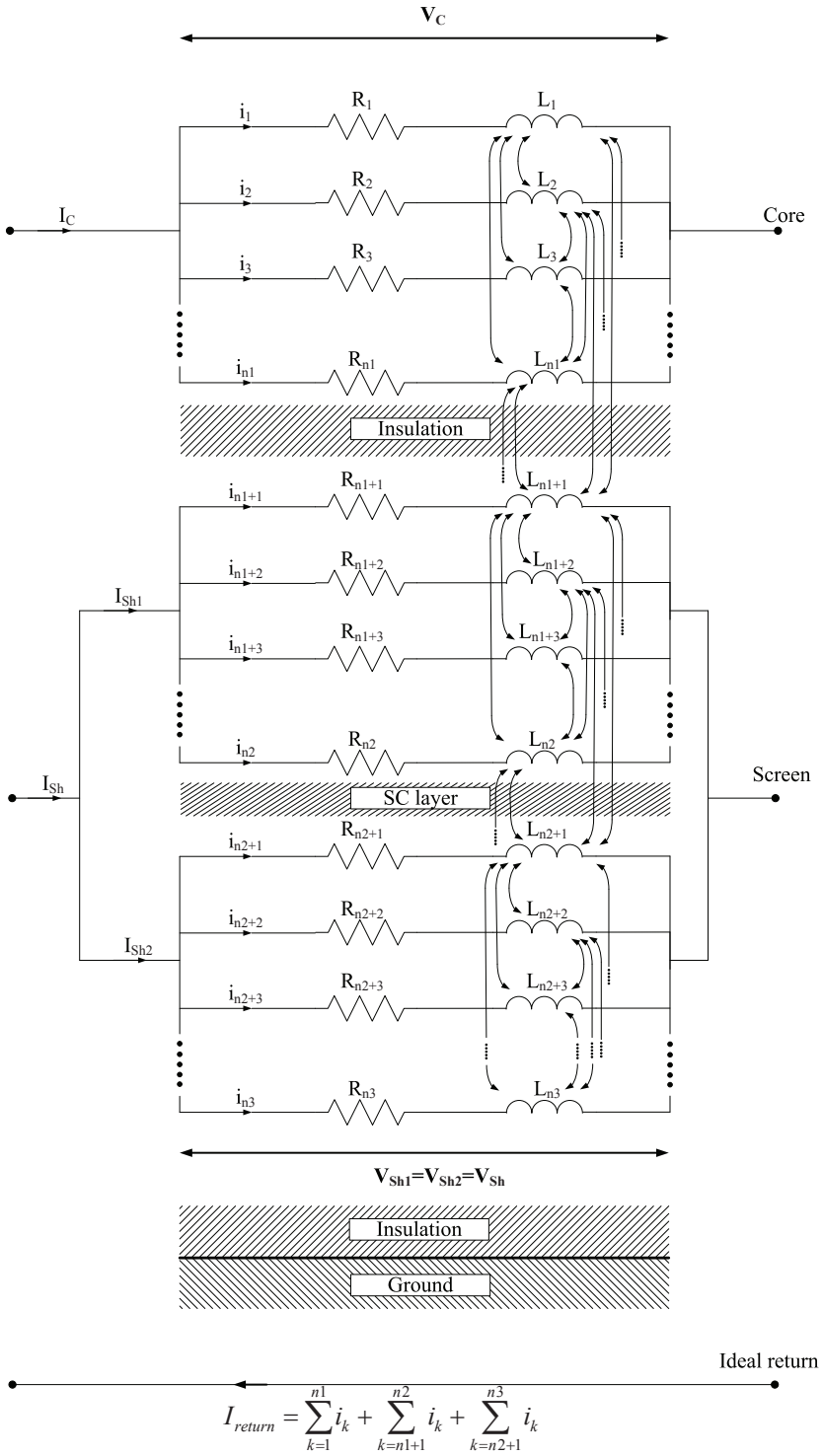

Figure 13.6: *Equivalent impedance scheme of the lumped constant parameters for subdivision of conductors of one cable. The dots · illustrate a continuing (as previous) further many connections.*

$$\begin{bmatrix} V_C \\ V_{Sh1} \\ V_{Sh2} \end{bmatrix} = [R] \cdot \begin{bmatrix} I_C \\ I_{Sh1} \\ I_{Sh2} \end{bmatrix} + j\omega [L] \begin{bmatrix} I_C \\ I_{Sh1} \\ I_{Sh2} \end{bmatrix} \tag{13.3}$$

where $[R]$ and $[L]$ are matrices of the size NxN with $N = n1 + n2 + n3$.

For an element with uniform current distribution, the resistance is simply calculated from equation 13.4 for each element i of a conductor n.

$$R_i = \frac{\rho_n}{A_i}\ \Omega/m \tag{13.4}$$

The inductance on the other hand is a bit more complicated to calculate. The inductance is divided into loop self inductance and mutual inductance between two loops. The mutual inductance is caused by current flowing in one loop due to flux linkage with a loop containing current. This is described by equation 13.5 [45] for linear medium such as each subconductor with uniform resistivity and current distribution.

$$L_{ii} = \frac{\Psi_{ii}}{I_i} \tag{13.5a}$$

$$L_{ij} = \frac{\Psi_{ij}}{I_i} \tag{13.5b}$$

where L_{ii} is the flux linkage in the loop itself per unit current and
L_{ij} is the flux linkage from loop j to i per unit current in loop i.

In order to calculate the flux linkage, the magnetic field because of an element itself and between two elements, with the fictitious return path, must be calculated. Flux linkage between an element and its return path is given by equation 13.6 where the relative permeability of the element and return path are $\mu_i = \mu_q = \mu$.

$$\begin{aligned} \Psi &= \int_{D_{ij}}^{D_{iq}} \frac{\mu_0 \mu_i I_i}{2\pi} \frac{1}{x} dx + \int_{D_{q_1 q_2}}^{D_{jq}} \frac{\mu_0 \mu_q I_i}{2\pi} \frac{1}{x} dx \\ &= \frac{\mu_0 I_i \mu}{2\pi} ln\left(\frac{D_{iq} D_{jq}}{D_{ij} D_{q_1 q_2}}\right) \end{aligned} \tag{13.6}$$

where the first part of the right side in the equation is for *element i to j and return* and the second part is for *return to itself and back to element j*
D is the GMD between two current paths.
i and j are two elements.
q is the return path.

When using a circular current path, enclosing all subconductors, and choosing its radius r_q as $r_q >> D_{iq}$ for any element i, then it can be assumed that $D_{iq} = D_{jq} = D_{q_1 q_2} = r_q$. The self and mutual inductances for the elements can then be calculated from equation 13.7, where $ln(D)$ is a logarithmic mean distance.

$$L_{ii} = \frac{\Psi_{ii}}{I_i} = \frac{\mu_0 \mu}{2\pi} ln\left(\frac{r_q}{D_{ii}}\right) \tag{13.7a}$$

$$L_{ij} = \frac{\Psi_{ij}}{I_i} = \frac{\mu_0 \mu}{2\pi} ln\left(\frac{r_q}{D_{ij}}\right) \tag{13.7b}$$

13.3 Impedance matrix

The impedance matrix for three cables including three conductors (core and two screens) divided into subconductors, has the form of equation 13.8 for every frequency point. As the return path is lossless and fictitious, [R] is a diagonal matrix. If each core is divided into n_1 subconductors, each inner screen into n_2 subconductors and each outer screen into n_3 subconductors, the size of the matrices in equation 13.8 is NxN with $N = 3 \cdot (n_1 + n_2 + n_3)$.

$$\begin{bmatrix} [R_{c1}] & & \\ & [R_{c2}] & \\ & & [R_{c3}] \end{bmatrix} + j\omega \begin{bmatrix} [L_{c1}] & [L_{c1c2}] & [L_{c1c3}] \\ [L_{c1c2}] & [L_{c2}] & [L_{c2c3}] \\ [L_{c1c3}] & [L_{c2c3}] & [L_{c3}] \end{bmatrix} \tag{13.8}$$

where $c1$, $c2$ and $c3$ denote cables 1, 2 and 3 respectively.
$[R_{ci}]$ is given by equation 13.9.
$[L_{ci}]$ is given by equation 13.10.
$[L_{cicj}]$ is given by equation 13.11.

$$[R_{ci}] = \begin{bmatrix} R_{ci_1} & & & & & & & & \\ & \ddots & & & & & & & \\ & & R_{ci_{n_1}} & & & & & & \\ & & & R_{ci_{n_1+1}} & & & & & \\ & & & & \ddots & & & & \\ & & & & & R_{ci_{n_2}} & & & \\ & & & & & & R_{ci_{n_2+1}} & & \\ & & & & & & & \ddots & \\ & & & & & & & & R_{ci_{n_3}} \end{bmatrix} \tag{13.9}$$

where n_1 is the number of subconductors in core conductor.
n_2 is the number of subconductors in the inner screen conductor.
n_3 is the number of subconductors in the outer screen conductor.

$$[L_{ci}] = \begin{bmatrix} L_{ci_1} & L_{ci_1ci_2} & \dots & L_{ci_1ci_{n_1}} & \dots & L_{ci_1ci_{n_2}} & \dots & L_{ci_1ci_{n_3}} \\ L_{ci_2ci_1} & L_{ci_2} & \dots & L_{ci_2ci_{n_1}} & \dots & L_{ci_2ci_{n_2}} & \dots & L_{ci_2ci_{n_3}} \\ \vdots & & & \ddots & & & & \vdots \\ L_{ci_{n_1}ci_1} & L_{ci_{n_1}ci_2} & \dots & L_{ci_{n_1}} & \dots & L_{ci_{n_1}ci_{n_2}} & \dots & L_{ci_{n_1}ci_{n_3}} \\ \vdots & & & & \ddots & & & \vdots \\ L_{ci_{n_2}ci_1} & L_{ci_{n_2}ci_2} & \dots & L_{ci_{n_2}ci_{n_1}} & \dots & L_{ci_{n_2}} & \dots & L_{ci_{n_2}ci_{n_3}} \\ \vdots & & & & & \ddots & & \vdots \\ L_{ci_{n_3}ci_1} & L_{ci_{n_3}ci_2} & \dots & L_{ci_{n_3}ci_{n_1}} & \dots & L_{ci_{n_3}ci_{n_2}} & \dots & L_{ci_{n_3}} \end{bmatrix} \tag{13.10}$$

$$[L_{cicj}] = \begin{bmatrix} L_{ci_1cj_1} & L_{ci_1cj_2} & \dots & L_{ci_1cj_{n_1}} & \dots & L_{ci_1cj_{n_2}} & \dots & L_{ci_1cj_{n_3}} \\ L_{ci_2cj_1} & L_{ci_2cj_2} & \dots & L_{ci_2cj_{n_1}} & \dots & L_{ci_2cj_{n_2}} & \dots & L_{ci_2cj_{n_3}} \\ \vdots & & & \ddots & & & & \vdots \\ L_{ci_{n_1}cj_1} & L_{ci_{n_1}cj_2} & \dots & L_{ci_{n_1}cj_{n_1}} & \dots & L_{ci_{n_1}cj_{n_2}} & \dots & L_{ci_{n_1}cj_{n_3}} \\ \vdots & & & & \ddots & & & \vdots \\ L_{ci_{n_2}cj_1} & L_{ci_{n_2}cj_2} & \dots & L_{ci_{n_2}cj_{n_1}} & \dots & L_{ci_{n_2}cj_{n_2}} & \dots & L_{ci_{n_2}cj_{n_3}} \\ \vdots & & & & & \ddots & & \vdots \\ L_{ci_{n_3}cj_1} & L_{ci_{n_3}cj_2} & \dots & L_{ci_{n_3}cj_{n_1}} & \dots & L_{ci_{n_2}cj_{n_2}} & \dots & L_{ci_{n_3}cj_{n_3}} \end{bmatrix} \tag{13.11}$$

The desired impedance matrix for three single core cables is a 6x6 matrix, for every frequency point, as shown in equation 12.5 on page 130. In order to obtain such a 6x6 matrix, first the two screen layers must be joined into one as is explained for the new improvements of layered screen in chapter 12. Then the remaining matrix must be reduced to form only single element for all 6 conductors (3 cores and 3 screen conductors). These reductions are explained in chapters 13.3.1-13.3.2.

13.3.1 Matrix reduction, single screen

From figure 13.6 it is obvious that the voltage drops over each subconductor of the two screen layers are identical because of the parallel connection, see equation 13.12. For simplification, equation 13.12 is shown only for 1 out of 3 cables. Same procedure is used for all three cables.

$$\begin{bmatrix} V_{Sh} \\ V_{Sh} \\ V_{Sh} \\ \vdots \\ V_{Sh} \end{bmatrix} = \begin{bmatrix} Z_{n_1+1} & \dots & Z_{(n_1+1)(n_2)} & \dots & Z_{(n_1+1)(n_3)} \\ \vdots & \ddots & & & \vdots \\ Z_{(n_2)(n_1+1)} & \dots & Z_{(n_2)} & \dots & Z_{(n_2)(n_3)} \\ \vdots & & \ddots & & \vdots \\ Z_{(n_3)(n_1+1)} & \dots & Z_{(n_3)(n_2)} & \dots & Z_{(n_3)} \end{bmatrix} \cdot \begin{bmatrix} i_{n_1+1} \\ \vdots \\ i_{n_2} \\ \vdots \\ i_{n_3} \end{bmatrix} \tag{13.12}$$

Because of these parallel connections and identical voltage drops, it is possible to bundle the subconductors and forming a single screen with voltage/current relationship for all subconductors of both screen layers. This procedure is based on [59] for OHL and is explained in appendix D.3. It is possible to bundle the two screen layers in such a way, even though they are made of entirely different materials and separated by a SC layer. This is because of the fact that at every single junction, the two screen layers are directly connected and hence they have identical voltage drop between two minor section ends. The result after bundling the two screens into a single screen with a subset of subconductors is shown in equation 13.13. This solution is for a single cable only, similar procedure is used for all three cables.

$$\begin{bmatrix} V_{Sh} \\ \vdots \\ V_{Sh} \end{bmatrix} = \begin{bmatrix} Z'_{n_1+1} & \dots & Z'_{(n_1+1)(n_2)} \\ \vdots & \ddots & \vdots \\ Z'_{(n_2)(n_1+1)} & \dots & Z'_{(n_2)} \end{bmatrix} \cdot \begin{bmatrix} i_{n_1+1} \\ \vdots \\ i_{n_2} \end{bmatrix} \tag{13.13}$$

where $Z'_{ik} = Z_{ik} - (Z_{kn_3} - Z_{k(n_1+1)})(Z_{n_3} - Z_{(n_1+1)n_3})^{-1} Z_{in_3}$

After reducing the two layered screen into a single conductor divided into n_2 subconductors, the size of the impedance matrix in equation 13.8 is N'xN' with $N' = 3 \cdot (n_1 + n_2)$.

13.3.2 Matrix reduction, conductor matrix

In order to reduce the matrices even further and obtain the desired size of 6x6, similar reduction method is used again in order to remove all subconductor rows/columns except for the first row/column of every main conductor (i.e. 3 cores and 3 screens). As explained in appendix D.3, first the first line of every conductor is placed in top of the matrix and all other subcondcutors are placed below.

The full elemental matrix for three cables after submerging screens and re-ordering is as shown in equation 13.14, where ci represents cable i.

$$\begin{bmatrix} V_{c1_1} \\ V_{c2_1} \\ V_{c3_1} \\ V_{c1_{n_1+1}} \\ V_{c2_{n_1+1}} \\ V_{c3_{n_1+1}} \\ V_{c1_2} \\ \vdots \\ V_{c1_{n_1}} \\ V_{c1_{n_1+2}} \\ \vdots \\ V_{c1_{n_2}} \\ V_{c2_2} \\ \vdots \\ V_{c2_{n_1}} \\ V_{c2_{n_1+2}} \\ \vdots \\ V_{c2_{n_2}} \\ V_{c3_2} \\ \vdots \\ V_{c3_{n_1}} \\ V_{c3_{n_1+2}} \\ \vdots \\ V_{c3_{n_2}} \end{bmatrix} = \begin{bmatrix} [Z_1] & [Z_2] \\ [Z_3] & [Z_4] \end{bmatrix} \cdot \begin{bmatrix} i_{c1_1} \\ i_{c2_1} \\ i_{c3_1} \\ i_{c1_{n_1+1}} \\ i_{c2_{n_1+1}} \\ i_{c3_{n_1+1}} \\ i_{c1_2} \\ \vdots \\ i_{c1_{n_1}} \\ i_{c1_{n_1+2}} \\ \vdots \\ i_{c1_{n_2}} \\ i_{c2_2} \\ \vdots \\ i_{c2_{n_1}} \\ i_{c2_{n_1+2}} \\ \vdots \\ i_{c2_{n_2}} \\ i_{c3_2} \\ \vdots \\ i_{c3_{n_1}} \\ i_{c3_{n_1+2}} \\ \vdots \\ i_{c3_{n_2}} \end{bmatrix} \tag{13.14}$$

where Z_1 is of the size [6x6] when all three cables are included and contains the first rows/columns of each conductor.
Z_2 is of the size [6x(n_1-1+n_2-1)] when all three cables are included and contains the first rows and columns $2, \ldots, n_1, n_1+2, \ldots, n_2$ of each conductor.
Z_3 is of the size [(n_1+n_2-2)x6] when all three cables are included and contains rows $2, \ldots, n_1, n_1+2, \ldots, n_2$ and the first columns of each conductor.
Z_4 is of the size [(n_1+n_2-2)c(n_1+n_2-2)] when all three cables are included and contains rows/-columns $2, \ldots, n_1, n_1+2, \ldots, n_2$ of each conductor.

When the order has been changed in such a way, the matrix is reduced by same method as in chapter 13.3.1 and the result is shown in equation 13.15.

$$[Z_{reduced}] = \begin{bmatrix} Z_{c1_{cc}} & 0 & 0 & Z_{c1_{cs}} & 0 & 0 \\ 0 & Z_{c2_{cc}} & 0 & 0 & Z_{c2_{cs}} & 0 \\ 0 & 0 & Z_{c3_{cc}} & 0 & 0 & Z_{c3_{cs}} \\ Z_{c1_{cs}} & 0 & 0 & Z_{c1_{ss}} & Z_{c1_{ss}c2_{ss}} & Z_{c1_{ss}c3_{ss}} \\ 0 & Z_{c2_{cs}} & 0 & Z_{c1_{ss}c2_{ss}} & Z_{c2_{ss}} & Z_{c2_{ss}c3_{ss}} \\ 0 & 0 & Z_{c3_{cs}} & Z_{c1_{ss}c3_{ss}} & Z_{c2_{ss}c3_{ss}} & Z_{c3_{ss}} \end{bmatrix} \tag{13.15}$$

where $[Z_{reduced}] = [Z1] - [Z2][Z4]^{-1}[Z3]$.
$Z_{ci_{cc}}$ is the impedance of the core conductor for cable i.
$Z_{ci_{cs}}$ is the impedance of the mutual between core and screen of cable i.
$Z_{ci_{ss}}$ is the impedance of the layered screen conductor for cable i.
$Z_{ci_{ss}cj_{ss}}$ is the impedance between screens of two cables.
There is no mutual impedance between cores of two cables because they are screened.
There is no mutual impedance between core-screen ($Z_{ci_{cs}}$) loops of two cables.

A more into deep explanation of the matrix reduction from elemental matrix to conductor matrix is given in appendix D.4.

As explained before, in order to calculate the subconductor inductances, a lossless fictitious return path was introduced. Then it is possible to calculate the impedance of each element, where there is no total current flowing in the fictitious return. When there is no total current flowing in the fictitious return, then for each cable $[I_{Sh}] = -[I_C]$. If the screen voltage is subtracted from the core voltage, the loop impedance between core and screen can be calculated from equation 13.16.

$$\begin{aligned} \begin{bmatrix} V_C - V_{Sh} \\ V_{Sh} \end{bmatrix} &= \begin{bmatrix} Z_{cc} - Z_{cs} & Z_{cs} - Z_{ss} \\ Z_{cs} & Z_{ss} \end{bmatrix} \begin{bmatrix} I_C \\ -I_C \end{bmatrix} \\ V_C - V_{Sh} &= (Z_{cc} - 2Z_{cs} + Z_{ss})I_C \\ V_{Sh} &= (Z_{cs} - Z_{ss})I_C \\ V_C &= (Z_{cc} - 2Z_{cs} + Z_{ss})I_C + (Z_{cs} - Z_{ss})I_C = (Z_{cc} - Z_{cs})I_C \end{aligned} \tag{13.16}$$

Therefore the reduced impedance matrix with the effect of the fictitious return path removed is as shown in equation 13.17.

$$[Z_{reduced}] = \begin{bmatrix} Z_{c1_{cc}} & 0 & 0 & Z'_{c1_{cs}} & 0 & 0 \\ 0 & Z_{c2_{cc}} & 0 & 0 & Z'_{c2_{cs}} & 0 \\ 0 & 0 & Z_{c3_{cc}} & 0 & 0 & Z'_{c3_{cs}} \\ Z'_{c1_{cs}} & 0 & 0 & Z_{c1_{ss}} & Z_{c1_{ss}c2_{ss}} & Z_{c1_{ss}c3_{ss}} \\ 0 & Z'_{c2_{cs}} & 0 & Z_{c1_{ss}c2_{ss}} & Z_{c2_{ss}} & Z_{c2_{ss}c3_{ss}} \\ 0 & 0 & Z'_{c3_{cs}} & Z_{c1_{ss}c3_{ss}} & Z_{c2_{ss}c3_{ss}} & Z_{c3_{ss}} \end{bmatrix} \tag{13.17}$$

where $Z'_{ci_{cs}} = Z_{ci_{cc}} - 2Z_{ci_{cs}} + Z_{ci_{ss}}$.

As only the impedances of the 6 conducting layers have been calculated, the insulation and ground must be evaluated in order to construct the full phase impedance matrix used for terminal condition calculations.

13.3.3 Impedances of non-conducting layers and ground

The proximity effect only appears in conducting material, as it is related to current distribution because of magnetic field of two close conductors. Therefore only conductors are subdivided. For obtaining the full impedance matrix for cable simulations, the impedances of insulation layers and ground must be included. Impedance of the non-conducting layers can be calculated by use of the same analytical equations as previously used and explained in appendix B. Those impedances are:

$$Z_{inner-ins}(\omega) = \frac{j\omega\mu_{inner-ins}}{2\pi} ln\left(\frac{r_2}{r_1}\right)$$
$$Z_{outer-ins}(\omega) = \frac{j\omega\mu_{outer-ins}}{2\pi} ln\left(\frac{r_4}{r_3}\right)$$

where $\mu_{inner-ins}$ and $\mu_{outer-ins}$ are the inner and outer insulations permeability.
r_2 and r_1 are respectively the outer and inner radius of the insulation.
r_4 and r_3 are respectively the outer and inner radius of the insulation.

The earth is yet another conducting layer in the cable system. It has however been shown in chapters 8.3.1 and 8.3.2 how the earth impedance does not largely influence the correctness of the simulation results. It is therefore sufficient for the purpose of this thesis to use previously explained ground impedances calculated by use of analytical equations in appendix B.1.7.

It has previously been explained how at higher frequencies the ground return has smaller and smaller influence on the simulation results. Furthermore, the proximity effect only has influence at higher frequencies. Therefore, for studies requiring the subdivision of conductors, most often analytical calculations for the ground impedance will be sufficient. For cases, when ground return needs to be more accurately simulated, it is possible to add the ground as another conductor to be subdivided by the same principles as explained in chapter 13.2. The size of the ground subconductors should be made smaller close to the cables, than farther away. This can be obtained by an exponential distribution of subconductors.

By introducing the ground as a subconductor, the number of calculations will increase and hence will also simulation time. It has already been shown for both flat formation and tight trefoil formation, in chapters 7.3.2 and 8.3.1 respectively, how the analytical calculations of core conductor impedances are accurate and correct. It is therefore not necessary to subdivide the core conductor but possible to make use of analytical calculations. This will decrease again the increment in simulation time, making it feasible to subdivide the ground conductor.

In the case used in this thesis though, the ground impedance is analytically calculated and the core conductor is subdivided.

13.3.4 Full phase impedance matrix

The full phase impedance matrix is explained in chapter 2.1. This matrix is re-given in equation 13.18.

$$[Z_{phase}] = \begin{bmatrix} z^1_{11} & -z^1_{12} & z_{gm_{12}} & z_{gm_{12}} & z_{gm_{13}} & z_{gm_{13}} \\ -z^1_{12} & z^1_{22} & z_{gm_{12}} & z_{gm_{12}} & z_{gm_{13}} & z_{gm_{13}} \\ z_{gm_{12}} & z_{gm_{12}} & z^2_{11} & -z^2_{12} & z_{gm_{23}} & z_{gm_{23}} \\ z_{gm_{12}} & z_{gm_{12}} & -z^2_{12} & z^2_{22} & z_{gm_{23}} & z_{gm_{23}} \\ z_{gm_{13}} & z_{gm_{13}} & z_{gm_{23}} & z_{gm_{23}} & z^3_{11} & -z^3_{12} \\ z_{gm_{13}} & z_{gm_{13}} & z_{gm_{23}} & z_{gm_{23}} & -z^3_{12} & z^3_{22} \end{bmatrix} \tag{13.18}$$

where $z^i_{11} = (Z^i_{C_{outer}} + Z^i_{CSh_{ins}} + Z^i_{Sh_{inner}}) + (Z^i_{Sh_{outer}} + Z^i_{ShG_{ins}} + Z^i_{ground}) - 2Z^i_{Sm}$ is the impedance of the current path through core conductor with return in ground.
$z^i_{22} = Z^i_{Sh_{outer}} + Z^i_{ShG_{ins}} + Z^i_{ground}$ is the impedance of the current path through screen conductor with return in ground.
$z^i_{12} = (Z^i_{Sh_{outer}} + Z^i_{ShG_{ins}} + Z^i_{ground}) - Z^i_{Sm}$.
Z^i_{Sm} is the mutual impedance of the loops core-screen and screen-ground.
$z_{gm_{ij}}$ is the mutual ground impedance between cables i and j.

When using subdivision of conductors, the impedances of equation 13.17 can be related to equation 13.18 as follows:

Z_{cc}	is the impedance of conducting material (except for earth) in the current path through core conductor with return in ground.
Z_{ss}	is the impedance of conducting material (except for earth) in the current path through screen conductor with return in ground.
Z_{cs}	is the impedance of conducting material in the mutual of the loops core-screen and screen-ground.
$Z_{ci_{ss}cj_{ss}}$	is the mutual conducting impedance (except for earth) between screens of adjacent cables.

Therefore, when subdividing core and screen conductors and using analytical calculations for insulations and ground impedances, the parameters of the matrix in equation 13.18 will be as shown in equation 13.19.

$$\begin{aligned} Z^i_1 &= Z_{ci_{cc}} + Z_{ci_{inner-ins}} + Z_{ci_{outer-ins}} + Z_{ci_{ground}} \\ Z^i_2 &= Z_{ci_{ss}} + Z_{ci_{outer-ins}} + Z_{ci_{ground}} \\ Z^i_{SM} &= Z'_{ci_{cs}} + Z_{ci_{outer-ins}} + Z_{ci_{ground}} \\ Z^i_{gmij} &= Z_{ci_{ss}cj_{ss}} + Z_{cij_{ground}} \end{aligned} \tag{13.19}$$

The expression in equation 13.19 gives the full impedance matrix, which is the output of the program. This output will be used as an input to the cable terminal simulation. An output at 1 MHz for the three phase system of HR2, explained in chapter 8 is shown in equation 13.20.

$$[Z_{phase}] = \begin{bmatrix} 1.18+7.52i & -1.17+8.49i & 1.17+5.01i & 1.17+5.01i & 1.17+5.02i & 1.17+5.02i \\ -1.17+8.49i & 1.18+5.71i & 1.17+5.01i & 1.17+5.01i & 1.17+5.02i & 1.17+5.02i \\ 1.17+5.01i & 1.17+5.01i & 1.18+7.52i & -1.17+8.49i & 1.17+5.02i & 1.17+5.02i \\ 1.17+5.01i & 1.17+5.01i & -1.17+8.49i & 1.17+5.71i & 1.17+5.02i & 1.17+5.02i \\ 1.17+5.02i & 1.17+5.02i & 1.17+5.02i & 1.17+5.02i & 1.17+7.54i & -1.17+7.58i \\ 1.17+5.02i & 1.17+5.02i & 1.17+5.02i & 1.17+5.02i & -1.17+7.58i & 1.17+5.73i \end{bmatrix} \tag{13.20}$$

For gaining an insight into the results of the calculated impedances, figures 13.7-13.9 compares real and imaginary parts of the impedances for analytical calculations and by use of equation 13.19.

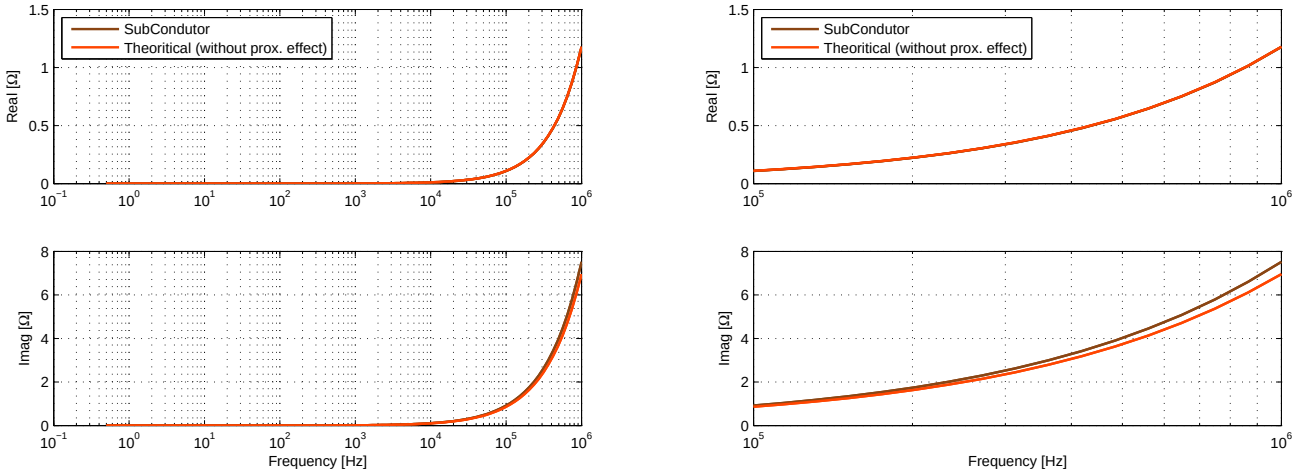

Figure 13.7: *Changes in the impedance matrix when including the proximity effect, compared to analytical calculations. The calculations show differences in Z_1^1 from equation 13.18.*

From figures 13.7-13.9 it can be seen how the imaginary part of the subconductor calculations becomes considerably larger above 100 kHz for subdivision method compared to the analytical method. This difference is due to the proximity effect at higher frequencies.

Furthermore it can be seen that at 1 MHz (frequency at which damping for the intersheath mode has been shown to be inaccurate, chapter 8.3.2) the difference is as large as 42% for the mutual impedance.

13.4 Terminal conditions

As explained in chapter 2.1 the terminal conditions of a cable are as shown in equation 13.21.

$$I_{\text{send}} = Y_c \cdot V_{\text{send}} - H \cdot (Y_c \cdot V_{\text{rec}} - I_{\text{rec}}) \tag{13.21a}$$
$$I_{\text{rec}} = Y_c \cdot V_{\text{rec}} - H \cdot (Y_c \cdot V_{\text{send}} - I_{\text{send}}) \tag{13.21b}$$

where all parameters are a function of ω
$I_{\text{send}}/V_{\text{send}}$ is the sending end current/voltage

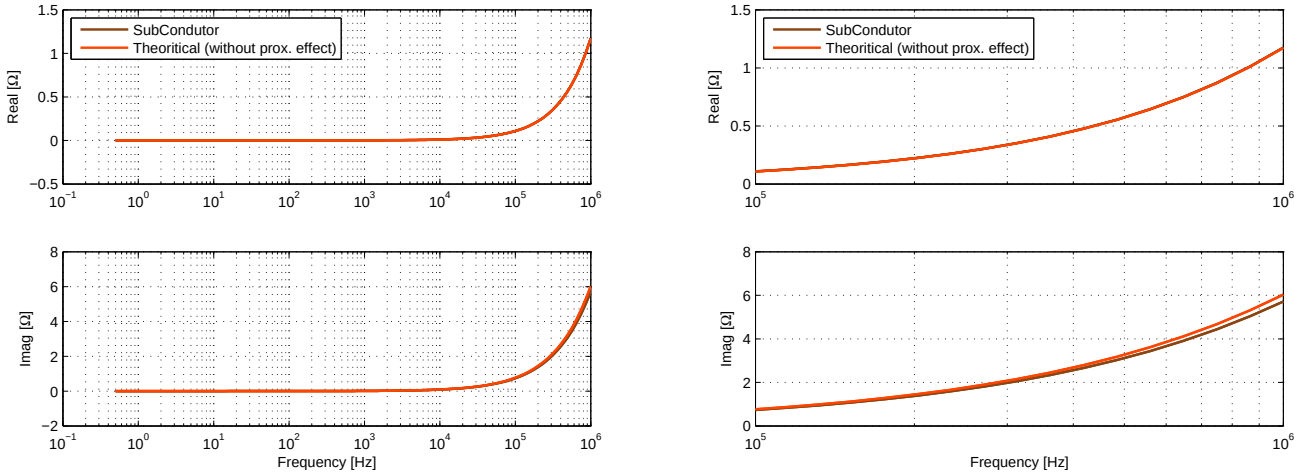

Figure 13.8: *Changes in the impedance matrix when including the proximity effect, compared to analytical calculations. The calculations show differences in Z_2^1 from equation 13.18.*

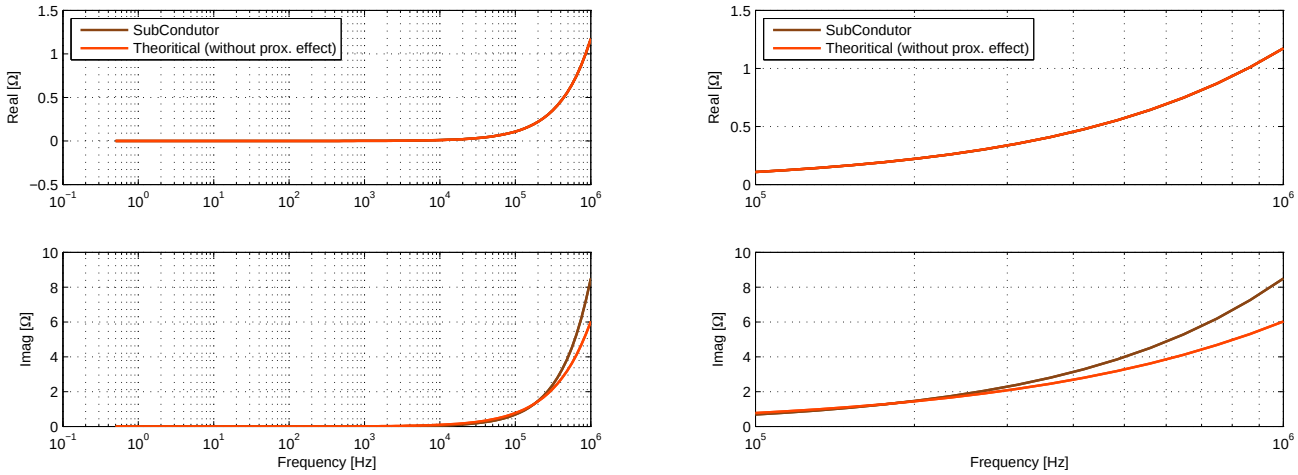

Figure 13.9: *Changes in the impedance matrix when including the proximity effect, compared to analytical calculations. The calculations show differences in Z_{SM}^1 from equation 13.18.*

$I_{\text{rec}}/V_{\text{rec}}$ is the receiving end current/voltage
$Y_c(\omega) = \frac{Y(\omega)}{\sqrt{Y(\omega) \cdot Z(\omega)}}$ is the cable's characteristic admittance
$H(\omega) = e^{-\gamma l} = e^{-\sqrt{Y(\omega)Z(\omega)}l}$ is the cable's propagation matrix

The cable model used in this thesis is the frequency dependent phase model (Universal Line Model) in EMTDC/PSCAD. This model uses analytical calculations of $Y(\omega)$ and $Z(\omega)$ for fitting Y_C and H in time domain.

The new program with results explained in chapter 13.3.4 delivers the full impedance matrix of $Z(\omega)$ as an output value. Therefore, in order to calculate the terminal conditions using this program, $Z(\omega)$ should be an input and only $Y(\omega)$ should be analytically calculated. Based on this, the Universal Line Model should fit Y_C and H.

At present, it is not possible to use externally calculated $Z(\omega)$ and $Y(\omega)$ as input for the frequency dependent phase model in EMTDC/PSCAD. Nevertheless, this option is an attractive possibility for the program and will be available in the near future. For now, in order to test the cable model, a MATLAB setup of the Universal Line Model, made by The Manitoba HVDC Research Centre (owner and distributor of EMTDC/PSCAD) is used. This MATLAB setup has been manipulated, such that it does not use analytical calculations, but imports $Z(\omega)$ from results obtained as explained in chapter 13.3.4.

13.4.1 Comparison of field measurements and simulations

The new modelling procedure, by including proximity effect, is verified against the intersheath field measurement results for setup $\#2$, in chapter 8.2.4. The simulation results when using subdivision of conductors to calculate $Z(\omega)$ are compared to both field measurement results and simulation results for the layered screen explained in chapter 12.1. The layered screen simulation results have in figure 12.5 of chapter 12.2 been compared to field measurement results and normal EMTDC/PSCAD simulations, showing significant improvements in frequencies below 10 kHz.

The method of subdividing the conductors, in chapters 13.1-13.3.4 include the layered screen and proximity effect. Figure 13.10 therefore shows comparison of including improvement of layered screen only and of taking also the proximity effect into account and therefore including both improvements.

As explained in chapter 12.2, only the lower frequency (below 10 kHz) damping was correctly simulated after adding layered screen as an improvement. The high frequency oscillations were not damped correctly. As shown in figure 13.10, the simulation results are very accurate when both layered screen and proximity effect are included. There is almost a perfect agreement between improved simulations and field measurement results.

Another conclusion drawn from results in figure 13.10, is regarding the simulation time. As explained before, the calculations of $Z(\omega)$ by use of subdivision method requires larger amount of calculations and simulation time than for analytical calculations. The subdivision calculations on the other hand only need to be performed once for each cable, as they will not change when terminal connections of the cable are changed. For simulations having wrong high frequency oscillations, in order to ensure convergence of the simulations, the simulation time step for every simulation needs to be very small. This requires long simulation time for each and every simulation performed. When the impedance has on the other hand been correctly calculated once, including the proximity effect and hence more damping at higher frequencies, the simulation time step for every simulation study of the cable system, can be increased. This is because the high frequency oscillations have been removed. This will in turn lower the simulation time for every cable system study performed, as the risk of non-convergence is much smaller.

When choosing cable data and during GMD calculations, some approximations are used:

- Number of subconductors is chosen such that increasing the number of subconductors by 1 per conductor, will not cause a change in the impedance, larger than 5%.
- Self GMD of elements is assumed $0.2215(l + w)$ instead of using exact calculations.
- Mutual GMD of elements is calculated with only 4 sectors, or 6 points, for calculating distances.

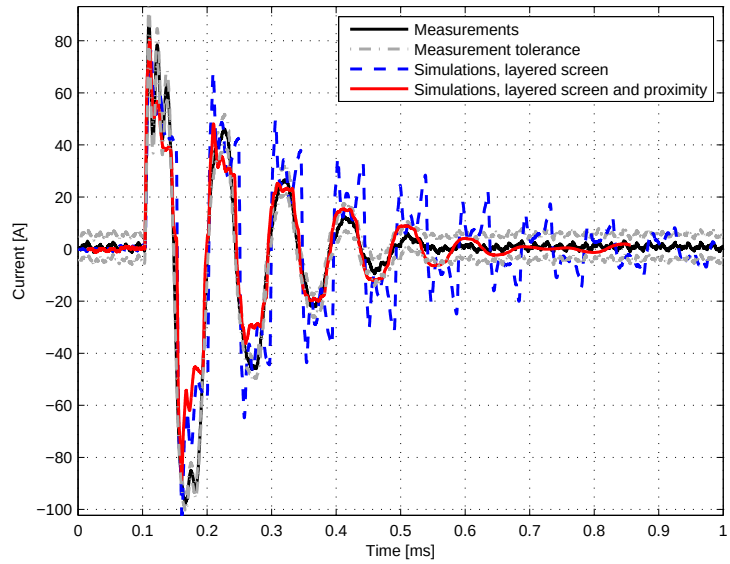

(a) Sending end current

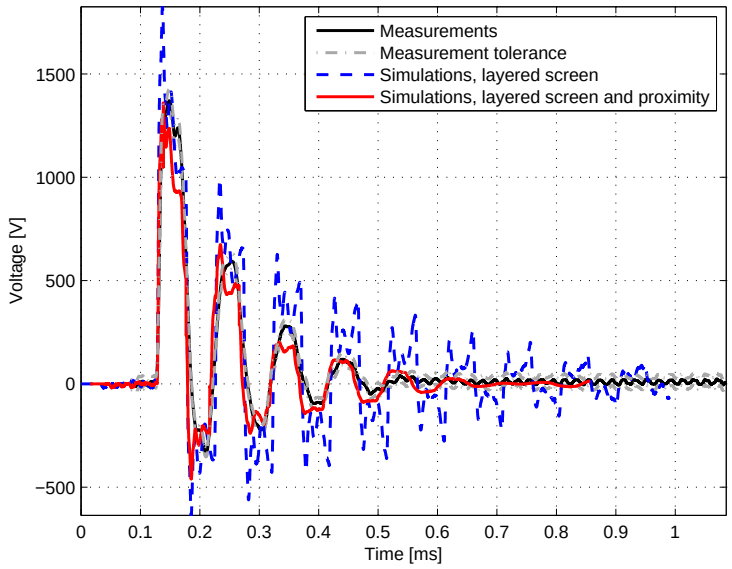

(b) Receiving end voltage

Figure 13.10: *Comparison of the sending end current and receiving end voltage on energised screen conductor for the intersheath mode.*

As the comparison of simulation and field measurement results gives such a good agreement, all of the above approximations can be accepted.

As the new modelling method has been verified for the intersheath mode setup, it is applicable to be

tested and validated for simulations of long HV AC cables, cables having crossbonding points.

CHAPTER 14

Improved model validation

As shown i part III, simulations and field test results agree quite well until the first intersheath reflection is measured. This indicates that the cable model as such is very good for cables without crossbondings as only coaxial modes are excited. The presence of crossbonding points in long cables causes intersheath current waves to propagate between the screens of adjacent cables. The propagation characteristics of these intersheath currents are strongly affected by proximity effects, which are not taken into account by the existing simulation software when calculating the series impedance. Therefore, after the intersheath waves reach the measurement point, large deviations develop and the existing simulation model is therefore insufficient for long crossbonded cable systems.

In chapters 12-13, two relevant improvements of the cable model have been described. Firtsly the physical layout of the screens are modelled more correctly and secondly both the correct physical screen layout is modelled and the proximity effect is taken into account. Furthermore, these improvements have been validated against measurements when explicitly exciting an intersheath mode. As new simulation results are in very good agreement with field measurements of purely the intersheath mode on a single minor section, they are assumed validated for crossbonded cables. In order to verify this, these improvements will now also be validated against field measurements of longer crossbonded cables. For this validation, field measurement set #3 in chapter 9 and set #4 in chapter 10 are used. As the cable model from chapter 13, based on subdivision of conductors, comprises both described improvements, this cable model is used for verification against field measurements on crossbonded cables.

14.1 Validation against a single major section, measurement set #3

The single major section is a 2510 m long 150 kV cable system having 3 minor sections. There are two crossbonding points but no grounding of the screen. The field measurements and results are given in chapter 9. When analysing the comparison of field measurement and simulation results, for a non-improved cable model, it was observed that the deviation between measurements and simulations appear when the intersheath mode starts flowing, see figure 9.10 in chapter 9.3. This comparison is therefore performed again, after improvements of simulating the intersheath mode have been included.

Figure 14.1 shows a comparison of simulation and field test results for the sending end current. In figure 14.1(a), simulation results from figure 9.9 are compared to simulations results of the improved cable model and in figure 14.1(b) only the simulated results from the improved model are compared to field test results.

As shown in figure 14.1(b), the simulation results are very accurate when both layered screen and proximity effect are included. There is almost a perfect agreement between improved simulations and field measurement results.

The first intersheath reflection is measured at approximately 20 μs, see chapter 9.3 on page 111. Both simulation results are therefore fully accurate until this point in time is reached, as only the coaxial wave

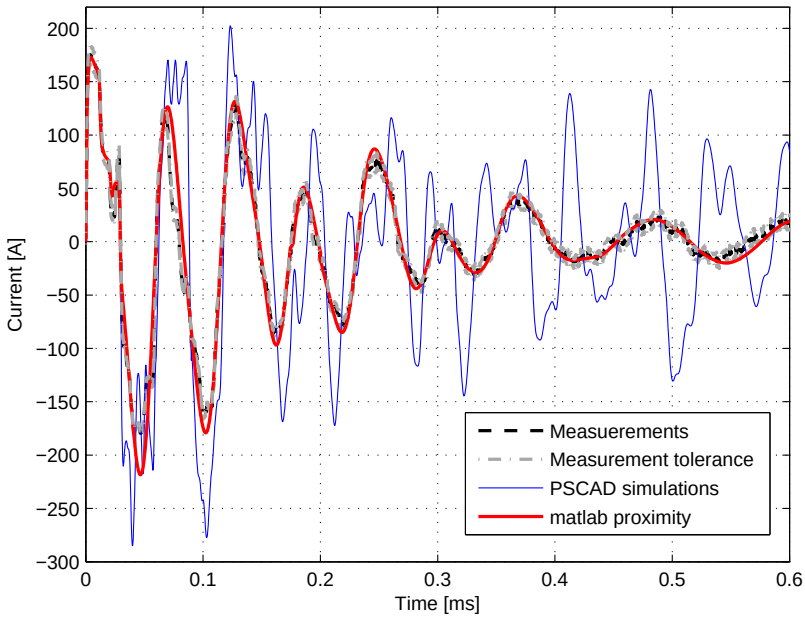

(a) Field measurements, Universal Line Model simulations (PSCAD simulations) and simulations using subdivision of conductors (MATLAB proximity simulations)

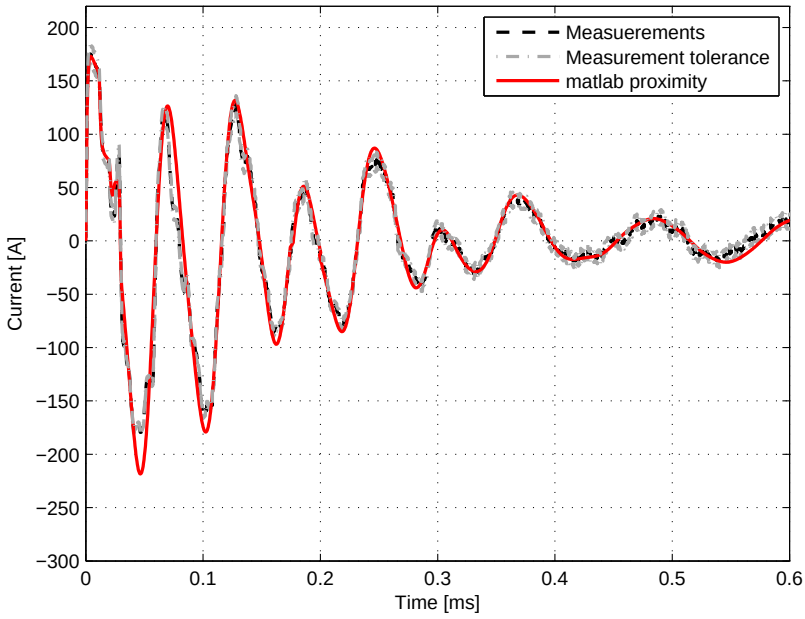

(b) Field measurements and simulations using subdivision of conductors (MATLAB proximity simulations)

Figure 14.1: *Comparison for the measured and simulated core current at the sending end of the energised phase for the single major section cable line.*

is measured which has already been proven to be correctly simulated by analytical calculations. After this time however, the measured and non-improved simulated current waves become more and more out of phase as the current becomes affected by more crossbondings and reflected waves. In this setup, there are no grounding points of the screen along the cable line, only at cable ends, and therefore only the crossbonding points are considered a source of deviation. It can also be observed how, despite deviation, some similarities between PSCAD simulations and measurements are shown, where the simulated wave appears to be less damped and delayed. this can be caused by inaccuracies in the real and imaginary parts of the characteristic admittance $Y_C = \frac{Y(\omega)}{\sqrt{Y(\omega)Z(\omega)}}$, where $Z(\omega)$ is calculated by different means in the improved modelling method of including proximity effect.

Because of correct screen impedances, the damping for the improved cable model is correct. The difference in impedances of the line constant calculations and the improved subdivision of conductors method is shown in figure 13.7-13.9 and calculated to be up to 42 $\%$ at 1 MHz. Correcting the impedance matrix as shown in these figures, results in a correct intersheath mode propagation damping, which is the cause for the much better simulation results. The damping at the higher frequencies (above 10 kHz), because of the proximity effect, is clearly seen by the fact that the high frequency oscillations of the PSCAD simulations in figure 14.1(a) are fully damped in the MATLAB simulations in figure 14.1(b). This does not only help with more accurate simulation results, but furthermore it allows for a larger time step giving faster simulations and less probability for an unstable model, which often is the case for long cables with many separately modelled minor sections and crossbonding points.

14.2 Validation against multiple major sections, measurement set #4

The multiple major section is a 55 km long 150 kV cable system having 11 major sections with total of 22 crossbonding points and 10 grounding of the screens, apart from at cable ends. The field measurements and results are given in chapter 10. As for the single major section, then when analysing the comparison of field measurement and simulation results of the multiple major sections, for a non-improved cable model, it was observed that the deviation between measurements and simulations appear when the intersheath mode starts flowing, see figure 10.6 on page 122. Furthermore, as shown in figure 10.6(b), the ground mode is equal to zero and will therefore not affect the simulation results. It is therefore assumed that improving only the simulations of intersheath mode will result in accurate simulation results. this will be validated in this chapter.

Figure 14.2 shows a comparison of simulation and field test results for the sending end current. In figure 14.2(a), simulation results from figure 10.5 are compared to simulations results of the improved cable model and in figure 14.2(b) only the simulated results from the improved model are compared to field test results.

As shown in figure 14.2(b), the simulation results are very accurate when both layered screen and proximity effect are included. There is almost a perfect agreement between improved simulations and field measurement results.

The first intersheath reflection is measured at approximately 11 μs, see chapter 10.3 on page 120. Both simulation results are therefore fully accurate until this point in time is reached. After this time however, the measured and non-improved simulated current waves become inaccurately damped as the current becomes affected by many crossbondings and reflected waves. As for the single major section, then despite deviation, some similarities between PSCAD simulations and measurements are shown, where the simulated wave appears to be less damped. A correctly calculated $Z(\omega)$ matrix, when including the actual physical layout of the screen and the proximity effect, results in the correct damping of the current

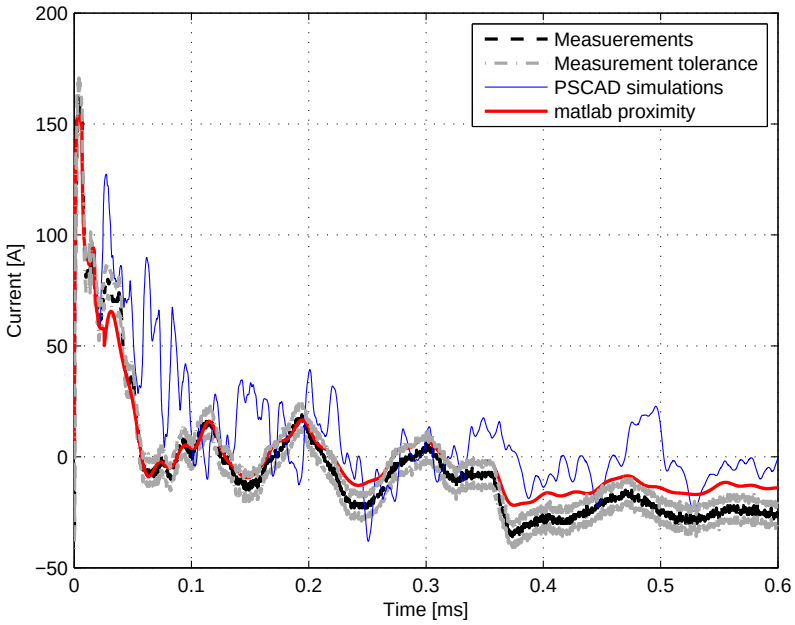

(a) Field measurements, Universal Line Model simulations (PSCAD simulations) and simulations using subdivision of conductors (MATLAB proximity simulations)

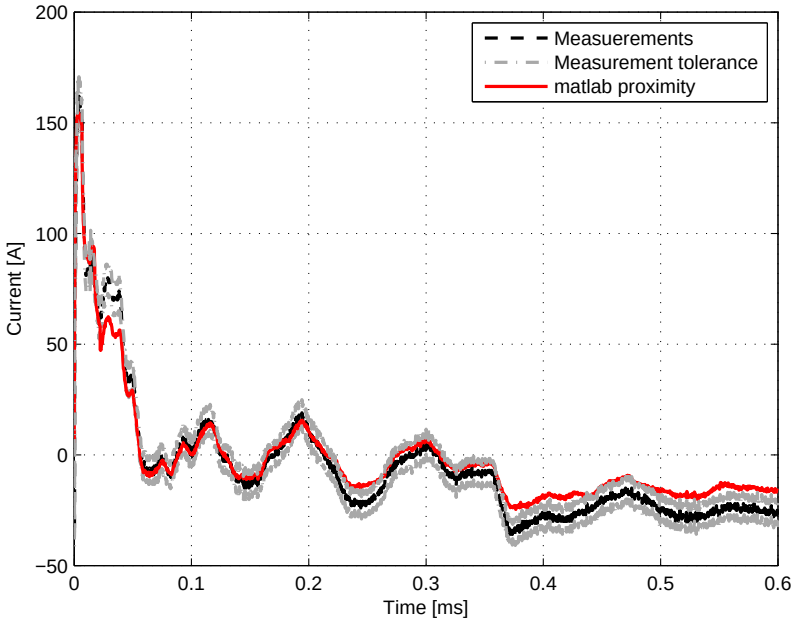

(b) Field measurements and simulations using subdivision of conductors (MATLAB proximity simulations)

Figure 14.2: *Comparison for the measured and simulated core current at the sending end of the energised phase for the multiple major section cable line.*

waves.

Correcting the impedance matrix, results in a correct intersheath mode propagation damping, which is the cause for the much better simulation results. The damping at the higher frequencies (above 10 kHz), because of the proximity effect, is seen by the fact that the high frequency oscillations of the PSCAD simulations in figure 14.2(a) are fully damped in the MATLAB simulations in figure 14.2(b). Only the modelling of the propagation characteristics of the intersheath mode have been improved and as the improved simulation results agree quite well with field measurements, the assumption of the ground mode not influencing the simulation results is correct. This was also to be expected, as the ground mode is shown to be equal to zero in figure 10.6(b) on page 122.

The improved cable model described in chapter 13 is therefore accurate and sufficient to fulfill the project aim of validating and verifying the improved model accuracy against long cable measurements.

CHAPTER 15

Summary for Cable Model Improvements

One of the major contributions from the research presented in this thesis is cable model improvements. The existing cable model has been shown to be inaccurate when it comes to modelling the intersheath mode, see chapters 7.3 and 8.3. The model is therefore improved with respect to the screen layers. In chapter 12 of this part of the thesis, the actual physical layout of the screen is modelled more accurately by use of layered screen and resulting in a more accurate damping of the lower frequencies (below 10 kHz). The more accurate damping is obtained because when the correct physical layout of the screen is implemented in the model, the series impedance matrix $Z(\omega)$ becomes more correct. The terminal conditions of the cable depend on $Y_C(\omega) = \frac{Y(\omega)}{\sqrt{Y(\omega)Z(\omega)}}$ and $H(\omega) = e^{-\sqrt{Y(\omega)Z(\omega)}l}$. Therefore when $Z(\omega)$ is more correct, the cable's simulated terminal conditions will become more correct.

Even though the simulations of when modelling the layered screen and field test results agree quite well regarding the damping in the waveforms of the lower frequency component, all simulation results still have inadequate damping of higher frequency oscillations. Because of this, it is not sufficient to increase the damping at lower frequencies by introducing the layered screen. As the intersheath current propagates between the screens of adjacent cables, their propagation characteristics are also affected by proximity effects which are not taken into account by the simulation software. The cable model improvements are therefore expanded and the proximity effect is included as shown in chapter 13. This results in more accurate simulation results at higher frequencies (above 10 kHz). This is validated to give precise simulation results when explicitly exciting the intersheath mode, the origin of deviation between original simulations and field measurements.

In order to validate the improved cable model for transmission cables, firstly field measurements on a single major section with 2 crossbonding points and secondly field measurements on a cable with 11 major sections are performed. Comparison of these field measurement results and simulations including both layered screen and proximity effect does not give deviation outside of the tolerance of the field measurements. The improved cable model described in chapter 13 is therefore accurate and sufficient and the final goal and aim of the project is fulfilled by delivering a reliable model for simulating long distance cables and a transmission system that is mostly or fully underground.

Part V

Conclusions

CHAPTER 16

Conclusions

In today's societies, interest towards using underground HV cables, in preference to the customary OHL, for power transmission has increased considerably. This is mainly due to the expansion of cities, further additions of land reserves and public resistance against erection of new OHLs in the vicinity of people's residence.

In Denmark, all existing 150 kV and 132 kV transmission network shall be undergrounded during the next 20 years and all existing 400 kV transmission lines will be undergrounded gradually as more experience is gathered. Furthermore shall all new transmission lines at all voltage levels be put in ground, except for a single 400 kV line connecting the country to Germany.

For various system studies it is necessary to have precise simulation models. Small errors for short cables can become a larger problem when length of the cables and number of crossbonding points are increased. It is therefore important that differences between simulations and measurements are identified, studied and eliminated. This PhD project has been formulated due to the lack of knowledge of actual accuracy and reliability of available cable models. The performed high frequency transient field measurements on long HV cables with several crossbondings and screen groundings allowed to reveal differences between the results of measurements and the results of simulations performed using the existing cable models.

16.1 Summary of the thesis

The aim of the project was to fulfil the requirements of describing cable modelling, validating and verifying model accuracy and improving if necessary, with the following goals:

- To theoretically analyse and investigate accuracy of existing cable models (solved in chapter 2-6)
- To perform field test measurements for model validation (solved in chapter 7-11)
- To investigate and identify the cause of inaccurate simulation results if there are any (solved in chapter 7-8)
- To improve the cable model and obtain acceptable simulation results if necessary (solved in chapter 12-13)
- To validate and verify the model accuracy against long cable measurements if necessary (solved in chapter 14-15)

The aim was to deliver a reliable model, which can be used as an instrument in planning and problem solving for long distance cables and a transmission system that is mostly or fully underground.

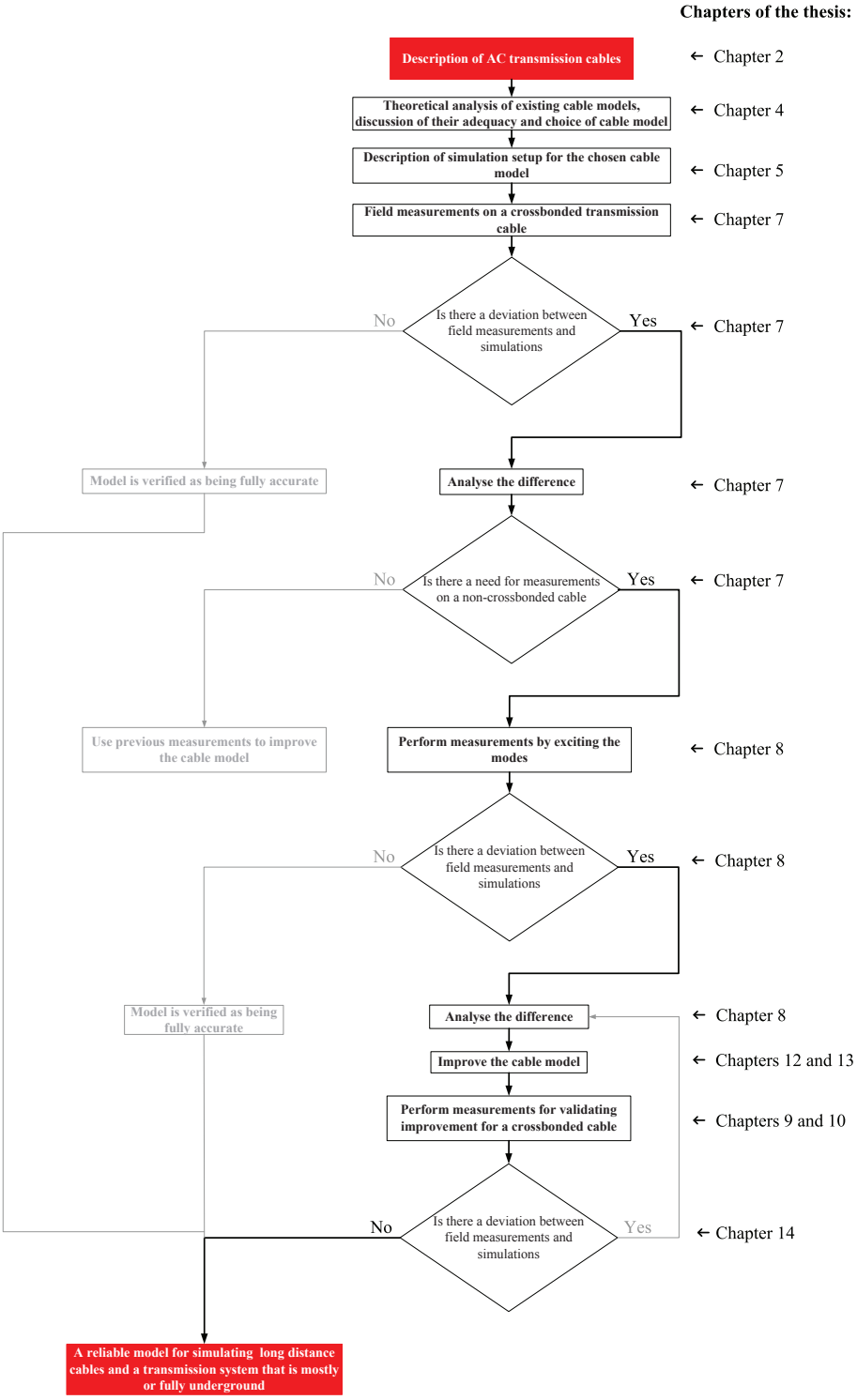

Figure 16.1: *Flow diagram for the solution process of the thesis.*

Figure 16.1 introduces the solution process of the thesis, in order to summarise the goals and aims and associate them with the thesis chapters.

The flow diagram in figure 16.1 gives an overview over the performed studies and to which chapter of the thesis the study is described. The flow diagram shows all possible routes of the project, where the paths not followed are light grey and the path followed in the project, because of findings during the research, is highlighted in a darker colour.

The project is begun with a general description of AC transmission cables. This is done for gaining an understanding of the nature of transmission cables before starting to simulate them. A physical and mathematical description of the cables, their parameters and terminal conditions is given. After describing AC transmission cables, the existing models, choice of model and how to perform simulations is described. Before starting to simulate long cables, validate the accuracy and perform improvements, the existing modelling techniques are analysed and described. The major literature on existing modelling methods is evaluated. Two cable models are considered to be most adequate for high frequency transient studies for validating cable parameters and modelling procedures with measurements. Those methods are the universal line model and the zcable model. Amongst those, the universal line model, which is available in EMTDC/PSCAD (named the Frequency Dependent Phase Model), is chosen to be used for simulations and model validations in the following chapters. Before using the model, the modelling procedure in EMTDC/PSCAD is described and documented.

Based on the chosen simulation model, the validation procedure begins. First field measurements on a crossbonded transmission cable are performed. These first field tests show deviation between simulation and field test results and indicate crossbonding points as being the origin of disagreement. In order to explicitly point out the origin of deviation, measurements on a non-crossbonded cable were performed. A coaxial mode and intersheath modes were excited and a deviation between simulation and field measurement results because of the intersheath mode was observed. This phenomena was observed for

- a 400 kV, 7.6 km cable laid in flat formation
- a 150 kV, 2.5 km cable laid in tight trefoil formation
- a 150 kV, 55 km cable laid in tight trefoil.

As the cable model has been proven to be inaccurate when it comes to modelling the intersheath mode, the model is improved in respect to the screen layers. The actual physical layout of the screen is modelled more accurately by use of layered screen and resulting in a more accurate damping of the lower frequencies (below 10 kHz). The proximity effect is also included, resulting in more accurate simulation results at higher frequencies (above 10 kHz). This is validated to give precise simulation results when explicitly exciting the intersheath mode, the origin of deviation between original simulations and field measurements.

In order to validate the improved cable model for transmission cables, firstly field measurements on a single major section with 2 crossbonding points and secondly field measurements on a cable with multiple major sections are performed. Comparison of these field measurement results and improved simulations does not give deviation outside of the tolerance of the field measurements. Hence the final goal and aim of the project is fulfilled by a delivery of a reliable model for simulating long distance cables and a transmission system that is mostly or fully underground.

16.2 New contributions

In this thesis the accuracy of an existing cable model, the Universal Line Model implemented in EMTDC/PSCAD (Frequency Dependent Phase Model), is tested against high frequency field measurements.

The usual practice for validating a cable model has been to compare the simulation results with frequency domain calculations transformed to the time domain by use of Inverse Fast Fourier Transform (IFFT). This, however, does not ensure the accuracy of the entry parameters of the modelling procedure (e.g. geometry), the parameter conversions, and the modelling assumptions. In this thesis, the focus has therefore been to use high frequency field test results for model validation.

- A major contribution from the research presented in this thesis is field measurements for model validation.
- A major contribution from the research presented in this thesis is a split impedance matrix from modal excitation, resulting in exact identification of wrong impedance calculations.

From comparison of field measurements and simulation results, more accurate modelling of the cable screen conductors is suggested. A deviation between simulations and field measurements appear because of intersheath mode resulting from crossbonding points. It is therefore concluded that the existing simulation model, the Universal Line Model, is precise and accurate for short cables or cables with no crossbonding points. This is because the presence of crossbonding points in long cables causes excitation of intersheath waves when the screens are shifted between cables. After the intersheath waves reach the measurement point, large deviations develop and the simulation model is therefore insufficient for (long) crossbonded cable systems.

Two different model improvements are implemented and tested both when the intersheath mode is explicitly energised and on long crossbonded cable lines. These model improvements are validated against excitation of the intersheath mode in order to verify the correctness of the improved simulations and against long crossbonded cable lines in order to verify the correctness when the intersheath mode is excited because of the crossbonding points and not because of the measurement setup.

Layered sheath

For improving the low frequency (below 10 kHz) impedance calculations of the cable model, a more accurate simulation of the physical layout of the screen is implemented. It is common to model the screen as a single solid hollow conductor with an increased resistivity. In this thesis, for the layered screen method, the screen is modelled as two hollow conductors with no potential difference and a semiconductive (SC) layer in-between.

- A major contribution from the research presented in this thesis is a new cable impedance equivalent circuit where two conducting layers connected in both ends and separated only by a SC layer are included. This method is different from the usual cable impedance equivalent of *conductor-insulator-conductor-insulator (-conductor-insulator)* representation.

Proximity effect

For improving the high frequency (above 10 kHz) impedance calculations, the proximity effect between cables and between each strand of the screen of each cable is included in the modelling procedure. The cable impedance matrix is calculated by use of a finite element approach called subdivision of conductors. The subdivision of conductors' method is a known solution to including proximity effect. The use of it in this thesis however does not only depend on [52, 53, 54], but also includes some new improvements.

- A major contribution from the research presented in this thesis is the usage of calculating the full phase impedance matrix where conductors are subdivided and insulation impedances are included by analytical calculations, where permeability in one insulation layer can vary from the next.
- A major contribution from the research presented in this thesis is the implementation of actual ground return path by use of analytical calculations. The fictious return path for inductance calculations is eliminated.
- A major contribution from the research presented in this thesis is a description of how practically the ground could be subdivided to increase the correctness of ground impedance calculations. This can be achieved by using analytical calculations for core conductor as from the split impedance matrix method, its impedance is validated as correct by analytical calculations.
- A major contribution from the research presented in this thesis is an implementation of two screen layers in the subdivision method. These layers are with same voltage potential and separated by a SC layer. This ensures that the screen no longer is modelled as two solid hollow conductors, but with one stranded and one solid conductor.
- A major contribution from the research presented in this thesis is a description and implementation of the subdivision method for a full three phase cable system, having 9 conductors, where each cable has two conducting screen layers.
- A major contribution from the research presented in this thesis is a validation of the subdivision method against field test measurements results.

16.3 Future work

It is shown in chapter 16.1-16.2 how the problem formulated for the project has been solved. Nevertheless, several topics worthwhile a more in-depth study have not been pursued in this thesis.

- Sensitivity analysis of the cables electrical parameters. The cable model has been shown to be sensitive to cable parameters, which often are not accurately given by manufacturers. A sensitivity analysis of each parameter and comparison of simulated and measured sending end current and receiving end voltage could give a better insight into which parameters are more important and what could be the worst case scenario for simulations.
- Implementation of the suggested ground return as a subdivided conductor. This method has been theoretically described but not implemented.
- Implementation of the external impedance matrix into EMTDC/PSCAD. At present, it is not possible to use externally calculated $Z(\omega)$ and $Y(\omega)$ as input for the frequency dependent phase model in EMTDC/PSCAD. Nevertheless, this option is an attractive possibility for the program and will be available in the near future.
- An in depth study of the reduction in simulation time, when increasing the simulation time step because of less higher oscillations after including proximity effect in impedance calculations.
- Comparison of improved simulation results to other modelling software, such as ATP and Power Factory.

Bibliography

[1] H. Shinozaki *et al.*, "Abnormal voltages of a core at crossbonding point," *J. Tech. Lab. Chugoku Electric Power Co.*, vol. 39, pp. 175–198, 1971.

[2] N. Nagaoka and A. Ametani, "Transient calculations on crossbonded cables," *IEEE Transactions on Power Apparatus and Systems*, vol. PAS-102, no. 4, pp. 779–787, april 1983.

[3] L. Martí, "Simulation of transients in underground cables with frequency-dependent modal transformation matrices," *IEEE Transactions on Power Delivery*, vol. 3, no. 3, pp. 1099–1110, july 1988.

[4] B. G. A. Morched and M. Tartibi, "A universal model for accurate calculation of electromagnetic transients on overhead lines and underground cables," *IEEE Transactions on Power Delivery*, vol. 14, no. 3, pp. 1032–1038, july 1999.

[5] T. Yu and J. Martí, "zcable model for frequency dependent modelling of cable transmission systems," in *Proc. IPST'01*, Rio De Janeiro, Brazil, 2001, paper IPST01-146.

[6] T. N. N. Nagaoka and A. Ametani, "Phase domain modelling of frequency-dependent transmission lines by means of an arma model," *IEEE Transactions on Power Delivery*, vol. 11, no. 1, pp. 401–411, january 1996.

[7] B. Gustavsen, J. Sletbak, and T. Henriksen, "Simulation of transient sheath overvoltages in the presence of proximity effects," *IEEE Transactions on Power Delivery*, vol. 10, no. 2, pp. 1066–1075, april 1995.

[8] C. F. Jensen, *Switching studies for the Horns Rev 2 wind farm main cable*. Aalborg, Denmark: Thesis from Master student, Aalborg University, 2009.

[9] E. F. Peschke and R. von Olshausen, *Cable Systems for High and Extra-High Voltage*. Munich, Germany: Pirelli, 1999, iSBN: 3-89578-118-5.

[10] L. Martí, "Simulation of electromagnetic transients in underground cables using the emtp," *IEE conference on Advances in Power System Control, Operation and Management*, pp. 147–152, December 1993.

[11] B. Gustavsen, *A study of overvoltages in high voltage cables with emphasis on sheath overvoltages*. Trondheim, Norway: PhD. Thesis, NTH, 1986.

[12] A. Ametani, "Transient calculation of a transmission line using superposition law," *IEE Proceedings*, vol. 133, no. 5, pp. 263–269, July 1986.

[13] ——, “Wave propagation characteristics of cables,” *IEEE Transactions on Power Apparatus and Systems*, vol. PAS-99, no. 2, pp. 499–505, March/April 1980.

[14] H. W. Dommel, *EMTP Theory Book*, 2nd ed. Vancouver, British Columbia Canada: Microtran Power System Analysis Corporation, Vancouver, British Columbia, 1996.

[15] S. A. Schelkunoff, “The electromagnetic theory of coaxial transmission lines and cylindrical shields,” *The Bell System Technical Journal*, vol. 13, no. 4, pp. 532–579, 1934.

[16] A. Ametani, “Frequency-dependent parameter of cables,” *Text of EMTP Summer Course at Leuven EMTP Center*, 24 July to 28 July 1989.

[17] N. Watson and J. Arrillaga, *Power systems electromagnetic transient simulation*, 1st ed. London, United Kingdom: The Institution of Electrical Engineers (IEE), 2003, iSBN: 0-85296-106-5.

[18] N. Tleis, *Power Systems Modelling and Fault Analysis*. Oxford, UK: Newnes, 2008, iSBN-13: 978-0-7506-8074-5.

[19] M. H. R. C. Inc., *PSCAD Online Help - Bergeron Model*, v4.2.1 ed. Winnipeg, Canada: Manitoba HVDC Research Centre Inc., 2006.

[20] ——, *PSCAD Online Help - Bergeron Line Model*, v4.2.1 ed. Winnipeg, Canada: Manitoba HVDC Research Centre Inc., 2006.

[21] ——, *PSCAD Online Help - Model Selection*, v4.2.1 ed. Winnipeg, Canada: Manitoba HVDC Research Centre Inc., 2006.

[22] ——, *PSCAD Online Help - Frequency Dependent (Phase) Model*, v4.2.1 ed. Winnipeg, Canada: Manitoba HVDC Research Centre Inc., 2006.

[23] L. M. Wedepohl and C. S. Indulkar, “Switching overvoltages in long crossbonded cable systems using the fourier transform,” *IEEE Transactions on Power Apparatus and Systems*, vol. PAS-98, no. 4, pp. 1476–1480, July/August 1979.

[24] A. Budner, “Introduction of frequency-dependent line parameters into an electromagnetic transients program,” *IEEE Transactions on Power Apparatus and Systems*, vol. PAS-89, no. 1, pp. 88–97, January 1970.

[25] J. K. Snelson, “Propagation of travelling waves on transmission lines- -frequency dependen parameters,” *IEEE Transactions on Power Apparatus and Systems*, vol. PAS-91, no. 1, pp. 85–91, January/February 1972.

[26] W. S. Meyer and H. W. Dommel, “Numerical modelling of frequency-dependent transmission-line parameters in an electromagnetic transients program,” *IEEE Transactions on Power Apparatus and Systems*, vol. PAS-93, pp. 1401–1409, September/October 1974.

[27] J. R. Martí, “Accurate modelling of frequency-dependent transmission lines in electromagnetic transient simulations,” *IEEE Transactions on Power Apparatus and Systems*, vol. PAS-101, no. 1, pp. 147–157, January 1982.

[28] C. Dufour and H. Le-Huy, “Highly accurate modeling of frequency-dependent balanced transmission lines,” *IEEE Transactions on Power Delivery*, vol. 15, no. 2, pp. 610–615, April 2000.

[29] T.-C. Yu and J. R. Martí, "A robust phase-coordinates frequency-dependent underground cable model (zcable) for the emtp," *IEEE Transactions on Power Delivery*, vol. 18, no. 1, pp. 189–194, January 2003.

[30] B. Gustavsen and A. Semlyen, "Rational approximation of frequency domain responses by vector fitting," *IEEE Transactions on Power Delivery*, vol. 14, no. 3, pp. 1052–1061, July 1999.

[31] J. B. Fraleigh and R. A. Beauregard, *Linear Algebra*, 3rd ed. New York: Addison Wesley, 1995, iSBN: 0-201-52675-1.

[32] F. Castellanos and J. Martí, "Full frequency-dependent phase domain transmission line modal," *IEEE Transactions of Power Systems*, vol. 12, no. 3, pp. 1331–1339, August 1997.

[33] F. M. F. Castellanos and J. Martí, "Phase-domain multiphase transmission line models," *International Journal of Electrical Power and Energy Systems*, vol. 19, no. 4, pp. 241–248, May 1997.

[34] Fluke. (Seen on 19-11-2008) Earth ground resistance - principles, testing methods and applications. [Online]. Available: http://www.newarkinone.thinkhost.com/brands/promos/Earth_Ground_Resistance.pdf

[35] B. Gustavsen, "Panel session on data for modeling system transients - insulated cables," *IEEE Power Engineering Socity Winter Meeting*, vol. 2, pp. 718–723, 2001.

[36] B. Gustavsen, J. A. Martinez, and D. Durbak, "Parameter determination for modeling system transients - part ii: insulated cables," *IEEE Transactions on Power Delivery*, vol. 20, no. 3, pp. 1045–2050, July 2005.

[37] E. Kuffel, W. Zaengl, and J. Kuffel, *High Voltage Engineering: Fundamentals*, 2nd ed. New York: Butterworth-Heinemann, 2000, iSBN: 0-7506-3634-3.

[38] V. M. Atlason, M. Benesz, and J. Kessel, *Analysis and simulation of lightning performance of the 150 kV transmission system in Aalborg*. Aalborg, Denmark: Thesis from Master students, Aalborg University, 2008.

[39] Tektronix. (Seen on 25-9-2008) Digital phosphor oscilloscopes-tds3000b series. [Online]. Available: http://www.tequipment.net/pdf/tektronix/TDS3000B_datasheet.pdf

[40] ——. (Seen on 22-11-2008) P5200 high voltage differential probe. [Online]. Available: http://www.tmsinc.co.kr/02_product/03_probe/04_Differential/Data/P5200.pdf

[41] P. E. M. Ltd., *RGF specification*, PEM.

[42] LEM, *Current Probe Model PR30*. [Online]. Available: http://www.tek-up.com/pdf/PR30_DS.pdf

[43] Tektronix, *TDS3000B Series Digital Phosphor Oscilloscopes*, Tektronix, iSBN: 071-0957-00.

[44] ——, *Service Manual, P5210 High Voltage Differential Probe*, Tektronix, iSBN: 070-9895-03.

[45] D. Cheng, *Field and Wave Electromagnetics*, 2nd ed. Massachusetts: Addison-Wesley publishing company, 1999, iSBN: 0201128195.

[46] A. Ametani, "A general formulation of impedance and admittance of cables," *IEEE Transactions on Power Apparatus and Systems*, vol. PAS-99, no. 3, pp. 902–910, May/June 1980.

[47] L. Wedepohl and D. Wilcox, “Transient analysis of underground power-transmission systems,” *IEE Proceedings*, vol. 120, no. 2, pp. 253–260, February 1973.

[48] A. Greenwood, *Electrical Transients in Power Systems*. New York, USA: Wiley-Interscience, 1971, iSBN: 0 471 32650.

[49] P. E. M. Ltd., *CWT specification*, PEM.

[50] H. D. Silva, *Accuracy and stability improvements in electromagnetic simulations of power transmission lines and cables*. Winnipeg, Canada: PhD. Thesis, University of Manitoba, 2008.

[51] P. Schavemaker and L. van der Sluis, *Electrical power system essentials*, 1st ed. England: John Wiley & Sons, Ltd., 2009, iSBN: 978-0470-51027-8.

[52] P. de Arizon and H. W. Dommel, “Computation of cable impedances based on subdivision of conductors.” *IEEE Transactions on Power Delivery*, vol. PWRD-2, no. 1, pp. 21–27, January 1987.

[53] R. Lucas and S. Talukdar, “Advances in finite element techniques for calculating cable resistances and inductances,” *IEEE Transactions on Power Apparatus and Systems*, vol. PAS-97, no. 3, pp. 875–883, May/June 1978.

[54] R. A. Rivas and J. R. Martí, “Calculation of frequency-dependent parameters of power cables: matrix partitioning techniques,” *IEEE Transactions on Power Delivery*, vol. 17, no. 4, pp. 1085–1092, October 2002.

[55] W. T. Weeks, L. L. Wu, M. F. McAllister, and A. Singh, “Resistive and inductive skin effect in rectangular conductors,” *IBM Journal of research and Development*, vol. 23, no. 6, pp. 652–660, November 1979.

[56] A. J. Sinclair and J. A. Ferreira, “Analysis and design of transmission-line structures by means of the geometric mean distance,” in *1996 IEEE Africon 4th africon conference in africa*, vol. 2, Stellenbosch, South Africa, september 1996, pp. 1062 – 1065.

[57] S. A. Nasar, *Theory and Problems of Electric Power Systems*, 1st ed. New York: Schaum’s, McGraw-Hill, 1990, iSBN: 0-07-045917-7.

[58] F. W. Grover, *Inductance Calculations*, 1st ed. New York: Dover Phoenix Editions, 1946, iSBN: 0-486-49577-9.

[59] M. H. Hesse, “Electromagnetic and electrostatic transmission-line parameters by digital computer,” *IEEE Transactionson Power Apparatus and Systems*, vol. 82, no. 66, pp. 282–291, June 1963.

[60] O. Saad, G. Gaba, and M. Giroux, “A closed-form approximation for ground return impedance of underground cables,” *IEEE Transactions on Power Delivery*, vol. 11, no. 3, pp. 1536–1545, July 1996.

[61] U. S. Gudmundsdottir and et. al., “Field test and simulation of a 400 kv crossbonded cable system,” *IEEE Transactions on Power Delivery*.

[62] T. Nguyen, “Earth-return path impedances of underground cables. part 1: Numerical integration of finite integrals,” *IEE Proceedings*, vol. 145, no. 6, pp. 621–626, November 1998.

[63] A. Deri, G. Tevan, A. Semlyen, and A. Castanheira, "The complex ground return plane - a simplified model for homogeneous and multi-layer earth return," *IEEE Transactions on Power Apparatus and Systems*, vol. PAS-100, no. 8, pp. 3686–3693, August 1981.

[64] V. F. Pollaczek, "Über das feld einer unendlich langen wechselstromdurchflossenen einfachleitung (in german)," *Elektrische Nachrichtentechnik*, vol. 9, no. 3, pp. 339–360, July 1926.

[65] F. Uribe, "Assessing closed-form approximations for underground cable earth impedances," *Power Engineering Society General Meeting, IEEE*, vol. 2, pp. 649–654, July 2003.

[66] V. F. Pollaczek, "Über die felter der wechselstromleitung mit erde und der horizontalantenne (in german)," *Elektrische Nachrichtentechnik*, vol. 7, no. 4, pp. 295–304, May 1927.

[67] N. Srivallipuranandan, *Series impedance and shunt admittance matrices of an underground cable systems*. Vancouver, Canada: M.A.Sc. Thesis, University of British Columbia, 1986.

Part VI

Appendices

APPENDIX **A**

Cable's terminal conditions

When simulating a transmission system, the knowledge of system components is essential. A transmission system is highly frequency dependent and includes many parameters. In order to ensure a correct simulation, these parameters must be correctly represented in the simulation software. For representing the cable transmission line parameters, a CC (Cable Constants) calculation routine is used [14].

Before looking into the CC routine, lets see how the cable parameters affect the calculation of the cable terminal conditions.

In order to model a transmission cable, the well know line equations, A.1a, must be solved.

$$\begin{aligned} \frac{\delta}{\delta x}V(x,\omega) &= Z(\omega)I(x,\omega) \\ \frac{\delta}{\delta x}I(x,\omega) &= Y(\omega)V(x,\omega) \end{aligned} \tag{A.1a}$$

$$\begin{aligned} \Rightarrow \frac{\delta^2}{\delta x}V(x,\omega) &= Z(\omega)\frac{\delta I(x,\omega)}{\delta x} \\ \Rightarrow \frac{\delta^2}{\delta x}I(x,\omega) &= Y(\omega)\frac{\delta V(x,\omega)}{\delta x} \end{aligned} \tag{A.1b}$$

$$\begin{aligned} \Rightarrow \frac{\delta^2}{\delta x}V(x,\omega) &= Z(\omega)Y(\omega)V(x,\omega) = \gamma^2(\omega)V(x,\omega) \\ \Rightarrow \frac{\delta^2}{\delta x}I(x,\omega) &= Y(\omega)Z(\omega)I(x,\omega) = \gamma^2(\omega)I(x,\omega) \end{aligned} \tag{A.1c}$$

$$\begin{aligned} V(x,\omega) &= V_0^+ e^{-\gamma x} + V_0^- e^{\gamma x} \\ I(x,\omega) &= I_0^+ e^{-\gamma x} + I_0^- e^{\gamma x} \end{aligned} \tag{A.1d}$$

For modelling purposes, the voltages/currents at the terminals are of interest. Equations A.2 give the terminal conditions at the sending end $(x = 0)$ and equations A.3 give the terminal conditions at the receiving end $(x = l)$.

$$V_{\text{send}}(\omega) = V_0^+(\omega) + V_0^-(\omega) \tag{A.2a}$$

$$I_{\text{send}}(\omega) = \sqrt{\frac{Y(\omega)}{Z(\omega)}}V_0^+(\omega) - \sqrt{\frac{Y(\omega)}{Z(\omega)}}V_0^-(\omega) \tag{A.2b}$$

$$V_{\text{rec}}(\omega) = e^{-\gamma l} V_0^+(\omega) + e^{\gamma l} V_0^-(\omega) \tag{A.3a}$$

$$I_{\text{rec}}(\omega) = \sqrt{\frac{Y(\omega)}{Z(\omega)}} e^{-\gamma l} V_0^+(\omega) - \sqrt{\frac{Y(\omega)}{Z(\omega)}} e^{\gamma l} V_0^-(\omega) \tag{A.3b}$$

In order to model the relationship between the sending and receiving end of the cable, the unknown incident and reflected traveling waves in A.2 and A.3 must be eliminated. This is shown in equations A.4.

[from A.2a:]

$$V_0^+(\omega) = V_{\text{send}}(\omega) - V_0^-(\omega) \tag{A.4a}$$

[Substitute this into A.2b]:

$$\begin{aligned} I_{\text{send}}(\omega) &= \sqrt{\frac{Y(\omega)}{Z(\omega)}} (V_{\text{send}}(\omega) - V_0^-(\omega)) - \sqrt{\frac{Y(\omega)}{Z(\omega)}} V_0^-(\omega) \\ &= \sqrt{\frac{Y(\omega)}{Z(\omega)}} V_{\text{send}}(\omega) - 2\sqrt{\frac{Y(\omega)}{Z(\omega)}} V_0^-(\omega) \end{aligned} \tag{A.4b}$$

[multiply A.3a by $\sqrt{Y(\omega)/Z(\omega)}$ and subtract A.3b]:

$$\begin{aligned} \sqrt{\frac{Y(\omega)}{Z(\omega)}} \cdot V_{\text{rec}}(\omega) - I_{\text{rec}}(\omega) &= 2\sqrt{\frac{Y(\omega)}{Z(\omega)}} V_0^-(\omega) e^{\gamma l} \\ \Rightarrow 2\sqrt{\frac{Y(\omega)}{Z(\omega)}} V_0^-(\omega) &= e^{-\gamma l} \cdot \left(\sqrt{\frac{Y(\omega)}{Z(\omega)}} \cdot V_{\text{rec}}(\omega) - I_{\text{rec}}(\omega) \right) \end{aligned} \tag{A.4c}$$

[substitute $2\sqrt{\frac{Y(\omega)}{Z(\omega)}} V_0^-(\omega)$ in A.4b by A.4c]:

$$I_{\text{send}}(\omega) = \sqrt{\frac{Y(\omega)}{Z(\omega)}} V_{\text{send}}(\omega) - e^{-\gamma l} \cdot \left(\sqrt{\frac{Y(\omega)}{Z(\omega)}} \cdot V_{\text{rec}}(\omega) - I_{\text{rec}}(\omega) \right) \tag{A.4d}$$

Similar method is used for the receiving end current in order to optain equation A.5

$$I_{\text{rec}}(\omega) = \sqrt{\frac{Y(\omega)}{Z(\omega)}} V_{\text{rec}}(\omega) - e^{-\gamma l} \cdot \left(\sqrt{\frac{Y(\omega)}{Z(\omega)}} \cdot V_{\text{send}}(\omega) - I_{\text{send}}(\omega) \right) \tag{A.5}$$

Now for simplification, the characteristic admittance matrix $Y_c(\omega)$ and the propagation matrix $H(\omega)$ are used, A.6.

$$\begin{aligned} Y_c(\omega) &= \frac{Y(\omega)}{\sqrt{Y(\omega) \cdot Z(\omega)}} \\ H(\omega) &= e^{-\gamma l} = e^{-\sqrt{Y(\omega)Z(\omega)}l} \end{aligned} \tag{A.6}$$

The relationship between the sending and receiving end of the cable are then rewritten as in A.7, where all parameters are a function of ω. Note that here I_{send} and I_{rec} are defined in the same direction; I_{send} into the cable and I_{rec} out of the cable at opposite end.

$$I_{\text{send}} = Y_c \cdot V_{\text{send}} - H \cdot (Y_c \cdot V_{\text{rec}} - I_{\text{rec}}) \tag{A.7a}$$

$$I_{\text{rec}} = Y_c \cdot V_{\text{rec}} - H \cdot (Y_c \cdot V_{\text{send}} - I_{\text{send}}) \tag{A.7b}$$

From the above, it is obviously neccessary to calculate the series impedance matrix, Z, and the shunt admittance matrix, Y, in order to find the true relationship between the sending and receiving end in frequency domain.

APPENDIX **B**

Cable's parameter calculations

The cable parameters Y_C and H are given by equation B.1.

$$Y_c(\omega) = \frac{Y(\omega)}{\sqrt{Y(\omega) \cdot Z(\omega)}} \tag{B.1a}$$

$$H(\omega) = e^{-\gamma l} = e^{-\sqrt{Y(\omega)Z(\omega)}l} \tag{B.1b}$$

For calculating the cable parameters, the series impedance matrix $Z(\omega)$ and the shunt admittance matrix $Y(\omega)$ must be calculated. This appendix demonstrates how these matrices can be calculated.

B.1 Series impedance matrix Z of one single conductor cable

For simplifications, the description starts by using one single core cable with only two conducting layers, a conductor and a screen.

For simplifying the setup of the impedance matrix, a new domain is introduced, [50]. This domain is called mesh domain and is based on simple current loops between each conductor of the cable system. For instance current flowing in core returns in nearest screen, the screen. Current flowing in screen returns in the armour and current flowing in armour returns in ground. The simple case of a two layer cable is shown in figure B.1.

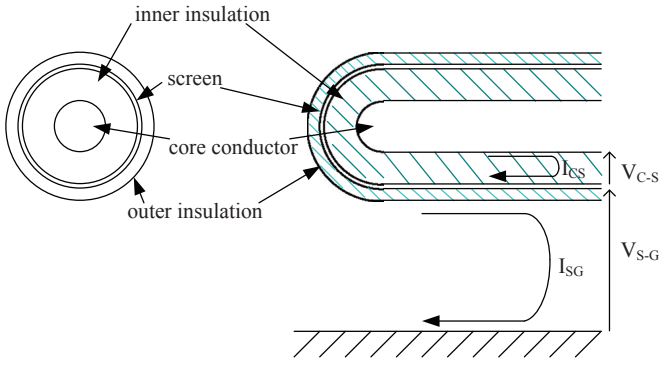

Figure B.1: *A principal cross section of a typical single core XLPE cable with two conductive layers and the current loops for this cable.*

For the cable in figure B.1, there are two current loops. Conductor-screen loop and screen-ground loop. This is expressed in equation B.2.

$$\begin{bmatrix} V_{c-s} \\ V_{s-g} \end{bmatrix} = \overbrace{\begin{bmatrix} z_1 & z_2 \\ z_3 & z_4 \end{bmatrix}}^{Z_{series}} \cdot \begin{bmatrix} I_{cs} \\ I_{sg} \end{bmatrix} \tag{B.2}$$

where $z_1 = Z_{c_{outer}} + Z_{cs_{insul}} + Z_{s_{inner}}$ is the impedance of the loop conductor-screen
$z_4 = Z_{s_{outer}} + Z_{sg_{insul}} + Z_{ground}$ is the impedance of the loop screen-ground
$z_2 = z_3 = -Z_{Sm}$ is the mutual impedance of the loops conductor-screen and screen-ground

Notice that the ground impedance only influences z_4 in the mesh domain equations. For explaining the calculations of the series impedance, each of the z-parts in B.2 are separately calculated. All impedances are given for unit length of the cable.

B.1.1 Calculation of the conductor series impedance $z_{c_{outer}}$

The series impedance of the conductor depends on the resistivity of the conductor, the layout of the conductor and the penetration depth. In simulation programs the resistivity is included for a solid conductor. Normally the conductor is stranded, so that the resistivity must be corrected accordingly, [36]. For the purposes of describing Z_{series} calculations, a solid conductor is considered.

At low frequencies the conductor series impedance approaches the DC resistance of the conductor. At high frequencies the conductor series impedance is equal to the skin effect impedance [60]. This is approximated using B.3 [47]

$$z_{approx} = \frac{\rho m}{2\pi r_1} coth(mr_1) \tag{B.3}$$

where $m = \sqrt{\frac{j\omega\mu}{\rho}}$ is the reciprocal of complex penetration depth (skin depth)
μ is the permeability of the conductor
ρ is the resistivity of the conductor
r_1 is the radius of the conductor.

At high frequencies, $coth(\omega)$ approaches 1 and therefore B.3 also approaches $\frac{\rho m}{2\pi r_1} = \frac{\rho}{2\pi r_1} \cdot \frac{1}{\delta}$, where δ is the skin depth. This is the skin effect impedance.
At low frequencies, $m \cdot coth(mr_1)$ approaches 1 and therefore B.3 also approaches $\frac{\rho}{2\pi r_1}$. This is close to, but not equal to the DC resistance of the conductor. In order to improve the approximation, a degree of freedom is introduced, [47].

$$z_{c_{outer}}(\omega) = \frac{\rho m}{2\pi r_1} coth(kmr_1) + \frac{\rho}{\pi r_1^2}\left(1 - \frac{1}{2k}\right) \tag{B.4}$$

where k is an arbitrary constant to optimize the formula at DC.

B.4 now approaches $\frac{\rho m}{2\pi r_1} + \frac{\rho}{\pi r_1^2}\left(1 - \frac{1}{2k}\right)$ at high frequencies and $\frac{\rho}{2\pi r_1} + \frac{\rho}{\pi r_1^2}\left(1 - \frac{1}{2k}\right)$ at low frequencies. This approximation does not give the exact values for high and low frequencies and can introduce

error in the impedance calculations. Especially for DC calculations and fast transients containing high frequencies. This error has been addressed by a PhD project published in the end of 2008: "'Accuracy and stability improvements in electromagnetic simulations of power transmission lines and cables"' [50]. In the research presented here, the fitting of the propagation and admittance matrixes use the exact DC resistance and skin impedance formulas at low and high frequencies (i.e. below 1 mHz and above 10 kHz respectively).

B.1.2 Calculation of the inner insulation series impedance $z_{cs_{insul}}$

The impedance of the inner insulation, due to the time varying magnetic field, is related to the magnetic permeability of the inner insulation.

$$z_{cs_{insul}}(\omega) = \frac{j\omega\mu_{cs_{insul}}}{2\pi} ln\left(\frac{r_2}{r_1}\right) \tag{B.5}$$

where $\mu_{cs_{insul}}$ is the insulation permeability
r_2 and r_1 are respectively the outer and inner radius of the insulation.

Equation B.5 does not take account for any solenoid effect due to helically wound wired screen. Therefore when the parameters are set for a cable model, the permeability must be corrected to include the solenoid effect, [61], see equation B.6.

$$\mu_{d_{sol}} = \mu_d + \frac{\mu_d}{ln(r_i/r_o)} 2\pi^2 N^2 (r_i^2 - r_o^2) \tag{B.6}$$

where $\mu_d = 4\pi \cdot 10^{-7}$ is the permeability of the insulation.
N is the number of turns per unit length of the cable, r_i is the inner radius of the screen and r_o is the outer radius of the conductor.

By including the correct permeability, the insulation series impedance is fairly accurate and does not include any simplifications that might cause problems when calculating the total series impedance matrix.

B.1.3 Calculation of the screen inner series impedance $z_{s_{inner}}$

As the screen is a cylindrical shell conductor, the internal impedance of the screen is a function of the first and second kind modified Bessel functions, [62]. Where modified Bessel functions are the unique solutions for $y(x)$ of the differential equation $x^2\frac{d^2y(x)}{dx^2} + x\frac{dy(x)}{dx} - (x^2 - n^2)y(x) = 0$, for problems of cylindrical coordinates, [45].

The description on how to obtain the two kinds of modified Bessel functions can be found in various school books on electromagnetism. For summing up the solution is given here:
Modified Bessel function of first kind:

$$I_n(x) = j^{-n} J_n(jx) \tag{B.7}$$

Modified Bessel function of second kind:

$$K_n(x) = \frac{\pi}{2} \frac{I_{-n}(x) - I_n(x)}{sin(n\pi)} \tag{B.8}$$

where $J_n(x)$ is a Bessel function of first kind, a solution to the differential equation $x^2\frac{d^2y(x)}{dx^2} + x\frac{dy(x)}{dx} + (x^2 - n^2)y(x) = 0$
n is the order of the Bessel function
x is the argument of the Bessel function.

The screen internal inner impedance is related to the longditudal voltage difference on the inner surface of the screen because of unit current return through the inner conductor (separated from the screen by the insulation). The screen inner series impedance is therefore, [47]:

$$z_{s_{inner}} = \frac{\rho m}{2\pi r_2} \cdot \frac{I_0(mr_2)K_1(mr_3) + K_0(mr_2)I_1(mr_3)}{I_1(mr_3)K_1(mr_2) - I_1(mr_2)K_1(mr_3)} \tag{B.9}$$

where $I_n(mr_i)$ is the modified Bessel function of first kind of order n and argument mr_i
$K_n(mr_i)$ is the modified Bessel function of second kind of order n and argument mr_i
$m = \sqrt{\frac{j\omega\mu}{\rho}}$ is the reciprocal of complex penetration depth (skin depth)
μ is the permeability of the screen
ρ is the resistivity of the screen
r_2 is the inner radius of the screen
r_3 is the outer radius of the screen.

At the extremes of 0 Hz and very high frequency (for instance 10 MHz or higher), B.9 is equal to the DC resistance and the skin impedance respectively. Therefore, similar to the inner conductor, an approximation for B.9 is:

$$z_{s_{inner}}(\omega) = \frac{\rho m}{2\pi r_2} coth(m(r_3 - r_2)) - \frac{\rho}{2\pi r_2(r_2 + r_3)} \tag{B.10}$$

where $\frac{\rho}{2\pi r_2(r_2+r_3)}$ is to optimize the formula at low frequencies.

B.10 now approaches $\frac{\rho m}{2\pi r_2} - \frac{\rho}{2\pi r_2(r_2+r_3)}$ at high frequencies and $\frac{\rho}{2\pi r_2} - \frac{\rho}{2\pi r_2(r_2+r_3)}$ at low frequencies. This approximation does not give the exact values for high and low frequencies and can introduce error in the impedance calculations. Especially for DC calculations and fast transients containing high frequencies. This error has been addressed by a PhD project published in the end of 2008: "'Accuracy and stability improvements in electromagnetic simulations of power transmission lines and cables"' [50]. In this project, the fitting of the propagation and admittance matrixes use the exact DC resistance, $\frac{\rho}{\pi(r_3^2 - r_2^2)}$, and skin effect impedance, $\frac{\rho m}{2\pi r_2}$, at low and high frequencies (i.e. below 1 mHz and above 10 kHz respectively).

B.1.4 Calculation of the screen outer series impedance $z_{s_{outer}}$

The screen internal outer impedance is related to the longditudal voltage difference on the outer surface of the screen because of unit current return through the ground (separated from the screen by the insulation). The approximate of the Bessel functions for the screen outer series impedance is therefore, [47]:

$$z_{s_{outer}}(\omega) = \frac{\rho m}{2\pi r_3} coth(m(r_3 - r_2)) + \frac{\rho}{2\pi r_3(r_2 + r_3)} \tag{B.11}$$

As for the screen internal inner impedance, B.11 now approaches $\frac{\rho m}{2\pi r_2} + \frac{\rho}{2\pi r_2(r_2+r_3)}$ at high frequencies and $\frac{\rho}{2\pi r_2} + \frac{\rho}{2\pi r_2(r_2+r_3)}$ at low frequencies. This approximation does not give the exact values for high and low frequencies and can introduce error in the impedance calculations. Especially for DC calculations and fast transients containing high frequencies. This error has been addressed by a PhD project published in the end of 2008: "'Accuracy and stability improvements in electromagnetic simulations of power transmission lines and cables"' [50]. In this project, the fitting of the propagation and admittance matrixes use the exact DC resistance, $\frac{\rho}{\pi(r_3^2-r_2^2)}$, and skin effect impedance, $\frac{\rho m}{2\pi r_3}$, at low and high frequencies (i.e. below 1 mHz and above 10 kHz respectively).

B.1.5 Calculation of the outer insulation series impedance $z_{sg_{insul}}$

As for the inner insulation, the impedance of the outer insulation, due to the time varying magnetic field, is related to the magnetic permeability of the insulation.

$$z_{sg_{insul}}(\omega) = \frac{j\omega\mu_{sg_{insul}}}{2\pi} ln\left(\frac{r_4}{r_3}\right) \tag{B.12}$$

where r_4 and r_3 are respectively the outer and inner radius of the insulation.

The outer insulation series impedance is fairly accurate and does not include any simplifications that might cause problems when calculating the total series impedance matrix.

B.1.6 Calculation of the mutual series impedance of the two loops z_{mutual}

This impedance is also called the screen mutual impedance. The screen mutual impedance is related to

- the voltage difference longditudally on the outer surface of the screen because of unit current return through the inner conductor
- the longditudal voltage difference on the inner conductor because of unit current return through the outer surface of the screen (equal to each other)

The modified Bessel functions for the screen mutual impedance are given in B.13.

$$z_{mutual} = \frac{\rho}{2\pi r_2 r_3} \frac{1}{I_1(mr_3)K_1(mr_2) - I_1(mr_2)K_1(mr_3)} \tag{B.13}$$

At low frequencies the screen mutual impedance is represented by the screen DC resistance. At very high frequencies, the penetration depth is so small, that the mutual impedance becomes 0. Therefore an approximation of the modified Bessel function for the screen mutual impedance is, [47]:

$$z_{mutual}(\omega) = \frac{\rho m}{\pi(r_2 + r_3)} csch(m(r_3 - r_2)) \tag{B.14}$$

Now for large x, $csch(x)$ approaches 0, and therefore B.14 approaches 0 at high frequencies. At low frequencies, $m \cdot csch(mx)$ approaches 1, and therefore B.14 approaches $\frac{\rho}{\pi(r_2+r_3)}$. This approximation

does not give the exact values for low frequencies and can introduce error in the impedance calculations. This error has been addressed by a PhD project published in the end of 2008: "'Accuracy and stability improvements in electromagnetic simulations of power transmission lines and cables"' [50]. In this project, the fitting of the propagation and admittance matrixes use the exact DC resistance, $\frac{\rho}{\pi(r_3^2-r_2^2)}$ at low frequencies (i.e. below 1 mHz).

B.1.7 Calculation of the ground self series impedance z_{ground}

This impedance has been the subject of many different papers, for instance [47, 60, 62, 63, 64, 65]. This is the most difficult impedance to calculate and the one with largest errors.

The analytical calculations of the earth return impedance was first developed by Pollaczek in 1926 [66].

If considering the cable homogeneous in the longitude direction, the earth return impedance in (x, y) coordinates can be expressed as a function of the modified Bessel function of second kind, [64, 66].

$$z_{ground}(\omega) = \frac{\rho m^2}{2\pi}\left[K_0(mr_4) - K_0(m\sqrt{r_4^2+4d^2}) + \int_{-\infty}^{\infty}\frac{e^{-2d\sqrt{\alpha^2+m^2}}}{|\alpha|+\sqrt{\alpha^2+m^2}}e^{j\alpha r_4}d\alpha\right] \quad \text{(B.15)}$$

where d is the buried depth of the cable
r_4 is the outer radius of the cable's outer insulation
Permeability $\mu_{earth} = \mu_{air}$ is assumed.

The calculation of B.15 requires computation of the modified Bessel functions using available standard methods and the more difficult computation of the integral using numerical methods [62]. For simplification, many have introduced approximate formulas for B.15, as will be shown in the following.

$z_{ground}(\omega)$ calculated by Wedepohl and Wilcox

Wedepohl and Wilcox introduced the approximate formula [47]:

$$z_{ground}(\omega) = \frac{j\omega\mu}{2\pi}\left[-ln\left(\frac{\gamma m r_4}{2}+\frac{1}{2}-\frac{4md}{3}\right)\right] \quad \text{(B.16)}$$

where $\gamma = \lim_{n\to\infty}\sum_{k=1}^{n}\left[\frac{1}{k} - ln(n)\right] = 0.577215665$ is Euler's constant

It was shown in 1986 by Srivallipuranandan, [67], that this approximation is valid as long as $|mr_4| < 0.25$, [14]. Furthermore T.T. Nguyen showed that the approximation gives large errors at high frequency, or 35% error in the earth return resistance for 1 MHz, [62]. Therefore, this widely used, simplified formula is not acceptable for transient studies.

$z_{ground}(\omega)$ calculated by Saad, Gaba and Giroux

In 1996 Saad, Gaba and Giroux introduced a closed form approximation of Pollaczek's equation [60]. They used similar procedures as Deri, Tevan, Semlyen and Castanheira used for simplifying Carson's

integral for OHL in 1981 [63]. They start by finding an approximation for the integral in B.15 by use of Cauchy integral theory for two closed paths in the complex ground return plane.

$$z_{ground}(\omega) = \frac{\rho m^2}{2\pi}\left[K_0(mr_4) - K_0(m\sqrt{r_4^2+4d^2}) + K_0(m\sqrt{r_4^2+4d^2}) + \frac{2}{4+m^2r_4^2}e^{-2dm}\right] \quad \text{(B.17)}$$

By assuming $\frac{r_4}{d} < 1$, which is usually the case
$\frac{\sqrt{\delta^2+1}}{\delta+\sqrt{\delta^2+1}} = \frac{1+e^{-2\delta}}{2}$, where $\delta = \frac{\alpha}{m}$ is a dimensionless complex integration variable.

The latter assumption above has been shown to give only up to 3% error [60] compared with the exact value.
The Saad, Gaba and Giroux approximation then becomes as in equation B.18.

$$z_{ground}(\omega) = \frac{\rho m^2}{2\pi}\left[K_0(mr_4) + \frac{2}{4+m^2r_4^2}e^{-2dm}\right] \quad \text{(B.18)}$$

$z_{ground}(\omega)$ calculated by Ametani from Carson's theory

By recognising that for low frequencies, $|m| << |\alpha|$, then $e^{-2d\sqrt{\alpha^2+m^2}} \rightarrow e^{-2d\alpha}$, Ametani showed how the integral part of equation B.15 becomes identical to Carson's earth return impedance [14]. This can be justified by that at low frequencies, the penetration depth of the earth return current is so deep, that one can approximate it by using equations for OHL's. This makes the earth return impedance quite simple and is very accurate for frequencies of up to 10 kHz [14].

$$z_{ground}(\omega) = \frac{\rho m^2}{2\pi}\left[K_0(mr_4) - K_0(m\sqrt{r_4^2+4d^2}) + \int_{-\infty}^{\infty}\frac{e^{-2d|\alpha|}}{|\alpha|+\sqrt{\alpha^2+m^2}}e^{j\alpha r_4}d\alpha\right] \quad \text{(B.19)}$$

Summary for earth return impedance

As shown in above, there are several different approximations for Pollaczek's earth return impedance theorem. When using such approximations, one must be careful as they are not valid for the whole frequency range. With today's computational capacity, it is more and more easy to use numerical methods for directly calculating the integral term of equation B.15.

For analytical calculation of the earth return impedance EMTDC/PSCAD uses a modified version of the Wedepohl and Wilcox approximation. This modified method takes account for higher frequencies and is highly accurate ($< 1.5\%$) for very low frequencies and up to several hundreds of MHz.

B.2 Series impedance matrix of multiple single conductor cables

For a three cable system consisting of 3 single core cables, the total mesh domain series impedance matrix can be expressed by:

$$Z_{series_{mesh}} = \begin{bmatrix} Z_{11} & Z_{12} & Z_{13} \\ Z_{21} & Z_{22} & Z_{23} \\ Z_{31} & Z_{32} & Z_{33} \end{bmatrix} \tag{B.20}$$

where $Z_{ii} = \begin{bmatrix} z_1 & z_2 \\ z_3 & z_4 \end{bmatrix}$ is explained in section B.1.

Z_{ij} is a two by two matrix for single core conductors having only two conducting layers, core conductor and screen.

$$Z_{ij} = \begin{bmatrix} z_{m1} & z_{m2} \\ z_{m3} & z_{m4} \end{bmatrix}$$

where $z_{m1} = 0$ is the mutual for conductor-screen loops of cable i and cable j
$z_{m2} = 0$ is the mutual for conductor-screen loop of cable i and screen-ground loop of cable j
$z_{m3} = 0$ is the mutual for screen-ground loop of cable i and conductor-screen loop of cable j
$z_{m4} = z_{ground-mutual}$ is the mutual for screen-ground loops of cable i and j.

The mutual earth return impedance, $z_{ground-mutual}$, is calculated in a similar manner as the self earth impedance, where r_4 is replaced by x, the horizontal distance between cables i and j, and $4d^2$ is replaced by $(d_i - d_j)^2$, the difference in buried depths of cables i and j. The mutual earth return impedance is:

$$\begin{aligned} z_{ground-mutual} = \frac{\rho m^2}{2\pi} \Bigg[& K_0(mx) - K_0(m\sqrt{(x^2 + (d_i - d_j)^2)}) \\ & + \int_{-\infty}^{\infty} \frac{e^{-(d_i+d_j)\sqrt{\alpha^2+m^2}}}{|\alpha| + \sqrt{\alpha^2 + m^2}} e^{j\alpha x} d\alpha \Bigg] \end{aligned} \tag{B.21}$$

This is not the final form of the impedance matrix used in phase domain model calculations. First the mesh domain results must be used and implemented in phase domain.
Figure B.2 is used for gaining an understanding of the relationship between mesh and phase domain equations.

Figure B.2 shows the equivalent circuit for unit length impedances. In mesh domain the voltages and currents for each loop is considered, equation B.22.

$$\begin{bmatrix} V^1_{C-S} \\ V^1_{S-G} \\ V^2_{C-S} \\ V^2_{S-G} \\ V^3_{C-S} \\ V^3_{S-G} \end{bmatrix} = \begin{bmatrix} z^1_1 & z^1_2 & 0 & 0 & 0 & 0 \\ z^1_3 & z^1_4 & 0 & z_{gm12} & 0 & z_{gm13} \\ 0 & 0 & z^2_1 & z^2_2 & 0 & 0 \\ 0 & z_{gm12} & z^2_3 & z^2_4 & 0 & z_{gm23} \\ 0 & 0 & 0 & 0 & z^3_1 & z^3_2 \\ 0 & z_{gm13} & 0 & z_{gm23} & z^3_3 & z^3_4 \end{bmatrix} \cdot \begin{bmatrix} I^1_{CS} \\ I^1_{SG} \\ I^2_{CS} \\ I^2_{SG} \\ I^3_{CS} \\ I^3_{SG} \end{bmatrix} \tag{B.22}$$

where z^1_i, z^2_i and z^3_i are impedances of cable 1, 2 and 3 respectively.
V^1_i, V^2_i and V^3_i are mesh voltages of cable 1, 2 and 3 respectively.
I^1_i, I^2_i and I^3_i are mesh currents of cable 1, 2 and 3 respectively.
z^i_1, z^i_2, z^i_3 and z^i_4 are given in equation B.2.
z_{gmij} is the mutual ground impedance between cables i and j.

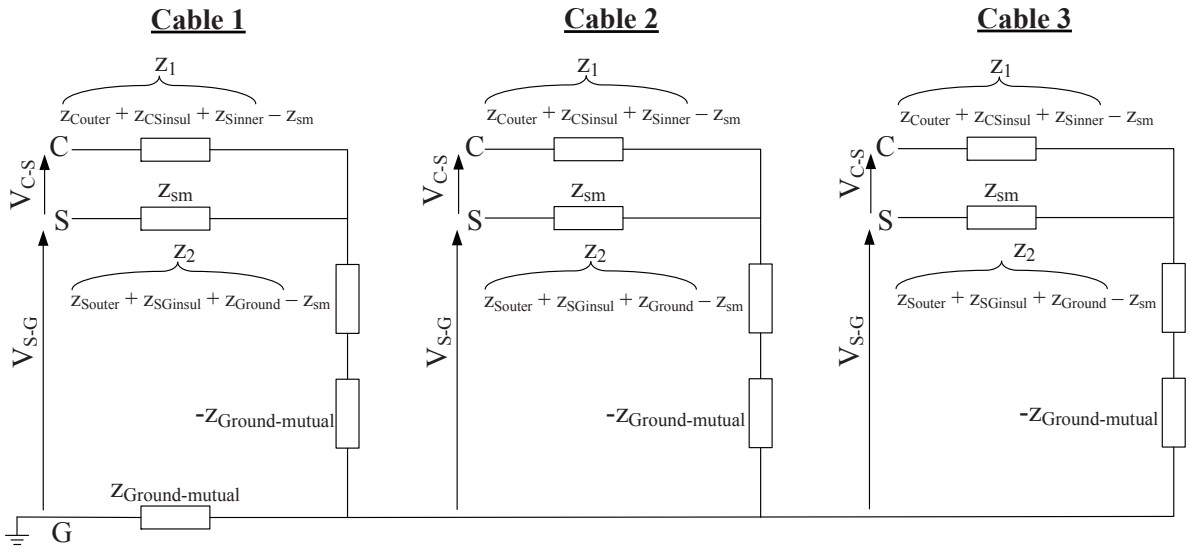

Figure B.2: *Mesh domain equivalent circuit for unit length impedances.*

For reaching the phase domain solutions, figure B.2 is used with phase currents and voltages as variables instead of mesh currents and voltages. Therefore now I^1_{CG}, I^1_{SG}, I^2_{CG}, I^2_{SG}, I^3_{CG}, I^3_{SG}, V^1_{C-G}, V^1_{S-G}, V^2_{C-G}, V^2_{S-G}, V^3_{C-G} and V^3_{S-G} are the variables.

By using these variables, the phase domain impedance matrix can be constructed from figure B.2, see equation B.23.

$$\begin{bmatrix} V^1_{C-G} \\ V^1_{S-G} \\ V^2_{C-G} \\ V^2_{S-G} \\ V^3_{C-G} \\ V^3_{S-G} \end{bmatrix} = \begin{bmatrix} z^1_{11} & -z^1_{12} & z_{gm12} & z_{gm12} & z_{gm13} & z_{gm13} \\ -z^1_{12} & z^1_{22} & z_{gm12} & z_{gm12} & z_{gm13} & z_{gm13} \\ z_{gm12} & z_{gm12} & z^2_{11} & -z^2_{12} & z_{gm23} & z_{gm23} \\ z_{gm12} & z_{gm12} & -z^2_{12} & z^2_{22} & z_{gm23} & z_{gm23} \\ z_{gm13} & z_{gm13} & z_{gm23} & z_{gm23} & z^3_{11} & z^3_{12} \\ z_{gm13} & z_{gm13} & z_{gm23} & z_{gm23} & -z^3_{12} & z^3_{22} \end{bmatrix} \cdot \begin{bmatrix} I^1_{CG} \\ I^1_{SG} \\ I^2_{CG} \\ I^2_{SG} \\ I^3_{CG} \\ I^3_{SG} \end{bmatrix} \tag{B.23}$$

where $z^i_{11} = z^i_1 + z^i_4 - 2z^i_2$
$z^i_{12} = z^i_4 - z^i_2$
$z^i_{22} = z^i_4$

B.3 Mathematical expression of the cable shunt admittance matrix Y

The shunt admittance matrix Y_{shunt} is somewhat simpler to construct than the series impedance matrix. The mesh domain equations from figure B.1 for the admittance matrix is

$$\begin{bmatrix} I_c \\ I_s \end{bmatrix} = \overbrace{\begin{bmatrix} y_1 & -y_1 \\ -y_1 & y_2 \end{bmatrix}}^{Y_{shunt}} \cdot \begin{bmatrix} V_{c-s} \\ V_{s-g} \end{bmatrix} \tag{B.24}$$

For the case of one single conductor cable the admittances are calculated from the insulation parameters.

$$y_i = G_i + j\omega C_i \tag{B.25}$$

where G_i is the shunt conductance per unit length for insulation layer i
$C_i = \frac{2\pi\epsilon_i}{ln\left(\frac{b}{a}\right)}$ is the capacitance per unit length of insulation layer i with permittivity ϵ_i, outer radius b and inner radius a.

Equation B.25 does not take account for the semiconductive layers. Therefore when the parameters are set for a cable model, the permittivity must be corrected to include the semiconductive layers, [36], see equation B.26.

$$\epsilon = \epsilon_{is} \cdot \frac{ln(r_i/r_o)}{ln(b/a)} \tag{B.26}$$

where ϵ_{is} is 2.3 for pure XLPE.
r_i is the inner radius of the screen and r_o is the outer radius of the conductor.

For multiple single conductor cables, there is no mutual coupling in the admittances of adjacent cables. Therefore the full mesh domain shunt admittance matrix for a three cable system with three single core cables is:

$$Y_{shunt_{mesh}} = \begin{bmatrix} Y_{11} & 0 & 0 \\ 0 & Y_{22} & 0 \\ 0 & 0 & Y_{33} \end{bmatrix} \tag{B.27}$$

where Y_{ii} is the shunt admittance matrixes explained in equation B.24.

Now similarly as for the impedance matrix in chapter B.2 the phase domain admittance matrix can be constructed as shown in equation B.28.

$$Y_{shunt_{mesh}} = \begin{bmatrix} y_1^1 & -y_1^1 & 0 & 0 & 0 & 0 \\ -y_1^1 & y_1^1 + y_2^1 & 0 & 0 & 0 & 0 \\ 0 & 0 & y_1^2 & -y_1^2 & 0 & 0 \\ 0 & 0 & -y_1^1 & y_1^2 + y_2^2 & 0 & 0 \\ 0 & 0 & 0 & 0 & y_1^3 & -y_1^3 \\ 0 & 0 & 0 & 0 & -y_1^1 & y_1^1 + y_2^1 \end{bmatrix} \tag{B.28}$$

where y_1^i and y_2^i for each cable i is given in equation B.25.

There are no assumptions in the calculations for the shunt admittances and therefore this admittance is fairly correct in all cases. One must though be aware of that equation B.25 does not take account for semiconductive layers. Therefore when the parameters are set for a cable model, the permittivity must be corrected to include the semiconductive layers.

APPENDIX **C**

Physical data of cable used in simulated examples

Field measurements are performed on two different cable systems. For planning the field measurements, and later for model validation, the two cable systems are modelled using the Frequency Dependent Phase Model in EMTDC/PSCAD. For such modelling purposes, this appendix gives all needed cable data. The data in appendix C.1 are used in chapter 7, while the data in appendix C.2 are used in chapters 8-10.

C.1 The measured 400 kV cable system

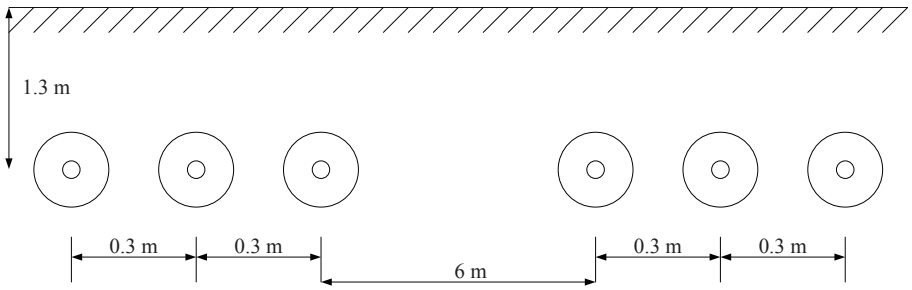

Figure C.1: *Cross sectional layout for the measured 400 kV cable system. The line consists of two 2 parallel three phase systems placed in flat formation 1.3 m below the surface.*

Cable interface	
Input parameters	**Installed values**
Number of cables	3
Cable Electrical Connections	Cond & Sheath

Table C.1: *Parameters for cable interface of the measured 400 kV cable system*

Cable configuration - FDPM options	
Input parameters	**Installed values**
Steady-State Frequency	50 Hz
	Interpolate Travel Times No detailed output files Not a reflectionless line
Lower frequency limit	0.5 Hz
Upper frequency limit	1 MHz
Total number of frequency increments	100
Max # of poles for surge admittance	20
Max # of poles for propagation function	20
Maximum fitting error for surge admittance	0.2 %
Maximum fitting error for propagation function	0.2 %
0 to F0	1
F0:	1
F0 to max	1

Table C.2: *Parameters for cable configuration - Frequency dependent phase model options of the measured 400 kV cable system*

Cable configuration - Ground plane	
Input parameters	**Installed values**
Ground resistivity	150 Ωm
Relative ground permeability	1
Earth return formula	Analytical approximation

Table C.3: *Parameters for cable configuration - ground plane options of the measured 400 kV cable system*

Cable configuration - Cable constants Coax cable data	
Input parameters	**Installed values**
Depth of cable	1.3 m
X position of cable	there are 0.3 m between the phases
Cable configuration	C1-I1-C2-I2
	Last metallic layer is not grounded
C1 inner radius	0 m
C1 outer radius	21.6 mm
C1 resistivity	$3.4567 \cdot 10^{-8}\ \Omega m$
C1 relative permeability	1
I1 outer radius	51.02 mm
I1 relative permittivity	2.7588
I1 relative permeability	1.0385
C2 outer radius	53.41 mm
C2 resistivity	$5.66 \cdot 10^{-8}\ \Omega m$
C2 relative permeability	1
I2 outer radius	57.71 mm
I2 relative permittivity	2.5
I2 relative permeability	1

Table C.4: *Parameters for cable configuration - cable data of the measured 400 kV cable system*

C.2 The measured 150 kV cable system

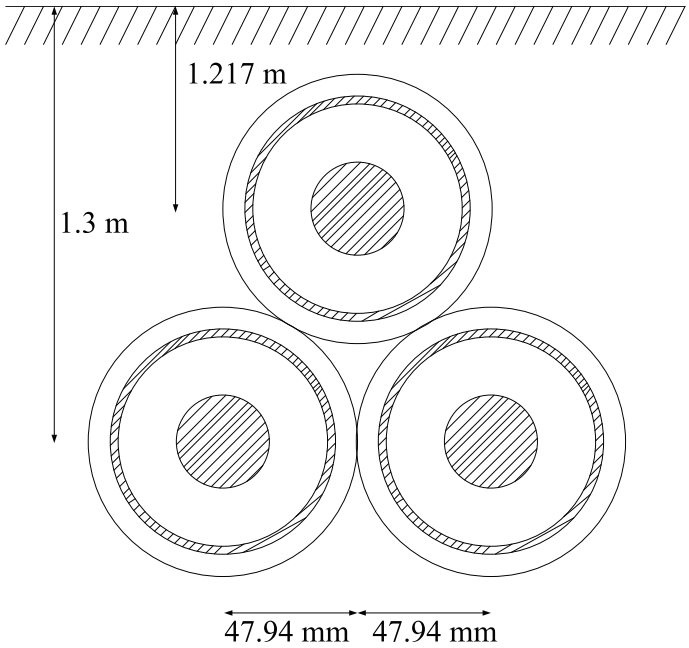

Figure C.2: *Cross sectional layout for the 150 kV cable system.*

Cable interface	
Input parameters	**Installed values**
Number of cables	3
Cable Electrical Connections	Cond & Sheath

Table C.5: *Parameters for cable interface of the measured 150 kV cable system*

Cable configuration - FDPM options	
Input parameters	**Installed values**
Steady-State Frequency	50 Hz
	Interpolate Travel Times No detailed output files Not a reflectionless line
Lower frequency limit	0.5 Hz
Upper frequency limit	100 MHz
Total number of frequency increments	100
Max # of poles for surge admittance	20
Max # of poles for propagation function	20
Maximum fitting error for surge admittance	0.2 %
Maximum fitting error for propagation function	0.2 %
0 to F0	1
F0:	1
F0 to max	1

Table C.6: *Parameters for cable configuration - Frequency dependent phase model options of the measured 150 kV cable system*

Cable configuration - Ground plane	
Input parameters	**Installed values**
Ground resistivity	100 Ωm
Relative ground permeability	1
Earth return formula	Analytical approximation

Table C.7: *Parameters for cable configuration - ground plane options of the measured 150 kV cable system*

Cable configuration - Cable constants Coax cable data		
Input parameters	**Installed values**	**Layered screen**
Depth of cable	1.3 m	
X position of cable	see figure C.2	
Cable configuration	C1-I1-C2-I2	
	Last metallic layer is not grounded	
C1 inner radius	0 m	
C1 outer radius	20.75 mm	
C1 resistivity	$3.19 \cdot 10^{-8}\ \Omega m$	
C1 relative permeability	1	
I1 outer radius	40.85 mm	
I1 relative permittivity	2.68	
I1 relative permeability	1.08	
C2 outer radius	42.76 mm	41.96 mm (wired screen) 42.76 mm (laminate screen)
C2 resistivity	$1.19 \cdot 10^{-7}\ \Omega m$	$0.91 \cdot 10^{-7}\ \Omega m$ (wired screen) $2.83 \cdot 10^{-8}\ \Omega m$ (laminate screen)
C2 relative permeability	1	
I2 outer radius	47.94 mm	
I2 relative permittivity	2.5	
I2 relative permeability	1	

Table C.8: *Parameters for cable configuration - cable data of the measured 150 kV cable system*

APPENDIX **D**

Examples for improvements of cable model

D.1 Placement of elements

The elements are placed by use of x-y coordinates, where the (0,0) coordinates is in the centre of one of the three cables. Figure D.1 shows the placement of three cables in a tight trefoil with their centres defined and one random element highlighted in red. How this element is placed in the program is shown in the following.

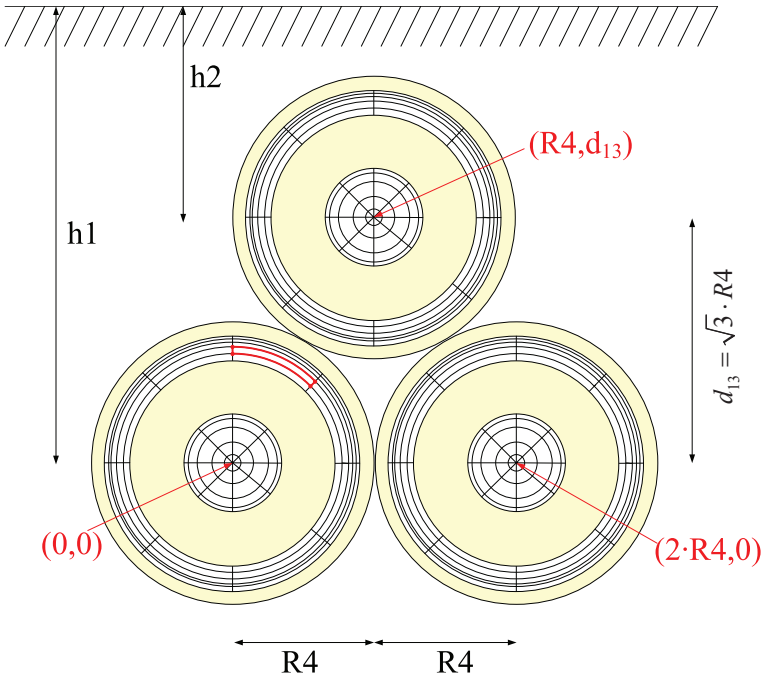

Figure D.1: *Cross sectional layout for a three phase single core cable system with subdivision of conductors. A single element for giving example of elemental placement is highlighted in red.*

When placing the element, a base coordinate is given at the centre of the bottom of the element, $(subX, subY)$ in figure D.2(b). This point is calculated from the angle A of the element and the radius of the central arc in the element, purple line in figure D.2(b). For finding the size of the element, the length of the central arc inside the element and the width of the element are given. This is shown in figure D.2(a) .

As the impedance calculations use the geometric mean distance (GMD) between two elements, it is helpful to divide each element into a number of points (6 points in this case) and calculate the GMD between two points of elements. These points are placed such that there is always the same angle and distance between a set of two points, see points in figure D.2(b). Furthermore they are placed on the central arc

inside the elements. For two elements, each containing 6 points, 36 distances will be calculated.

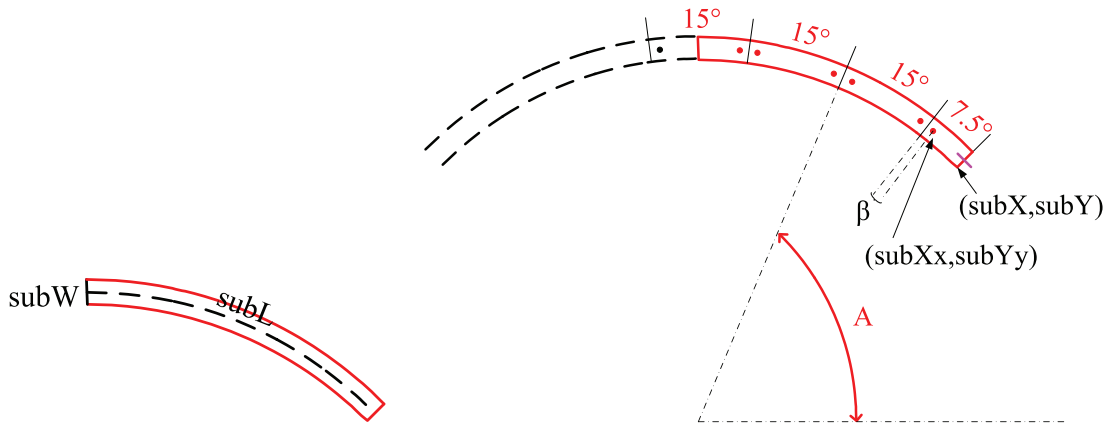

(a) Central arc and size of element. (b) Central points for GMD calculations and base coordinate.

Figure D.2: *Coordinates, placement and size of the sample element from figure D.1.*

The output from placing the element will be following:

$$
\begin{aligned}
&(subX, subY) = x0 + (R1 + subR)cos(A)\\
&subL = 2\pi(R1 + subR)/Ns\\
&subW = 2 * subR\\
&[subXx\ subYy] \quad = \quad
\begin{bmatrix}
x0 + (R1 + subR)cos(A - 15° - \beta) & y0 + (R1 + subR)sin(A - 15° - \beta)\\
x0 + (R1 + subR)cos(A - 15° + \beta) & y0 + (R1 + subR)sin(A - 15° + \beta)\\
x0 + (R1 + subR)cos(A - \beta) & y0 + (R1 + subR)sin(A - \beta)\\
x0 + (R1 + subR)cos(A + \beta) & y0 + (R1 + subR)sin(A + \beta)\\
x0 + (R1 + subR)cos(A + 15° - \beta) & y0 + (R1 + subR)sin(A + 15° - \beta)\\
x0 + (R1 + subR)cos(A + 15° + \beta) & y0 + (R1 + subR)sin(A + 15° + \beta)
\end{bmatrix}
\end{aligned}
$$

Where R1 is the inner radius of the conductor containing the subconductor element, subR is the half of the thickness of the element, Ns is the number of subconductors (elements) in each strand, A is the angle of the element, $\beta = 0.564 \cdot 7.5°$ is the placement of the point within the divided element, x0 and y0 are the x-y coordinates of the center of the subdivided conductor; (0,0) in this case.

For placement of all elements, these outputs will be given for each and every subconductor of the three cables.

D.2 GMD between elements

For calculating the GMD between elements with suitable accuracy, each element is divided into sectors and the GMD between points in each sector of two elements is calculated. An example of such distances between two elements is shown in figure D.3. This example is based on the same elemental placement as explained in appendix D.1. The figure only shows distances from two points in one element.

Before the GMD's are calculated, the elements are placed with central points as explained in appendix D.1. Each x and y coordinates of each point in every element of every conductor of all three cables is

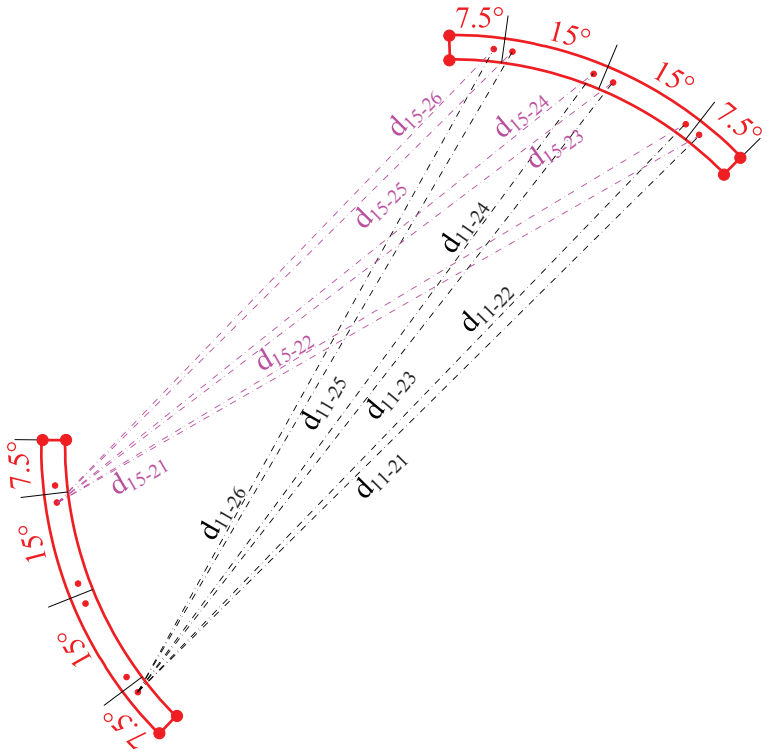

Figure D.3: *An example of distance between two points in one element and all points in another element for GMD calculations.*

placed in a matrix. By calling the correct points in the matrix, it is possible to calculate the GMD of every element. For the example in figure D.3 this is done as shown in equation D.1.

$$\begin{aligned} d_{ik-jm} &= \sqrt{(x_{ik}-x_{jm})^2+(y_{ik}-y_{jm})^2} \\ GMD_{ij} &= \sqrt[36]{d_{11-21}d_{11-22}d_{11-23}d_{11-24}d_{11-25}d_{11-26}\cdot d_{12-21}\ldots d_{12-26}\cdot\ldots\cdot d_{16-26}} \end{aligned} \quad \text{(D.1)}$$

where i and j are two elements.
k and m are points within elements i and j respectively.
d_{ik-jm} is the distance between point k in element i and point m in element j.
GMD_{ij} is the GMD between elements i and j.

D.3 Bundling of parallel conductors

When several impedances are connected in parallel, it is possible to eliminate all except one voltage/current relationships and hence reduce the impedance matrix. As an example, a single cable with 3 conductors, core and two screens, is considered. For reduction, the third conductor shall be removed.

$$\begin{bmatrix} V_C \\ V_{Sh1} \\ V_{Sh2} \end{bmatrix} = \begin{bmatrix} Z_{11} & Z_{12} & Z_{13} \\ Z_{12} & Z_{22} & Z_{23} \\ Z_{13} & Z_{23} & Z_{33} \end{bmatrix} \cdot \begin{bmatrix} i_C \\ i_{Sh1} \\ i_{Sh2} \end{bmatrix} \quad \text{(D.2)}$$

where $V_{Sh1} = V_{Sh2}$.

For equation D.2, the second row is subtracted from the third and the second column is subtracted from the third resulting in equation D.3. This can be done because $V_{Sh1} = V_{Sh2}$

$$\begin{bmatrix} V_C \\ V_{Sh1} \\ 0 \end{bmatrix} = \begin{bmatrix} Z_{11} & Z_{12} & Z_{13} - Z_{12} \\ Z_{12} & Z_{22} & Z_{23} - Z_{22} \\ Z_{13} - Z_{12} & Z_{23} - Z_{22} & Z_{33} - 2Z_{23} + Z_{22} \end{bmatrix} \cdot \begin{bmatrix} i_C \\ i_{Sh1} + i_{Sh2} \\ i_{Sh2} \end{bmatrix} \tag{D.3}$$

From equation D.3, the i_{Sh2} current can be calculated as shown in equation D.4.

$$\begin{aligned} 0 &= (Z_{13} - Z_{12})i_C + (Z_{23} - Z_{22})(i_{Sh1} + i_{Sh2}) + (Z_{33} - 2Z_{23} + Z_{22})i_{Sh2} \\ &\Rightarrow \quad i_{Sh2} = -(Z_{33} - Z_{23})^{-1}[(Z_{13} - Z_{12})i_C + (Z_{23} - Z_{22})i_{Sh1}] \end{aligned} \tag{D.4}$$

By substituting equation D.4 into D.3 the impedance matrix can be reduced to a 2x2 matrix as shown in equation D.5.

$$\begin{bmatrix} V_C \\ V_{Sh1} \end{bmatrix} = \begin{bmatrix} Z'_{11} & Z'_{12} \\ Z'_{12} & Z'_{22} \end{bmatrix} \cdot \begin{bmatrix} i_C \\ i_{Sh1} \end{bmatrix} \tag{D.5}$$

where $Z'_{11} = Z_{11} - (Z_{13} - Z_{12})(Z_{33} - Z_{23})^{-1} Z_{13}$
$Z'_{12} = Z_{12} - (Z_{23} - Z_{22})(Z_{33} - Z_{23})^{-1} Z_{23}$
$Z'_{21} = Z'_{12}$
$Z'_{22} = Z_{22} - (Z_{23} - Z_{22})(Z_{33} - Z_{23})^{-1} Z_{23}$

or $Z'_{ik} = Z_{ik} - (Z_{k3} - Z_{k2})(Z_{33} - Z_{23})^{-1} Z_{i3}$

This reduction method can be used on every voltage/current relationship matrices, when the voltage is identical for all current loops.

D.4 Reduction of elemental matrix to conductor matrix

Voltage/current relationship for a three phase cable system, where each cable has two subdivided conductors is as shown in equation D.6.

$$\begin{bmatrix} V_{c1_1} \\ \vdots \\ V_{c1_{n1}} \\ V_{c1_{n1+1}} \\ \vdots \\ V_{c1_{n2}} \\ V_{c2_1} \\ \vdots \\ V_{c2_{n1}} \\ V_{c2_{n1+1}} \\ \vdots \\ V_{c2_{n2}} \\ V_{c3_1} \\ \vdots \\ V_{c3_{n1}} \\ V_{c3_{n1+1}} \\ \vdots \\ V_{c3_{n2}} \end{bmatrix} = \begin{bmatrix} [Z_{c1}] & [Z_{c1c2}] & [Z_{c1c3}] \\ [Z_{c1c2}] & [Z_{c2}] & [Z_{c2c3}] \\ [Z_{c1c3}] & [Z_{c2c3}] & [Z_{c3}] \end{bmatrix} \cdot \begin{bmatrix} i_{c1_1} \\ \vdots \\ i_{c1_{n1}} \\ i_{c1_{n1+1}} \\ \vdots \\ i_{c1_{n2}} \\ i_{c2_1} \\ \vdots \\ i_{c2_{n1}} \\ i_{c2_{n1+1}} \\ \vdots \\ i_{c2_{n2}} \\ i_{c3_1} \\ \vdots \\ i_{c3_{n1}} \\ i_{c3_{n1+1}} \\ \vdots \\ i_{c3_{n2}} \end{bmatrix} \tag{D.6}$$

where subscripted ci represents cable i.
$V_{ci_1} = V_{ci_2} = \cdots = V_{ci_{n1}}$
$V_{ci_{n1+1}} = V_{ci_{n1+2}} = \cdots = V_{ci_{n2}}$
$V_{ci_1} \neq V_{ci_{n1+1}}$
$V_{c1_1} \neq V_{c2_1} \neq V_{c3_1}$
$V_{c1_{n1+1}} \neq V_{c2_{n1+1}} \neq V_{c3_{n1+1}}$
subscripted ci_1-ci_{n_1} relate to subconductors of core conductor of cable i
subscripted ci_{n_1+1}-ci_{n_2} relate to subconductors of screen conductor of cable i

Each of the impedance matrices in equation D.6 are shown in equations D.7 - D.8, where the form of the matrices is given. The placement of individual impedances can be related to the subscripting in the voltage vector of equation D.6.

$$Z_{ci} = \begin{bmatrix} Z_{ci_1} & \cdots & Z_{ci_1ci_{n1}} & \cdots & \cdots & Z'_{ci_1ci_{n2}} \\ \vdots & \ddots & & & & \vdots \\ \vdots & & Z_{ci_{n1}} & & & \vdots \\ \vdots & & & Z'_{ci_{n1+1}} & & \vdots \\ \vdots & & & & \ddots & \vdots \\ Z'_{ci_1ci_{n2}} & \cdots & \cdots & \cdots & \cdots & Z'_{ci_{n2}} \end{bmatrix} \tag{D.7}$$

$$Z_{cicj} = \begin{bmatrix} Z_{ci_1cj_1} & \cdots & Z_{ci_1cj_{n1}} & \cdots & \cdots & Z'_{ci_1cj_{n2}} \\ \vdots & \ddots & & & & \vdots \\ \vdots & & Z_{ci_{n1}cj_{n1}} & & & \vdots \\ \vdots & & & Z'_{ci_{n1+1}cj_{n1+1}} & & \vdots \\ \vdots & & & & \ddots & \vdots \\ Z'_{ci_1cj_{n2}} & \cdots & \cdots & \cdots & \cdots & Z'_{ci_{n2}cj_{n2}} \end{bmatrix} \tag{D.8}$$

Where for $n1 + 1$ to $n2$ the impedances are marked Z' because they are the result after merging the layered screen into 1, as shown in chapter 13.3.1.

Before performing reduction, the matrices need to be re-ordered such that the first subconductor of each conductor for the three cables is moved to the top. This re-ordering is shown in equation D.9.

$$\begin{bmatrix} V_{c1_1} \\ V_{c2_1} \\ V_{c3_1} \\ V_{c1_{n1+1}} \\ V_{c2_{n1+1}} \\ V_{c3_{n1+1}} \\ V_{c1_2} \\ \vdots \\ V_{c1_{n1}} \\ V_{c1_{n1+2}} \\ \vdots \\ V_{c1_{n2}} \\ V_{c2_2} \\ \vdots \\ V_{c2_{n1}} \\ V_{c2_{n1+2}} \\ \vdots \\ V_{c2_{n2}} \\ V_{c3_2} \\ \vdots \\ V_{c3_{n1}} \\ V_{c3_{n1+2}} \\ \vdots \\ V_{c3_{n2}} \end{bmatrix} = \begin{bmatrix} [Z_1] & [Z_2] \\ [Z_3] & [Z_4] \end{bmatrix} \cdot \begin{bmatrix} i_{c1_1} \\ i_{c2_1} \\ i_{c3_1} \\ i_{c1_{n1+1}} \\ i_{c2_{n1+1}} \\ i_{c3_{n1+1}} \\ i_{c1_2} \\ \vdots \\ i_{c1_{n1}} \\ i_{c1_{n1+2}} \\ \vdots \\ i_{c1_{n2}} \\ i_{c2_2} \\ \vdots \\ i_{c2_{n1}} \\ i_{c2_{n1+2}} \\ \vdots \\ i_{c2_{n2}} \\ i_{c3_2} \\ \vdots \\ i_{c3_{n1}} \\ i_{c3_{n1+2}} \\ \vdots \\ i_{c3_{n2}} \end{bmatrix} \tag{D.9}$$

For understanding how $[Z_1]$, $[Z_2]$, $[Z_3]$ and $[Z_4]$ are calculated, equations D.10-D.13 show the form of the matrices, where each subscript in red (appointed to subconductors of cores and screens of the cables) relate to the correct voltages and currents in equation D.9. Because of the size and complexity of the matrices, only the form and relation to given subconductors is shown.

$$
Z_1 = \begin{array}{c} \\ c1_1 \rightarrow \\ c2_1 \rightarrow \\ c3_1 \rightarrow \\ c1_{n1+1} \rightarrow \\ c2_{n1+1} \rightarrow \\ c3_{n1+1} \rightarrow \end{array}
\begin{array}{c}
\begin{array}{cccccc} c1_1 & c2_1 & c3_1 & c1_{n1+1} & c2_{n1+1} & c3_{n1+1} \end{array} \\
\begin{bmatrix}
Z_{ci_1cj_1} & \cdots & Z_{ci_1cj_{n1}} & \cdots & \cdots & Z_{ci_1cj_{n2}} \\
\vdots & \ddots & & & & \vdots \\
\vdots & & Z_{ci_{n1}cj_{n1}} & & & \vdots \\
\vdots & & & Z'_{ci_{n1+1}cj_{n1+1}} & & \vdots \\
\vdots & & & & \ddots & \vdots \\
Z'_{ci_1cj_{n2}} & \cdots & \cdots & \cdots & \cdots & Z'_{ci_{n2}cj_{n2}}
\end{bmatrix}
\end{array}
\tag{D.10}
$$

$$
Z_2 = \begin{array}{c} \\ c1_1 \rightarrow \\ c2_1 \rightarrow \\ c3_1 \rightarrow \\ c1_{n1+1} \rightarrow \\ c2_{n1+1} \rightarrow \\ c3_{n1+1} \rightarrow \end{array}
\begin{array}{c}
\begin{array}{ccccccccccc} c1_2 & \cdots & c1_{n1} & c1_{n1+2} & \cdots & c1_{n2} & c2_2 & \cdots & c2_{n2} & c3_2 & \cdots & c3_{n2} \end{array} \\
\begin{bmatrix} \\ \\ \\ \\ \\ \\ \end{bmatrix}
\end{array}
\tag{D.11}
$$

$$
Z_3 = \begin{array}{c} \\ c1_2 \rightarrow \\ \vdots \\ c1_{n1} \rightarrow \\ c1_{n1+2} \rightarrow \\ \vdots \\ c1_{n2} \rightarrow \\ c2_2 \rightarrow \\ \vdots \\ c2_{n1} \rightarrow \\ c2_{n1+2} \rightarrow \\ \vdots \\ c2_{n2} \rightarrow \\ c3_2 \rightarrow \\ \vdots \\ c3_{n1} \rightarrow \\ c3_{n1+2} \rightarrow \\ \vdots \\ c3_{n2} \rightarrow \end{array}
\begin{array}{c}
\begin{array}{cccccc} c1_1 & c2_1 & c3_1 & c1_{n1+1} & c2_{n1+1} & c3_{n1+1} \end{array} \\
\begin{bmatrix} \\ \end{bmatrix}
\end{array}
\tag{D.12}
$$

$$
Z_4 = \begin{array}{c} \\ c1_2 \rightarrow \\ \vdots \\ c1_{n1} \rightarrow \\ c1_{n1+2} \rightarrow \\ \vdots \\ c1_{n2} \rightarrow \\ c2_2 \rightarrow \\ \vdots \\ c2_{n1} \rightarrow \\ c2_{n1+2} \rightarrow \\ \vdots \\ c2_{n2} \rightarrow \\ c3_2 \rightarrow \\ \vdots \\ c3_{n1} \rightarrow \\ c3_{n1+2} \rightarrow \\ \vdots \\ c3_{n2} \rightarrow \end{array}
\begin{array}{c}
\begin{array}{ccccccccccccc} c1_2 & \dots & c1_{n1} & c1_{n1+2} & \dots & c1_{n2} & c2_2 & \dots & c2_{n2} & c3_2 & \dots & c3_{n2} \end{array} \\
\left[\begin{array}{ccccccccccccc} & & & & & & & & & & & & \\ & & & & & & & & & & & & \\ & & & & & & & & & & & & \\ & & & & & & & & & & & & \\ & & & & & & & & & & & & \\ & & & & & & & & & & & & \\ & & & & & & & & & & & & \\ & & & & & & & & & & & & \\ & & & & & & & & & & & & \\ & & & & & & & & & & & & \\ & & & & & & & & & & & & \\ & & & & & & & & & & & & \\ & & & & & & & & & & & & \\ & & & & & & & & & & & & \\ & & & & & & & & & & & & \\ & & & & & & & & & & & & \\ & & & & & & & & & & & & \\ & & & & & & & & & & & & \\ & & & & & & & & & & & & \end{array} \right]
\end{array}
\tag{D.13}
$$

After re-ordering, the matrix can be reduced as explained in appendix D.3, where the first rows/columns of each conductor are subtracted from the rest. When subtracting, one must be careful to relate the subconductors of same conductor. For instance not to perform the subtraction $Z_{c1_{n1+3}} - Z_{c1_3}$,as the first is a member of cable 1 screen and the second is a member of cable 1 core. Correct subtraction for any member of cable 1 screen would be $Z_{c1_{n1+x}} - Z_{c1_{n1+1}}$ where $x > 1$ and $n1 + x$ is a subconductor of the cable 1 screen. Only subconductors having identical voltage drop are subtracted from each other.

As explained in appendix D.3, after performing the subtraction, the matrix can be reduced by merging the subconductors having identical voltage drop. The reduced matrix is therefore calculated from $[Z1] - [Z2][Z4]^{-1}[Z3]$. The result for the reduced matrix is given in equation D.14.

$$
\begin{bmatrix} V_{c1_1} \\ V_{c2_1} \\ V_{c3_1} \\ V_{c1_{n1+1}} \\ V_{c2_{n1+1}} \\ V_{c3_{n1+1}} \end{bmatrix} = \begin{bmatrix} [Z_{cc}] & [Z_{cs}] \\ [Z_{cs}] & [Z_{ss}] \end{bmatrix} \cdot \begin{bmatrix} i_{c1_1} \\ i_{c2_1} \\ i_{c3_1} \\ i_{c1_{n1+1}} \\ i_{c2_{n1+1}} \\ i_{c3_{n1+1}} \end{bmatrix} \tag{D.14}
$$

where $[Z_{cc}]$ is a 3x3 matrix containing core impedances for all three cables.

$[Z_{ss}]$ is a 3x3 matrix containing layered screen impedances for all three cables.
$[Z_{cs}]$ is a 3x3 matrix containing impedance of the core-screen loop.

APPENDIX **E**

Papers

Following is a list of submitted and published papers related to the research work presented in this thesis.

Paper title	**Place of publication**	**Status of publication**
Measurements for validation of high voltage underground cable modelling	IPST09	Published
Field Test and Simulation of a 400 kV Crossbonded Cable System	IEEE Transactions on Power Delivery	Awaiting publication after second review (minimal comments)
Wave propagation and benchmark measurements for cable model validation	IEEE Transactions on Power Delivery	Awaiting acceptance after first review
Double Layered Sheath in Accurate HV XLPE Cable Modeling	IEEE PES GM 2010	Published
Modeling of long High Voltage AC Underground Cables	PhD seminar, Denmark	Published
High Frequency Field Measurements on a 150 kV Underground Cable; Single Minor, Single Major and Several Major Sections	CIGRE International Symposium, Brazil 2011	Abstract submitted in May 2010
Impulse voltage measurements for parameter validation of a 42 km long 150 kV three phase submarine cable	CIGRE International Symposium, Brazil 2011	Abstract submitted in May 2010